

Virtual Reference Interferometry:

Theory & Experiment

By

Michael Anthony Galle

A thesis submitted in conformity with the requirements
for the degree of Doctor of Philosophy

Department of Electrical & Computer Engineering
University of Toronto

© Copyright by Michael Anthony Galle 2014

Virtual Reference Interferometry: Theory & Experiment

Michael Anthony Galle

Doctor of Philosophy

Department of Electrical & Computer Engineering
University of Toronto

2014

Abstract

This thesis introduces the idea that a simulated interferogram can be used as a reference for an interferometer. This new concept represents a paradigm shift from the conventional thinking, where a reference is the phase of a wavefront that traverses a known path. The simulated interferogram used as a reference is called a virtual reference. This thesis develops the theory of virtual reference interferometry and uses it for the characterization of chromatic dispersion in short length ($<1\text{m}$) fibers and optical components.

Characterization of chromatic dispersion on short length fiber and optical components is a very difficult challenge. Accurate measurement of first and second order dispersion is important for applications from optical component design to nonlinear photonics, sensing and communications. Techniques for short-length dispersion characterization are therefore critical to the development of many photonic systems. The current generation of short-length dispersion measurement techniques are either easy to operate but lack sufficient accuracy, or have sufficient accuracy but are difficult to operate. The use of a virtual reference combines the advantages of these techniques so that it is both accurate and easy to operate. Chromatic dispersion measurements based on virtual reference interferometry have similar accuracy as the best conventional measurement techniques due to the ability to measure first and second order dispersion directly from the interference pattern.

Unique capabilities of virtual reference interferometry are demonstrated, followed by a derivation of the operational constraints and system parameters. The technique is also applied to the characterization of few-mode fibers, a hot topic in telecommunications research where mode division multiplexing promises to expand network bandwidth. Also introduced is the theory of dispersive virtual reference interferometry, which can be used to overcome the bandwidth limitations associated with the measurement of near-zero dispersion-length optical components via

compression of the interference pattern. Additionally, a method for utilizing the virtual reference interferometer in a low-coherence setup is introduced, enabling characterization in new wavelength ranges and further reducing the cost of characterization.

Acknowledgments

This thesis is the culmination of over 8 years of study, during which I built a small company (Inometrix Inc. www.inometrix.com) and attended the University of Toronto for my Master's and Ph.D. In that time I also married my wife Elisa and we have had two children: Sophia (5) and Luca (1). In the journey to this point I have had the opportunity to wear many hats; husband, father, scientist, businessperson, and student. Although this thesis focuses on my time as a student, these other elements both shaped and motivated me.

I would like to thank my wife Elisa for believing in me and for her love, support and encouragement throughout all these years.

I would like to express my sincere gratitude to my Supervisor Professor Li Qian for both inspiring me and guiding me during my years as a Master's and Ph.D. student. I am truly grateful for her dedication and encouragement.

I would like to thank Professor Simarjeet Saini at the University of Waterloo, Professor Waleed Mohammed at the University of Bangkok and Eric Zhu at the University of Toronto for their encouragement, collaboration, support and friendship over the years.

I would like to thank my committee members Professor David Sinton and Professor Ofer Levi for their guidance, encouragement and support in the preparation of this Thesis.

I would like to thank my parents for encouraging me to follow my dreams and for their love and support throughout my many years in school.

Finally, I would like to thank the Vanier Canada Graduate Scholarship program for enabling the pursuit of my Ph.D. I could not have done it without the support of this program.

For Sophia and Luca

Table of contents

Abstract.....	ii
Acknowledgments	iv
Table of contents	vi
List of tables	ix
List of figures	x
List of abbreviations	xvii
List of symbols	xviii
Chapter 1. Introduction & background	1
1.1 Overview	1
1.2 Motivation	4
1.3 Objectives.....	6
1.4 Organization of thesis.....	6
Chapter 2. Conventional dispersion characterization techniques	7
2.1 Time-of-flight.....	7
2.2 Modulation-phase-shift	8
2.3 Temporal interferometry	9
2.4 Spectral interferometry.....	10
2.4.1 Unbalanced spectral interferometry	11
2.4.2 Balanced spectral interferometry	22
2.5 Summary & comparison.....	31
Chapter 3. Virtual reference interferometry.....	34
3.1 Introduction & motivation.....	34
3.2 Theory	35
3.3 Unique capabilities of VRI.....	40
3.3.1 Spectral compression	40
3.3.2 Cascaded elements	41
3.3.3 Characterization of narrow-band devices.....	42
3.3.4 Ultra-low dispersion measurements	45
3.4 System parameters.....	46
3.4.1 Minimum required source bandwidth	46
3.4.2 Minimum separation between balance points	47
3.4.3 Measurable bandwidth of the dispersion plots	48
3.4.4 Spectral resolution of dispersion plots	48
3.4.5 Minimum fiber length.....	49

3.4.6	Maximum fiber length	49
3.5	Experiments.....	50
3.5.1	Validation Experiments.....	50
3.5.2	Experiments demonstrating unique or important capabilities of VRI	53
3.6	Conclusion.....	59
Chapter 4.	Virtual reference interferometry: few-mode characterization	62
4.1	Introduction & motivation.....	62
4.2	Theory	64
4.2.1	Polarization modes	64
4.2.2	Transverse modes.....	67
4.3	Experiments.....	69
4.4	Results	70
4.5	Conclusion.....	72
Chapter 5.	Dispersive virtual reference interferometry	73
5.1	Introduction & motivation.....	73
5.2	Theory	75
5.2.1	Minimum bandwidth & spectral compression	78
5.2.2	Design of a dispersive virtual reference	80
5.2.3	Role of the parameters of the dispersive reference	82
5.2.4	Cost of using a dispersive reference: VRI vs. DVRI.....	84
5.3	Experiments.....	85
5.3.1	Experimental validation of theory.....	86
5.3.2	Characterization of gain fiber.....	87
5.3.3	Characterization of dispersion shifted fiber	89
5.4	Conclusion.....	90
Chapter 6.	Low-coherence virtual reference interferometry	91
6.1	Introduction & motivation.....	91
6.2	Theory	93
6.3	Experiment	96
6.4	Conclusion.....	96
Chapter 7.	Conclusions & future directions.....	97
7.1	A paradigm shift - the interferogram as reference.....	97
7.2	A <i>difference</i> approach	98
7.3	Practical significance.....	99
7.3.1	Significance to researchers in academia and industry	103
7.4	Commercial significance	104
7.4.1	Current application: chromatic dispersion test.....	104

7.5	Contributed publications and patents	105
7.6	Prospective & future applications	105
7.7	Conclusion.....	108
	References	109
	Appendix A: Detailed background	114
	A.1. Material dispersion	114
	A.2. Waveguide dispersion	115
	Appendix B: Alternative dispersion extraction techniques.....	122
	Appendix C: Comparison of resolution/scatter in USI vs. BSI (VRI)	126
	C.1. Resolution and scatter in USI	126
	C.2. Resolution and scatter in BSI.....	137
	C.3. Comparison of the resolution and scatter in USI to BSI (VRI)	139
	Appendix D: Comparison of standard VRI and DVRI	141
	D.1. Calibration error	141
	D.2. Interference phase noise	142
	D.3. Effects of interference phase noise on peak/valley location	142
	D.4. Effect of error in peak/valley location on balance point.....	144
	D.5. Effect of peak/valley error on first order dispersion.....	144
	D.6. Effects of wavelength error on second order dispersion.....	147
	Appendix E: Why BSI/VRI cannot be used to extract the phase or the effective index	154
	Appendix F: Matlab code	156
	F.1. Matlab code to simulate SMF28	156
	Copyright acknowledgements	159

List of tables

Table 2-1: Typical precision for each dispersion measurement technique	32
Table 2-2: Comparison of several performance metrics for each dispersion measurement technique.	33
Table 3-1: Typical precision for each dispersion measurement technique	60
Table 3-2: Comparison of several performance metrics for each dispersion measurement technique	61
Table 7-1: Summary of practical advantages of using a virtual reference for first and second order dispersion measurements.....	103
Table E.2.1: Capabilities of each measurement type	155

List of figures

Fig. 1-1. Illustration of the difference between phase velocity and group velocity	2
Fig. 1-2. Chromatic dispersion causes broadening of the pulse width leading to intersymbol interference and reduction in system bandwidth.	3
Fig. 2-1. Time-of-flight dispersion measurement techniques (a) via measurement of temporal separation between pulses of different wavelength (b) via direct measurement of pulse broadening.	8
Fig. 2-2. Dispersion measurements via the modulation phase shift technique	9
Fig. 2-3. Temporal interferometry based dispersion measurement technique	10
Fig. 2-4. Conversion of temporal (spatial delay length) interferogram to spectral interferogram via a Fourier transform. The envelope on the temporal interferogram is due to the coherence function of the source.	10
Fig. 2-5. Unbalanced spectral interferometry using (a) swept wavelength source (b) swept wavelength detection.	12
Fig. 2-6. (a) Common path configuration eliminates the calibration error due to imbalance in the leads of a coupler and is equivalent to (b) a dual arm configuration (Michelson interferometer) with coupler leads of equal length and a zero length air path. Note that for the common path configuration, multiple reflections due to the Fabry-Perot effect are ignored due to the low magnitude of the reflections from the fiber facets.	13
Fig. 2-7. Unbalanced spectral interference pattern	14
Fig. 2-8. Fourier transform on $I_{\text{Real}}(\lambda)$ followed by selection of the frequency content on one side of the Fourier spectrum.	15
Fig. 2-9. Simulation of effect of noise on polynomial fit to (a) phase measurements and the resulting effect on (b) the group delay measurement (from the fit to the phase measurement).	18
Fig. 2-10. (a) Windowed section of the interference pattern and (b) result of Fourier transform applied on windowed section.	19
Fig. 2-11. Illustration of the uncertainty between the wavelength at centre of window λ_{window} and the wavelength $\lambda(\nu_0)$ where the interference fringe period is measured to be $ \nu_0 $	21
Fig. 2-12. Simulation of effect of noise on polynomial fits to (a) group delay measurements and the resulting effect on (b) the dispersion \times length measurement	22
Fig. 2-13. Schematic of a balanced spectral interferometry experiment	23
Fig. 2-14. Pattern with a single maximum (in red) superimposed with a pattern with two maxima (in blue).	23
Fig. 2-15. Free-space variable optical-delay-line with precision translation stage. Optical path length varied using precision translation stage. The folded optical beam path is illustrated in red, the translation is illustrated in green, the lens is drawn as an overlay to the image in blue and the mirrors are drawn as an overlay in orange.	28
Fig. 2-16. Minimum bandwidth required in balanced spectral interferometry	30

Fig. 3-1. Block diagram showing the sequential steps used to extract first and second-order dispersion using a virtual reference interferometer. Adapted (re-colored) with permission from [50].....35

Fig. 3-2. Schematic for the generation of a real spectral interferogram using a common path (or Fabry-Perot) interferometer. An FC/APC (Ferrule connector/angled physical contact) to FC/PC (Ferrule connector/physical contact) connection is used as the first reflection point. A virtual cavity ($L_{V(1)}$), with a simulated group delay separation between V_0 and V_1 (equal to that in the real cavity (L_r) between U_0 and U_1), is shown in blue. Adapted (re-colored) with permission from [50].36

Fig. 3-3. Second order interference pattern in VRI. The finer interference fringes are not resolved in this depiction and appear black. Only the envelope (i.e. the amplitude modulation) of the interferogram is of interest. Adapted (re-colored) with permission from [50].39

Fig. 3-4. (a) Second-order interference pattern produced via virtual referencing of the first harmonic. (b) Second-order interference pattern produced via virtual referencing of the second harmonic, resulting in spectral compression. Adapted (re-colored) with permission from [50].41

Fig. 3-5. Cascade of N elements with FC/PC to FC/APC connections as the reflection points. Used with permission from [50].....41

Fig. 3-6. Schematic diagram for the measurement of the dispersion of a Fiber Bragg Grating. The virtual free space path (cavity) with equivalent group delay is shown in blue. Adapted (re-colored) with permission from [50]. .42

Fig. 3-7. Sample interference generated by the setup in Fig. 3-6. Adapted (re-colored) with permission from [50]. 43

Fig. 3-8. Virtually referenced (and balanced) interference pattern generated by the setup shown in Fig. 3-6. Adapted (re-colored) with permission from [50].43

Fig. 3-9. Schematic diagram for Ultra-Low dispersion measurement made using two independent measurements. Used with permission from [50].45

Fig. 3-10. (a) Simulated second order interference pattern and (b) the result of low-pass filtering to extract the balance wavelengths separated by the sum of half the minimum bandwidth required by each element. Inset above (a) shows a magnified spectral region around a balance wavelength. Adapted (re-colored and re-organized) with permission from [51].48

Fig. 3-11. Comparison between simulation and virtual reference measurement of group delay on a 42cm length of SMF28. The RMS error is with respect to simulation. Adapted (re-colored) with permission from [49].....51

Fig. 3-12. Dispersion parameter measurements made via virtual referencing of a 42cm length of SMF28 and single arm 3-wave measurements (previously reported in [34] [35]) on a 39.5cm length of SMF28. The RMS errors are with respect to simulation. Adapted (re-colored, secondary axis added) with permission from [49].51

Fig. 3-13. Dispersion parameter measurements on dispersion compensating fiber (DCF). The virtual reference measurement was made on a 0.25 m length of DCF, the single arm 3-wave measurement (previously reported in [34] [35]) was made on a 0.165 m length of DCF and the Agilent 86037C measurement was made on a

91.5m length of DCF. The standard deviations shown are with respect to linear fit. Adapted (re-colored, secondary axis added) with permission from [49].	52
Fig. 3-14. Virtual referencing of the first harmonic (N=1) of an 11 cm length of SMF28 fiber illustrating the uncompressed case. Adapted (re-colored) with permission from [50].	53
Fig. 3-15. Virtual referencing of the second harmonic (N=2) of an 11 cm length of SMF28 fiber resulting in the compression of the period of the amplitude modulation. Adapted (re-colored) with permission from [50].	54
Fig. 3-16. Comparison of group delay measurements of an 11 cm length of SMF28 fiber both with and without compression. Adapted (re-colored) with permission from [50].	54
Fig. 3-17. Comparison of dispersion \times length measurements of an 11 cm length of SMF28 fiber with and without compression. Adapted (re-colored) with permission from [50].	55
Fig. 3-18. Two element cascade used in the experiment, where $L_{f1} = 46$ cm, $L_{f2} = 31.4$ cm and $L_{f3} = L_{f1} + L_{f2}$. Adapted (re-colored) with permission from [50].	55
Fig. 3-19. Power spectrum generated by the cascade in Fig. 3-18. Peak 1 corresponds to cavity length L_{f2} , peak 2 corresponds to L_{f1} and peak 3 corresponds to $L_{f1} + L_{f2}$. Used with permission from [50].	55
Fig. 3-20. Sample second-order interference patterns from Virtual Referencing (and balancing) of each of the three cavities in Fig. 3-18. Adapted (re-colored) with permission from [50].	56
Fig. 3-21. Group delay for each of the three cavities in Fig. 3-18 where $L_{f1} = 46$ cm (peak 2), $L_{f2} = 31.4$ cm (peak 1) and $L_{f3} = L_{f1} + L_{f2}$ (peak 3). Adapted (re-colored) with permission from [50].	57
Fig. 3-22. Dispersion \times length for the cavities in Fig. 3-18. Adapted (re-colored) with permission from [50].	57
Fig. 3-23. Group delay measurements of a fiber Bragg grating using VRI agree well with those made using a commercial system based on the MPS technique (SWS-OMNI). Adapted (re-colored) with permission from [50].	58
Fig. 3-24. Direct measurement of the dispersion \times length of a fiber Bragg grating using VRI. Adapted (re-colored) with permission from [50].	58
Fig. 3-25. Ultra-low group delay measurement made by taking the difference between two VRI measurements as illustrated in Fig. 3-9. Adapted (re-colored) with permission from [50].	59
Fig. 3-26. Ultra-low dispersion \times length measurement made by taking the difference between two VRI measurements as illustrated in Fig. 3-9. Adapted (re-colored) with permission from [50].	59
Fig. 4-1. Model for the interference in a polarization maintaining fiber. Adapted (re-colored) with permission from [51].	65
Fig. 4-2. Simulated second order interference pattern (upper graph) and the result of low-pass filtering (lower graph) used to extract the balance wavelengths, from which absolute group delay and second order dispersion of the individual modes can be obtained. Inset above shows a magnified spectral region around a balance wavelength. Although both modes (the slow axis balanced at $\hat{\lambda}_1$ and the fast axis balanced at $\hat{\lambda}_2$) are illustrated in the figure, only one mode is typically within the scan range of the tunable laser for a given L_v ,	

which is varied to extract group delay and second order dispersion of both modes as a function of wavelength. Adapted (re-colored) with permission from [51].	67
Fig. 4-3. Model for the interference in a few-mode fiber. Adapted (re-colored) with permission from [51].	68
Fig. 4-4. Experimental setup for measurement of (a) polarization modes in PM fiber using VRI, (b) transverse modes in an FMF using VRI, and (c) transverse modes using BSI. Adapted (re-colored) with permission from [51].	69
Fig. 4-5. Simultaneous absolute (a) group delay and (b) dispersion \times length measurements for both polarization modes of a 47.2 cm long Panda polarization maintaining fiber. Adapted (re-colored and axis labels corrected in (b)) with permission from [51].	70
Fig. 4-6. Absolute group delay measurements of a 69.9 cm long few-mode fiber measured using balanced spectral interferometry and virtual reference interferometry. Adapted (re-colored) with permission from [51].	71
Fig. 4-7. Comparison of the dispersion \times length measurements for the (a) LP01 mode, (b) LP11, (c) LP02 mode, and (d) LP21 mode of a 69.9 cm length of few-mode fiber measured via Balanced Spectral Interferometry and Virtual Reference Interferometry. Adapted (re-colored) with permission from [51].	71
Fig. 5-1. Amplitude modulated interference pattern described by Eq. 5-3. The fast varying interference is shown in blue and is not resolved in the figure. The slow varying amplitude modulation with phase described by Eq. 5-4 is shown. Adapted (re-colored) with permission from [67].	76
Fig. 5-2. Plot of the dispersive virtual reference interferograms and group index \times length curves for (a) $K=0$ (VRI with a non-dispersive reference) and (b) DVRI using $K=-8.68e+3$. Two $N_{gv}(\lambda)L_v$ curves are superimposed to show the curves that generate intersections at $\lambda_0 = a$ and $\lambda_0 = \lambda_{0\text{new}}$. Adapted (re-colored) with permission from [67].	83
Fig. 5-3. Setup for dispersion measurement of (a) standard fibers (b) polarization maintaining gain fiber. Used with permission from [67].	85
Fig. 5-4. Setup for the measurement of gain in PM (birefringent) gain fiber.	86
Fig. 5-5. Measurements of (a) group delay and (b) dispersion parameter on a 20 cm length of SMF28 using VRI and DVRI ($K=-2e+3$). Adapted (re-colored, secondary axis K added to (b)) with permission from [67].	87
Fig. 5-6. (a) Gain and (b) group delay curves for a 23.3 cm length of erbium doped PM gain fiber pumped at 980 nm at various pump power conditions for both fast axis and slow axis measured using DVRI ($K=-7.75e+3$). Adapted (re-colored) with permission from [67].	88
Fig. 5-7. Dispersion parameter curves for a 23.3 cm length of erbium doped PM gain fiber pumped at 980 nm for both (a) fast and (b) slow axes at various pump power conditions measured via DVRI ($K=-7.75e+3$). Adapted (re-colored) with permission from [67].	88
Fig. 5-8. Measurements of (a) group delay (b) dispersion parameter on a 28.6 cm length of dispersion shifted fiber via direct measurement using DVRI ($K=-8e+3$). Adapted (re-colored) with permission from [67].	89
Fig. 6-1. Experimental setup for both a BSI and LC-VRI measurement. Adapted (re-colored) with permission from [69].	93

Fig. 6-2. Interference pattern produced in (a) BSI where the reference path length is chosen to balance the interferometer at a wavelength within the scan range (at 1525 nm) (b) USI and LC-VRI by choosing a reference path length that balances the interferometer at a wavelength outside (to the left of) the scan range. Used with permission from [69].94

Fig. 6-3. Second order interference pattern produced by point-by-point multiplication of an interference pattern produced by an unbalanced interferometer with a virtual reference interference pattern produced by simulating a path length equal to the physical imbalance. The amplitude modulation (solid black line) is obtained by applying a low-pass filter to the second order interference pattern (solid grey line). The solid black line is equivalent to the interference pattern produced by BSI in Fig. 6-2(a). Adapted (re-colored) with permission from [69].95

Fig. 6-4. (a) Group delay and (b) dispersion parameter measurements on a 73.5 cm length of SMF28. Results compare LC-VRI, BSI and simulations using the manufacturer's specification [7]. Adapted (re-colored, organized horizontally and secondary axis added to (b)) with permission from [69].96

Fig. 7-1. Comparison of unbalanced techniques (which measure the degree of similarity or 'best fit' of the measured interference pattern to single frequency sinusoids, ignoring the phase variation) to virtual reference techniques that directly utilize the phase variation to directly measure phase difference (from the resulting amplitude modulation).....99

Fig. 7-2. Images of the Virtual Reference Dispersion Analyser from Inometrix Inc.104

Fig. 7-3. (a) An illustration of a typical dual arm interferometric setup used in optical coherence tomography and (b) a possible setup for calibration of the dual arm interferometer using a dispersive reference to measure the difference in second order dispersion between the test and reference path.....106

Fig. 7-4. Capabilities of virtual reference interferometry demonstrated for dispersion characterization of a (a) fiber cascade in Chapter 3 (b) few-mode fiber in Chapter 4 could be potentially extended for (c) depth based imaging.107

Fig. 7-5. Potential configuration of a fiber based multi-parameter sensor employing a virtual reference. A twin-hole fiber could be used to bring the evanescent field of light in the core into contact with the gas/liquid over the entire length of the fiber, increasing the interaction length.107

Fig. A-1. Cross sectional geometry of an optical fiber (core size exaggerated).115

Fig. B-1. Plot generated using all the peaks and valleys in the interferogram123

Fig. C-1. Windowing a section of the interference pattern is equivalent to multiplication of the cosine with the rectangular function.126

Fig. C-2. Visualization of Fourier transform on a windowed section of the interference pattern for small window size.128

Fig. C-3. An illustration showing how a reduction in the window size (i.e. increasing the magnitude of a) results in a broadening of the peak of the $\text{sinc}(\)$ function in the spatial frequency domain.....129

Fig. C-4. Minimum separation between peaks of each $\text{sinc}(\)$ function129

Fig. C-5. The $\text{sinc}(\)$ function reaches half its maximum value when $x = 0.6$ 130

Fig. C-6. Multiple small windows used to take into account the aperiodicity in the interference pattern due to dispersion (in a large window) and the resulting Fourier transforms for each of the small windows.131

Fig. C-7. Relationship between beat frequency and group delay separation135

Fig. C-8. Equivalence of (a) spectral resolution (b) scatter in the group delay curve136

Fig. C-9. Relationship between minimum spectral separation and minimum bandwidth137

Fig. C-10. Equivalence of (a) spectral resolution and (b) scatter in the group delay curve138

Fig. D-1. Amplitude modulation extracted from second order interference pattern via low pass filtering. The phase error in the raw interference pattern (due to interference phase noise) leads to errors in the peak locations $\lambda_{-2}, \lambda_{-1}, \lambda_1, \lambda_2$ 144

Fig. D-2. Comparison of uncertainty in the group delay measurement for VRI (non-dispersive virtual reference), DVRI with a first order dispersive reference, and DVRI with a second order dispersive reference. The illustration shows that VRI has no uncertainty in the group delay (slope is zero); however for DVRI the uncertainty depends on the slope of the simulated group delay curve (i.e. the simulated second order dispersion).146

Fig. D-3. Comparison of uncertainty in the second order dispersion measurement using VRI (non-dispersive virtual reference), DVRI with a first-order dispersive reference, and DVRI with a second order dispersive reference. The illustration shows that both VRI and DVRI with a first order dispersive reference have no additional uncertainty in the second order dispersion plot, however for DVRI with a second order dispersive reference the uncertainty depends on the slope of the simulated second order dispersion curve (i.e. the simulated dispersion slope (or third order dispersion))152

List of Appendices

Appendix A: Detailed background

- A.1. Material dispersion
- A.2. Waveguide dispersion

Appendix B: Alternative dispersion extraction techniques

- B.1.1. Extraction of second order dispersion from the group delay curve
- B.1.2. Extraction of the second order dispersion via a polynomial fit
- B.1.3. Extraction of the second order dispersion: multiple measurements
- B.1.4. Combined matrix & multiple measurements

Appendix C: Comparison of resolution/scatter in USI vs. BSI (VRI)

- C.1. Resolution and scatter in USI
- C.2. Resolution and scatter in BSI
- C.3. Comparison of the resolution and scatter in USI to BSI (VRI)

Appendix D: Comparison of standard VRI and DVRI

- D.1. Calibration error
- D.2. Interference phase noise
- D.3. Effects of interference phase noise on peak/valley location
- D.4. Effect of error in peak/valley location on balance point
- D.5. Effect of peak/valley error on first order dispersion
 - D.5.1. Standard VRI
 - D.5.2. Dispersive VRI
- D.6. Effects of wavelength error on second order dispersion
 - D.6.1. Standard VRI
 - D.6.2. Dispersive VRI

Appendix E: Why BSI/VRI cannot be used to extract the phase or the effective index

Appendix F: Matlab code

- F.1. Matlab code to simulate SMF28

List of abbreviations

BSI	Balanced spectral interferometry
CFBG	Chirped fiber Bragg grating
DAQ	Data acquisition
DC	Zero frequency component of an oscillation
DCF	Dispersion compensating fiber
DC-PCF	Dispersion compensating photonic crystal fiber
DGD	Differential group delay
D	Second order dispersion parameter
DL	Second order dispersion-length product
DSF	Dispersion shifted fiber
DVRI	Dispersive virtual reference interferometry
EDF	Erbium doped fiber
EDFA	Erbium doped fiber amplifier
FBG	Fiber Bragg grating
FC/APC	Ferrule connector / angled physical contact
FC/PC	Ferrule connector / physical contact
FFT	Fast Fourier transform
FMF	Few mode fiber
FUT	Fiber under test
FWHM	Full width at half maximum
L	Length of test fiber
LC-VRI	Low-coherence virtual reference interferometry
LED	Light emitting diode
MDM	Mode division multiplexing
MPS	Modulation phase shift
PCF	Photonic crystal fiber
PM	Polarization maintaining
QPM	Quasi phase matching
RMS	Root mean square
SI	Spectral interferometry or spectral interferogram
THF	Twin hole fiber
TI	Temporal interferometry or temporal interferogram
TOF	Time of flight
USI	Unbalanced spectral interferometry
USI-WFT	Unbalanced spectral interferometry via windowed Fourier transform
VRI	Virtual reference interferometry

List of symbols

λ	Optical wavelength
c	Speed of light in vacuum
λ_0	Balance wavelength where group delay in test path is equal to that in the reference path
n_{eff_f}	Effective refractive index of test path / fiber under test
k_0	Propagation constant of free space
β_f	Propagation constant of the test path / fiber under test
ϕ	Phase of the interference pattern
$\phi_{Amp. mod.}$	Phase of the amplitude modulation of a second order interference pattern
N_{g_f}	Group index of the test path / fiber under test
τ_{g_f}	Group delay of the test path / fiber under test
D_f	Second order dispersion parameter of the test path / fiber under test
L_f	Length of the test path / fiber under test
$D_f L_f$	Second order dispersion-length product of the test path / fiber under test
L_{air}	Length of a free space (air) path
n_{eff_v}	Effective refractive index of dispersive virtual reference
β_v	Propagation constant of a dispersive virtual reference
N_{g_v}	Group index of a dispersive virtual reference
D_v	Second order dispersion parameter of a dispersive virtual reference
L_v	Length of a dispersive virtual reference path
$D_v L_v$	Second order dispersion-length product of a dispersive virtual reference
K	Slope of the group delay curve of a first order dispersive reference
$\Delta\lambda_0$	Error in measuring the balance point
Δ	Difference in second order dispersion-length product between test and reference paths
B_{min}	Minimum required spectral bandwidth for a dispersion measurement to be possible
B_{source}	Spectral bandwidth of the source
B_{meas}	Spectral bandwidth of dispersion measurement results

Chapter 1.

Introduction & background

1.1 Overview

We live in the information age, where the creation, dissemination and consumption of information are significant cultural and socioeconomic activities. Our modern lifestyles are heavily dependent on the telecommunication technologies that enable instant communication between people anywhere on our planet. From our modern smartphones that stream text, messaging and video data to our high definition televisions, laptops, tablets and personal computers, our appetite for data and bandwidth grows daily. To support our data rich lifestyles, high-throughput wide-bandwidth fiber optic telecommunications systems are critical. Fiber optic cable is a low-loss medium capable of carrying signals great distances and its wide bandwidth enables frequency based signal multiplexing. Today a single channel in a fiber deployed in existing networks can carry as much as 40Gbit/s, which is the amount of information in over 1 million telephone conversations or more than 15 thousand streaming high definition videos. This is much more data than can be transmitted on standard electrical Ethernet cables which typically carry up to 1 Gbit/s. Despite this impressive capability we are approaching the limits of the information carrying capacity of our current generation of optical networks. Considerable research is being done to develop the next generation of optical networks with bit rates beyond 400Gbit/s, including technologies that multiplex signals across time, frequency and space [1] [2] [3] [4] [5]. Regardless of the multiplexing technique used to increase data throughput, the performance of current and future optical telecommunications channels depends heavily on the compensation of transmission impairments. Impairments that affect the performance of an optical channel include stress, thermal fluctuations, chemical pollutants, loss, and chromatic dispersion. Of these impairments chromatic dispersion has the greatest effect on data throughput. Because of this, accurate dispersion characterization of all photonic devices in an optical network is of critical importance.

Chromatic dispersion is the phenomenon that causes different frequencies of light to travel at different velocities due to the wavelength (frequency) dependence of the refractive index of a material [6]. The effect can be observed in the spreading of light into colors through a prism. Since white light is comprised of a broad spectrum of wavelengths, when it passes through a prism each wavelength encounters a different index of refraction and is bent at a different angle according to the Snell-Descartes law of refraction [6]. In an optical waveguide the index variation is caused by the optical properties of the material (material dispersion) and by the optical confinement produced by the geometry of the waveguide (waveguide dispersion). A detailed analysis of both material and waveguide dispersion is presented in [Appendix A](#). The refractive index observed in a waveguide due to both material and waveguide effects is referred to as the effective refractive index (n_{eff}). The variation of the effective refractive index with wavelength can be related to the first, second, third and higher order dispersion in the waveguide. The higher order

dispersion is best understood from a mathematical perspective via a Taylor expansion around a specific wavelength λ_0 as

$$n_{eff}(\lambda) = n_{eff}(\lambda_0) + (\lambda - \lambda_0) \left. \frac{dn_{eff}}{d\lambda} \right|_{\lambda_0} + (\lambda - \lambda_0)^2 \left. \frac{d^2 n_{eff}}{d\lambda^2} \right|_{\lambda_0} + (\lambda - \lambda_0)^3 \left. \frac{d^3 n_{eff}}{d\lambda^3} \right|_{\lambda_0} + \dots \quad \text{Eq. 1-1}$$

All of the optical phenomena to be discussed in this thesis may be derived from this expansion. For example, the phase velocity of a particular wavelength of light λ_0 in a medium, is the distance traversed by that phase front over a given period of time. The phase velocity can be related to the effective index of the medium by

$$V_p(\lambda_0) = \frac{c}{n_{eff}(\lambda_0)} \quad \text{Eq. 1-2}$$

where c is the speed of light in vacuum. The phase of an optical signal that has traversed a path L_f with an effective phase index $n_{eff}(\lambda_0)$ is given by

$$\phi(\lambda_0) = \frac{2\pi}{\lambda_0} n_{eff}(\lambda_0) L_f \quad \text{Eq. 1-3}$$

The first order dispersion is often referred to as the group velocity, group index or group delay. The term *first order* is used since it relates to the first two (linear) terms in the expansion in Eq. 1-1. Group velocity refers to the distance traversed by the *envelope* of a specific wavelength λ_0 of an optical pulse over a given period of time and is given as

$$V_g(\lambda_0) = \frac{c}{N_g(\lambda_0)} \quad \text{Eq. 1-4}$$

where the envelope of the optical pulse of wavelength λ_0 that travels at the speed of light c in vacuum has its velocity reduced by the group index $N_g(\lambda_0)$ within the waveguide. The differences between the phase velocity and the group velocity are illustrated in Fig. 1-1.

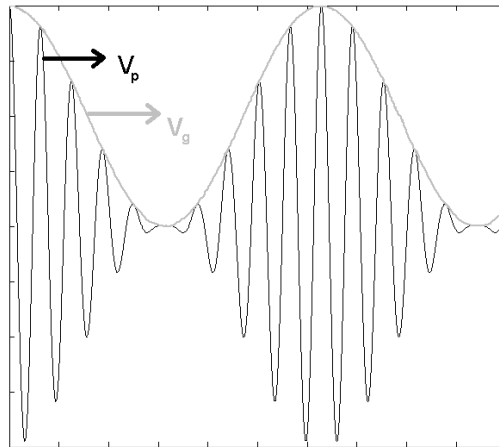


Fig. 1-1. Illustration of the difference between phase velocity and group velocity

The group index is related to the first two terms in Eq. 1-1 as

$$N_g(\lambda_o) = n_{eff}(\lambda_o) - \lambda_o \left. \frac{dn_{eff}}{d\lambda} \right|_{\lambda_o} \quad \text{Eq. 1-5}$$

The group delay $\tau_g(\lambda_o)$ refers to the time taken for the envelope of an optical pulse of wavelength λ_o to traverse a given distance L_f and may be described by

$$\tau_g(\lambda_o) = \frac{N_g(\lambda_o)L_f}{c} = -\frac{\lambda_o^2}{2\pi c} \left. \frac{d\phi}{d\lambda} \right|_{\lambda_o} \quad \text{Eq. 1-6}$$

The second order dispersion is related to the slope of the group delay curve or the third term in Eq. 1-1 and may be described as

$$D(\lambda_o)L_f = \left. \frac{d\tau_g}{d\lambda} \right|_{\lambda_o} = \frac{1}{c} \left. \frac{dN_g}{d\lambda} \right|_{\lambda_o} L_f = -\frac{\lambda_o}{c} \left. \frac{d^2 n_{eff}}{d\lambda^2} \right|_{\lambda_o} L_f = -\frac{\lambda_o}{2\pi c} \left[2 \left. \frac{d\phi}{d\lambda} \right|_{\lambda_o} - \lambda_o \left. \frac{d^2 \phi}{d\lambda^2} \right|_{\lambda_o} \right] L_f \quad \text{Eq. 1-7}$$

The second order dispersion is of particular importance in a telecommunication system as it can cause pulse broadening. The pulse broadening in the time domain is related to the range of wavelengths that make up an optical pulse and the second order dispersion parameter of the fiber as

$$\Delta\tau \approx D(\lambda_o)L_f\Delta\lambda \quad \text{Eq. 1-8}$$

It is important to note that the approximation in Eq. 1-8 assumes that the pulse broadening is dominated by the second order dispersion. When the second order dispersion is small the effects of the third and higher order dispersion may not be ignored. In a digital optical telecommunications system, since a pulse is used to represent the binary digit 1 and the absence of a pulse represents binary 0, the chromatic dispersion of the fiber causes pulses (used to represent 1 or 0) to broaden beyond their allocated bit slot. Pulse broadening causes adjacent bits to overlap and makes it difficult for the receiver to distinguish between 1 and 0, in an effect known as intersymbol interference [7]. This effect makes it necessary to use wider bit slots, which effectively lowers the number of bits that can be transmitted over a given period of time. This effectively results in a reduction in the system bandwidth (data throughput capacity). The effect of intersymbol interference is illustrated in Fig. 1-2.

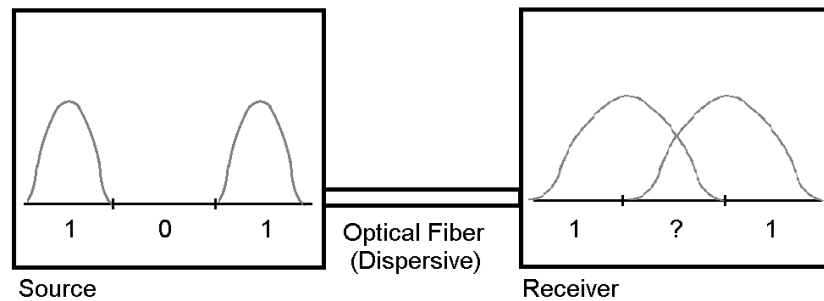


Fig. 1-2. Chromatic dispersion causes broadening of the pulse width leading to intersymbol interference and reduction in system bandwidth.

In a telecommunications system the pulse broadening caused by chromatic dispersion can be compensated for by using bulk or distributed dispersion compensation schemes. Chirped fiber Bragg gratings (CFBG) are one example of a bulk dispersion compensation scheme [7]. Dispersion compensating fiber (DCF) is an example of a distributed compensation scheme since these fibers can be placed at periodic points in a transmission line to compensate for second order dispersion in an optical fiber [7]. In either compensation scheme, the goal is to ensure that the total dispersion \times length of the optical channel is reduced to zero such that

$$D_{fiber}L_{fiber} + D_{compensation}L_{compensation} = 0 \quad \text{Eq. 1-9}$$

Where D_{fiber} is the second order chromatic dispersion of the transmission fiber, L_{fiber} is its length, $D_{compensation}$ is the second-order chromatic dispersion of the compensation element (DCF or CFBG) and $L_{compensation}$ is its length. In order to achieve this balance, accurate dispersion characterization of each element is crucial. Accurate dispersion characterization is also important for the design of individual network components, such as sources and receivers. For example, pulsed fiber lasers are an important source in a fiber optic network. Pulses are typically generated in fiber lasers using some form of active or passive mode locking mechanism. Within these laser cavities the dispersion of the gain fiber is often balanced by that of a dispersion compensating fiber (with negative dispersion) to prevent pulse spreading within the laser cavity itself. This is one example where accurate short length dispersion is essential.

Although nonlinear applications requiring dispersion characterization are not directly covered in this work, they are worth noting to indicate the widespread need for this capability by the research community. In non-linear systems, dispersion affects the magnitude, phase and the efficiency of the nonlinear process [8] [9] [10] [11]. One example of a nonlinear application is the generation of optical solitons [9] [10]. In order to generate an optical soliton the effects of chromatic dispersion and self phase modulation [9] (a phenomenon in which the intensity profile of a pulse modifies the phase of the pulse and can be used to compress it [8]) must be in balance with each other. Therefore in order to generate a soliton the dispersion must first be well characterized so that the intensity of the optical pulse can be appropriately selected to ensure that the pulse spreading effect of chromatic dispersion is balanced by the pulse compression effect of self phase modulation. Other nonlinear effects such as second harmonic generation, three-wave mixing and four-wave mixing require knowledge of chromatic dispersion since it determines the interaction lengths between the individual waves produced by these effects, which are at different wavelengths. One technique used to increase the interaction length between two waves of different wavelength produced via second harmonic generation is known as Quasi-Phase Matching (QPM) [12]. Since QPM attempts to match the group delay between two waves of different wavelength, an accurate knowledge of the dispersion is essential.

1.2 Motivation

The primary motivation of this thesis is to measure the dispersion of short-length, low-dispersion optical fibers and components and to develop a method for their characterization. The ability to make dispersion measurements using short lengths of optical fiber is important when testing fibers for effects associated with aging (i.e. heat, chemical infiltration) since short sections can be tested without the need to sacrifice an entire reel. Another important

application is in testing fiber properties at various locations along a fiber. This is particularly important in determining the quality of the fiber drawing process as non-uniformity in the fiber diameter can be measured from the variation in chromatic dispersion between fiber samples [13]. Short length characterization is also particularly important in the testing of new or experimental specialty fibers and optical components where long lengths are usually too costly to acquire or not readily available. As a result, conventional dispersion measurement techniques requiring long lengths of fiber (described in [Chapter 2](#)) cannot be used for characterization. Twin hole fiber (THF), characterized in [Chapter 3](#), and photonic crystal fiber (PCF) [14] are two examples of a specialty fiber for which long spans are very costly and generally not available. These fibers have many possible design configurations and it is very difficult to develop a theoretical model that describes the dispersion of a particular design. Another class of fibers where this is also the case includes Few-mode fibers (FMFs), characterized in [Chapter 4](#). These fibers, which will be critical to expanding the information carrying capacity of modern telecommunications networks, can have multiple transverse or polarization modes for which the dispersion parameter may vary dramatically. An additional consideration for these types of specialty fibers is that fiber geometry is not always uniform along its length, resulting in a variation in fiber dispersion along its length. As a result, the characterization must be performed on the particular span of fiber to be used in an experiment or photonic system.

Certain types of specialty fibers, such as erbium doped fiber (EDF) and dispersion compensating fiber (DCF) are often used in short length spans for loss and dispersion compensation. EDF (characterized in [Chapter 5](#)), for example, is often used in short length spans to build erbium doped fiber amplifiers (EDFAs) to compensate for losses in a telecommunication channel [15] or as a gain medium in a fiber laser [9]. Dispersion in these fibers is particularly important for mode-locked fiber lasers for, which the optical pump power [16] [17], affects the group velocity of optical pulses in the laser cavity [7] (demonstrated in [Chapter 5](#)), and changes the mode-locking condition [9]. Knowledge of the dispersion in this type of gain fiber is critical if the additional dispersion added to the channel by gain fiber is to be compensated. Dispersion compensating fiber (DCF), characterized in [Chapter 3](#), as well as dispersion compensating photonic crystal fiber (DC-PCF) [14] are often used in short length spans to compensate the dispersion introduced in an optical channel by both EDFAs and standard telecommunication fiber (SMF28). These fibers allow a high degree of control over the dispersion properties via modification of the fiber geometry. It is therefore critical to experimentally test how close the fabricated fiber dispersion is to the design. Experimental verification and dispersion compensation is most accurate when the specific short sections of fiber used in the channel are tested individually. A class of fiber for which dispersion characterization is difficult is known as dispersion shifted fiber (DSF) (characterized in [Chapter 5](#)). In these fibers the dispersion parameter is close to zero and actually crosses zero somewhere within the scan range (i.e. scan range typically used in telecommunications). The characterization of this type of fiber near its zero-dispersion wavelength is difficult because wide bandwidths (possibly exceeding available sources) are required. For this fiber and specialty fibers like it, a specialized technique capable of both short length and low dispersion characterization is required. A short length low dispersion characterization technique is also essential for the analysis of dispersion in optical components. For example, chirped fiber Bragg gratings (CFBGs) (characterized in [Chapter 3](#)) are often used for dispersion compensation in high repetition rate fiber lasers that require short cavity lengths or to compensate for

dispersion in long length telecommunication channels. These optical components are short in length and therefore can only be characterized using a short-length characterization technique.

1.3 Objectives

The primary objective of this thesis is the development of a practical technique that can quickly and easily characterize the dispersion in short-length fibers and optical components with small dispersion-length (DL) products. To this end, the first objective is the introduction and verification of the technique in its simplest form. Verification will be carried out via the characterization of dispersion standards as well as comparison of experimental results to those obtained using conventional measurements techniques. A second objective is to provide a detailed analysis of the theoretical framework of the technique, including system parameters and limitations. A third objective is to demonstrate that the technique is a fast, accurate, practical and easy to implement method that is capable of characterizing short-length fibers and optical components. A fourth objective is to demonstrate that the technique is of practical utility for measuring leading edge optical components, employing spatial division multiplexing schemes, by showing that it can simultaneously characterize polarization and transverse modes in a few-mode fiber. A fifth objective is to delve deeper into the possibilities for increasing the flexibility and versatility of the technique by showing how a dispersive virtual reference may be used to enable measurements that would otherwise be impossible using a limited bandwidth source. The final objective is to consider how the technique may be used in applications outside dispersion characterization.

1.4 Organization of thesis

This thesis is organized into seven chapters. [Chapter 1](#) provides an introduction to the basic concepts, background, motivation and objective behind this work. [Chapter 2](#) describes the conventional techniques that may be used for characterizing dispersion and illustrates the gap in conventional techniques that motivated the development of virtual reference interferometry. [Chapter 3](#) then formally introduces virtual reference interferometry and demonstrates its advantages in comparison to conventional techniques as well as some important and unique capabilities. [Chapter 4](#) demonstrates how VRI can be used to simultaneously characterize polarization and transverse modes in state-of-the-art few-mode-fibers used in mode-division-multiplexing based telecom systems. [Chapter 5](#) dives deeper into the implications of using a virtual reference by adding a new dimension to VRI, a dispersive-virtual reference. The addition of dispersion into the reference allows for measurements to be made that would otherwise be impossible with a limited bandwidth source. [Chapter 6](#) extends the virtual reference to low-coherence dual arm interferometer configurations to demonstrate how the technique may be used for these configurations and the advantages it brings. [Chapter 7](#) concludes this thesis by outlining the wider significance of this work both academically and practically (i.e. in industry) while considering the potential future applications.

Chapter 2.

Conventional dispersion characterization techniques

In this chapter, conventional measurement techniques for the characterization of chromatic dispersion are introduced. The techniques include those based on time-of-flight (TOF) [18] [19] [20] [21], modulation-phase-shift (MPS) [22] [19] [23] [24] and interferometry [19] [13]. Among these, TOF and MPS are the most widely used commercial (field) measurement techniques. Interferometric techniques, on the other hand, are more widely used in academic laboratories. This chapter provides a review of the conventional dispersion measurement techniques and compares their performance. The introduction of these techniques sets the stage for the introduction of virtual reference interferometry in [Chapter 3](#) which can be used in both academic and commercial settings.

2.1 Time-of-flight

In a time-of-flight (TOF) based measurement technique [18] [19] [20] [21] a tunable laser sends optical pulses through an optical fiber toward a detector, as illustrated in Fig. 2-1. The second order dispersion (dispersion-length product) may then be determined by using Eq. 1-7 in one of two ways. The first is to send individual pulses at different wavelengths (λ_1 and λ_2) with a spectral separation $\Delta\lambda = |\lambda_2 - \lambda_1|$ along a fiber and to measure the change in the group delay $\Delta\tau_g$ between the two pulses, as illustrated in Fig. 2-1(a). The second method for measuring the second order dispersion using Eq. 1-7 is to measure the pulse broadening $\Delta\tau_g$ directly (temporal width of pulse) as well as directly measuring the spectral bandwidth $\Delta\lambda$ of the pulse, as illustrated in Fig. 2-1 (b).

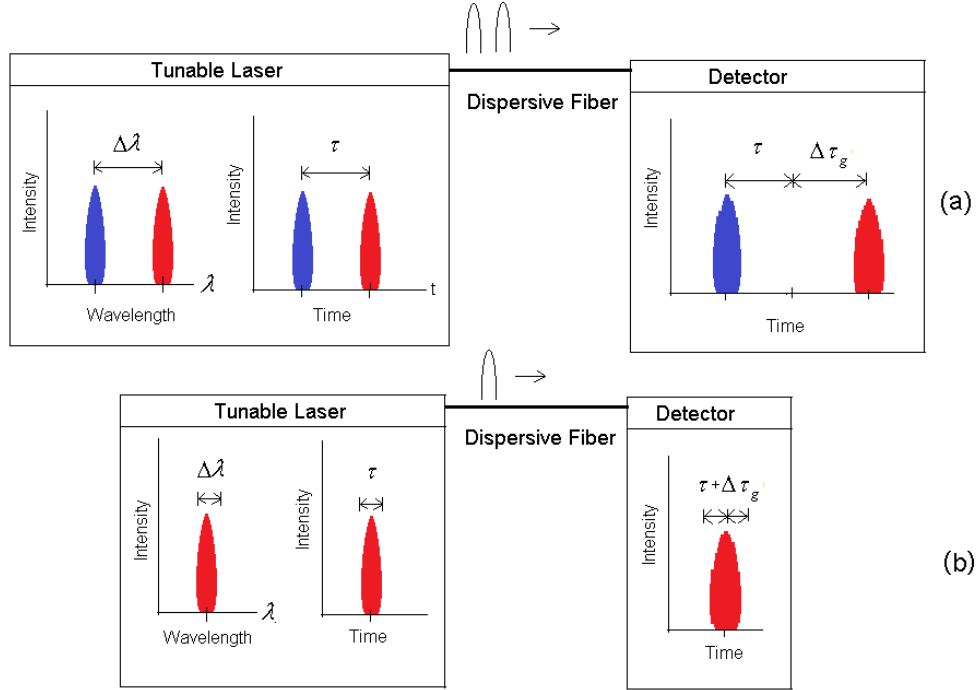


Fig. 2-1. Time-of-flight dispersion measurement techniques (a) via measurement of temporal separation between pulses of different wavelength (b) via direct measurement of pulse broadening.

The TOF technique has a measurement precision between $\Delta(D(\lambda_o)L_f) = 0.1$ to 1 ps/nm [19] [20] depending on the speed of the electronics, but typically requires several kilometers of fiber to accumulate a temporal change that is large enough to be detected. For example, if we assume the dispersion is that of SMF28 (i.e. 18 ps/nm·km) and that the relative error of the dispersion plot cannot exceed 1% such that

$$E_{\text{Rel}\%} = \frac{\Delta(D(\lambda_o)L_f)}{D(\lambda_o)L_f} = 1\% \quad \text{Eq. 2-1}$$

then the fiber length required to achieve this would be between 0.56 and 5.6 kilometers. Using a TOF technique for the characterization of short length (<1 m) fiber samples, however, is not feasible as the requirements on both the pulsed tunable laser and electronic sampling speed becomes prohibitive. The next section discusses another technique that is also typically used for the characterization of long fiber samples.

2.2 Modulation-phase-shift

In techniques based on modulation-phase-shift (MPS) [22] [23] [24] an RF signal amplitude modulates a single wavelength continuous-wave optical signal. The dispersion in the fiber under test can be measured by detecting the phase changes in amplitude modulated RF envelope (at the detector) as the wavelength of the continuous wave optical signal is varied, as illustrated in Fig. 2-2.

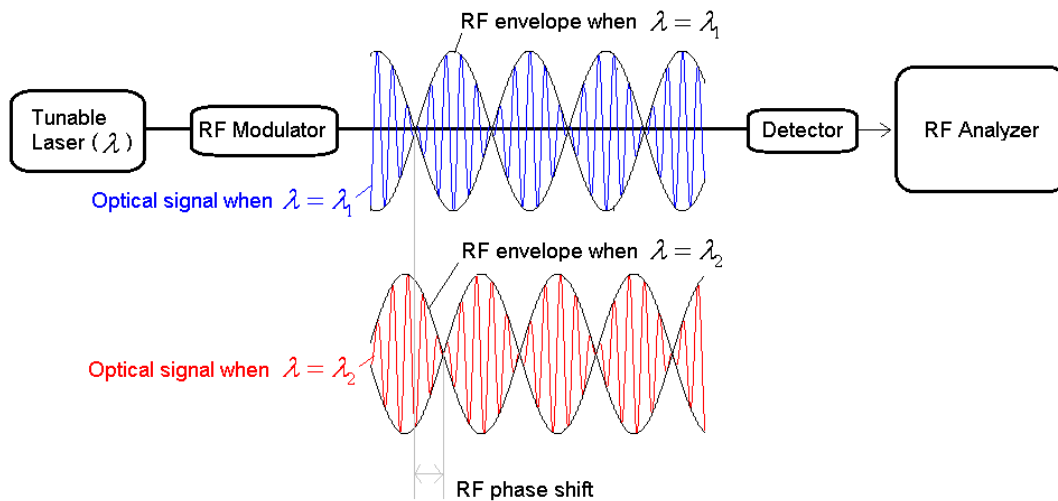


Fig. 2-2. Dispersion measurements via the modulation phase shift technique

The relative phase change in the amplitude modulated signal at different wavelengths can then be measured and the group delay calculated using Eq. 1-6. The second order dispersion may also be calculated using Eq. 1-7. The MPS technique has a precision very similar to the TOF technique with $\Delta(D(\lambda_o)L_f) = 0.1$ to 1 ps/nm [23] [24]. As a result, the fiber lengths required by the MPS technique are similar to that required in the TOF technique. The precision depends on the frequency and jitter of the RF modulator (smaller period in modulation and low jitter makes small phase shifts easier to detect). To characterize short length fiber, however, the requirements for the frequency of the RF modulator and the sampling speeds become prohibitive. For this reason the MPS technique is typically used for the characterization of long length fiber.

Both the MPS and TOF techniques require long lengths of fiber to produce dispersion plots with a reasonable standard error. The characterization of long length fiber is feasible for standard fibers, for which long length spans are readily available. However, for the characterization of specialty fibers [14] [25] [26] [27] and short length optical components (where long-length samples are either too costly or unavailable), short length (<1 meter) characterization techniques are desirable. For short-length dispersion characterization, interferometric [13] [17] [19] [27] [28] [29] [30] measurements are generally preferred. Interferometric dispersion measurements may either be based on temporal interferometry or spectral interferometry. Both types will be discussed in the following sections.

2.3 Temporal interferometry

In temporal interferometry, light from a broadband source passes through the test fiber and a variable reference path. As the variable reference path is moved at a constant speed the interference pattern produced is sampled by a detector (as a function of time; later correlated to position) [16] [17] [28] [31] [32], as illustrated in Fig. 2-3. A tracking laser is often used to track position directly and increase accuracy [28].

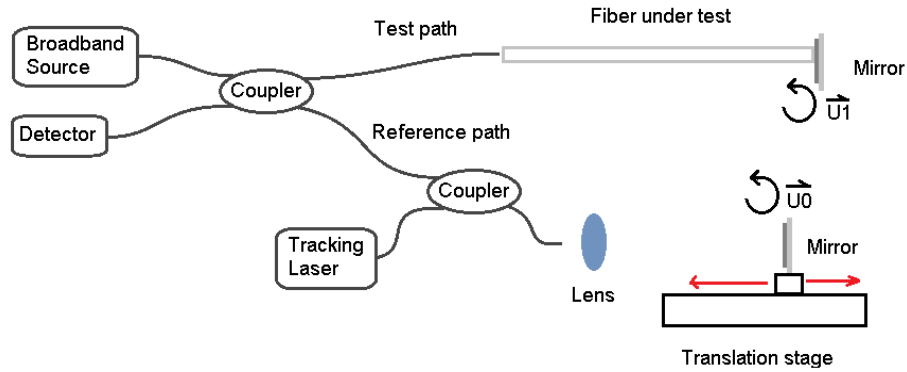


Fig. 2-3. Temporal interferometry based dispersion measurement technique

A Fourier transform of the interference pattern then converts the spatial domain signal to a spectral domain signal as illustrated in Fig. 2-4.

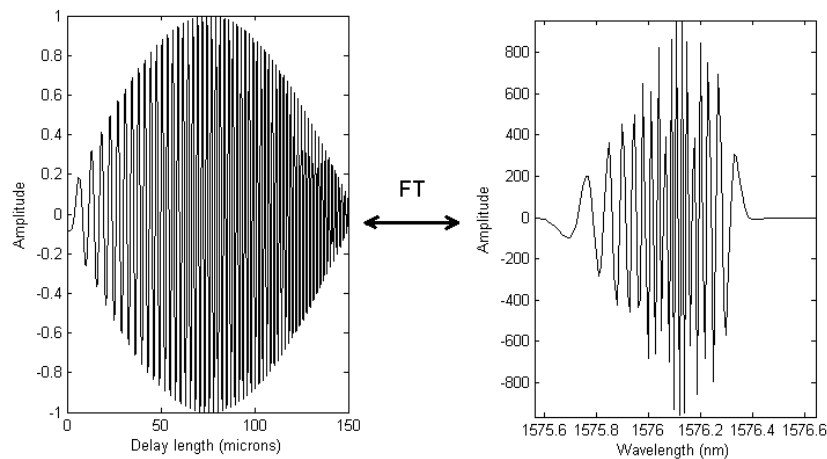


Fig. 2-4. Conversion of temporal (spatial delay length) interferogram to spectral interferogram via a Fourier transform. The envelope on the temporal interferogram is due to the coherence function of the source.

The chromatic dispersion can then be measured from the spectral interferogram using one of the unbalanced spectral interferometry techniques presented in the next section. The main problem with temporal interferometry is that the need to translate the reference path means that noise is introduced into the temporal interference pattern due to vibration. As a result, the highest reported measurement precision using this technique was ± 0.0015 ps/nm (measured on a 0.814 meter long photonic crystal fiber [28]).

2.4 Spectral interferometry

In a spectral interferometer, an interference pattern is produced by holding the test and reference arms of an interferometer static while tuning the wavelength of a source or receiver. Spectral interferometers are important as they have been shown to accurately characterize short-length fiber (<1 m) [28] [29] [33] [34] [35] [36] [37] [38] [39] [40] [41], where analysis of the spectral interference pattern yields the dispersion information. Spectral interferometers are preferred for the characterization of short length optical fiber and components because they have no moving parts that would be susceptible to vibration (as in temporal interferometry). Conventional spectral

interferometry is segmented into two categories; unbalanced spectral interferometry (USI) and balanced spectral interferometry (BSI). Virtual reference interferometry (VRI) (this work) will be shown to be a hybrid of both; combining their advantages while eliminating their individual disadvantages. As a result, more time will be spent in this important section since an understanding of conventional spectral interferometry (i.e. USI and BSI) is critical to the understanding of VRI. Much of this material will be referenced in later chapters. The following sections focus on USI and BSI, whereas the virtual reference interferometer will be introduced in the next chapter once an understanding of the advantages and disadvantages of these conventional techniques is clearly established.

[Section 2.4.1.1](#) discusses USI based techniques that characterize first and second order dispersion by analytically differentiating a fit to the phase of a fast Fourier transform (FFT) of the interferogram via Eq. 1-6 and Eq. 1-7. This section demonstrates that the problem with this approach is that noise in the measured phase greatly affects the slope and curvature of the fit. The conclusion of this section is that the noise in the phase measurement results in different first and second order dispersion curves depending on the type of fit chosen, resulting in large errors in the first order dispersion and even larger errors in the second order dispersion.

[Section 2.4.1.2](#) discusses USI based techniques that extract the first order dispersion (group delay) directly from the interferogram by using a windowed Fourier transform of sections of the interference pattern. The second order dispersion is then obtained by analytically differentiating a fit to the group delay curve using Eq. 1-7. This section demonstrates that the noise (scatter) in the group delay is dependent on the window size chosen. Since an optimum window size that results in the lowest scatter cannot be known a priori, the scatter cannot be minimized. Furthermore since the second order dispersion is obtained by differentiating the fit to the first order dispersion this technique is also problematic as the noise will affect the curvature and slope of the fit. This results in a similar conclusion as that in the previous section, where the second order dispersion curve depends on the type of fit chosen, resulting in large errors in the second order dispersion curves.

[Section 2.4.2](#) discusses BSI based techniques that are able to measure group delay and second order dispersion directly from the interference pattern, without differentiation. This section will show that this capability makes BSI based techniques the most accurate for measuring second order dispersion, capable of measuring second-order dispersion to 10^{-5} ps/nm [13]. It will also show that the disadvantages of using BSI is that it is slow in comparison to USI and that it requires a precision variable delay line which must be aligned, stabilized, balanced and isolated from the environment. The need for a variable delay line makes the setup and execution of BSI based measurements much more difficult than those that use USI. In addition, the dispersion in the physical reference arm must be calibrated [42], a process that introduces error into the measurement.

2.4.1 Unbalanced spectral interferometry

In unbalanced spectral interferometry (USI) [28] [29] [41], the group delay in the test path is balanced by that of the reference path at some wavelength *outside* the scan range. A spectral interference pattern is produced by sweeping the wavelength of the source while using a detector to sample the intensity variation (as a function of the wavelength

of the source), as illustrated in Fig. 2-5(a). Alternatively it may be produced by using a broadband source and sweeping the wavelength of an optical spectrum analyzer (or spectrometer), as illustrated in Fig. 2-5(b).

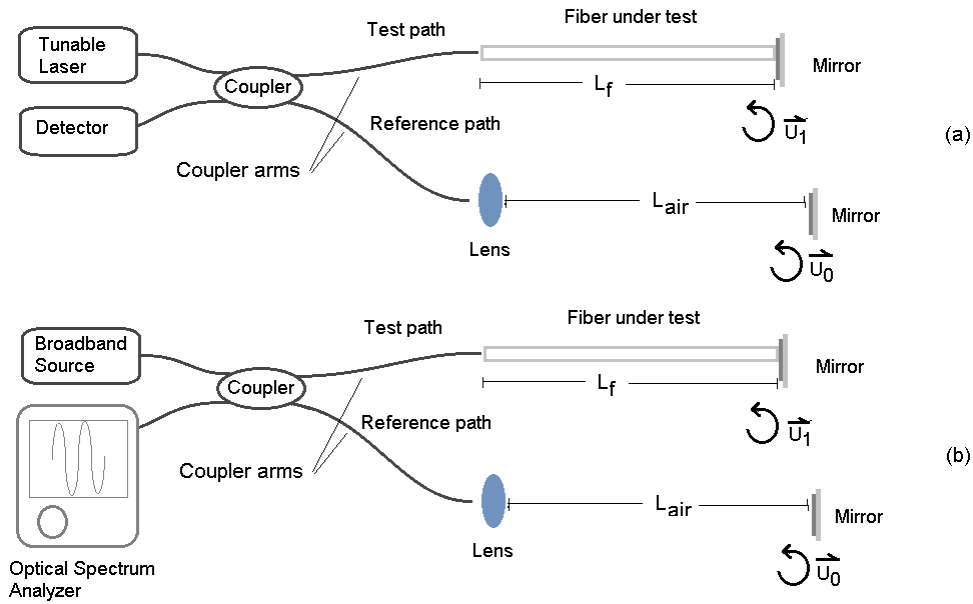


Fig. 2-5. Unbalanced spectral interferometry using (a) swept wavelength source (b) swept wavelength detection

The swept source configuration in Fig. 2-5(a) is typically used when high wavelength resolution is required to adequately sample the interference pattern. This is necessary when the path length imbalance between the test and reference path is large, resulting in a high frequency interference pattern. This can be seen in the expression for the interference pattern (in either setup) which is described by

$$\begin{aligned}
 I_{\text{Real}}(\lambda) &= |\overline{U}_0 + \overline{U}_1|^2 \\
 &= |\overline{U}_0|^2 \left| 1 + e^{-j2((\beta_f(\lambda)L_f - k_0L_{\text{air}}) + \Delta\mathcal{G})} \right|^2 \\
 &= 2|\overline{U}_0|^2 \left(1 + \cos\left(2\left((\beta_f(\lambda)L_f - k_0L_{\text{air}}) + \Delta\mathcal{G}\right)\right) \right)
 \end{aligned} \tag{Eq. 2-2}$$

where it has been assumed, for simplicity, that both reflections have equal magnitudes (i.e. $|\overline{U}_0| = |\overline{U}_1|$). $\beta_f(\lambda)$ is the propagation constant in the fiber under test, L_f is the length of the fiber under test, L_{air} is the length of the air path in the reference arm, k_0 is the propagation constant in free space (air path) and $\Delta\mathcal{G} = \beta_{f(\text{Coupler arms})}\Delta L_{\text{Coupler arms}}$ accounts for any length difference between the pigtails of the coupler in the test and reference arms, where $\beta_{f(\text{Coupler arms})}$ is the propagation constant of the coupler arms and $\Delta L_{\text{Coupler arms}} = L_{\text{Coupler arm test}} - L_{\text{Coupler arm ref}}$ is the length difference in the coupler arms. It is important to note that this length difference between the coupler arms must be calibrated out of every measurement, which introduces

calibration error into any measurements using this setup. One way to eliminate this source of calibration error and make $\Delta\theta = 0$ in Eq. 2-2 is to make the arms of the coupler equal in length. Since in practice it is difficult to make the arms of the coupler exactly equal in length, one solution is to fold the two arms of the coupler into a single optical path and employ a common path interferometer configuration, as illustrated in Fig. 2-6(a). In this configuration the light is not split into two separate paths since both phase fronts \vec{U}_0 and \vec{U}_1 pass through the launch fiber of a fiber optic circulator. Notice that this configuration is mathematically equivalent to a Michelson interferometer with equal length coupler arms and an air path of length zero, as illustrated in Fig. 2-6(b).

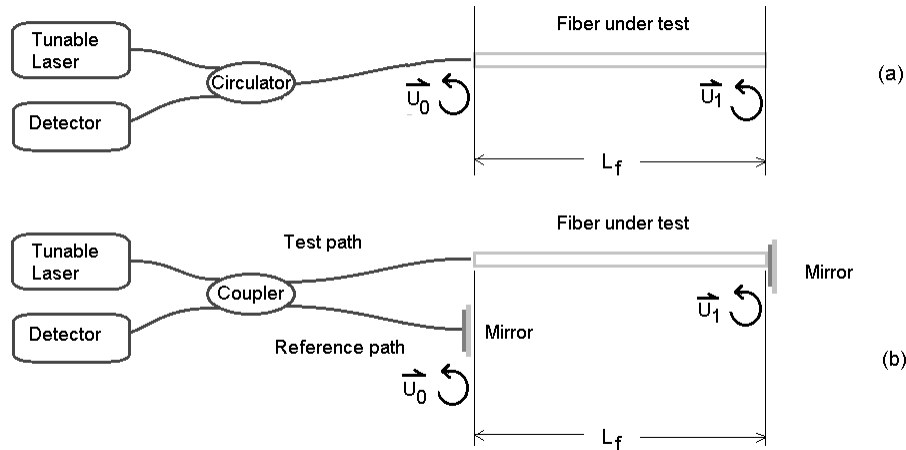


Fig. 2-6. (a) Common path configuration eliminates the calibration error due to imbalance in the leads of a coupler and is equivalent to (b) a dual arm configuration (Michelson interferometer) with coupler leads of equal length and a zero length air path. Note that for the common path configuration, multiple reflections due to the Fabry-Perot effect are ignored due to the low magnitude of the reflections from the fiber facets.

To simplify the expressions in the techniques for analyzing the spectral interference pattern, the common path configuration will be assumed. An example of an unbalanced spectral interferogram is presented in Fig. 2-7. Notice that the frequency of the interference varies continuously as a function of wavelength.

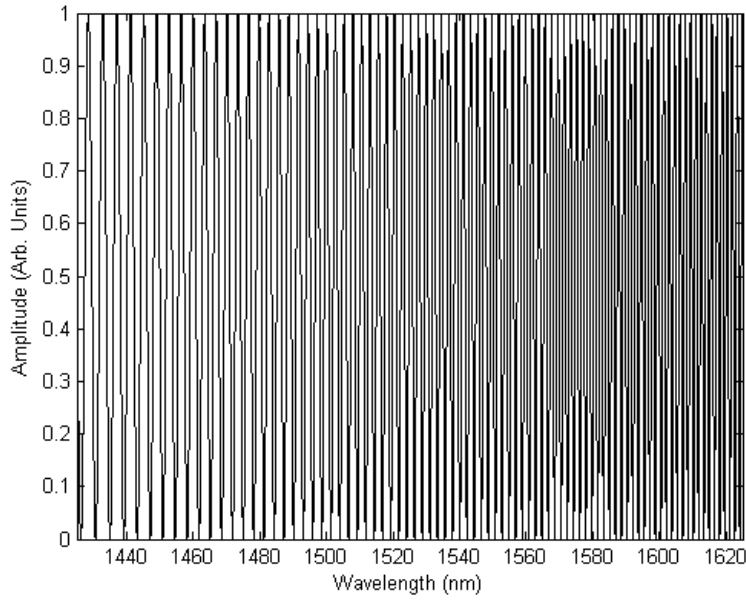


Fig. 2-7. Unbalanced spectral interference pattern

In general, there are two approaches used to extract the dispersion information from an unbalanced spectral interference pattern, one attempts to directly extract the phase of the interference pattern and the other attempts to directly extract the group delay.

2.4.1.1 Direct phase measurement

The first approach to extracting dispersion information from an unbalanced spectral interference pattern that is non-periodic is to attempt to measure the phase directly from the interference pattern from the phase of its Fourier transform [43] [44]. Recall that an unbalanced spectral interference pattern may be described by Eq. 2-2. Assuming, for simplicity, that a common path configuration is used so that $L_{\text{air}} = 0$ and $\Delta\vartheta = 0$, the interference pattern can be simplified as

$$I_{\text{Real}}(\lambda) = 2|\overline{U}_0|^2 \left(1 + \cos \left(\frac{2\beta_f(\lambda)L_f}{\phi(\lambda)} \right) \right) \quad \text{Eq. 2-3}$$

where the phase is given by $\phi(\lambda)$. Further simplification of the expression for the interference pattern may be obtained by filtering the zero frequency components and normalizing the amplitude so that it may be expressed as

$$I_{\text{Real}}(\lambda) = \cos \left(\frac{2\beta_f(\lambda)L_f}{\phi(\lambda)} \right) \quad \text{Eq. 2-4}$$

The most common method for extracting the phase $\phi(\lambda)$ of the interference pattern is to use a Fourier transform and examine the phase response [29] [45] [46] [43] [44]. This is done by considering that the interference pattern may be equivalently described as

$$I_{\text{Real}}(\lambda) = \cos(2\pi|\nu_0|\lambda + \phi_{\text{rel}}(\lambda)) = \frac{1}{2} \left(e^{j(2\pi|\nu_0|\lambda + \phi_{\text{rel}}(\lambda))} + e^{-j(2\pi|\nu_0|\lambda + \phi_{\text{rel}}(\lambda))} \right) \quad \text{Eq. 2-5}$$

where $|\nu_0|$ is the average spatial frequency of the interference pattern in the spectral scan and $\phi_{\text{rel}}(\lambda)$ represents the relative phase of the non-periodic fringe pattern with respect to this average (i.e. the deviation in frequency as a function of wavelength from the average frequency). Applying a Fourier transform on $I_{\text{Real}}(\lambda)$ gives

$$\begin{aligned} \hat{I}_{\text{Real}}(\nu) &= \int I_{\text{Real}}(\lambda) e^{-j2\pi\nu\lambda} d\lambda \\ &= \frac{1}{2} \int \left(e^{j(2\pi|\nu_0|\lambda + \phi_{\text{rel}}(\lambda))} + e^{-j(2\pi|\nu_0|\lambda + \phi_{\text{rel}}(\lambda))} \right) e^{-j2\pi\nu\lambda} d\lambda \\ &= \frac{1}{2} \int \left(e^{-j(2\pi(\nu - |\nu_0|)\lambda + \phi_{\text{rel}}(\lambda))} + e^{-j(2\pi(\nu + |\nu_0|)\lambda + \phi_{\text{rel}}(\lambda))} \right) d\lambda \end{aligned} \quad \text{Eq. 2-6}$$

which is illustrated in Fig. 2-8. Note that ν is the spatial frequency of the interference pattern.

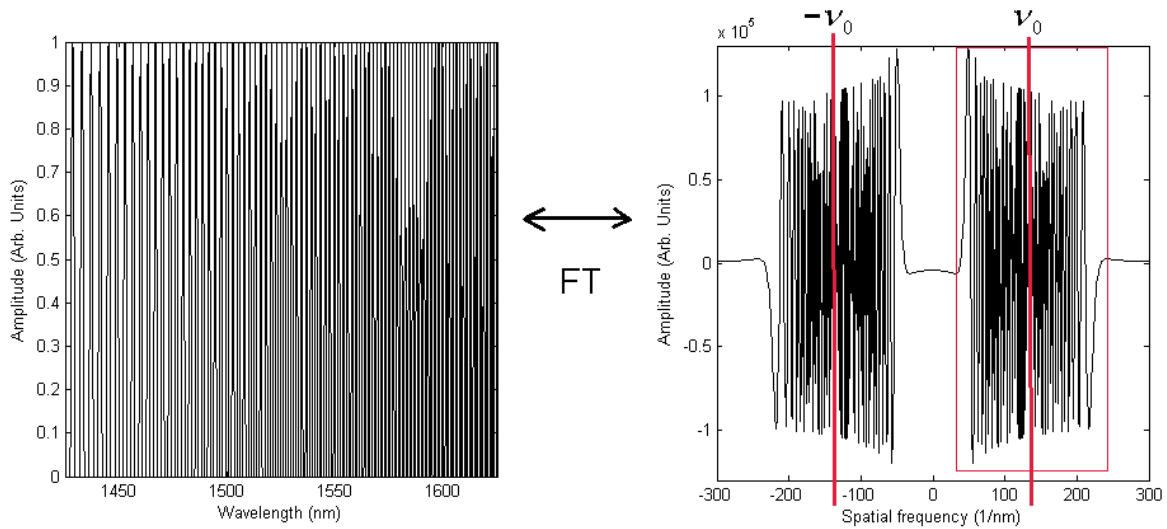


Fig. 2-8. Fourier transform on $I_{\text{Real}}(\lambda)$ followed by selection of the frequency content on one side of the Fourier spectrum.

Since the Fourier transform is symmetric across the zero frequency, only one side of the frequency spectrum is required. Selecting one side of the Fourier spectrum only, using an appropriate filter, the expression for $\hat{I}_{\text{Real}}(\nu)$ simplifies to

$$\begin{aligned}
\hat{I}_{\text{Real}}(\nu) &= \frac{1}{2} \int \left(e^{-j(2\pi(\nu-|\nu_0|)\lambda + \phi_{\text{rel}}(\lambda))} \right) d\lambda \\
&= j \frac{1}{4\pi(\nu-|\nu_0|)} e^{-j(2\pi(\nu-|\nu_0|)\lambda)} \int e^{-j(\phi_{\text{rel}}(\lambda))} d\lambda \\
&= \left(j \frac{1}{4\pi(\nu-|\nu_0|)} e^{-j(2\pi(\nu-|\nu_0|)\lambda)} \right) \left(-jA(\lambda) e^{-j(\phi_{\text{rel}}(\lambda))} \right) \\
&= \frac{A(\lambda)}{4\pi(\nu-|\nu_0|)} e^{-j(2\pi(\nu-|\nu_0|)\lambda + \phi_{\text{rel}}(\lambda))}
\end{aligned}$$

Eq. 2-7

where $A(\lambda)$ is a real function. Applying an inverse Fourier transform on $\hat{I}_{\text{Real}}(\nu)$ gives

$$\begin{aligned}
I_{\text{Real}}(\lambda) &= \int \frac{A(\lambda)}{4\pi(\nu-|\nu_0|)} e^{-j(2\pi(\nu-|\nu_0|)\lambda + \phi_{\text{rel}}(\lambda))} e^{j2\pi\nu\lambda} d\nu \\
&= \int \frac{A(\lambda)}{4\pi(\nu-|\nu_0|)} e^{j(2\pi(|\nu_0|)\lambda + \phi_{\text{rel}}(\lambda))} d\nu \\
&= \frac{A(\lambda) e^{j(2\pi|\nu_0|\lambda + \phi_{\text{rel}}(\lambda))}}{4\pi} \left(\int \frac{1}{(\nu-|\nu_0|)} d\nu \right) \\
&= \frac{A(\lambda) e^{j(2\pi|\nu_0|\lambda + \phi_{\text{rel}}(\lambda))}}{4\pi} \ln(\nu-|\nu_0|) \\
&= \frac{A(\lambda)}{4\pi} \ln(\nu-|\nu_0|) \left(\underbrace{\cos(2\pi|\nu_0|\lambda + \phi_{\text{rel}}(\lambda))}_{\text{Re}} + j \underbrace{\sin(2\pi|\nu_0|\lambda + \phi_{\text{rel}}(\lambda))}_{\text{Im}} \right)
\end{aligned}$$

Eq. 2-8

$I_{\text{Real}}(\lambda)$ is a complex function with real and imaginary components. It therefore has an amplitude and phase

$$I_{\text{Real}}(\lambda) = |I_{\text{Real}}(\lambda)| \angle \theta(\lambda)$$

Eq. 2-9

where

$$|I_{\text{Real}}(\lambda)| = \left(\text{Re}(I_{\text{Real}}(\lambda))^2 + \text{Im}(I_{\text{Real}}(\lambda))^2 \right)^{\frac{1}{2}} = \left| \frac{A(\lambda)}{4\pi} \ln(\nu-|\nu_0|) \right|$$

Eq. 2-10

The magnitude spectrum $|I_{\text{Real}}(\lambda)|$ is not used in this analysis as it does not contain the phase information. The phase of $I_{\text{Real}}(\lambda)$ may be obtained as

$$\begin{aligned}
\angle\theta(\lambda) &= \arctan\left(\frac{\text{Im}(I_{\text{Real}}(\lambda))}{\text{Re}(I_{\text{Real}}(\lambda))}\right) \\
&= \arctan\left(\frac{\sin(2\pi|v_0|\lambda + \phi_{\text{rel}}(\lambda))}{\cos(2\pi|v_0|\lambda + \phi_{\text{rel}}(\lambda))}\right) \\
&= \arctan\left(\tan(2\pi|v_0|\lambda + \phi_{\text{rel}}(\lambda))\right) \\
&= 2\pi|v_0|\lambda + \phi_{\text{rel}}(\lambda)
\end{aligned}
\tag{Eq. 2-11}$$

Therefore from this analysis the phase of the spectral interference pattern $I_{\text{Real}}(\lambda)$ can be determined by

$$\phi(\lambda) = \phi_{\text{rel}}(\lambda) + 2\pi|v_0|\lambda = \angle\theta(\lambda)
\tag{Eq. 2-12}$$

The problem when this approach is used for the measurement of dispersion, however, is that multiple derivatives of the phase are required to extract first and second order dispersion from the phase [29]. For example, Eq. 1-6 shows that to extract the group delay from the phase requires first order differentiation of the phase. Furthermore Eq. 1-7 shows that extraction of the second order dispersion from the phase requires a second order derivative of the phase. The problem with the need to take multiple derivatives to extract dispersion information from the phase of a *real* interference pattern is the unavoidable presence of noise. Because of the presence of noise in the interference pattern, the points in the resulting phase plot also contain noise (scatter). It is therefore not practical to numerically differentiate the phase. This means that the measured phase must be fit with an appropriate function and then analytically differentiated. For most fiber, the phase is an approximately linear function (curvature of phase is the second order dispersion (Eq. 1-7) which is intentionally small in fiber). Using this technique for the measurement of dispersion, therefore, requires the fitting of a higher order function (e.g. Sellmeier or polynomial) to phase measurement plots that are approximately linear and contain noise. The presence of noise, greatly affects the fit to the phase, as illustrated in Fig. 2-9, making the results of the group delay measurements dependent on the choice of fit, which results in large errors [46].

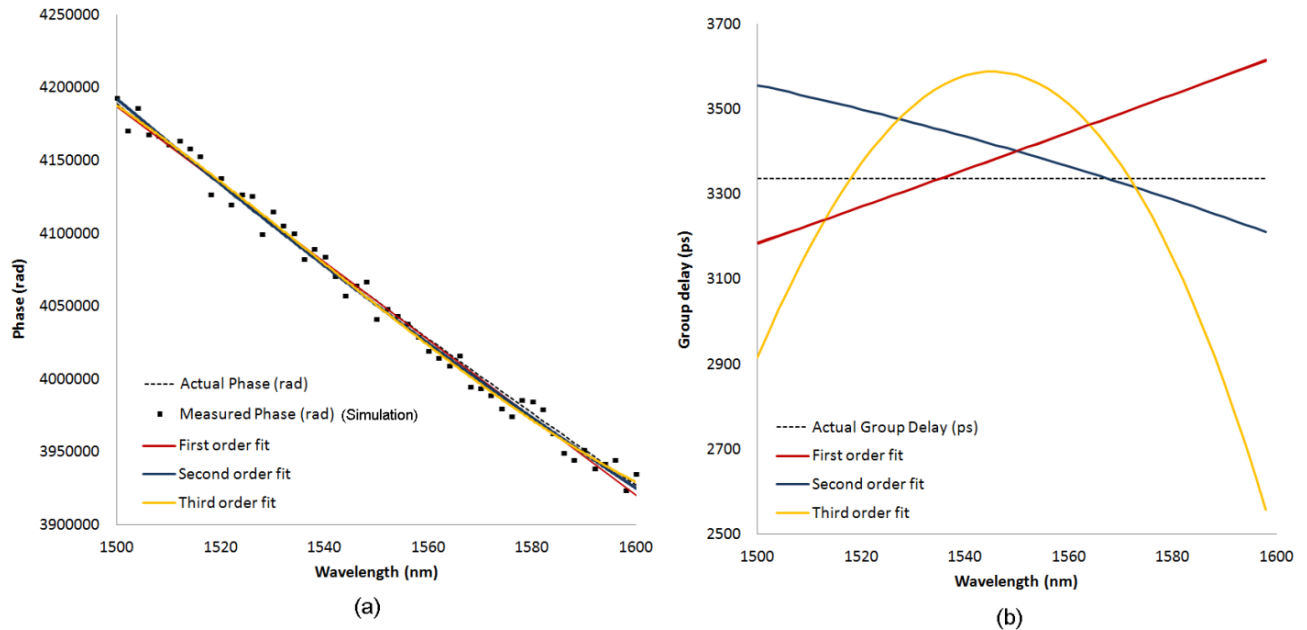


Fig. 2-9. Simulation of effect of noise on polynomial fit to (a) phase measurements and the resulting effect on (b) the group delay measurement (from the fit to the phase measurement).

Since the second order dispersion is determined from the slope of the group delay curve it is clear that the dispersion parameter curve would have even larger error given the large variation in the group delay curves. It is interesting to point out, however, that since this technique directly measures the phase, it is the best technique for measuring the effective index of the fiber, whereas techniques that measure the first and second order dispersion directly would have trouble measuring the effective index since a fit would be required by these techniques to measure the effective index. This point is discussed further in [Appendix E](#) for the interested reader. The focus of this thesis, however, is to obtain the best measurements of the first and second order dispersion.

To overcome the problems associated with directly measuring the phase, the next section discusses an approach for measuring the first order dispersion (group delay) directly from an unbalanced interference pattern.

2.4.1.2 Direct group delay measurement

One method of directly measuring the group delay via unbalanced spectral interferometry is to employ a windowed Fourier transform (USI-WFT) to extract the amplitude spectrum [29] [40] [41] [45] in Eq. 2-7. In this technique, a windowed section of the bandwidth is chosen. Taking the amplitude of the Fourier transform (Eq. 2-2 with $\phi(\lambda) = 0$) results in two peaks that are symmetric across zero frequency (Fig. 2-10(b)). The dependent axis of the Fourier transform was converted from index location, m , to spatial frequency using

$$|v_0| = \frac{m}{M} v_{\text{sampling}} \quad \text{Eq. 2-13}$$

where M is the number of samples on one side of the zero frequency in the Fourier domain and v_{sampling} is the sampling frequency of the points in $I_{\text{Real}_{\text{window}}}(\lambda)$. Using this conversion, the dependent axis the spatial frequency plot in Fig. 2-10(b) may be used directly to obtain $|v_0|$. Moving the window across the spectrum allows the (average) frequency to be obtained as a function of wavelength. Note that this technique assumes that the frequency of the fringes within each windowed section is approximately constant (i.e. $\phi(\lambda) = 0$ in Eq. 2-2), which is not entirely accurate.

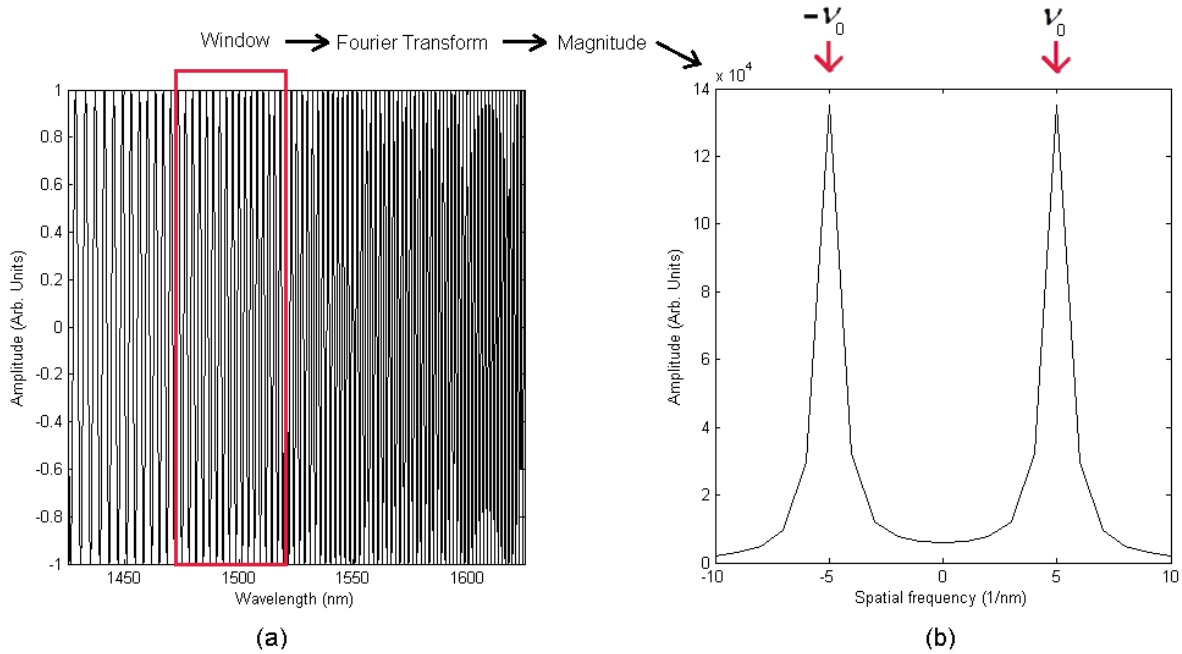


Fig. 2-10. (a) Windowed section of the interference pattern and (b) result of Fourier transform applied on windowed section.

Obtaining $|v_0|$ from the peak of a Fourier transform and assuming that

$$I_{\text{Real}_{\text{window}}}(\lambda) = \cos\left(\underbrace{2\beta_f(\lambda)L_f}_{\phi(\lambda)}\right) \cong \cos(2\pi|v_0|\lambda) \quad \text{Eq. 2-14}$$

(i.e. the frequency within the windowed section is constant), one may obtain

$$2\beta_f(\lambda)L_f \cong 2\pi|v_0|\lambda \quad \text{Eq. 2-15}$$

Taylor expansion of $\beta_f(\lambda)$ around a centre wavelength λ_0 gives

$$\beta_f(\lambda) = \beta_f(\lambda_0) + \frac{(\lambda - \lambda_0)}{1!} \left. \frac{d\beta_f}{d\lambda} \right|_{\lambda_0} + \frac{(\lambda - \lambda_0)^2}{2!} \left. \frac{d^2\beta_f}{d\lambda^2} \right|_{\lambda_0} + \dots \quad \text{Eq. 2-16}$$

Substitution of Eq. 2-16 into Eq. 2-15 gives

$$2L_f \left(\beta_f(\lambda_0) + \frac{(\lambda - \lambda_0)}{1!} \left. \frac{d\beta_f}{d\lambda} \right|_{\lambda_0} + \frac{(\lambda - \lambda_0)^2}{2!} \left. \frac{d^2\beta_f}{d\lambda^2} \right|_{\lambda_0} + \dots \right) \cong 2\pi |v_0| \lambda \quad \text{Eq. 2-17}$$

The right hand side of the equation is proportional to λ , whereas the only component on left hand side that is proportional to λ is the $\left. \frac{d\beta_f}{d\lambda} \right|_{\lambda_0}$ component, therefore

$$2L_f \left. \frac{d\beta_f}{d\lambda} \right|_{\lambda_0} \lambda \cong 2\pi |v_0| \lambda \quad \text{Eq. 2-18}$$

and since

$$\beta_f(\lambda) = \frac{2\pi}{\lambda} n_{\text{eff}}(\lambda) \quad \text{Eq. 2-19}$$

this means that

$$\left. \frac{d\beta_f}{d\lambda} \right|_{\lambda_0} = -\frac{2\pi}{\lambda_0^2} \left(n_{\text{eff}}(\lambda_0) - \lambda_{0\text{avg}} \left. \frac{dn_{\text{eff}}}{d\lambda} \right|_{\lambda_0} \right) \cong -\frac{2\pi}{\lambda_0^2} N_g(\lambda_0) \quad \text{Eq. 2-20}$$

Substitution of Eq. 2-20 into Eq. 2-18 gives

$$|v_0| \cong \frac{2N_g(\lambda_0)L_f}{\lambda_0^2} \quad \text{Eq. 2-21}$$

Rearranging the terms

$$N_g(\lambda_0)L_f \cong \frac{|v_0|\lambda_0^2}{2} \quad \text{Eq. 2-22}$$

The group delay may then be determined from Eq. 1-6 and Eq. 2-22 as

$$\tau_g(\lambda_0) = \frac{N_g(\lambda_0)L_f}{c} \cong \frac{|v_0|\lambda_0^2}{2c} \quad \text{Eq. 2-23}$$

This technique is better than the phase based technique since it is capable of measuring the first order dispersion (group delay) directly from the interference pattern. One problem with this technique, however, is that it assumes that the wavelength location of the group delay measurement is the centre of the window. This would be true if the interference pattern was truly periodic, however, since the spectral interference patterns are non-periodic as a function of wavelength, this is not accurate. As a result, there is uncertainty in the wavelength location of the group

delay measurement. This means that the larger the window size the larger the uncertainty in the wavelength location of the group delay measurement, as illustrated in Fig. 2-11.

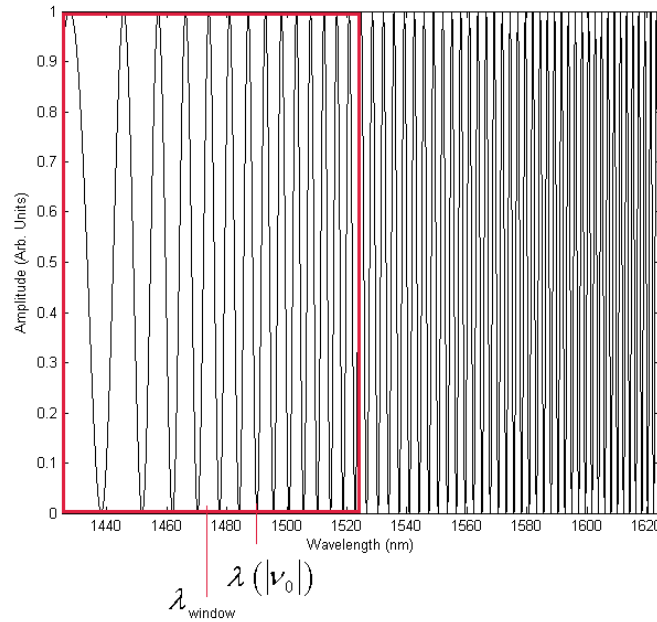


Fig. 2-11. Illustration of the uncertainty between the wavelength at centre of window λ_{window} and the wavelength $\lambda(|\nu_0|)$ where the interference fringe period is measured to be $|\nu_0|$

Another problem with this technique is that second order dispersion cannot be measured directly from the interference pattern but must be obtained indirectly from a fit to the first order dispersion (group delay) using Eq. 1-7. This would not be a problem if the group delay plot could be obtained with high accuracy and low noise. However, since the interference pattern contains noise, the group delay plot produced by this technique will also contain noise (scatter). This means that the group delay cannot be numerically differentiated but must be fit with an appropriate function and analytically differentiated to obtain the second order dispersion. For most fiber, the group delay is an approximately linear function (the slope of group delay gives the second order dispersion via Eq. 1-7, which is intentionally small in fiber). Using this technique for the measurement of dispersion, therefore, requires the fitting of a higher order function (e.g. a second or third order polynomial) to the group delay measurement plot that is approximately linear and contains noise. The presence of noise greatly affects the fit and makes the first order dispersion measurement from the fit dependent on the choice of fit used. As in the last section this also results in large errors [46], as illustrated in Fig. 2-12.

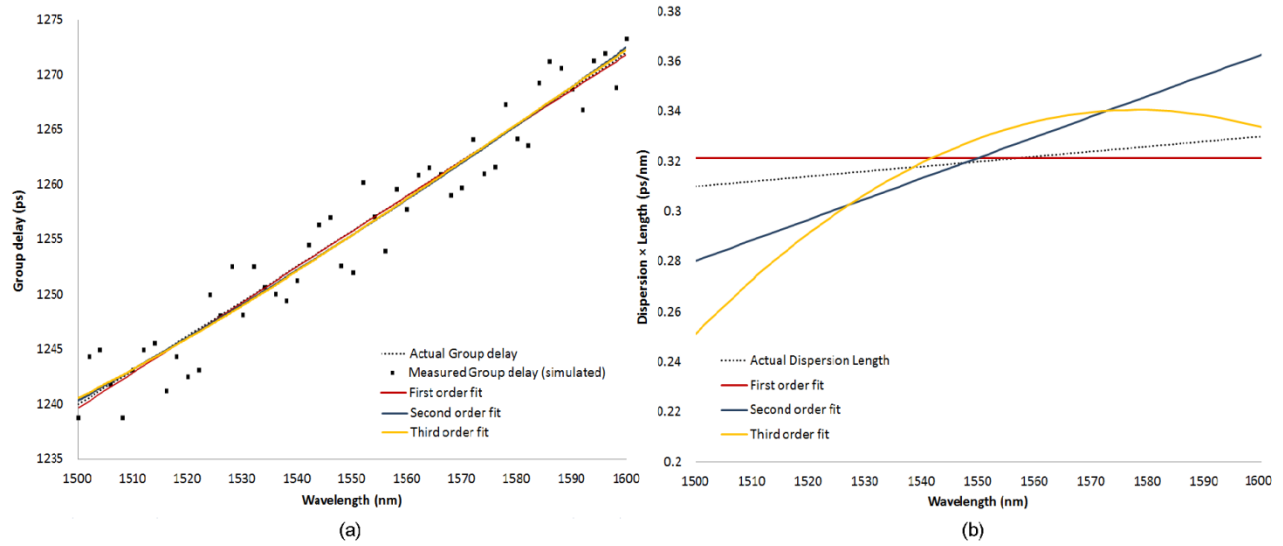


Fig. 2-12. Simulation of effect of noise on polynomial fits to (a) group delay measurements and the resulting effect on (b) the dispersion \times length measurement

A very important point about this technique is that the noise (scatter) in the group delay plot is not only a function of the noise in the interference pattern but also a function of the size of the window used. Choosing a large window size increases the width of the spectral peaks in Fig. 2-10 by adding frequency content (interference pattern is non-periodic due to dispersion), which increases the error in the measured value of $|\nu_0|$. Choosing a small window size cannot overcome this issue since this also leads to broadening of the peaks in Fig. 2-10, due to the inverse nature of the bandwidth of a signal and the bandwidth its Fourier transform [47]. This means that there is an optimum window size that results in the narrowest peak (smallest scatter in the group delay plot) but it cannot be known apriori. The result is that the scatter in the first order dispersion (group delay) plot cannot be minimized. The increased scatter also affects the fit to the group delay, from which the second order dispersion is obtained (as previously discussed). For mathematical rigor and completeness [Appendix C.1](#) formally derives the first order dispersion (group delay) resolution (and scatter) in USI. The result of this derivation is that the resolution in USI is dependent on the window size used in the Fourier transform. However, since an optimum window size cannot be known apriori, it is impossible to maximize the resolution. Later the resolution of USI will be compared to that of BSI and it will be shown that the resolution of USI approaches that of BSI only if the optimum window size is known. However, since an optimum cannot be known, BSI techniques will be shown to have higher resolution.

2.4.2 Balanced spectral interferometry

In balanced spectral interferometry (BSI) [13] [28] [29] [33] [34] [35] [40] [42] [48] the group delay in the test arm of an interferometer is balanced by that of the reference arm at a wavelength within the spectral scan, as illustrated in Fig. 2-13. A balanced interference pattern has a large central peak at the balance point (wavelength) λ_0 , with the frequency of the interference pattern increasing on both sides.

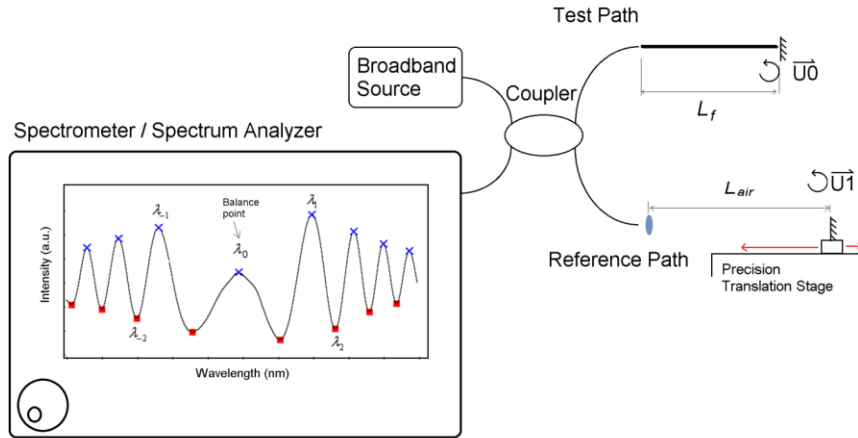


Fig. 2-13. Schematic of a balanced spectral interferometry experiment

An important part of measurements based on balanced spectral interferometry (will also be used for VRI) is the pattern recognition process used to determine if a particular interference pattern is acceptable (i.e. balanced within the scan range and with a high enough signal-to-noise ratio, etc). Fig. 2-14(a) shows the interferogram with peaks (marked with blue crosses) superimposed and valleys (red squares) in the interferogram. The pattern recognition process begins with measuring the period between either all the peaks or all the valleys in the interferogram. This process produces a plot of the period between peaks or valleys. The period plot has either a single maximum point or two points that are very close in magnitude. The period of the peaks and valleys are shown in Fig. 2-14(b). The period of the valleys trace the first acceptable pattern and the period of the peaks trace the second.

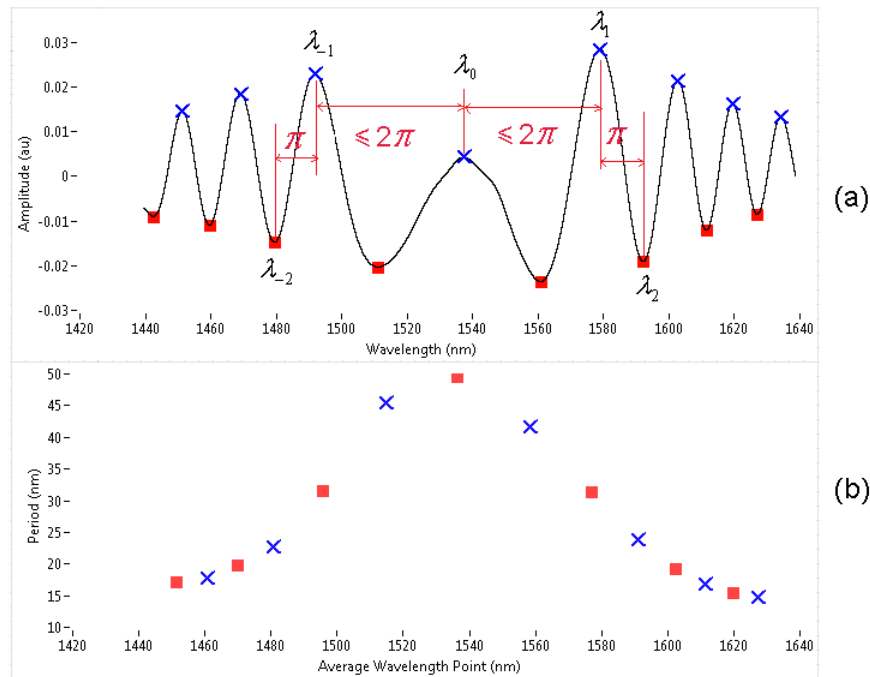


Fig. 2-14. Pattern with a single maximum (in red) superimposed with a pattern with two maxima (in blue)

It is not always easy to distinguish between the two types of interferograms algorithmically. One method to distinguish between the two cases is to compare the difference between the largest and second largest period to the difference between the second largest and the third largest period in Fig. 2-14(b). If the difference between the largest and second largest period is greater than the difference between the second largest and third largest period, then the pattern is that of the single maxima (red squares). Otherwise the pattern is that with two maxima (blue crosses). Determining which pattern is correct is critical to the dispersion measurement, since it determines the wavelength location of the measurement. If the pattern has a single maxima then the location of λ_0 is determined using the wavelengths corresponding to the second, third, fourth and fifth largest periods. If the pattern has two maxima, then the location of λ_0 is determined from the wavelengths corresponding to the first, second, third and fourth largest periods. Regardless of which four wavelength locations are chosen (i.e. $\lambda_{-2}, \lambda_{-1}, \lambda_1, \lambda_2$ in Fig. 2-14(a)), the location of λ_0 is determined from the average of these four wavelengths converted to the frequency domain where the interference pattern is symmetric around λ_0 as

$$\lambda_0 = \left(\frac{1/\lambda_{-2} + 1/\lambda_{-1} + 1/\lambda_1 + 1/\lambda_2}{4} \right)^{-1} \quad \text{Eq. 2-24}$$

Once the pattern recognition process has determined that a particular interference pattern is useable and locates the balance point, the first and second order dispersion can then be extracted from the interference pattern. Since the balancing of the group delay in the test and reference paths effectively cancels the first order dispersion (large linear portion of the phase) in the test path, the spectral interference pattern may be used to obtain both first and second order dispersion separately and directly from the interference pattern. To demonstrate this mathematically, assume for simplicity that the arms of the coupler are exactly the same length (i.e. $\Delta\theta = 0$ in Eq. 2-2), that the dispersion of the lens in the reference path may be ignored and that the rest of the reference arm is a free space variable delay line (with a length that may be varied using a precision translation stage), as shown in Fig. 2-13. The interference pattern produced by the reflections $\overline{U0}$ and $\overline{U1}$ was described by Eq. 2-2, where setting $\Delta\theta = 0$ this equation simplifies to

$$I_{\text{Real}}(\lambda) = 2|\overline{U0}|^2 \left(1 + \cos \left(2 \left(\beta_f(\lambda)L_f - k_o(\lambda)L_{\text{air}} \right) \right) \right) \quad \text{Eq. 2-25}$$

Recall that $\beta_f(\lambda)$ is the propagation constant of the fiber placed in the test path and L_f is its length, $k_o(\lambda)$ is the propagation constant in free space and L_{air} is the length of the air path (free space) in the reference arm. The phase of the interference pattern is therefore

$$\varphi(\lambda) = 2 \left(\beta_f(\lambda)L_f - k_o(\lambda)L_{\text{air}} \right) \quad \text{Eq. 2-26}$$

The propagation constant of the fiber β_f is related to the effective index n_{eff} via

$$\beta_f(\lambda) = k_o n_{eff_f}(\lambda) = \frac{2\pi}{\lambda} n_{eff_f}(\lambda) \quad \text{Eq. 2-27}$$

Taylor expansion of the effective index around the wavelength λ_0 gives

$$n_{eff_f}(\lambda) = n_{eff_f}(\lambda_0) + \frac{(\lambda - \lambda_0)}{1!} \left. \frac{dn_{eff_f}}{d\lambda} \right|_{\lambda_0} + \frac{(\lambda - \lambda_0)^2}{2!} \left. \frac{d^2 n_{eff_f}}{d\lambda^2} \right|_{\lambda_0} + \frac{(\lambda - \lambda_0)^3}{3!} \left. \frac{d^3 n_{eff_f}}{d\lambda^3} \right|_{\lambda_0} + \dots \quad \text{Eq. 2-28}$$

Collecting terms in Eq. 2-28 where

$$N_g(\lambda_0) = n_{eff_f}(\lambda_0) - \lambda_0 \left. \frac{dn_{eff_f}}{d\lambda} \right|_{\lambda_0} \quad \text{Eq. 2-29}$$

followed by substitution of Eq. 2-29 into Eq. 2-27 gives

$$\varphi(\lambda) = 4\pi \left\{ \underbrace{\left(N_g(\lambda_0) L_f - L_{air} \right)}_{=0} + \left. \frac{dn_{eff_f}}{d\lambda} \right|_{\lambda_0} L_f + \left[\frac{(\lambda - \lambda_0)^2}{2! \lambda} \left. \frac{d^2 n_{eff_f}}{d\lambda^2} \right|_{\lambda_0} L_f + \frac{(\lambda - \lambda_0)^3}{3! \lambda} \left. \frac{d^3 n_{eff_f}}{d\lambda^3} \right|_{\lambda_0} L_f + \dots \right] \right\} \quad \text{Eq. 2-30}$$

At the balance point, illustrated by λ_0 in Fig. 2-13 and Fig. 2-14 the group delay in the test path is equal to that in the reference path because the phase function in Eq. 2-30 is minimized at λ_0 (i.e. $d\varphi/d\lambda|_{\lambda=\lambda_0} = 0$) so that

$$N_g(\lambda_0) L_f = L_{air} \quad \text{Eq. 2-31}$$

where the group delay is related to the optical (group) path length using both Eq. 2-31 and Eq. 1-6. This means that the first term in Eq. 2-30 is zero. With the first term set to zero, the large linear part of the phase is removed, leaving only the higher order terms in Eq. 2-30. The $dn_{eff_f}/d\lambda|_{\lambda_0}$ term may also be removed from the expression by taking the phase difference between two points in the interferogram (i.e. peaks or valleys) with a known phase separation (illustrated in Fig. 2-14). For example, Using Eq. 2-30, an expression for the phase separation between a peak or valley at λ_m and a peak or valley at λ_n results in

$$\begin{aligned} |\varphi(\lambda_m) - \varphi(\lambda_n)| &= 4\pi \left\{ \left[\frac{(\lambda_m - \lambda_0)^2}{2! \lambda_m} - \frac{(\lambda_n - \lambda_0)^2}{2! \lambda_n} \right] \left. \frac{d^2 n_{eff_f}}{d\lambda^2} \right|_{\lambda_0} L_f + \left[\frac{(\lambda_m - \lambda_0)^3}{3! \lambda_m} - \frac{(\lambda_n - \lambda_0)^3}{3! \lambda_n} \right] \left. \frac{d^3 n_{eff_f}}{d\lambda^3} \right|_{\lambda_0} L_f + \dots \right\} \\ &= |m - n| \pi \end{aligned} \quad \text{Eq. 2-32}$$

where $|m - n|$ is the number of peak-to-valley or valley-to-peak transitions between λ_m and λ_n , which are both on the same side of λ_0 . Note that λ_m is chosen to be the peak or valley that is furthest from λ_0 . What is important is

that Eq. 2-32 contains only the higher order terms and may be used to solve for $d^2n_{eff}/d\lambda^2|_{\lambda_0}$ which gives the second order dispersion directly from the interference pattern via Eq. 1-7.

The first and second order dispersion may then be plotted as a function of wavelength by varying the length of the air path (variable delay line) by a small well known incremental amount and re-scanning the interference pattern. This changes the length of L_{air} and shifts the balance point λ_0 to a new wavelength where the first and second order dispersion can be measured again. Various methods for extracting first and second order dispersion using Eq. 2-31 and Eq. 2-32 are now discussed.

First order dispersion may be extracted using Eq. 2-31 if the air path length L_{air} (or alternatively the change in the air path length, ΔL_{air}) of the reference is known with high precision. By varying the length of L_{air} , a plot of λ_0 vs. L_{air} may be produced. If the value of L_{air} is known absolutely then it can be converted to absolute group delay via

$$\tau_g(\lambda_0) = \frac{L_{air}}{c} = \frac{N_g(\lambda_0)L_f}{c} \quad \text{Eq. 2-33}$$

Alternatively, if L_{air} is not known absolutely then the incremental changes from a reference length (i.e. ΔL_{air}) can be used to produce a relative group delay plot via

$$\Delta\tau_g(\lambda_0) = \frac{\Delta L_{air}}{c} = \frac{\Delta N_g(\lambda_0)L_f}{c} \quad \text{Eq. 2-34}$$

For this to be accurate, a precision translation stage is required. In this type of measurement, L_{air} is the independent parameter (known) and λ_0 is the dependent parameter (unknown).

The standard method for extraction of the second order dispersion from the balanced interference pattern was first demonstrated in [13]. In this method Eq. 2-32 is used to obtain a system of equations using the phase difference between peaks and/or valleys (i.e. λ_1 and λ_2 on the right side of λ_0 and to λ_{-1} and λ_{-2} on the left side of λ_0 in Fig. 2-14). Neglecting the expansion terms above $d^3n_{eff}/d\lambda^3|_{\lambda_0}$ allows this system to be solved with two equations. Using the phase differences illustrated in Fig. 2-14, the system of equations may be given by

$$|\varphi(\lambda_2) - \varphi(\lambda_1)| = \left\{ \begin{array}{l} \left[\frac{(\lambda_2 - \lambda_0)^2}{\lambda_2} - \frac{(\lambda_1 - \lambda_0)^2}{\lambda_1} \right] \frac{d^2 n_{eff_f}}{d\lambda^2} \Big|_{\lambda_0} L_f + \\ \left[\frac{(\lambda_2 - \lambda_0)^3}{3\lambda_2} - \frac{(\lambda_1 - \lambda_0)^3}{3\lambda_1} \right] \frac{d^3 n_{eff_f}}{d\lambda^3} \Big|_{\lambda_0} L_f + \dots \end{array} \right\} = \frac{1}{2} \quad \text{Eq. 2-35}$$

$$|\varphi(\lambda_{-2}) - \varphi(\lambda_{-1})| = \left\{ \begin{array}{l} \left[\frac{(\lambda_{-2} - \lambda_0)^2}{\lambda_{-2}} - \frac{(\lambda_{-1} - \lambda_0)^2}{\lambda_{-1}} \right] \frac{d^2 n_{eff_f}}{d\lambda^2} \Big|_{\lambda_0} L_f + \\ \left[\frac{(\lambda_{-2} - \lambda_0)^3}{3\lambda_{-2}} - \frac{(\lambda_{-1} - \lambda_0)^3}{3\lambda_{-1}} \right] \frac{d^3 n_{eff_f}}{d\lambda^3} \Big|_{\lambda_0} L_f + \dots \end{array} \right\} = \frac{1}{2}$$

Although it is possible in principle to solve for the higher order terms by adding more equations to the system (i.e. selecting more pairs) it is generally not necessary in practice since the noise in the interference pattern typically makes these terms impossible to extract. The system of equations may then be written in the Matrix form

$$\begin{bmatrix} p & q \\ r & s \end{bmatrix} \begin{bmatrix} d^2 n_{eff_f} / d\lambda^2 \Big|_{\lambda_0} \\ d^3 n_{eff_f} / d\lambda^3 \Big|_{\lambda_0} \end{bmatrix} L_f \cong \begin{bmatrix} \frac{1}{2} \\ \frac{1}{2} \end{bmatrix} \quad \text{Eq. 2-36}$$

Where the parameters p , q , r and s are determined by locating λ_1 , λ_2 , λ_{-1} and λ_{-2} . Eq. 2-36 may be solved explicitly by multiplying both sides by the inverse of the square matrix as

$$\begin{bmatrix} d^2 n_{eff_f} / d\lambda^2 \Big|_{\lambda_0} \\ d^3 n_{eff_f} / d\lambda^3 \Big|_{\lambda_0} \end{bmatrix} L_f = \frac{1}{(ps - qr)} \begin{bmatrix} s & -q \\ -r & p \end{bmatrix} \begin{bmatrix} \frac{1}{2} \\ \frac{1}{2} \end{bmatrix} \quad \text{Eq. 2-37}$$

Since we are typically only interested in calculating the second order dispersion (the dispersion parameter \times length) we are interested in the $d^2 n_{eff_f} / d\lambda^2 \Big|_{\lambda_0}$ term which is given by.

$$d^2 n_{eff_f} / d\lambda^2 \Big|_{\lambda_0} L_f = \frac{s - q}{2(ps - qr)} \quad \text{Eq. 2-38}$$

The second order dispersion \times length can then be found by substitution of Eq. 2-38 into Eq. 1-7 which results in

$$D(\lambda_0) L_f = -\frac{\lambda_0}{c} \frac{s - q}{2(ps - qr)} \quad \text{Eq. 2-39}$$

This matrix approach is typically useful when the effect of the third order dispersion term $d^3 n_{eff_f} / d\lambda^3 \Big|_{\lambda_0}$ is non negligible and its effects must be included in the calculation of second order dispersion. Typically, however, the

effect of the third order dispersion is many orders of magnitude smaller and it can be ignored. Alternative dispersion extraction techniques with a high immunity to noise in the interferogram (which require third and higher order dispersion to be negligible) are discussed in [Appendix B](#). The ability to extract first and second order dispersion (group delay and dispersion parameter) directly from the phase of the interference pattern gives balanced spectral interferometric measurements a precision of 0.00007 ps/nm [13], which is the best precision of all interferometric measurement techniques. This makes BSI the preferred method for characterizing short-length optical components [19]. The main problem with BSI, however, is the need for a variable (free space) delay line with precision translational control. An example of a free space optical delay line (that I built) is shown in Fig. 2-15.

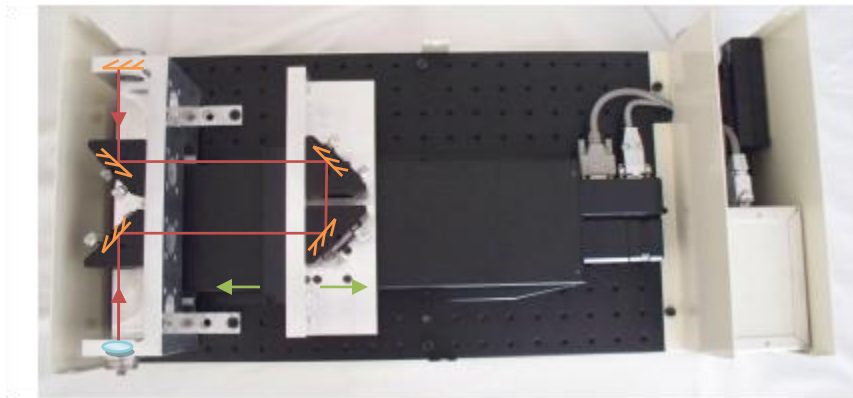


Fig. 2-15. Free-space variable optical-delay-line with precision translation stage. Optical path length varied using precision translation stage. The folded optical beam path is illustrated in red, the translation is illustrated in green, the lens is drawn as an overlay to the image in blue and the mirrors are drawn as an overlay in orange.

The type of free space optical delay line required in balanced spectral interferometry is costly, difficult to setup and time consuming to operate. Its high cost comes from the need for precision control of the free space optical path. The need for precision control comes from the necessity to vary the optical path length of the reference by small, well controlled increments. This is because the plot of the group delay relies on accurate knowledge of the position (or relative change in position) in the reference path length. The increments must also be small so that the change in the balance point wavelength is small enough that it does not move outside the scan range too quickly (i.e. so that several points can be obtained). For this reason, a precision (optical grade) translation stage is required, which can be quite costly. The free space optical delay line is also very difficult to set up because the beam path must maintain its alignment as the position of the translation stage is varied. Additionally, the fiber from the coupler arm must be placed precisely at the focal point of the lens; otherwise the beam will diverge/converge and will not couple back into the fiber on the return path. The alignment of the variable reference path alone is an incredibly difficult practical problem to solve. This is because there are two degrees of freedom (polar angle and azimuth angle) for every lens or mirror in the delay line. Even if a folded optical path (shown in Fig. 2-15) is not used (i.e. on a long optical table in a lab setup) there would still be four degrees of freedom that must be maintained over the entire travel path. Note that this is another reason for the high cost of the translation stage since its must track perfectly straight (low deviation tolerance in the manufacturing process). For a commercial delay line, which must be folded to fit within a small

package (box) (as shown in Fig. 2-15), this difficulty is further exacerbated by the additional mirrors required. For a single fold in the optical path (shown in Fig. 2-15), five mirrors are required, in addition to the lens. This means that there are 12 degrees of freedom to the alignment. In addition to the high cost and difficult setup, balanced spectral interferometers require a new spectral scan of the interference pattern (new balance point) for every point (wavelength) desired in the dispersion plot. This can be quite a time consuming, especially when large numbers of data points are required. The time consuming nature of this process means that the reference path must be sealed (sometime hermetically) to prevent changes in temperature, pressure or air flow from affecting the results.

The translation stage also has a physical limit on the smallest increment it can vary the optical path length (and accurately resolve) in the path length of the reference. This limits the smallest spacing between measured points in the first and second order dispersion plots. The reason for this is that the balance point λ_0 is varied by changing the length of the reference path via Eq. 2-31 and scanning the interference pattern. The relationship between the smallest increment in the reference path and the spectral change in λ_0 may be found by substitution of Eq. 2-29 into Eq. 2-31 and differentiation of both sides of Eq. 2-31 with respect to λ , followed by substitution of Eq. 1-7 into the result as

$$\begin{aligned}
 \left. \frac{dL_{air}}{d\lambda} \right|_{\lambda_0} &= \left. \frac{dN_g}{d\lambda} \right|_{\lambda_0} L_f \\
 &= \frac{d}{d\lambda} \left(n_{eff_f}(\lambda_0) - \lambda_0 \left. \frac{dn_{eff_f}}{d\lambda} \right|_{\lambda_0} \right) L_f \\
 &= \left(-\lambda_0 \left. \frac{d^2 n_{eff_f}}{d\lambda^2} \right|_{\lambda_0} \right) L_f \\
 &= cD(\lambda_0) L_f
 \end{aligned} \tag{Eq. 2-40}$$

Therefore the change in λ_0 with respect to the change in L_{air} is given as

$$\frac{d\lambda_0}{dL_{air}} = \frac{1}{cD(\lambda_0) L_f} \tag{Eq. 2-41}$$

Therefore the change in the location of λ_0 is related to the change in air path as

$$d\lambda_0 = dL_{air} \frac{1}{cD(\lambda_0) L_f} \tag{Eq. 2-42}$$

Since conventional balanced spectral interferometers are in a dual arm configuration, the dispersion in the reference path must be calibrated. The source of this error could be due to the fact that the coupler arms (see Fig. 2-13) cannot be cut to exactly the same length or due to the dispersion of the lens in the reference arm, which may not be negligible. This need for calibration introduces calibration error into measurement results.

Another important limitation of techniques based on balanced spectral interferometry is that to locate the balance point λ_0 , at least one peak and one valley must be present within the bandwidth of the scan on each side of λ_0 , as described by Eq. 2-24. A minimum of two points on each side of the balance point are also required to measure the second order dispersion directly from the balanced interferogram, as described by Eq. 2-37. Since these phase points must be present in the scan bandwidth for a dispersion measurement to be possible, there is a minimum bandwidth required for a dispersion measurement to be possible using balanced spectral interferometry. The minimum bandwidth is the separation between λ_2 and λ_{-2} in Fig. 2-16.

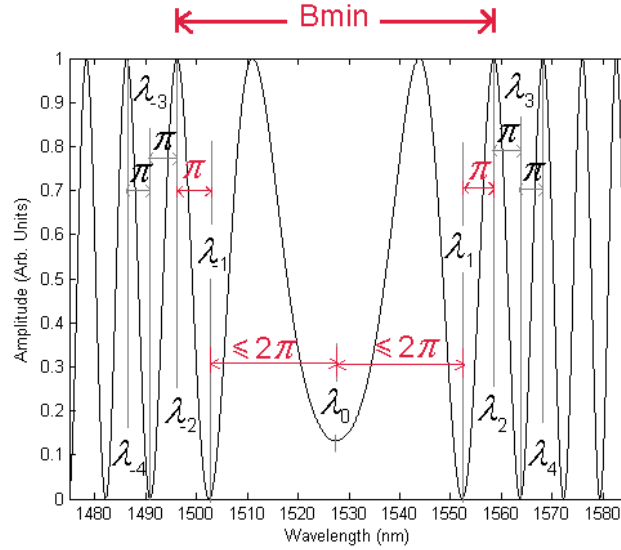


Fig. 2-16. Minimum bandwidth required in balanced spectral interferometry

The next part in this section develops an expression for the minimum bandwidth required in a balanced spectral interferometric measurement. The derivation begins by ignoring the third and higher order terms in Eq. 2-32, so that the phase separation between λ_1 and λ_0 in Fig. 2-16 can be described by

$$\varphi(\lambda_1) - \varphi(\lambda_0) = 4\pi \frac{(\lambda_1 - \lambda_0)^2}{2! \lambda_1} \frac{d^2 n_{eff}}{d\lambda^2} \Big|_{\lambda_0} L_f \leq 2\pi \quad \text{Eq. 2-43}$$

Substitution of Eq. 1-7 into Eq. 2-43 results in

$$\varphi(\lambda_1) - \varphi(\lambda_0) = 4\pi c \frac{(\lambda_1 - \lambda_0)^2}{2! \lambda_1 \lambda_0} D(\lambda_0) L_f \leq 2\pi \quad \text{Eq. 2-44}$$

If we assume that $|\lambda_1 - \lambda_0| \ll \lambda_0$ then $\lambda_1 \lambda_0 \cong \lambda_0^2$ and Eq. 2-44 may be used to solve $(\lambda_1 - \lambda_0)$ as

$$(\lambda_1 - \lambda_0) \leq \frac{\lambda_0}{(cL_f D(\lambda_0))^{1/2}} \quad \text{Eq. 2-45}$$

Using Eq. 2-32 and again ignoring the expansion terms above the second order, an expression for the known phase separation between λ_1 and λ_2 can be expressed as

$$|\varphi(\lambda_2) - \varphi(\lambda_1)| = \frac{4\pi c}{\lambda_0} \left[\frac{(\lambda_2 - \lambda_0)^2}{2! \lambda_2} - \frac{(\lambda_1 - \lambda_0)^2}{2! \lambda_1} \right] D(\lambda_0) L_f = \pi \quad \text{Eq. 2-46}$$

Substitution of the result in Eq. 2-45 into Eq. 2-46 and assuming $|\lambda_2 - \lambda_0| \ll \lambda_0$ so that $\lambda_2 \lambda_0 \cong \lambda_0^2$ results in an expression for the maximum wavelength spacing $(\lambda_2 - \lambda_0)$ given by

$$(\lambda_2 - \lambda_0) \leq \sqrt{\frac{3}{2}} \frac{\lambda_0}{(cL_f D(\lambda_0))^{1/2}} \quad \text{Eq. 2-47}$$

Thus a conservative estimate for the minimum bandwidth required is given by

$$B_{min} = 2(\lambda_2 - \lambda_0) = \sqrt{6} \frac{\lambda_0}{(cL_f D(\lambda_0))^{1/2}} \quad \text{Eq. 2-48}$$

The need for a minimum bandwidth has an effect on the resolution of this technique as well as the scatter in the group delay plot. For mathematical completeness and rigor, the derivations for the resolution and scatter in BSI are developed in [Appendix C.2](#). Furthermore, in [Appendix C.3](#) the resolution in USI is compared to that in BSI and it is shown that the resolution in USI only approaches that in BSI if the optimum window size is chosen. However, since the optimum window size cannot be known a priori, BSI techniques generally provide higher resolution (lower scatter) than USI techniques. Low scatter in the group delay curve produced via USI is important since the second order dispersion can only be measured via curve fitting (since cannot be measured directly) followed by analytical differentiation [29] [40] [41] [45] and since the scatter greatly affects the slope of the fit. This is the key problem with all USI based techniques and is one reason why experimentalists go to the trouble of setting up a reference path so that BSI can be used. It should also be noted here that the comparisons USI and BSI will also apply to USI and virtual reference interferometry (VRI) (introduced in the next chapter) since the virtual reference will take the place of the physical reference in BSI making the two techniques equivalent.

2.5 Summary & comparison

This section summarizes and compares all of the conventional techniques used for chromatic dispersion characterization. For both the time-of-flight (TOF) and modulation-phase-shift (MPS) techniques, the minimum device length that can be characterized is limited by the speed of the electronics. Because of cost considerations this typically limits the minimum device length from several tens to hundreds of meters. For shorter length characterization, however, interferometric techniques are required. Temporal interferometric (TI) techniques are not typically preferred due to the need to move the variable delay line while scanning the spectrum as this introduces vibrational noise into the interference pattern. The preferred techniques for characterizing short length are based on spectral interferometry, since the test and reference paths are held stationary during the scan, so that there is no vibrational noise added to the interference pattern. Spectral interferometric techniques can have test and reference paths that are either unbalanced or balanced. Unbalanced techniques (USI) typically involve the use of a Fourier transform in which either the amplitude or phase spectrum is used to extract dispersion. Techniques that extract the

phase of the interference pattern are required to fit the phase measurement with an appropriate function to measure the first and second order dispersion via analytical differentiation of the fitted curve. The problem with this technique, however, is that the presence of noise in the phase plot makes the results obtained dependent on the choice of fit (resulting in large error). Techniques that use the amplitude spectrum of a Fourier transform (via USI-WFT) to directly measure the group delay do not require a fit and are generally more accurate for the measurement of the first order dispersion (group delay) than those that measure the phase. These techniques, however, must employ a windowed Fourier transform to extract the group delay curve as a function of wavelength. However, since there is no way to determine the optimum window size that results in the highest resolution in the group delay curve, the scatter in the group delay curve cannot be minimized. Since the second order dispersion is extracted by fitting to the group delay curve, the second order dispersion curve produced also depends on the choice of fit (resulting in large error). This leaves balanced spectral interferometric (BSI) measurements, for which the first and second order dispersion may be obtained directly from the interference pattern and the resolution is inherently optimized (low scatter in the group delay curve). The trouble with this technique, however, is that the need for a reference makes implementation costly, difficult and time consuming.

Table 2-1 compares the typical precision of various dispersion measurement techniques. It demonstrates that balanced spectral interferometry gives the highest precision, since dispersion is measured directly from the interference pattern, but is the most difficult to set up and operate.

Table 2-1: Typical precision for each dispersion measurement technique

Technique	Typical precision	Comment	References
TOF	$10^{-1} \text{ ps nm}^{-1}$	System cost inversely proportional to length. Need tens to hundreds of meters.	[19] [20]
MPS	$10^{-1} \text{ ps nm}^{-1}$	System cost inversely proportional to length. Need tens to hundreds of meters.	[22] [24]
TI	$10^{-3} \text{ ps nm}^{-1}$	Noise due to translation of mirror. Indirect measure of second order dispersion.	[48]
USI	$10^{-3} \text{ ps nm}^{-1}$	Indirect measure of second order dispersion. Fit to phase or group delay can have large error.	[29] [41] [13]
BSI	$10^{-5} \text{ ps nm}^{-1}$	Direct measure of second order dispersion. Best precision. Difficult setup, operation and high cost delay line.	[13]

Table 2-2 summarizes several performance metrics, including the ability to measure short length fiber, the ability to directly measure second order dispersion, experiment run time, experiment difficulty and the need for calibration.

Table 2-2: Comparison of several performance metrics for each dispersion measurement technique.

Technique	Measures short length?	Minimum scatter in group delay plot	Directly measures second order dispersion?	Fast (single scan)	Low difficulty setup and operation	No Calibration
TOF				√	√	
MPS				√	√	
TI	√			√	√	
USI	√			√	√	√ [*]
BSI	√	√	√			

* Possible using the common path configuration

The next chapter introduces a new technique, called virtual reference interferometry, which combines the advantages of unbalanced spectral interferometry and balanced spectral interferometry. This new technique is a hybrid between the two that is capable of directly measuring second order dispersion by producing a balanced spectral interference pattern using a single spectral scan (fast) without the need for a physical reference path (no calibration) or variable delay line.

Chapter 3.

Virtual reference interferometry

Virtual reference interferometry (VRI) is introduced in this chapter and used to characterize chromatic dispersion in short length (<1 m) fiber and optical components. This chapter develops a detailed mathematical description of the technique along with an analysis of its parameters and constraints as a basis for comparison with conventional BSI. Also presented are several unique or important capabilities of VRI, including the ability to reduce the bandwidth required for a measurement, to measure components in cascade and to measure both narrowband and ultra-short devices. The chapter concludes with experiments that validate the theory and important capabilities. The validation experiments (characterizing well-known dispersion standards) demonstrate that the technique has a group delay measurement accuracy (relative to simulation using manufacturers specifications) on the order of 10^{-3} ps/m (<0.0001% relative error) and a second order dispersion (dispersion-length product) measurement accuracy on the order of and 10^{-5} ps/nm (<0.5% relative error). Measurement precision (relative to linear fit) in the second order dispersion is demonstrated to be on the order of 10^{-5} ps/nm (<0.15% relative deviation).

3.1 Introduction & motivation

An understanding of chromatic dispersion is of practical importance to the design of photonic components, systems and devices as discussed in [Chapter 1](#). Recall from [Chapter 2.4](#), that spectral interferometric techniques are preferred for characterizing short length specialty fibers and optical components, where long length samples are too costly or unavailable [19]. Among the conventional interferometric techniques discussed in [Chapter 2.4](#), BSI [13] [28] [29] [34] [48] [42] was shown to have the highest accuracy for measuring both first and second order dispersion (capable of direct measurements). BSI, however, was shown to be more difficult and time consuming to set up and more time consuming to operate compared to USI [28] [29] [41], which could complete a measurement in a single scan. Recall from Eq. 2-1, that high accuracy (low scatter) is especially important in short-length, low second order dispersion fibers and optical components, where the magnitude of the first and second order dispersion can be quite small.

Virtual reference interferometry (VRI) [49] is introduced in this chapter to enable direct (accurate) measurement of first and second order dispersion (like BSI) without the need for a physical reference path and in a single scan (fast) measurement (like USI). Since VRI produces interference patterns equivalent to BSI it is effectively an alternative to BSI that does not require a physical reference path and can be performed in a single scan (like USI). It achieves this by introducing a paradigm shift in the concept of what a *reference* is. In BSI the reference is the phase of the wave front that traverses a well known reference path. It is therefore a *phase reference*. The reference used in VRI, however, is not a phase reference but an *interferogram reference*. The reason that an interferogram can be a referenced is that it records a phase difference between two points in space. As a result, if the phase difference between two points in space is well known (i.e. simulated to produce a virtual interferogram), it is possible to use this phase difference to compare (as a reference) with an unknown phase difference (i.e. interferogram produced by a physical phase difference). Therefore the resulting interference pattern produced will be a second order

interference pattern that gives the phase difference between the two sets of phase separations. The amplitude modulation of this second order interference is equivalent to that produced in BSI when the group delay difference in the simulated interferogram is equal to that in the physically generated interferogram. However, since the reference is simulated, only a single spectral scan is required to generate dispersion plots (unlike BSI where a new scan is required for every point in the dispersion plot). Since the need for a phase difference means that the physical configuration of the interferometer is the same as USI but the resulting interference pattern is equivalent to that in BSI, VRI is essentially a hybrid between USI and BSI. It combines the advantage of speed (single scan measurements) and simplicity (no variable reference path) of USI with the accuracy of BSI for the measurement of first and second order dispersion. Furthermore, since the technique produces an equivalent interferogram to that generated in BSI, the first and second order dispersion may be extracted directly from the generated interference pattern using exactly the same algorithms as those presented in [Chapter 2.4.2](#). Since VRI is equivalent to BSI, all of the comparisons between BSI and USI in [Chapter 2.4](#) (i.e. resolution and scatter) also apply to VRI and USI. The next section presents the detailed theory of virtual reference interferometry.

3.2 Theory

The virtual reference process is a method for extracting both first and second order dispersion directly from the spectral interference produced in an unbalanced spectral interferometer. This is achieved using a *virtual* reference path, in a similar manner to that of a physical (real) reference path in BSI. The virtual referencing process, summarized in Fig. 3-1 can be divided into four steps, as illustrated in Fig. 3-1.

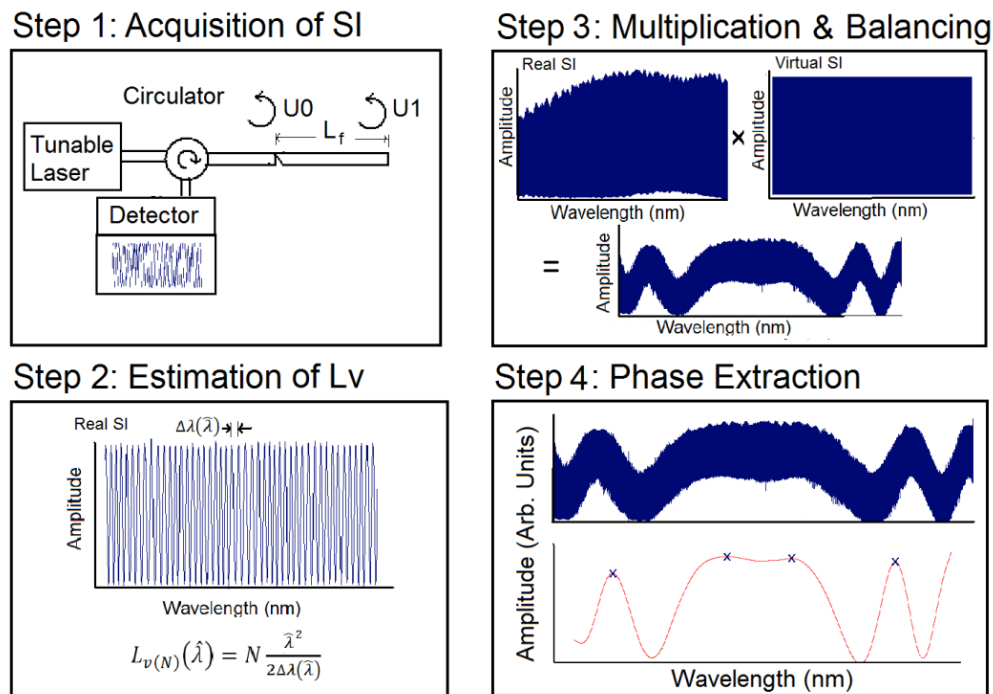


Fig. 3-1. Block diagram showing the sequential steps used to extract first and second-order dispersion using a virtual reference interferometer. Adapted (re-colored) with permission from [50].

The first step is the acquisition of a spectral interferogram (SI) from an unbalanced spectral interferometer (i.e. Michelson, Mach Zehnder, Fabry-Perot or common path). The second step is the estimation of the length of the virtual reference path using the period of the spectral interferogram acquired in the first step, followed by the generation of a virtual spectral interferogram, corresponding to the virtual path length (a simulated free-space cavity or interferometer). The third step is the multiplication of the spectral interferogram acquired in the first step with that produced in the second step resulting in the generation of a second-order interference pattern. If the virtual path (step 1) and the test path (step 2) are 'balanced' (i.e. the group delays in both paths are equal at a particular wavelength, λ_0), then the second-order interference pattern will exhibit a symmetric envelope with a spectrally flattened region (Fig. 3-1) centered at the 'balance' wavelength. Since the virtual reference path length determined in the second step is only an estimate, numerical variation of the virtual path length is required to balance the test path at a wavelength within the scan range. The fourth and final step is to extract the amplitude modulation of the second-order interference pattern and to use it to calculate the dispersion. Since the amplitude modulation is equivalent to the interference pattern generated by a balanced interferometer with a real reference path, the pattern recognition algorithms and the first and second order dispersion extraction techniques discussed in [Chapter 2.4.2](#) (with $L_v \equiv L_{air}$) may be used. Dispersion plots can be produced by repeating steps 3 and 4 at wavelengths within the scan range. The steps will be discussed in greater detail in the following sections.

Step 1 - Acquisition of the interference pattern

There are a variety of interferometric configurations that may be used to generate a spectral interference pattern. Since it is experimentally convenient to use a single-ended measurement, a Fabry-Perot (effects of multiple round trips not negligible) or common path (effects of multiple round trips negligible) configuration, shown in Fig. 3-2, is often chosen. Note that other configurations such as a Michelson or Mach Zehnder interferometer can work equally well with VRI. This single ended common path configuration is possible if a tunable laser source with sufficient coherence and wavelength resolution is used as the source. As the wavelength of the tunable laser is scanned, a real spectral interferogram (SI) ($I_{Real}(\lambda)$) is formed at the detector by the reflections U_0, U_1 (the reflected field amplitudes of the test fiber) and U_N (the field amplitudes of the multiple reflections thereafter).

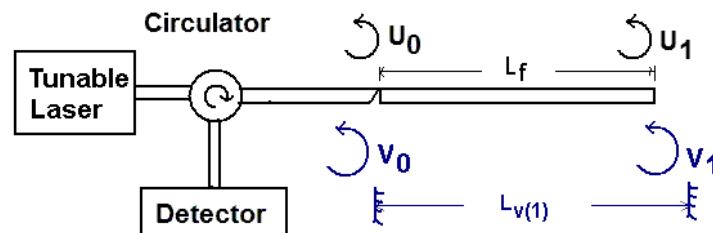


Fig. 3-2. Schematic for the generation of a real spectral interferogram using a common path (or Fabry-Perot) interferometer. An FC/APC (Ferrule connector/angled physical contact) to FC/PC (Ferrule connector/physical contact) connection is used as the first reflection point. A virtual cavity ($L_{v(1)}$), with a simulated group delay separation between V_0 and V_1 (equal to that in the real cavity (L_f) between U_0 and U_1), is shown in blue. Adapted (re-colored) with permission from [50].

The interference pattern seen at the detector is given in Eq. 3-1.

$$\begin{aligned}
 I_{Real}(\lambda) &= \left| U_0 + U_1 + \sum_2^{\infty} U_N \right|^2 \\
 &= U_{in}^2 l_1^4 R \left(1 - \frac{R^2 - 2R + 1}{R^2 - 2R \cos(2\beta_f L_f) + 1} \right) \\
 &= U_{in}^2 l_1^4 R \left[1 - (1-R)^2 \sum_{l=0}^{\infty} \left(R e^{-j2\beta_f L_f} \right)^l \sum_{m=0}^{\infty} \left(R e^{+j2\beta_f L_f} \right)^m \right]
 \end{aligned} \tag{Eq. 3-1}$$

where U_{in} is the amplitude of the input electric field from the tunable laser, $R = r_o^2$ is the reflectivity at the glass-air interface (where r_o is the amplitude reflection coefficient) and l_1 is the loss factor at the junction between the launch fiber and the test fiber. It is important to note that the loss factor does not include the reflection loss, which is accounted for by R in the expression. Furthermore, for simplicity of this analysis, the fiber is assumed to be lossless so that the amplitudes of U_0 and U_1 are approximately equal. An imbalance between the amplitude of U_0 and U_1 would result in a reduction in the fringe contrast of $I_{Real}(\lambda)$ but have no effect on its phase. The terms β_f and L_f are the propagation constant and physical length of the fiber under test, respectively. Where the propagation constant is defined as $\beta_f = \frac{2\pi}{\lambda} n_{eff}(\lambda)$ where n_{eff} is the effective index of the fiber under test at a given wavelength, λ . If the product term with $l=0$ and $m \neq 0$ in Eq. 3-1 is added to the product term with $m=0$ and $l \neq 0$, a set of harmonics $\cos(2N\beta_f L_f)$, is formed (with N being the order of the harmonic). Cross terms, generated when $l \neq m \neq 0$, result in the same $\cos(2N\beta_f L_f)$ harmonics. This means that the interference pattern $I_{Real}(\lambda)$ is essentially composed of harmonics with varying amplitudes and may therefore be simplified as

$$I_{Real}(\lambda) \propto \sum_{N=1}^{\infty} A_N R^N \cos(2N\beta_f L_f) \tag{Eq. 3-2}$$

where A_N is the magnitude of the N^{th} harmonic. Note that the expressions for A_N are not derived here, since they are of little interest as they do not contain the dispersion information and that the frequencies of the first and higher order harmonics are independent of R . If $R \ll 1$, as in optical fiber, then multiple reflections can be neglected (i.e. common path interferometer) and the expression for $I_{Real}(\lambda)$ simplifies to

$$I_{Real}(\lambda) \cong U_{in}^2 l_1^4 R \left(2 - 2 \cos(2\beta_f L_f) \right) \tag{Eq. 3-3}$$

Step 2 – Virtual cavity path-length estimation

Although the interference pattern produced in step 1 is aperiodic (i.e. period changes with wavelength due to dispersion), an estimate of the average period within a window near the centre of the scan range may be used to

calculate an initial estimate for the length of the virtual reference path, $L_{v(N)}$, that has a group delay equivalent to (i.e. 'balances') the test path that generated $I_{Real}(\lambda)$ at a wavelength near the scan range. The group delay of the virtual free-space path may be estimated by

$$L_{v(N)}(\lambda_{centre}) \cong N \frac{\lambda_{centre}^2}{2\Delta\lambda(\lambda_{centre})} \quad \text{Eq. 3-4}$$

where ($N=1,2,\dots$) round trips in the test fiber, λ_{centre} is the wavelength at the centre of the scan range, and $\Delta\lambda(\lambda_{centre})$ is the average period of the interference pattern within a certain wavelength range centered at λ_{centre} , the centre of the scan range. The average period can be measured directly from the interference pattern or using a Fourier transform (as discussed in [Chapter 2.4.1](#)). It is important to point out that this step only provides an estimate for the length of the virtual cavity due to the noise in the interference pattern. It can only partially balance the interferometer at a wavelength *near* the scan range. Fine tuning of the virtual cavity will be required in the next step to completely balance the interferometer at a wavelength *within* the scan range. Using the estimated value of $L_{v(N)}$ from Eq. 3-4, a virtual interference pattern may be generated numerically as

$$I_{virtual(N)}(\lambda, \lambda_{centre}) \propto \cos\left(2k_0 L_{v(N)}(\lambda_{centre})\right) \quad \text{Eq. 3-5}$$

where $k_0 = 2\pi/\lambda$ is the propagation constant in free-space. The interference pattern $I_{virtual(N)}$ is equivalent to what would be produced by a physical free space cavity with a group delay equivalent to that in the interferometer used to generate $I_{Real}(\lambda)$ [34] [35]. This effectively means that $L_{v(1)} \equiv L_{air}$ in Eq. 2-31. In practice, typically, $N=1$ is used in Eq. 3-5. A higher value of N (corresponding to the balancing of multiple round trips) is only used in the case of harmonic *compression*, as detailed later.

Step 3 – Multiplication and fine balancing

In this step the interference pattern generated in step 1 is multiplied point-by-point (alternatively added or subtracted) with the simulated interference pattern produced in step 2. After filtering out the zero-frequency (DC) term in $I_{Real}(\lambda)$ and ignoring the sum frequency terms in the result, a second order interference pattern with a low frequency amplitude modulation results, as described by

$$\begin{aligned} I_{SO}(\lambda, \lambda_{centre}) &= I_{Real}(\lambda) \cdot I_{virtual(N)}(\lambda, \lambda_{centre}) \\ &\propto A_N R^N \cos\left(2N(\beta_f L_f - k_0 L_{v(1)})\right) \end{aligned} \quad \text{Eq. 3-6}$$

This low frequency amplitude modulation in the second order interference pattern is depicted in Fig. 3-3 where λ_0 is the wavelength where the phase in Eq. 3-6 is minimized and the group delay in the virtual path (step 2) balances that in test fiber (step 1) (i.e. $L_{v(1)} = N_{g_f}(\lambda_0)L_f$). Note that fine tuning of the virtual reference path length $L_{v(1)}$ is

required in this step to balance the test and reference paths within the scan range (so that the balance point of the interference pattern λ_0 , which is illustrated in Fig. 3-3, is observed within the scan bandwidth).

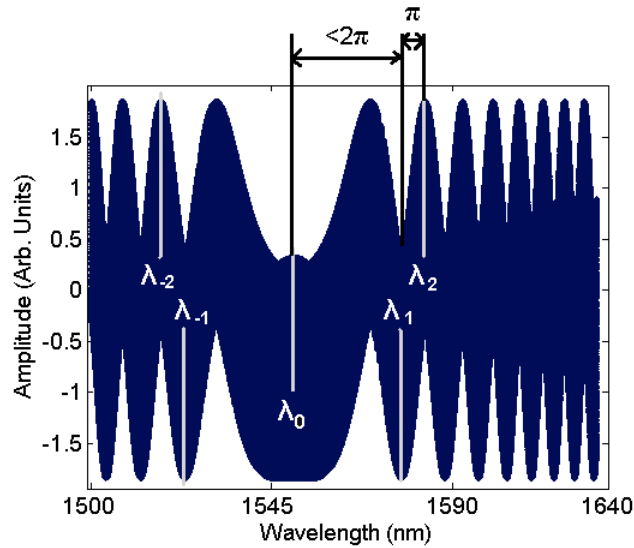


Fig. 3-3. Second order interference pattern in VRI. The finer interference fringes are not resolved in this depiction and appear black. Only the envelope (i.e. the amplitude modulation) of the interferogram is of interest. Adapted (re-colored) with permission from [50].

Step 4 – Extracting the phase and dispersion

The amplitude modulation in Fig. 3-3 is equivalent to the first order interference that would be produced in BSI if the length of the physical reference path was the same as the simulated reference path. The phase of the amplitude modulation, therefore, provides the information of interest. The amplitude modulation may be extracted from the second order interference via low pass filtering. For noisy interference patterns a subsequent curve fitting may be used to filter the noise further. Typically a spline fit is used for this purpose. A spline is a curve is produced by fitting different sections of a plot with multiple (piecewise defined) polynomials and ensuring that the multiple pieces are both continuous and smooth at the points where they connect. The balanced wavelength λ_0 may then be determined using Eq. 2-24 in conjunction with the pattern recognition algorithms described in [Chapter 2.4.2](#) (with $L_v \equiv L_{air}$). Step 3 is then repeated for each wavelength point of interest, such that $L_{v(1)}$, which is required to balance the interferometer at a given wavelength, is obtained as a function of wavelength. The group delay of the test fiber may then be determined using Eq. 2-33 where $L_v \equiv L_{air}$ as

$$\tau_g(\lambda_0) = \frac{N_g(\lambda_0)L_f}{c} = \frac{L_{v(1)}(\lambda_0)}{c} \quad \text{Eq. 3-7}$$

where $N_g(\lambda_0)$ is the group index of the test fiber, which is related to its effective refractive index, by the relation $N_g(\lambda_0) = n_{eff}(\lambda_0) - \lambda_0 \left. \frac{dn_{eff}}{d\lambda} \right|_{\lambda_0}$. Higher-order dispersion can be obtained by numerically differentiating $\tau_g(\lambda_0)$ or by directly extracting it from the second-order interference pattern, which has a phase given by

$$\varphi_{Amp.mod.}(\lambda) = 2Nk_0(n_{eff}L_f - L_{v(1)}) \quad \text{Eq. 3-8}$$

The second-order dispersion may then be extracted by measuring the separation between the peaks or valleys in the amplitude modulation, exactly the same way as in BSI, as detailed in [Chapter 2.4.2](#) (with $L_v \equiv L_{air}$) and in [13] [34].

3.3 Unique capabilities of VRI

Although VRI may seem to be simply a method for replacing physical balancing with numerical processes, this section describes its unique capabilities and advantages in comparison to BSI. These capabilities include spectral compression, the ability to characterize cascaded elements individually and collectively, the ability to characterize narrowband devices such as Fiber Bragg Gratings (FBGs), and the ability to characterize ultra-short devices using a difference measurement technique.

3.3.1 Spectral compression

In optical fiber where $R \ll 1$ in Eq. 3-6, the magnitude of higher order reflections (multiple round trips) drops off significantly. Despite this fact, the harmonics of the first few higher order reflections in $I_{Real}(\lambda)$ are usually still visible and can be independently referenced by multiplying (or adding/subtracting) $I_{Real}(\lambda)$ with an appropriate virtual spectral interferogram $I_{virtual(N)}$ having a frequency (simulated group delay) equal to one of the higher-order harmonics (i.e. balancing the group delay in higher order harmonic N). For example, virtual referencing of the second harmonic $\cos(4\beta_f L_f)$ (two round trips in the fiber), can be referenced by multiplication with $\cos(2k_0 L_{v(2)})$, where $L_{v(2)} = 2L_{v(1)}$. Note that in general, the virtual path length is an integer multiple of $L_{v(1)}$, ($L_{v(N)} = NL_{v(1)}$) where N corresponds to the order of the referenced harmonic. Referencing of higher-order harmonics ($N > 1$) has the effect of *spectrally compressing* the amplitude modulation, as shown in Fig. 3-4. More specifically, spectral compression refers to the reduction in the spectral separation between λ_2 and λ_{-2} in Fig. 3-4. Spectral compression by referencing a higher order harmonic, however, comes at the cost of fringe visibility (contrast), as illustrated in Fig. 3-4. The reduction in fringe visibility is due to the reflection loss at the fiber facets

which reduces visibility by a factor of R^N in the N^{th} harmonic. For uncoated fiber facets (with a low value of R) only the first and second harmonic typically generate sufficiently high fringe visibilities for extraction of dispersion information. In [Chapter 5](#) a method for compressing the interference pattern, without suffering from a reduction in fringe visibility, will be introduced.

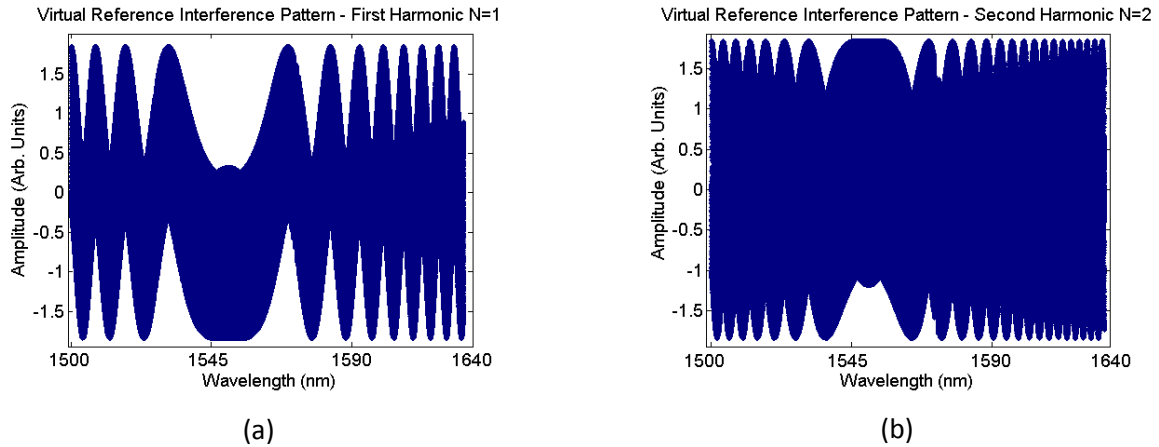


Fig. 3-4. (a) Second-order interference pattern produced via virtual referencing of the first harmonic. (b) Second-order interference pattern produced via virtual referencing of the second harmonic, resulting in spectral compression. Adapted (re-colored) with permission from [50].

3.3.2 Cascaded elements

Another unique feature of VRI is the ability to characterize the dispersion in a cascade of elements, both individually and collectively. A cascade of elements in which the multiple reflections within each element can be neglected (i.e. by using FC/PC to FC/APC connectors to increase cavity loss), is illustrated in Fig. 3-5.

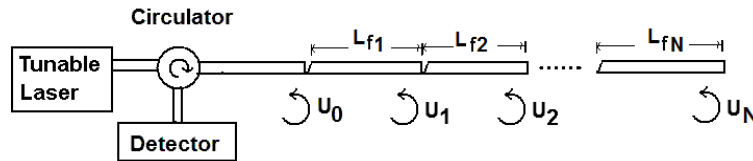


Fig. 3-5. Cascade of N elements with FC/PC to FC/APC connections as the reflection points. Used with permission from [50].

The interference pattern seen at the detector is described by

$$I_{\text{Real}} = U_{in}^2 R \left| 1 + \sum_{m=1}^N l_1^{2m} e^{-2j \sum_{k=1}^m \beta_{f(k)} L_{f(k)}} \right|^2 \quad \text{Eq. 3-9}$$

where $\beta_{f(k)}$ is the propagation constant and $L_{f(k)}$ is the physical length, of the k^{th} fiber in the cascade (i.e. between reflections U_m and U_{m-1} , where m is the reflection number). The magnitude of each successive reflection is reduced by the term l_1^{2m} . For a better understanding of the process an analytical expression for a *two* element cascade using Eq. 3-9 is given by

$$I_{Real}(\lambda) = U_{in}^2 R \begin{bmatrix} (1 + (l_1)^4 + (l_1)^8) \\ + 2(l_1)^2 \cos(2\beta_{f(1)}L_{f(1)}) \\ + 2(l_1)^4 \cos(2(\beta_{f(1)}L_{f(1)} + \beta_{f(2)}L_{f(2)})) \\ + 2(l_1)^6 \cos(2\beta_{f(2)}L_{f(2)}) \end{bmatrix} \quad \text{Eq. 3-10}$$

In this equation, there are three harmonic components corresponding to the first cavity, second cavity and to the collective cavity formed by the combination of the first and second cavity. The first cavity, between reflections \overline{U}_0 and \overline{U}_1 , generates the harmonic component with the largest amplitude of $2(l_1)^2$. The second cavity, between reflections \overline{U}_1 and \overline{U}_2 , generates the smallest amplitude since it is multiplied by $2(l_1)^6$. The cavity formed by the first and last reflection, \overline{U}_0 and \overline{U}_2 , in the cascade generates frequency content with amplitude $2(l_1)^4$. Each cavity in the cascade produces an individual balance point (when the virtual reference has a length that balances the group delay in the cavity). Each cavity can be virtually referenced independently and its dispersion information extracted accordingly (using the dispersion extraction algorithms described in [Chapter 2.4.2](#) (with $L_v \equiv L_{air}$)). It is important to point out that the cavities must be sufficiently different in length so that the balance points do not overlap. In the System Parameters section of this chapter, an expression for the minimum spectral separation will be developed.

3.3.3 Characterization of narrow-band devices

In this section, the ability to characterize the dispersion in a narrow-band fiber optic component, namely a Fiber Bragg Grating (FBG) is discussed. A schematic diagram for the measurement of a Fiber Bragg Grating is given in Fig. 3-6.

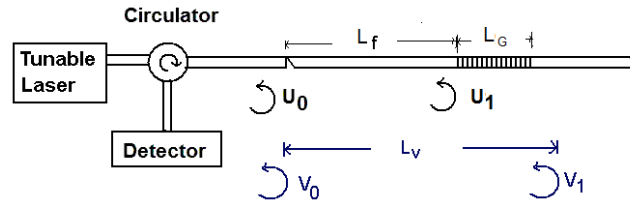


Fig. 3-6. Schematic diagram for the measurement of the dispersion of a Fiber Bragg Grating. The virtual free space path (cavity) with equivalent group delay is shown in blue. Adapted (re-colored) with permission from [50].

By using an FC/PC to FC/APC connector at the first reflection point the higher order reflections may be suppressed such that the spectral interference produced at the detector may be described by

$$I_{Real}(\lambda) = U_{in}^2 \left[\underbrace{A(\lambda)}_{\text{DC Amplitude}} + \underbrace{B(\lambda) \cos(2\beta_f L_f + \varphi_G)}_{\text{Frequency}} \right] \quad \text{Eq. 3-11}$$

where $A(\lambda) = (r_0^2 + (l_1)^4 r_G^2)$, $B(\lambda) = 2r_0 l_1^2 r_G$ and $r_G e^{j\varphi_G}$ is the complex reflection coefficient of the grating. r_0 is the amplitude reflection coefficient of the fiber. Fig. 3-7 illustrates a sample spectral interferogram generated by the setup in Fig. 3-6, showing the DC component and the higher frequency content.

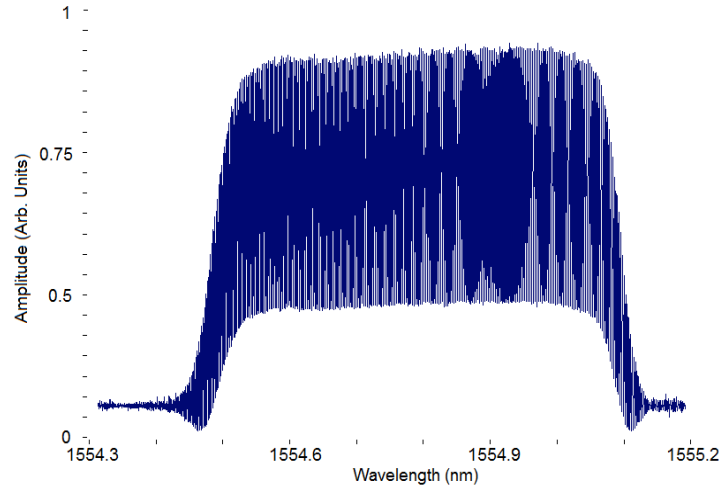


Fig. 3-7. Sample interference generated by the setup in Fig. 3-6. Adapted (re-colored) with permission from [50].

The dispersion information of the grating is extracted by multiplying $I_{Real}(\lambda)$ with the virtually generated SI pattern, expressed by

$$I_{virtual(1)}(\lambda) = \cos(2k_0 L_{v(1)}) \quad \text{Eq. 3-12}$$

In this case, $L_{v(1)}$ is the virtual reference path length with a group delay equal to that of both the fiber and the grating combined (i.e. the cavity formed by the reflections U_0 and U_1). The result of point-by-point multiplication of Eq. 3-11 and Eq. 3-12 is illustrated in Fig. 3-8 and described by Eq. 3-13.

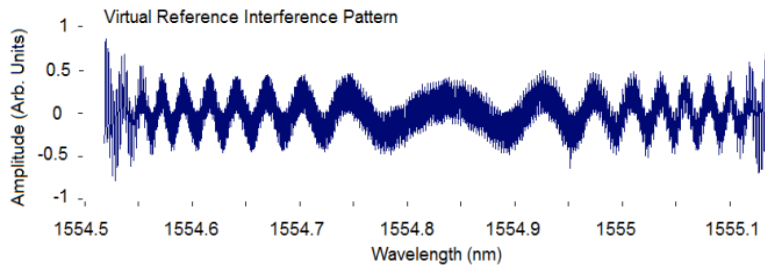


Fig. 3-8. Virtually referenced (and balanced) interference pattern generated by the setup shown in Fig. 3-6. Adapted (re-colored) with permission from [50].

$$\begin{aligned}
I_{SO}(\lambda) = & A(\lambda) \underbrace{\cos(2k_0 L_{v(1)})}_{\text{high freq}} \\
& + \frac{B(\lambda)}{2} \underbrace{\cos(\varphi_G + 2\beta_f L_f + 2k_0 L_{v(1)})}_{\text{high freq}} \underbrace{\cos(\varphi_G + 2\beta_f L_f - 2k_0 L_{v(1)})}_{\text{low freq}}
\end{aligned}
\tag{Eq. 3-13}$$

The resulting low frequency amplitude modulation contains information about both the fiber and the grating and the phase of the amplitude modulation is given by

$$\varphi_{Amp.mod.} = 2k_o \left(\frac{n_{effG} L_G}{2} + n_{eff} L_f - L_{v(1)} \right)
\tag{Eq. 3-14}$$

where $\varphi_G = k_0 n_{effG} L_G$ and n_{effG} is the equivalent effective index of the grating and L_G is the length of the grating.

Taylor expansion of n_{effG} and n_{eff} gives Eq. 3-15 and Eq. 3-16.

$$\begin{aligned}
n_{effG}(\lambda) = & n_{effG}(\lambda_0) + \frac{(\lambda - \lambda_0)}{1!} \left. \frac{dn_{effG}}{d\lambda} \right|_{\lambda_0} \\
& + \frac{(\lambda - \lambda_0)^2}{2!} \left. \frac{d^2 n_{effG}}{d\lambda^2} \right|_{\lambda_0} + \frac{(\lambda - \lambda_0)^3}{3!} \left. \frac{d^3 n_{effG}}{d\lambda^3} \right|_{\lambda_0} + \dots
\end{aligned}
\tag{Eq. 3-15}$$

$$n_{eff}(\lambda) \cong n_{eff}(\lambda_0) + \frac{(\lambda - \lambda_0)}{1!} \left. \frac{dn_{eff}}{d\lambda} \right|_{\lambda_0}
\tag{Eq. 3-16}$$

It is important to mention that the approximation made in Eq. 3-16 is valid over the narrow bandwidth of the grating where $n_{eff}(\lambda)$ in a fiber can be considered linear. The higher-order expansion terms must be included in the expansion for the grating ($n_{effG}(\lambda)$), however, as shown in Eq. 3-15. The result of substituting Eq. 3-15 and Eq. 3-16 into Eq. 3-14 is the expression for the phase given in Eq. 3-17.

$$\begin{aligned}
\varphi_{Amp.mod.}(\lambda) = & 2k_o \left(\left(N_{g(Grating)}(\lambda_0) \frac{L_G}{2} + N_{g(fiber)}(\lambda_0) L_f \right) - L_{v(1)} \right) \\
& + 4\pi \left(\left. \frac{dn_{eff}}{d\lambda} \right|_{\lambda_0} L_f + \left. \frac{dn_{effG}}{d\lambda} \right|_{\lambda_0} \frac{L_G}{2} \right) \\
& + 4\pi \frac{L_G}{2} \left(\left. \frac{(\lambda - \lambda_0)^2}{2!} \frac{d^2 n_{effG}}{d\lambda^2} \right|_{\lambda_0} + \left. \frac{(\lambda - \lambda_0)^3}{3!} \frac{d^3 n_{effG}}{d\lambda^3} \right|_{\lambda_0} + \dots \right)
\end{aligned}
\tag{Eq. 3-17}$$

where $N_{g(fiber)}(\lambda_0)$ and $N_{g(Grating)}(\lambda_0)$ are the group index of the fiber and grating, respectively. L_G is the physical length of the grating and L_f is the length of the fiber. Note that since the length of the virtual reference

$L_{v(1)}$ is chosen so that $L_{v(1)} = \left(N_{g(Grating)}(\lambda_0) \frac{L_G}{2} + N_{g(fiber)}(\lambda_0) L_f \right)$ the first term in Eq. 3-17 is zero. It also means that the sum of the group index of the grating and fiber are known values since they are equal to $L_{v(1)}$ at the balance wavelength, λ_0 . As a result, the group delay of the fiber and grating may be plotted as a function of λ_0 by locating the balance wavelength for a given value of $L_{v(1)}$. The second and higher order dispersion may also be extracted indirectly via numerical differentiation of the group delay plot or directly by measuring the phase difference between peaks and/or valleys in the amplitude modulation as described in [Chapter 2.4.2](#) using

$$\begin{aligned} |\Delta\varphi_{Amp.mod.}(\lambda_1, \lambda_2)| &= |\varphi_{Amp.mod.}(\lambda_2) - \varphi_{Amp.mod.}(\lambda_1)| \\ &\cong 4\pi \frac{L_G}{2} \left(\begin{aligned} &\left[\frac{(\lambda_2 - \lambda_0)^2}{2!\lambda_2} - \frac{(\lambda_1 - \lambda_0)^2}{2!\lambda_1} \right] \frac{d^2 n_{effG}}{d\lambda^2} \Big|_{\lambda_0} \\ &+ \left[\frac{(\lambda_2 - \lambda_0)^3}{3!\lambda_2} - \frac{(\lambda_1 - \lambda_0)^3}{3!\lambda_1} \right] \frac{d^3 n_{effG}}{d\lambda^3} \Big|_{\lambda_0} \end{aligned} \right) \end{aligned} \quad \text{Eq. 3-18}$$

3.3.4 Ultra-low dispersion measurements

This section describes a technique for the characterization of devices with a dispersion length so small that the minimum bandwidth required for its characterization exceeds the bandwidth of the source $B_{min} > B_{source}$ (note that an alternative approach for solving this problem will be discussed in [Chapter 5](#)). First a longer, higher dispersion fiber that can be characterized with the available bandwidth is measured. This fiber is then spliced to the short dispersion element (for which the bandwidth of the source is insufficient to measure the dispersion) as illustrated in Fig. 3-9. The two combined elements are then characterized. The dispersion of the short element can then be extracted from the difference between the second measurement and the first.

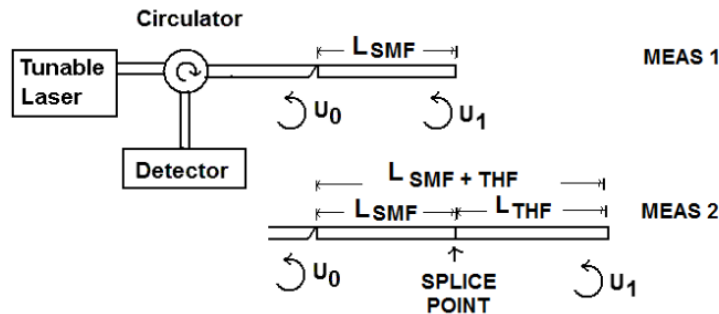


Fig. 3-9. Schematic diagram for Ultra-Low dispersion measurement made using two independent measurements. Used with permission from [50].

The shortest dispersion length that can be measured using this technique depends on both the accuracy of the individual measurements and on the magnitude of thermal changes in fiber length between scans. It is important to

point out that although this technique could also be used with a balanced interferometer it would be more susceptible to the thermal variation between scans since each point in the individual dispersion plots would require a separate scan (increasing the time required to produce each plot). This ultimately increases the length of the smallest dispersion length that can be measured in comparison to VRI (where each plot is generated quickly from a single scan [49]). Another important point to note is that if there is a reflection of sufficient magnitude at the splice point, the interference pattern produced looks like a two element cascade. In this case, results can be obtained from a single measurement by taking the difference between the combined cavity and that of the longer element to extract the dispersion of the short element. In this case there is no possibility for thermal fluctuation between scans since only one scan is required, resulting in superior measurement accuracy.

3.4 System parameters

In this section, the system parameters are derived for VRI to illustrate both the advantages and limitations of the technique in comparison to physically balanced interferometers. The parameters discussed include the minimum required source bandwidth, the minimum separation required between multiple balance points, the measurable bandwidth of the dispersion plots, the minimum fiber length, and the maximum fiber length that can be characterized (using the common path or Fabry-Perot configuration).

3.4.1 Minimum required source bandwidth

In order to locate the balance point to measure the first order dispersion or to be able to measure the second order dispersion from the period of the peaks and valleys surrounding λ_0 , as discussed in [Chapter 2.4.2](#), there must be at least two known phase points (e.g. λ_1 and λ_2) on each side of λ_0 (Fig. 3-3). This minimum bandwidth can be calculated from the phase separation between λ_2 and λ_0 in Fig. 3-3. To derive an analytical expression for the phase separation, one must start with Eq. 3-8 and Taylor expand n_{eff} as described in [Chapter 2.4.2](#). This results in a phase expression given by

$$\varphi(\lambda) = 4\pi \left\{ \underbrace{\left(N_g(\lambda_0)L_f - L_v \right)}_{=0} + \left. \frac{dn_{eff_f}}{d\lambda} \right|_{\lambda_0} L_f + \left. \frac{(\lambda - \lambda_0)^2}{2!\lambda} \frac{d^2 n_{eff_f}}{d\lambda^2} \right|_{\lambda_0} L_f + \left. \frac{(\lambda - \lambda_0)^3}{3!\lambda} \frac{d^3 n_{eff_f}}{d\lambda^3} \right|_{\lambda_0} L_f + \dots \right\} \quad \text{Eq. 3-19}$$

If the third and higher order terms in the expansion are ignored, the phase separation between λ_1 and λ_0 in Fig. 3-3 can be described by

$$\varphi(\lambda_1) - \varphi(\lambda_0) = 4\pi \frac{(\lambda_1 - \lambda_0)^2}{2!\lambda_1} \left. \frac{d^2 n_{eff_f}}{d\lambda^2} \right|_{\lambda_0} L_f \leq 2\pi \quad \text{Eq. 3-20}$$

Substitution of Eq. 1-7 into Eq. 3-20 results in

$$\varphi(\lambda_1) - \varphi(\lambda_0) = 4\pi c \frac{(\lambda_1 - \lambda_0)^2}{2! \lambda_1 \lambda_0} D(\lambda_0) L_f \leq 2\pi \quad \text{Eq. 3-21}$$

If we assume that $|\lambda_1 - \lambda_0| \ll \lambda_0$ then $\lambda_1 \lambda_0 \cong \lambda_0^2$ and Eq. 3-21 may be used to solve for $(\lambda_1 - \lambda_0)$ as

$$(\lambda_1 - \lambda_0) \leq \frac{\lambda_0}{(NcL_f D(\lambda_0))^{1/2}} \quad \text{Eq. 3-22}$$

where N is the referenced harmonic. Using Eq. 3-19 and ignoring the expansion terms above the second order, an expression for the known phase separation between λ_1 and λ_2 can be expressed by

$$|\varphi(\lambda_2) - \varphi(\lambda_1)| = \frac{4\pi c}{\lambda_0} \left[\frac{(\lambda_2 - \lambda_0)^2}{2! \lambda_2} - \frac{(\lambda_1 - \lambda_0)^2}{2! \lambda_1} \right] D(\lambda_0) L_f = \pi \quad \text{Eq. 3-23}$$

Substitution of the result in Eq. 3-22 into Eq. 3-23 and assuming $|\lambda_2 - \lambda_0| \ll \lambda_0$ so that $\lambda_2 \lambda_0 \cong \lambda_0^2$ results in an expression for the maximum wavelength spacing $(\lambda_2 - \lambda_0)$ given by

$$(\lambda_2 - \lambda_0) \leq \sqrt{\frac{3}{2}} \frac{\lambda_0}{(NcD(\lambda_0)L_f)^{1/2}} \quad \text{Eq. 3-24}$$

Thus a conservative estimate for the minimum bandwidth required is given by

$$B_{min} = 2(\lambda_2 - \lambda_0) = \sqrt{6} \frac{\lambda_0}{(NcD(\lambda_0)L_f)^{1/2}} \quad \text{Eq. 3-25}$$

Comparison of Eq. 3-25 with Eq. 2-48 shows that an advantage of VRI is that B_{min} can be divided by $N^{1/2}$, by referencing higher order harmonics, which is not possible in BSI.

3.4.2 Minimum separation between balance points

When two cavities in a cascade have similar lengths the spectral separation between the balance points is small. In order to ensure that the balance points can be uniquely resolved there must be sufficient spectral separation between the modes. The minimum spectral separation between two modes with balance points λ_{0_1} and λ_{0_2} is given by the sum of half the minimum bandwidth required by the first element $\frac{1}{2} B_{min_1}$ and half the minimum bandwidth required by the second element $\frac{1}{2} B_{min_2}$ as illustrated in Fig. 3-10.

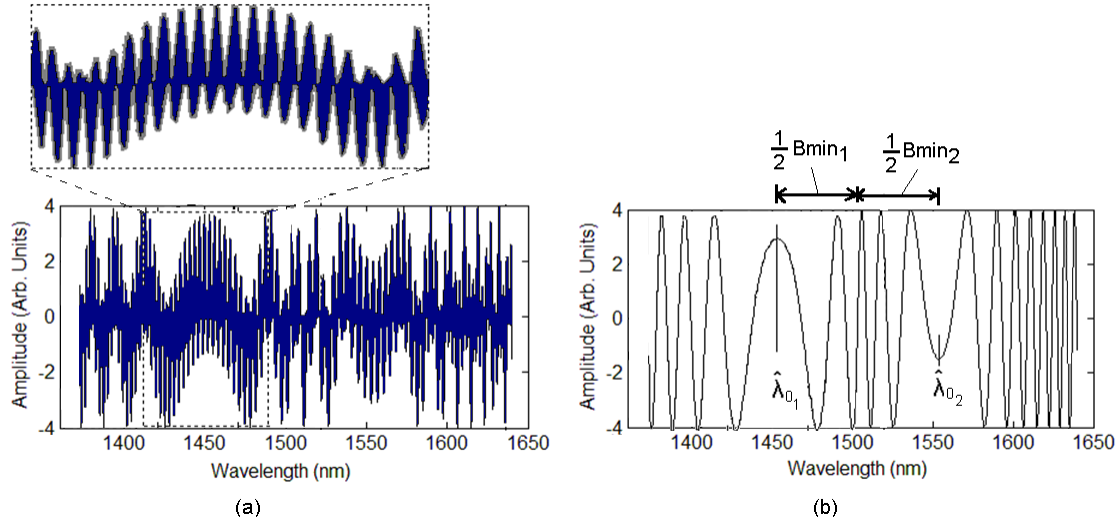


Fig. 3-10. (a) Simulated second order interference pattern and (b) the result of low-pass filtering to extract the balance wavelengths separated by the sum of half the minimum bandwidth required by each element. Inset above (a) shows a magnified spectral region around a balance wavelength. Adapted (re-colored and re-organized) with permission from [51].

The minimum spectral separation between the two balance points λ_{0_1} and λ_{0_2} produced by cascaded elements of similar length is given by

$$\hat{\lambda}_{0_2} - \hat{\lambda}_{0_1} \geq \frac{1}{2} \sum_{w=1}^2 \frac{\sqrt{6}}{(cD_w(\lambda_{0_w})L_{f_w})^{1/2}} \hat{\lambda}_{0_w} \quad \text{Eq. 3-26}$$

where $D_w(\hat{\lambda}_{0_w})$ and L_{f_w} are the second-order dispersion and length of element w and c is the speed of light.

3.4.3 Measurable bandwidth of the dispersion plots

The measurable bandwidth is determined by the difference between the bandwidth of the source and the minimum bandwidth required and is given by

$$B_{meas} = (B_{source} - B_{min}) \leq B_{source} - \sqrt{6} \frac{\lambda_0}{(NcD(\lambda_0)L_f)^{1/2}} \quad \text{Eq. 3-27}$$

Note that the minimum bandwidth is divided (reduced) by the $N^{1/2}$ term. This shows that using compression, the measurable bandwidth can be increased substantially in comparison to BSI based measurements [34].

3.4.4 Spectral resolution of dispersion plots

In balanced spectral interferometry ([Chapter 2.4.2](#)) the wavelength separation between measured points in the dispersion plots (both first and second order dispersion) depends on the minimum step size of the translation stage in the reference path since the balance point λ_0 is varied by changing the length of the reference path L_{air} in Eq. 2-31.

In VRI, however since the length of the reference path is simulated (i.e. $L_{air} \equiv L_{v(N)}$), arbitrarily small changes in path length can be used to make the separation between adjacent measured points as small as desired, to the limit of the wavelength resolution in locating λ_0 . Therefore Eq. 2-42 can be re-written for VRI as

$$d\lambda_0 = dL_{v(N)} \frac{1}{cD(\lambda_0)L_f} \quad \text{Eq. 3-28}$$

3.4.5 Minimum fiber length

The consequence of the need for a minimum bandwidth and the fact that the minimum bandwidth must be less than the available bandwidth of the source, (i.e. bandwidth of $I_{Real}(\lambda)$) is that the shortest length of fiber that can be characterized is limited. This limitation can be derived by asserting that the minimum bandwidth be less than that of the source and substituting in the expression for B_{min} . Since $B_{min} \leq B_{source}$ this results in the expression for the minimum fiber length

$$L_f \geq \frac{6\lambda_0^2}{NcD(\lambda_0)B_{source}^2} \quad \text{Eq. 3-29}$$

The ability to divide by the compression factor N allows for the measurement of smaller devices than with physically referenced interferometers [34].

3.4.6 Maximum fiber length

The physically generated interference pattern $I_{Real}(\lambda)$ must be resolved in order to extract the amplitude modulation. If the interferometer used to generate the interference $I_{Real}(\lambda)$ is modeled as a Fabry-Perot cavity, then wavelength resolution ($\Delta\lambda$) needed to resolve the raw interference pattern is given by

$$\Delta\lambda = \frac{T}{M} = \frac{\lambda^2}{2MN_g L_f} \quad \text{Eq. 3-30}$$

where M is the number of data points per period in $I_{Real}(\lambda)$. Although $M = 2$ sample points per period is the theoretical minimum number of points required to satisfy the Nyquist limit, the phase of the raw interference pattern must be resolved with a wavelength resolution that allows at least $M = 10$ points to be sampled per period in the raw interferogram. The reason for this is that the phase of the raw interference pattern must be extracted with high accuracy since it contains the dispersion information. The maximum fiber length that may be characterized using a common path configuration (as shown in Fig. 3-2) is therefore given by

$$L_{f_{max}} = \frac{\lambda^2}{2MN_g \Delta\lambda} \quad \text{Eq. 3-31}$$

It should be noted that this resolution (length) limitation will be mitigated later in [Chapter 6](#) where a low-coherence setup will be employed.

3.5 Experiments

In this section VRI is experimentally validated by measuring well-known dispersion standards and some of its unique or important capabilities are demonstrated experimentally. The experimental setup used in these experiments varies depending on the experiment. In each of the experiments, however, a tunable laser source (Agilent 81600B or Agilent 81642A) with a built in wavemeter is swept across a given bandwidth (experiment dependent) at 10 nm/s, while a detector (Thorlabs PDA10CS) connected to a data acquisition (DAQ) card samples the signal at 100 kHz. The built in wavemeter of the tunable laser is capable of automatic self wavelength calibration using a built in gas cell, giving it an absolute wavelength accuracy of ± 15 picometers and a relative wavelength accuracy of 0.1 pm. The tunable laser is connected to port 1 of a circulator, a detector is connected to port 3 and the device under test is connected at port 2, as illustrated in Fig. 3-2, Fig. 3-5, Fig. 3-6, Fig. 3-9 and Fig. 3-18. It is important to note that port 2 of the circulator is FC/APC connectorized and is connected to the FC/PC connectorized fiber under test to ensure a single reflection (i.e. $\overline{U0}$), at the interface. Another important note is that the 0.1 pm resolution of the tunable laser sets an upper limit to the maximum device length (based on the ability to adequately resolve the high frequency fringes in the interference pattern, i.e. Fig. 3-3) of approximately 0.8 meters using Eq. 3-31. As this represents the maximum imbalance that can be corrected for using a virtual reference, if a configuration with a reference path were to be used (i.e. dual arm configuration such as a Michelson or Mach-Zehnder interferometer) then the maximum group path length difference between the test path and the physical reference path would be 0.8 meters. Consequently the use of a reference path makes it possible to characterize longer length fibers if the dispersion in the reference fiber can be well characterized, however, calibration error cannot be avoided in this case. Although the focus of the technique is for the characterization of short length fiber, the possibility for the characterization of longer fiber lengths by using a physical reference to bring the imbalance to within 0.8 meters should not be forgotten (this will be demonstrated in [Chapter 6](#)).

3.5.1 Validation Experiments

In this section, VRI is validated and its accuracy and precision are determined experimentally. This is achieved by characterizing well-known dispersion standards, namely standard telecom fiber (SMF28) and dispersion compensating fiber (DCF). The setup for the experiment used to validate VRI via the measurement of well-known dispersion standards is illustrated in Fig. 3-2. The broadband tunable laser used in the validation experiments is an Agilent 81642A. The measurements are compared to simulation, to results from a commercial instrument (Agilent 86037C) and to previously demonstrated results from a single-arm 3-wave interferometer [34] [35] (a BSI based dispersion measurement technique that uses a common path configuration to eliminate calibration error).

In the first validation experiment, a short 42 centimeter length of SMF28 fiber is characterized and the results of the first and second order dispersion measurements are compared to simulation and experiment. The measurement of the first order dispersion (group delay) is illustrated in Fig. 3-11, where the group delay is normalized by sample length to compare with simulation. The average discrepancy between measured and simulated results is a root mean square (RMS) error of approximately 10^{-3} ps/m (<0.0001% relative error), an improvement over physically

referenced techniques which have $\sim 10^{-1}$ ps/m resolution [19] ($<0.01\%$ relative error). This improvement is likely due to the elimination of thermal and vibrational effects between scans in BSI based measurements.

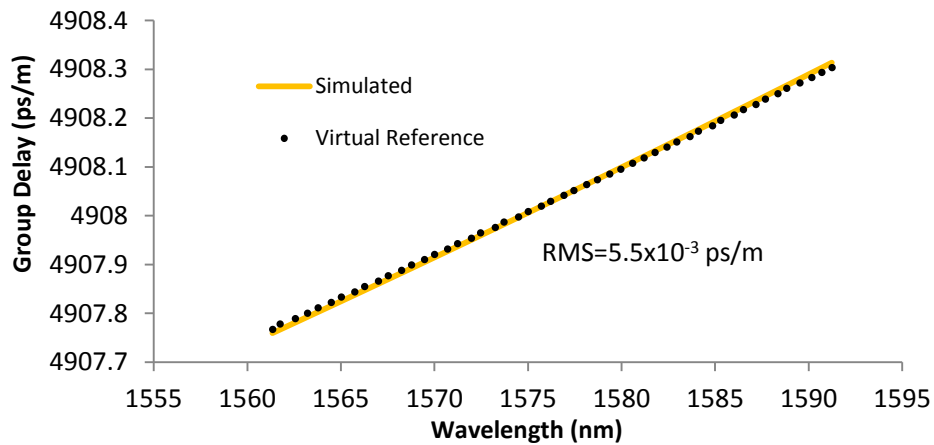


Fig. 3-11. Comparison between simulation and virtual reference measurement of group delay on a 42cm length of SMF28. The RMS error is with respect to simulation. Adapted (re-colored) with permission from [49].

The measurement of the second order dispersion (Dispersion parameter) is illustrated in Fig. 3-12, where the measurement is normalized by sample length to compare with simulation and experimental results from Single-Arm 3-Wave interferometer measurements, a BSI based measurement technique [34] [35].

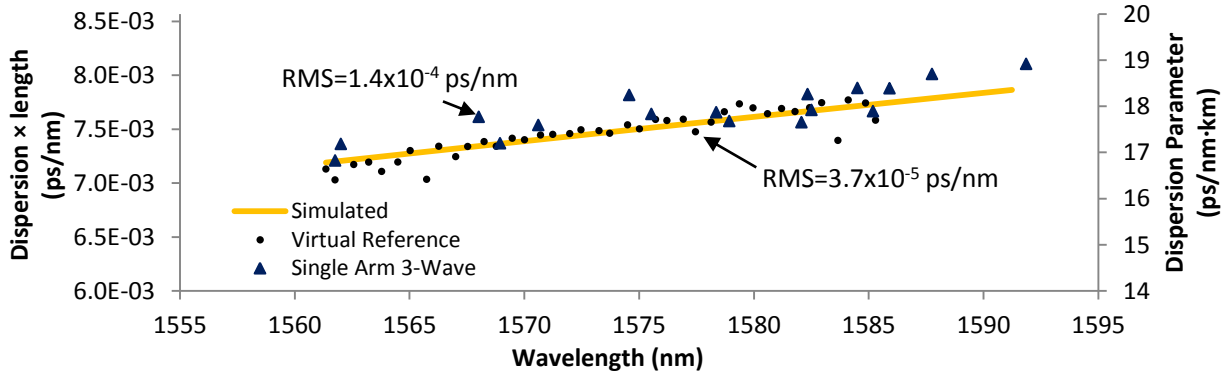


Fig. 3-12. Dispersion parameter measurements made via virtual referencing of a 42cm length of SMF28 and single arm 3-wave measurements (previously reported in [34] [35]) on a 39.5cm length of SMF28. The RMS errors are with respect to simulation. Adapted (re-colored, secondary axis added) with permission from [49].

This comparison is appropriate since the single-arm 3-wave technique also extracts the dispersion parameter from a second order interference pattern but employs a physical reference (since it is a BSI based technique) instead of a virtual one. The comparison presented in Fig. 3-12 shows that the virtual reference technique measures the dispersion parameter with an RMS error of approximately 10^{-5} ps/nm ($<0.5\%$ relative error) in comparison to simulation whereas the single-arm 3-wave technique also extracts the dispersion parameter with an RMS error of approximately 10^{-4} ps/nm (5% relative error). This order of magnitude improvement in accuracy is attributed to the fact that all data points are obtained with a single scan of the source (in approximately 14 seconds), making it less

susceptible to thermal fluctuations. The dispersion slope measured was found to be $0.053 \text{ ps/nm}^2\text{-km}$, which is in agreement with our simulation.

In the second experiment, the second order dispersion of a 0.25 m length of dispersion compensating fiber (DCF) is characterized. Comparison of the measured dispersion results produced using VRI, the single-arm 3-wave technique [34] [35] and a commercial dispersion measurement system (Agilent 86037C), which measures the second order dispersion using the modulation phase shift method [19], are illustrated in Fig. 3-13. The results indicate a precision for the virtual reference technique, of $4 \times 10^{-5} \text{ ps/nm}$ ($<0.15\%$ relative deviation with respect to a linear fit). This order of magnitude improvement in precision, compared to the single-arm 3-wave technique (BSI based), may be attributed to the immunity to thermal fluctuation in the reference path. The slight difference in the dispersion slope between the MPS technique and the VRI technique may be due to the differences in the way second order dispersion is measured. The MPS technique obtains the second order dispersion using Eq. 1-7 which requires two analytical derivatives of the fit (as described in [Chapter 2.2](#)), whereas VRI measures the second order dispersion directly (using the same method described in [Chapter 2.4.2](#) which includes third order dispersion). Another possibility is that the dispersion measured on the long length fiber (91.5 m) using MPS is slightly different to that on a short section (0.25 m) using VRI due to thermal variations in temperature that altered the core size leading to differences in waveguide dispersion. This is possible since waveguide dispersion is a dominant effect in DCF.

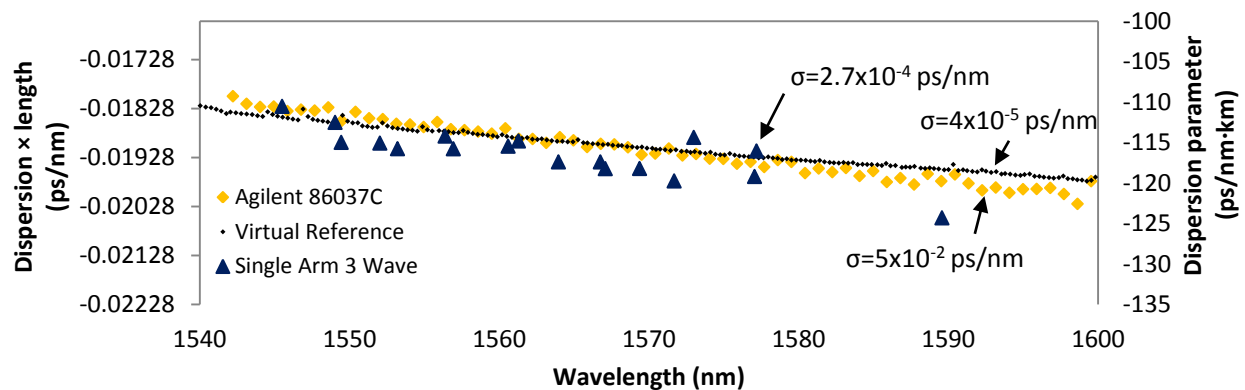


Fig. 3-13. Dispersion parameter measurements on dispersion compensating fiber (DCF). The virtual reference measurement was made on a 0.25 m length of DCF, the single arm 3-wave measurement (previously reported in [34] [35]) was made on a 0.165 m length of DCF and the Agilent 86037C measurement was made on a 91.5m length of DCF. The standard deviations shown are with respect to linear fit. Adapted (re-colored, secondary axis added) with permission from [49].

3.5.2 Experiments demonstrating unique or important capabilities of VRI

3.5.2.1 Demonstration of spectral compression

In a spectral compression measurement, a higher order harmonic of the cavity (multiple round trips) is referenced. The experimental setup for a compression measurement is the same as that for a standard measurement shown in Fig. 3-2. The higher the reflectivity of the facets, the lower the loss experienced by $\overline{U1}$. This is because $\overline{U1}$ makes multiple round trips, enabling higher order harmonics to exist within the cavity. In a standard fiber made of glass the reflectivity of the fiber facets is sufficient to allow the second harmonic to exist within the cavity.

In this experiment the device under test is an 11 cm length of SMF28 fiber. The tunable laser (Agilent 81600B) is swept across a 200 nm bandwidth from 1440 nm to 1640 nm and both the first and second harmonics are referenced. The first harmonic is referenced by setting $N=1$ in Eq. 3-5 and Eq. 3-6 and is illustrated in Fig. 3-14. The second harmonic is referenced by setting $N=2$ in Eq. 3-5 and Eq. 3-6 as illustrated in Fig. 3-15. This case illustrates the compression of the interference pattern.

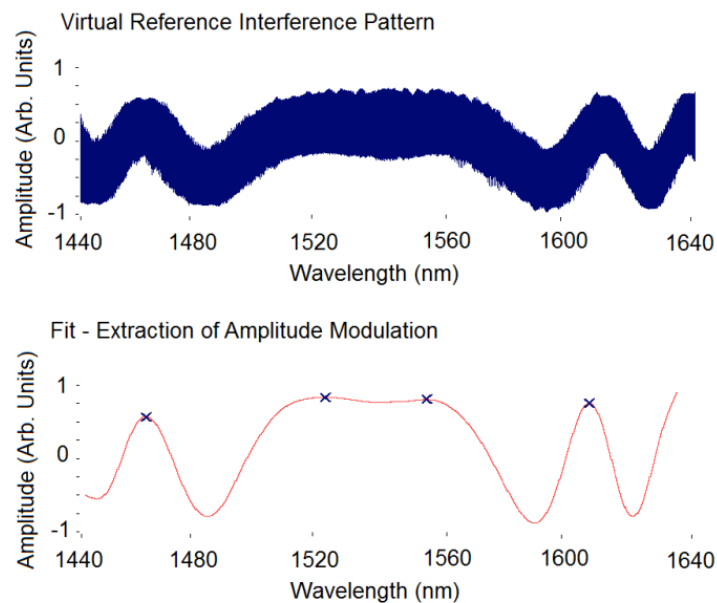


Fig. 3-14. Virtual referencing of the first harmonic ($N=1$) of an 11 cm length of SMF28 fiber illustrating the uncompressed case. Adapted (re-colored) with permission from [50].

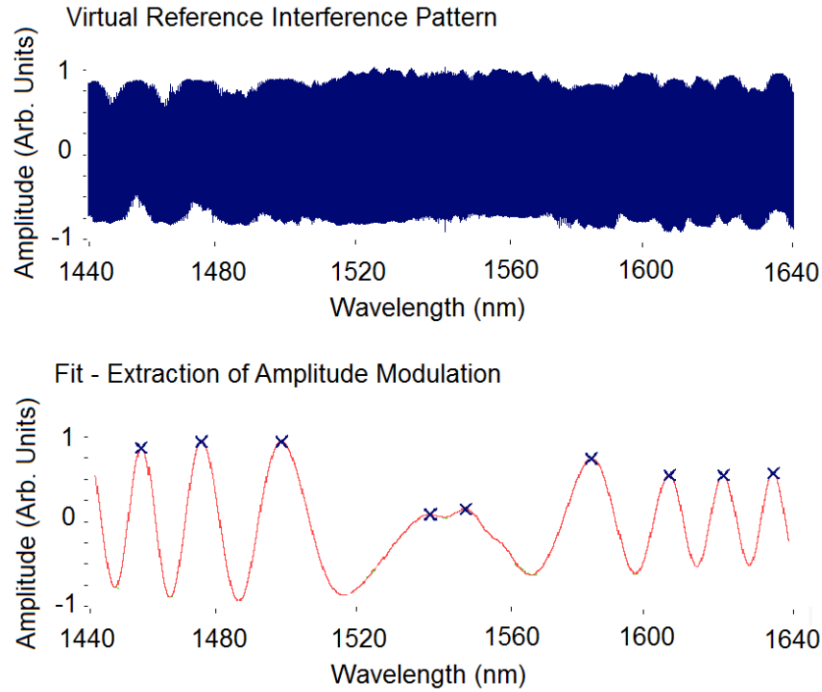


Fig. 3-15. Virtual referencing of the second harmonic ($N=2$) of an 11 cm length of SMF28 fiber resulting in the compression of the period of the amplitude modulation. Adapted (re-colored) with permission from [50].

The amplitude modulation is extracted from the second order interference pattern in Fig. 3-14 and Fig. 3-15 by using a low-pass filter and spline fit. Here the spline is used as a simple low-pass filter. Compression of the bandwidth in the $N = 2$ case (Fig. 3-15) reduces the minimum required source bandwidth in Eq. 3-25, increases the bandwidth of the measured dispersion plots in Eq. 3-27 and reduces the minimum measurable device length in Eq. 3-29. This capability is confirmed experimentally by the results in Fig. 3-16 and Fig. 3-17, which show agreement between the compressed and uncompressed case. The results of the measurements with compression are slightly more accurate since the (effective) device length being measured is twice that of the uncompressed case (i.e. the ratio between the wavelength and the device length is smaller, resulting in greater accuracy). As a result, there is a slight vertical offset between the curves.

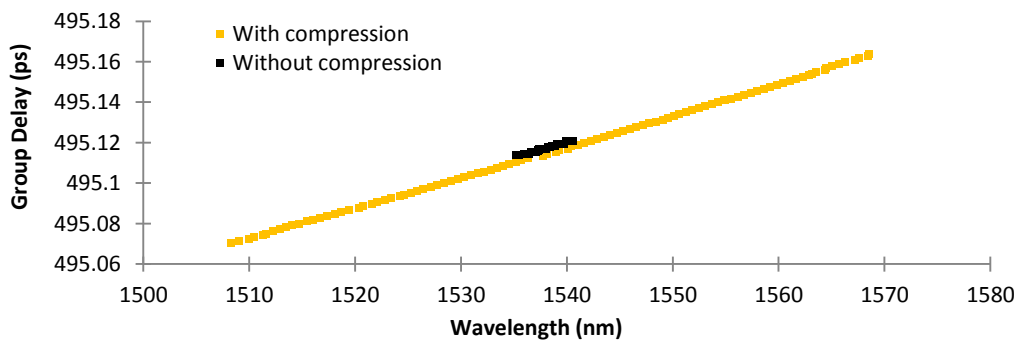


Fig. 3-16. Comparison of group delay measurements of an 11 cm length of SMF28 fiber both with and without compression. Adapted (re-colored) with permission from [50].

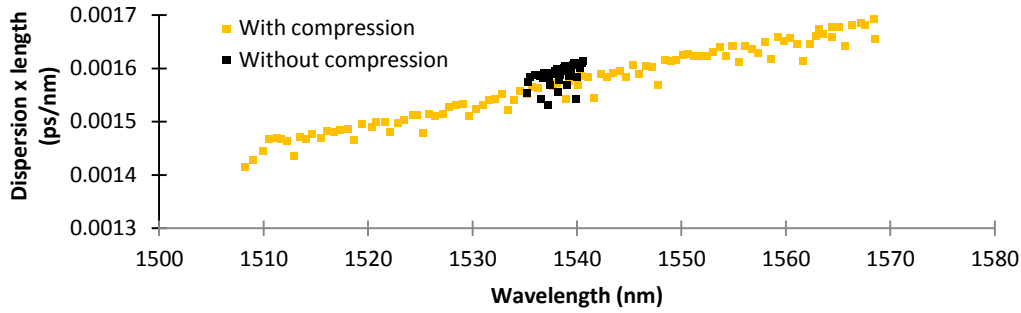


Fig. 3-17. Comparison of dispersion \times length measurements of an 11 cm length of SMF28 fiber with and without compression. Adapted (re-colored) with permission from [50].

3.5.2.2 Demonstration of a two element cascade

This experiment demonstrated the characterization of a two element cascade described by Eq. 3-10. The elements of the cascade are characterized individually and collectively. The experimental setup is illustrated in Fig. 3-18. The cavity lengths are $L_{f1} = 46$ cm, $L_{f2} = 31.4$ cm and $L_{f3} = L_{f1} + L_{f2} = 77.4$ cm. In this experiment the tunable laser (Agilent 81642A) is swept from 1510 nm to 1640 nm and the interference pattern is recorded. The frequency content (power spectrum) of the interference pattern, shown in Fig. 3-19, is used to extract the period (frequency) to approximate the virtual cavity lengths using Eq. 3-4.

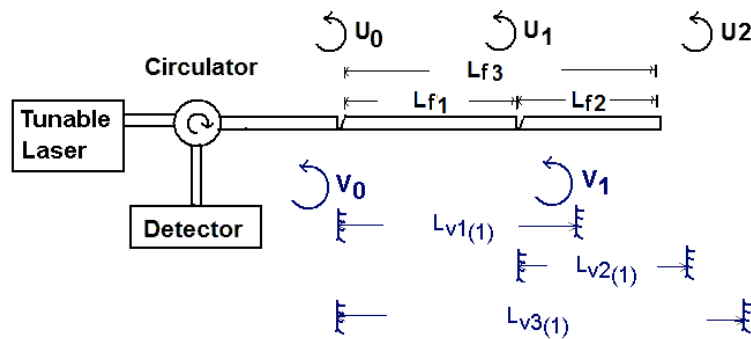


Fig. 3-18. Two element cascade used in the experiment, where $L_{f1} = 46$ cm, $L_{f2} = 31.4$ cm and $L_{f3} = L_{f1} + L_{f2}$. Adapted (re-colored) with permission from [50].

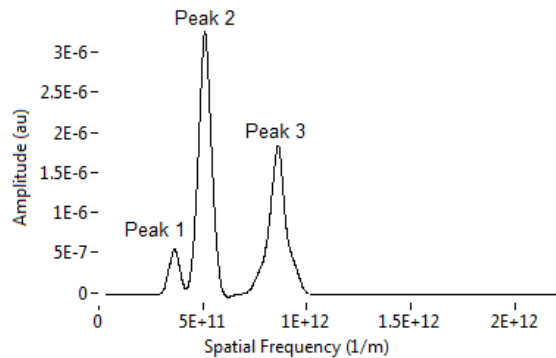


Fig. 3-19. Power spectrum generated by the cascade in Fig. 3-18. Peak 1 corresponds to cavity length L_{f2} , peak 2 corresponds to L_{f1} and peak 3 corresponds to $L_{f1} + L_{f2}$. Used with permission from [50].

Each peak in Fig. 3-19 corresponds to one of the cavities in the setup. Note that the relative magnitudes of the frequency components in Fig. 3-19 are in agreement with the theoretical development in Eq. 3-10 where Peak 1 corresponds to the shortest cavity in the experiment since it is at the lowest frequency and it has the lowest magnitude since it is the second cavity in a two element cascade. Peak 1 corresponds to $L_{f2} = 31.4$ cm, peak 2 corresponds to $L_{f1} = 46$ cm and peak 3 corresponds to $L_{f3} = L_{f1} + L_{f2} = 77.4$ cm. Sample second order interference patterns, generated by virtual referencing of each cavity (after the balancing step) are shown in Fig. 3-20. Characterization of the first and second order dispersion of the elements in the cascade (individually and collectively) is illustrated in Fig. 3-21 and Fig. 3-22. The increased scatter in the collective characterization of the second order dispersion of both elements in the cascade (Fig. 3-22 peak 3) is due to the increase in noise in the interference pattern (Fig. 3-20 peak 3) as the fiber length approaches the maximum allowed by the wavelength resolution of the source (Eq. 3-31). Additionally, the increased frequency of the amplitude modulation requires an increase in the maximum frequency allowed by the low pass filtering process. This allows more high frequency noise from the interferogram into the extracted amplitude modulation and adds noise to the dispersion measurements.

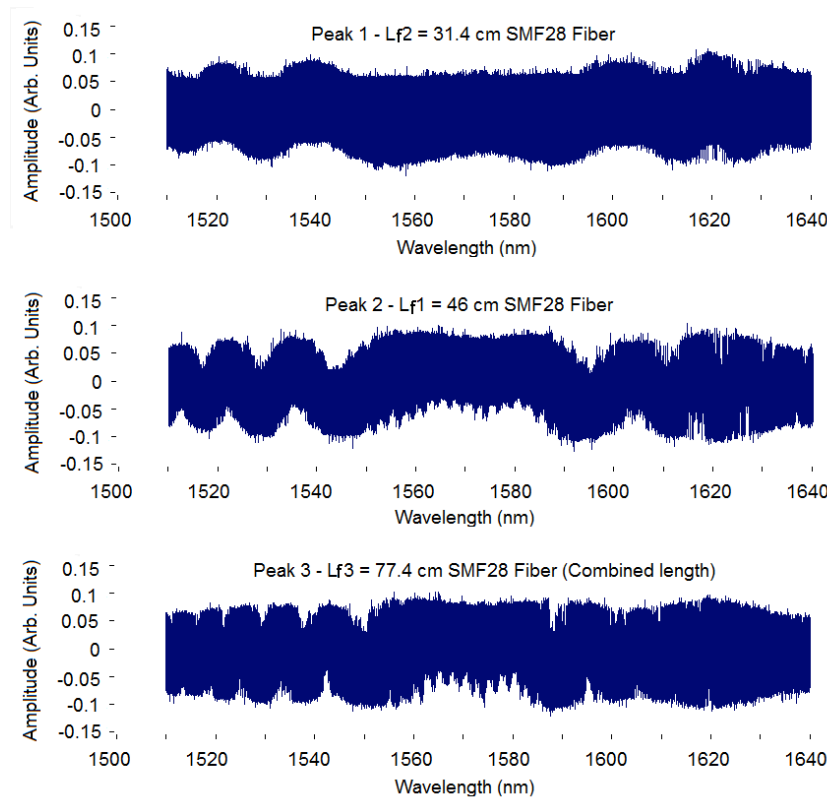


Fig. 3-20. Sample second-order interference patterns from Virtual Referencing (and balancing) of each of the three cavities in Fig. 3-18. Adapted (re-colored) with permission from [50].

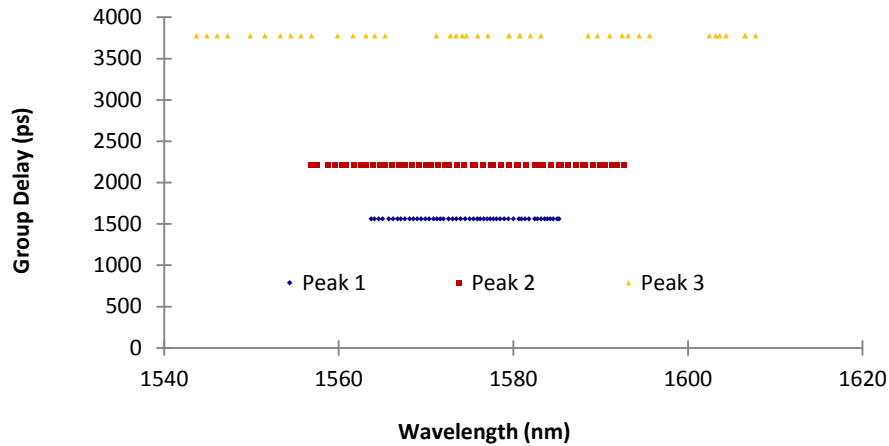


Fig. 3-21. Group delay for each of the three cavities in Fig. 3-18 where $L_{f1} = 46$ cm (peak 2), $L_{f2} = 31.4$ cm (peak 1) and $L_{f3} = L_{f1} + L_{f2}$ (peak 3). Adapted (re-colored) with permission from [50].

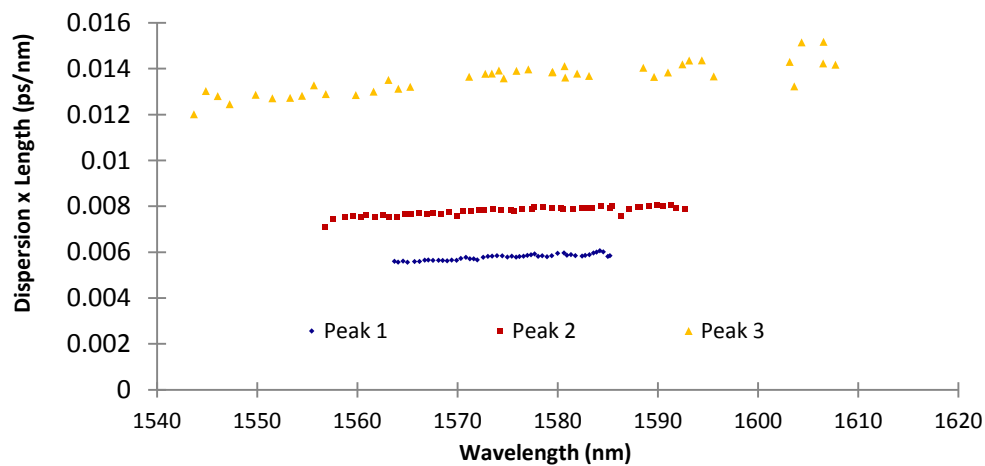


Fig. 3-22. Dispersion \times length for the cavities in Fig. 3-18. Adapted (re-colored) with permission from [50].

3.5.2.3 Narrowband dispersion measurement

This experiment demonstrates the dispersion characterization of a narrowband optical component, namely a fiber Bragg grating (FBG). The experiment uses the setup illustrated in Fig. 3-6 where the values of L_f and L_G are 35 cm and 2 cm, respectively. The interference pattern generated by sweeping the tunable laser (Agilent 81642A) from 1554.5 nm to 1555.1 nm is illustrated in Fig. 3-7. After virtual referencing (as well as coarse and fine balancing), the VRI pattern generated is given in Fig. 3-8. By sweeping the length of the virtual cavity and tracking the balance point, plots of the first and second order dispersion, shown in Fig. 3-23 and Fig. 3-24, are generated. The group delay measurement in Fig. 3-23 is compared to the group delay measured using a commercial dispersion measurement system (SWS-OMNI from JDSU), which is based on the MPS technique [23] [24]. This test was

performed using the MPS technique by attaching the grating to a long lead fiber. The group delay slope (second order dispersion), measured using VRI and the commercial MPS based system, is -1582 ps/nm and -1563 ps/nm, respectively, indicating agreement between the two results. The slope of the group delay is confirmed by the direct measurement of the dispersion \times length in Fig. 3-24. Note that the bandwidth of the results (Fig. 3-23 and Fig. 3-24) is less than the bandwidth of the grating. This is because the grating constrains the visible source bandwidth (i.e. $B_{source} \equiv B_{grating}$ in (22)), which limits the bandwidth of the results accordingly (i.e. only a narrow range of wavelengths $B_{grating}$ are reflected by the grating).

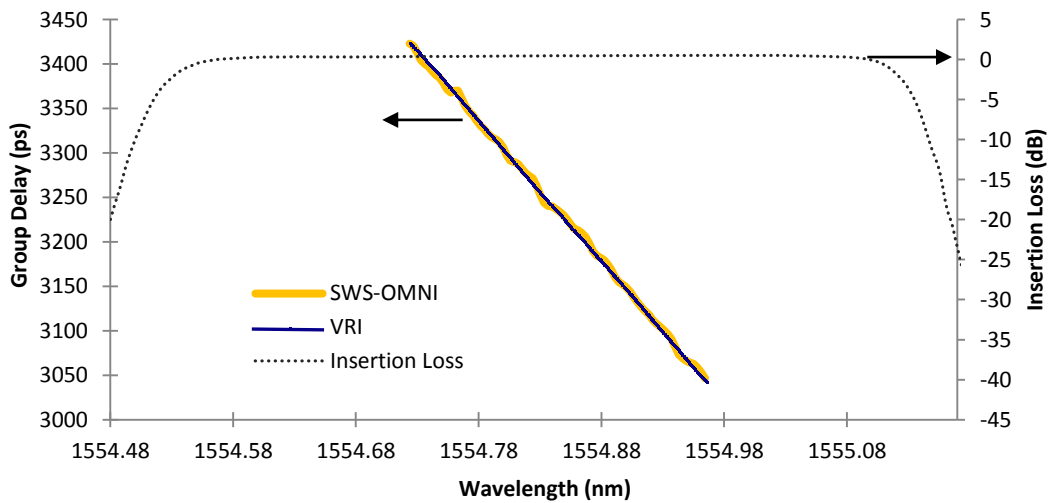


Fig. 3-23. Group delay measurements of a fiber Bragg grating using VRI agree well with those made using a commercial system based on the MPS technique (SWS-OMNI). Adapted (re-colored) with permission from [50].

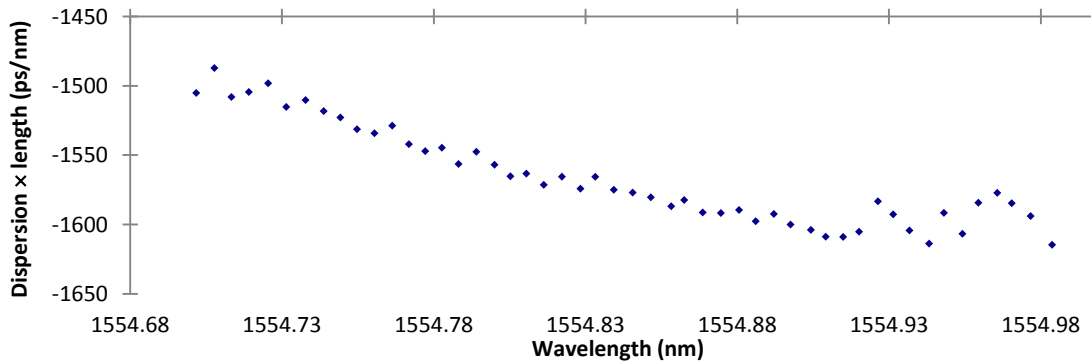


Fig. 3-24. Direct measurement of the dispersion \times length of a fiber Bragg grating using VRI. Adapted (re-colored) with permission from [50].

3.5.2.4 Ultra-low dispersion measurement

This experiment uses the two setups in Fig. 3-9 to demonstrate the characterization of a fiber that is smaller than allowed by Eq. 3-29 by taking the difference between two measurements using VRI. The length of SMF28 fiber in this experiment was $L_{SMF} = 30.5$ cm and the length of specialty fiber (short dispersion length sample to be tested), known as Twin Hole Fiber (THF), was $L_{THF} = 16.1$ cm. The tunable laser (Agilent 81642A) is swept from 1510 nm to 1640 nm and the interference pattern is recorded. The results of the dispersion characterization on the SMF28 fiber sample are then subtracted from the results of measurements made on the sample with the SMF28 fiber sample spliced to the THF to determine the dispersion characteristics of the THF. The results of this difference measurement are shown in Fig. 3-25 and Fig. 3-26.

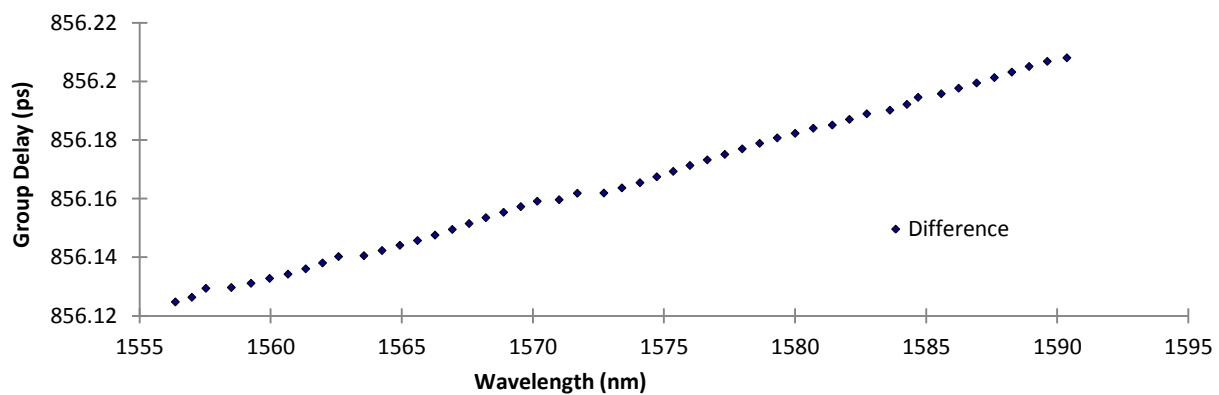


Fig. 3-25. Ultra-low group delay measurement made by taking the difference between two VRI measurements as illustrated in Fig. 3-9. Adapted (re-colored) with permission from [50].

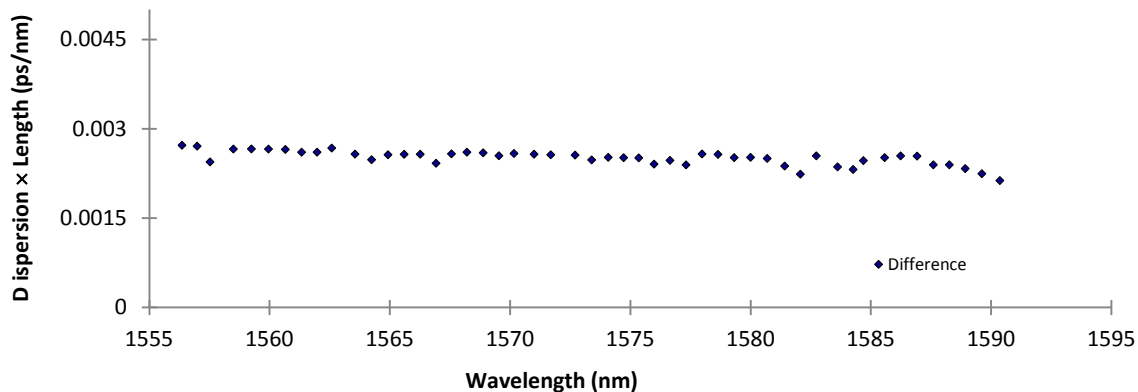


Fig. 3-26. Ultra-low dispersion \times length measurement made by taking the difference between two VRI measurements as illustrated in Fig. 3-9. Adapted (re-colored) with permission from [50].

3.6 Conclusion

This chapter introduced virtual reference interferometry as a hybrid between USI and BSI and discussed the theory behind the technique in detail. Particular attention was paid to defining its parameters and limitations. Also explored,

were several unique or important capabilities of the technique, including bandwidth compression, cascaded measurements, narrowband component characterization and ultra-short devices. Following experimental validation of the technique itself, the parameters and limitations as well as the unique capabilities were also verified experimentally. The validation experiments compared experimental results using VRI to simulation (using manufacturer's specifications) and to results obtained using conventional dispersion measurement techniques. These validation experiments allowed for the determination of the performance specifications of the technique. These performance metrics included both its accuracy and precision. Accuracy was shown to be high, with a relative error $<0.0001\%$ for group delay and $<0.5\%$ for the dispersion parameter. Precision was also shown to be high, with a relative deviation with respect to linear fit of $<0.15\%$. The high accuracy and precision is due to the ability to measure the dispersion parameter directly (i.e. as in BSI) from the interference pattern rather than indirectly via differentiation (i.e. as in USI or MPS). Direct measurements, were previously only possible using BSI which requires a variable delay line (requiring balancing, alignment and lots of time to run the experiment). With VRI, however, measurements are easy to set up and fast to carry out (compared to BSI) since first and second order dispersion plots may be produced from a single spectral scan. A revised version of the comparison charts presented in the last chapter, which now includes VRI is now be presented in Table 3-1 and Table 3-2.

Table 3-1: Typical precision for each dispersion measurement technique

Technique	Typical precision	Comment	References
TOF	$10^{-1} \text{ ps nm}^{-1}$	System cost inversely proportional to length. Need tens to hundreds of meters.	[19] [20]
MPS	$10^{-1} \text{ ps nm}^{-1}$	System cost inversely proportional to length. Need tens to hundreds of meters.	[22] [24]
TI	$10^{-3} \text{ ps nm}^{-1}$	Noise due to translation of mirror. Indirect measure of second order dispersion.	[48]
USI	$10^{-3} \text{ ps nm}^{-1}$	Indirect measure of second order dispersion. Fit to phase or group delay can have large error.	[29] [41] [13]
BSI	$10^{-5} \text{ ps nm}^{-1}$	Direct measure of second order dispersion. Highest precision. Difficult setup, operation, high cost delay line.	[13]
VRI	$10^{-5} \text{ ps nm}^{-1}$	Direct measure of second order dispersion. Highest precision. Easy setup and operation. No reference arm or delay line required.	This chapter

Table 3-2: Comparison of several performance metrics for each dispersion measurement technique

Technique	Measures short length?	Minimum scatter in group delay plot	Directly measures second order dispersion?	Fast (single scan)	Low difficulty Setup and operation	No Calibration
TOF				√	√	
MPS				√	√	
TI	√			√	√	
USI	√			√	√	√ [*]
BSI	√	√	√			
VRI	√	√	√	√	√	√ [*]

* Possible using the common path configuration

The virtual referencing technique is therefore a fast, accurate, practical and easy to implement alternative to the physical balancing required by BSI with several unique capabilities. In the next chapter we explore another unique capability of VRI, the simultaneous characterization of multiple modes in a few-mode-fiber from a single spectral scan.

Chapter 4.

Virtual reference interferometry: few-mode characterization

In this chapter, Virtual Reference Interferometry (VRI) is used for the characterization of first and second order dispersion in short length (<1m) Few-Mode fibers (FMF). The technique is shown to be capable of simultaneously measuring multiple modes of an FMF with a single scan of a tunable laser [51]. The characterization of both polarization and transverse modes is discussed. The motivation and importance of the dispersion characterization of FMFs to the telecommunications sector is also discussed. Recall that VRI generates results equivalent to balanced spectral interferometry (BSI) by simulating a virtual reference with a group delay equal to that of the physical interferometer. The result of mixing the physically generated interferogram with a virtually generated interferogram is a second order interferogram with an amplitude modulation that is equivalent to the first order interference that would be produced by physical balancing in BSI. However, in VRI the measurement results for multiple modes are generated in a single scan, with a simpler and more convenient setup. The advantages of the technique, therefore, include speed, simplicity, convenience and the capability for simultaneous measurement of multiple modes.

4.1 Introduction & motivation

In telecommunications, the pervasive need for increased network capacity has led to the development of a novel signal transmission strategy known as mode division multiplexing (MDM). In this strategy, further multiplexing (i.e. in addition to wavelength division multiplexing, for example) is achieved by discriminating signals according to their polarization or transverse mode. The bandwidth available using conventional multiplexing techniques can therefore be multiplied by the number of modes in a FMF using MDM. FMFs are also the topic of considerable research [1] [2] [3] [4] [5] [52] due to their compatibility with currently deployed single mode fibers and their resistance to intermodal coupling [5]. Recently, high-capacity transmission systems that use a combination of transverse and polarization mode multiplexed signals have been demonstrated [1] [3]. The design of these systems requires techniques for accurate dispersion characterization of both polarization and transverse modes.

Conventional characterization techniques focused almost exclusively on the measurement of the differential group delay (DGD) between two polarization modes, such as those present in a polarization maintaining (PM) fiber. To make this type of measurement, several techniques were developed, including those based on: Polarizer-analyzer [53], Jones matrix eigenanalysis [54] [55], temporal interferometry [56] [57] [58] and spectral interferometry [59] [60] [61]. These DGD-based techniques measure the relative difference between modes, but requires that one of the modes (typically the fundamental) is already well characterized (using another technique). This technique works well for the characterization of a fiber with two modes; however, potentially ambiguous results can be produced as the number of modes increases [62] [63] [64]. The difficulty of using this technique as the number of modes increases, is that when the power in a higher-order mode is comparable to that of the fundamental [63], it becomes

difficult to ascertain whether the measured differences are between that of the fundamental (well characterized mode) and a higher order mode or if the difference is between two higher order modes. In order to eliminate this potential ambiguity a technique capable of characterizing the absolute group delay (not the differential group delay) is required.

Some options for making absolute group delay measurements of all the modes include those based on time-of-flight (TOF) and interferometry (discussed in [Chapter 2](#)). Recently a TOF based technique was used to demonstrate the dispersion characterization of FMF [20] using a high speed (30 GHz) sampling oscilloscope and pulsed-tunable laser. In addition to the need for high speed (high cost) equipment, the problem with this technique is that the measurement required a 10.2 meter length FMF. The characterization of shorter fiber lengths (<1 meter) using TOF techniques, however, places prohibitive requirements on the sampling oscilloscope and pulsed laser. Interferometric techniques, on the other hand, are well suited for short length characterization. Temporal interferometric techniques (white-light interferometry) are capable of measuring the absolute group delay of each mode in an FMF [65]; however, they are susceptible to the vibrational noise caused by a moving variable delay line. For this reason, spectral interferometric techniques, which utilize a stationary reference arm, are generally preferred because they are not susceptible to this kind of vibrational noise.

Spectral interferometric techniques can be categorized into two classes; unbalanced spectral interferometry (USI) and balanced spectral interferometry (BSI), as discussed in [Chapter 2.4](#). Recall that the difference between the two techniques is that in BSI the group delay of the reference arm 'balances' (is equal to) that in the test arm, enabling the direct measurement of the second order dispersion, however, this technique is time consuming since each point in the dispersion plot requires a separate scan. On the other hand, USI based techniques are capable of characterizing the first order dispersion from a single spectral scan. An important class of USI based techniques employ a windowed Fast Fourier Transform (USI-WFT) to extract the group delay from an unbalanced interferometer [41] [45]. The problem with these techniques for characterizing multiple modes in an FMF is that the width of the spatial frequency peak generated by the Fourier transform depends on the size of the spectral window used. A window that is too large produces a broadened peak due to dispersion and a window that is too narrow generates a broadened peak due to the inverse nature of the bandwidth between a signal and its FFT. In short, since there is no way to know a priori the optimum window size it is difficult to prevent the overlap between spatial frequency peaks of different modes and ultimately to resolve individual modes. This problem was discussed in detail in [Chapter 2.4.2](#) and [Chapter 3.4.2](#) and proven mathematically in [Appendix C](#). Furthermore, FFT based techniques suffer from the additional limitation that second order dispersion can only be extracted by numerical differentiation of the group delay curve (or a fit to the group delay curve followed by analytical differentiation) and not directly from the interferogram. This can be a problem for fibers with several modes where the coupled power in each mode is low. With higher noise in the group delay curve, the choice of fit can have a significant impact on the second order dispersion generated by analytical differentiation.

BSI and VRI based dispersion characterization techniques [33] [34] [35] [13] [66], are advantageous (compared to USI-WFT techniques) for the measurement of FMF since they do not require the use of a spectral window, for which the ability to resolve individual modes of the FMF depends on a priori knowledge of the optimum window size. Furthermore, both first and second order dispersion measurements may be extracted directly and independently from the interferogram as discussed in [Chapter 2.4.2](#) independent of the group delay measurement. BSI techniques have been used to characterize the group delay of polarization modes of birefringent fiber [66]; however, they have not yet been demonstrated for transverse modes in an FMF with more than two modes. The drawback of using BSI based techniques, however, is that they require a *physical* reference for balancing. The construction, alignment and use of a free-space variable delay line are not trivial. Its use involves the need for calibration, which introduces calibration error into measurements and makes it susceptible to environmental fluctuations (i.e. temperature, pressure, etc.) in the reference path. This typically requires both the enclosure and isolation of the reference path. All of these additional considerations are in addition to the fact that each point in the dispersion curve requires a separate interference scan, resulting in extended experiment run times.

Virtual reference interferometry (VRI), proposed in [Chapter 3](#) as well as in [49] [50], is useful for overcoming the issues in both BSI and USI while maintaining the advantages of both. It is therefore a type of hybrid between balanced spectral interferometry and unbalanced spectral interferometry. The physical interferometer used to generate the real interference pattern is unbalanced, however, it is balanced virtually (i.e. the imbalance in the group delay between the test and reference phase fronts) via point-by-point multiplication with a simulated reference with a group delay imbalance equal to the imbalance in the physical interferometer. VRI has been demonstrated for the measurement of dispersion in single mode fibers and devices in [Chapter 3](#) and in [49] [50]. The focus of this chapter is to demonstrate the advantages of using VRI for the characterization of polarization and transverse modes in FMF, an important class of fiber in both academia and industry. An important advantage of the technique, highlighted in this chapter is that, for modes with sufficient spatial separation, absolute measurements of first and second order dispersion can be generated simultaneously, without the possibility of ambiguity in the results.

4.2 Theory

4.2.1 Polarization modes

The typical setup used to make dispersion measurements using VRI is the common path (or Fabry-Perot) configuration demonstrated in [Chapter 3](#). This configuration utilizes the reflections at the front and end facets of a fiber under test to take advantage of the simplicity of single-ended measurements. In a PM fiber, as illustrated in Fig. 4-1, the reflected electric fields may be described by $\vec{U}_o = A_1 \hat{i} + A_2 \hat{j}$ and $U_1 = A_1 e^{-2j\beta_1(\lambda)L_f} \hat{i} + A_2 e^{-2j\beta_2(\lambda)L_f} \hat{j}$. In these expressions $\beta_1(\lambda)$ and $\beta_2(\lambda)$ are the propagation constant in the fast and slow axis as a function of wavelength λ and L_f is the fiber length. A_1 and A_2 are the field amplitudes of the fast and slow components respectively, which remain constant for \vec{U}_o and \vec{U}_1 assuming there is no mode coupling.

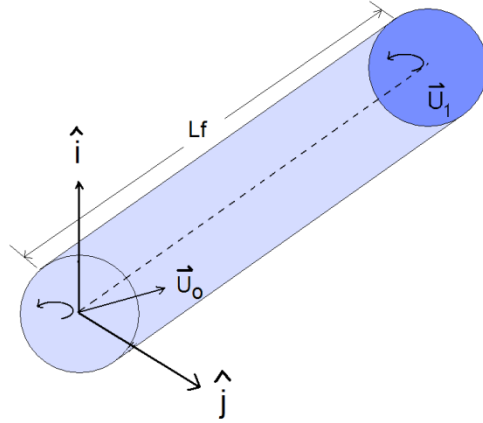


Fig. 4-1. Model for the interference in a polarization maintaining fiber. Adapted (re-colored) with permission from [51].

The interference pattern generated by the reflected electric fields is described by

$$I_{Real}(\lambda) = |\overline{U_0} + \overline{U_1}|^2 \quad \text{Eq. 4-1}$$

$$= 4K + 2(K + \Delta)\cos(2\beta_1 L_f) + 2(K - \Delta)\cos(2\beta_2 L_f)$$

where $K = (A_1^2 + A_2^2)/2$ and $\Delta = (A_1^2 - A_2^2)/2$. Setting $\Delta = 0$ by exciting the fiber with an input polarization 45° from fast axis, and removing the zero frequency (DC) term, Eq. 4-1 simplifies to

$$I_{Real}(\lambda)' = 4K \left(\underbrace{\cos(L_f(\beta_1 - \beta_2))}_{\text{Low freq. (Diff)}} \cos(L_f(\beta_1 + \beta_2)) \right) \quad \text{Eq. 4-2}$$

$$= 2K \left(\cos(2\beta_1 L_f) + \cos(2\beta_2 L_f) \right)$$

Although setting $\Delta = 0$ is not necessary for the measurements, it helps to simplify the mathematical expression. Once the real interference pattern is produced physically, the virtual reference interferogram described by

$$I_{virtual}(\lambda, \hat{\lambda}) = \cos(2k_0 L_v(\hat{\lambda}_w)) \quad \text{Eq. 4-3}$$

where k_0 is the free-space propagation constant, L_v is the length of the simulated virtual reference path and $\hat{\lambda}_w$ is the ‘balanced wavelength’ of mode w at which the group delay of the virtual reference path equals that of the measured mode as illustrated in Fig. 4-2. Point-by-point multiplication of the real interference pattern, described by Eq. 4-2, with a virtual reference interferogram described by Eq. 4-3 results in a second order interference pattern described by

$$I_{SO}(\lambda, \hat{\lambda}_w) = K \left(\underbrace{\cos(2(\beta_1 L_f - k_0 L_v(\hat{\lambda}_w)))}_{\text{Lowest freq. (Fast axis)}} + \underbrace{\cos(2(\beta_2 L_f - k_0 L_v(\hat{\lambda}_w)))}_{\text{Lowest freq. (Slow axis)}} \right) + \underbrace{2 \cos(L_f(\beta_1 - \beta_2)) \cos(L_f(\beta_1 + \beta_2) + 2k_0 L_v(\hat{\lambda}_w))}_{\text{Carrier}} \quad \text{Eq. 4-4}$$

Each of the first two terms in Eq. 4-4 contain a low- frequency amplitude modulation around a corresponding balanced wavelength, illustrated in Fig. 4-2 by $\hat{\lambda}_1$ for the slow axis and $\hat{\lambda}_2$ for the fast axis. The modulation frequency increases with spectral distance from the balance point. Given sufficient separation between $\hat{\lambda}_1$ and $\hat{\lambda}_2$, the influence on the low-frequency amplitude modulation around $\hat{\lambda}_1$ produced by the second term (cross talk), or the influence on the low frequency modulation on $\hat{\lambda}_2$ by the first term, can be easily removed by low-pass filtering. The third term in Eq. 4-4 may be easily removed by low pass filtering since it contains a slowly varying cosine (envelope) that modulates a fast varying cosine. Since this pattern is symmetric across the horizontal axis it therefore has a zero average value and is completely removed by low pass filtering. Note that the inset of Fig. 4-2 (magnified near $\hat{\lambda}_1$) shows the carrier (not resolved and appearing black) modulated by multiple ‘envelopes’ of different frequencies. The lowest-frequency amplitude modulation is used to locate $\hat{\lambda}_1$ and $\hat{\lambda}_2$, from which the group delay of each mode is obtained.

Dispersion plots for both first and second order dispersion may be produced as a function of wavelength by varying the value of $L_v(\hat{\lambda}_w)$ and locating the balance wavelength for each mode (as described in [Chapter 2.4.2](#) for BSI which is the same process used in [Chapter 3.2](#) and in [49] [50] for VRI). The precision of identifying balance wavelengths improves by removing sources of noise such as the high frequency carrier and cross talk from adjacent modes. This is achieved by low pass filtering, as shown in the lower plot of Fig. 4-2. In order to locate the balance points for each mode with low error, there must be sufficient spectral separation $\hat{\lambda}_2 - \hat{\lambda}_1$ between the balance points of each mode. This occurs as long as the wavelength location of the second peak to the left of $\hat{\lambda}_1$ is greater than the wavelength location of the second peak to the right of $\hat{\lambda}_2$. Following the analysis on the minimum separation between modes [Chapter 3.4.2](#) (assuming $N=1$) this condition is satisfied by

$$\hat{\lambda}_2 - \hat{\lambda}_1 \geq \frac{1}{2} \sum_{w=1}^2 \frac{\sqrt{6}}{(cL_f D(\hat{\lambda}_w))^{1/2}} \hat{\lambda}_w \quad \text{Eq. 4-5}$$

where $D(\hat{\lambda}_w)$ is the second-order dispersion parameter of mode w and c is the speed of light. Using typical dispersion parameters of SMF28, modes having a group index difference greater than 2.75×10^{-4} for a 1 meter long fiber can be resolved. The maximum fiber length that can be characterized using the common-path configuration, however, is dependent on the spectral resolution, $\Delta\lambda$, with which the interferogram is sampled, given in [Chapter 3](#)

as $L_f \leq \lambda^2 / (20N_g \Delta\lambda)$ [50]. The maximum measurable fiber length (typically ~0.8 meters with a wavelength resolution of 0.1 picometers) is sufficient for many applications, especially those in which only short lengths of fiber are available or desired. Furthermore, few mode fibers are used instead of multimode fibers since they are resistant to intermodal coupling (since the mode separation is large) [5]. Since this means that mode separation is large, there is no need to use long lengths of fiber to reduce the minimum spectral separation in Eq. 4-5 and therefore the fiber length is not a limitation for most practical cases.

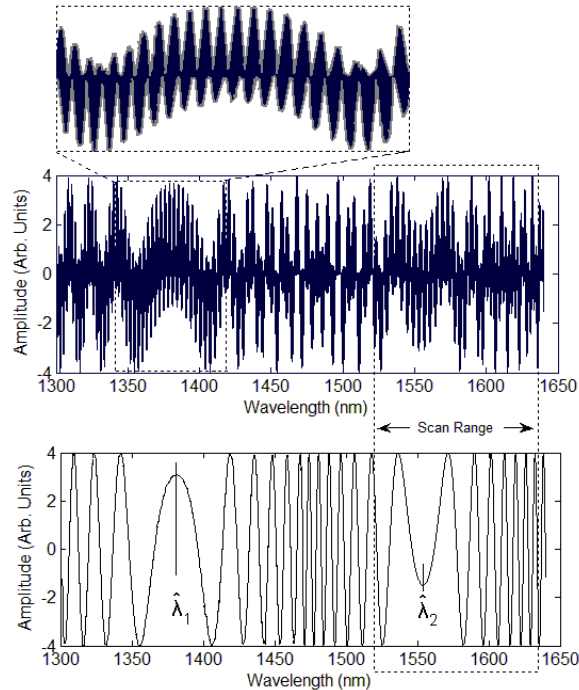


Fig. 4-2. Simulated second order interference pattern (upper graph) and the result of low-pass filtering (lower graph) used to extract the balance wavelengths, from which absolute group delay and second order dispersion of the individual modes can be obtained. Inset above shows a magnified spectral region around a balance wavelength. Although both modes (the slow axis balanced at $\hat{\lambda}_1$ and the fast axis balanced at $\hat{\lambda}_2$) are illustrated in the figure, only one mode is typically within the scan range of the tunable laser for a given L_f , which is varied to extract group delay and second order dispersion of both modes as a function of wavelength. Adapted (re-colored) with permission from [51].

4.2.2 Transverse modes

Illustrated in Fig. 4-3 is a model for the reflections at the front and end facets of a p-moded FMF with multiple transverse modes, used to generate spectral interference. The model assumes light can be launched simultaneously into all transverse modes.

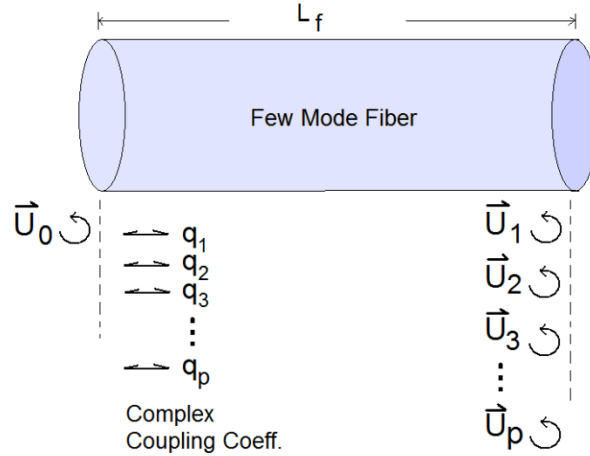


Fig. 4-3. Model for the interference in a few-mode fiber. Adapted (re-colored) with permission from [51].

The complex coupling coefficient $q_l = |q_l|e^{j\varphi_l}$ for each mode l of the fiber determines the field amplitudes of the modes. The reflected electric field of the l^{th} mode is described by $\overline{U}_l = |q_l|^2 \overline{U}_0 e^{-2j(\beta_l L_f + \varphi_l)}$ and the resulting interference pattern generated by all the reflections at the facets of the FMF are described by

$$\begin{aligned}
 I_{\text{Real}}(\lambda) &= |\overline{U}_0 + \dots + \overline{U}_p|^2 \\
 &= |\overline{U}_0|^2 \left(\underbrace{\left(1 + \sum_{l=1}^p |q_l|^4 \right)}_{\text{DC Term}} + \underbrace{\left(\sum_{l=1}^p 2|q_l|^2 \cos(2(\beta_l L_f + \varphi_l)) \right)}_{\text{High frequency (Absolute measurement)}} \right. \\
 &\quad \left. + \underbrace{\left(\sum_{l=1}^{p-1} \sum_{m=l+1}^p 2|q_l|^2 |q_m|^2 \cos(2((\beta_l - \beta_m)L_f + (\varphi_l - \varphi_m))) \right)}_{\text{Low Frequency (Differential measurement)}} \right)
 \end{aligned} \tag{Eq. 4-6}$$

In Eq. 4-6, the first term (DC term) contains the zero frequency components which results from the sum of the amplitudes of the coupling coefficients of each mode. The second term (high frequency components) contains the information on the individual propagation constants from which *absolute* measurements can be obtained using VRI. The third term (low frequency components) contains information about the relative differences between the propagation constants of the modes, from which *differential* measurements between modes can be obtained. In this chapter, VRI is used to reference the high frequency terms to allow for the measurement of *absolute* group delay and second order dispersion, avoiding the ambiguity possible in differential (relative) measurements. Note that for the FMF experiment, VRI is performed for characterizing transverse modes exactly as described for polarization modes.

4.3 Experiments

The experiments demonstrated in this chapter include the characterization of the polarization modes in a Panda fiber and the transverse modes in a four-mode FMF using VRI. Both experiments use the same tunable laser source (Agilent 81642A), with a built-in wavemeter (wavelength resolution of 0.1 pm), swept from 1510 nm to 1640 nm. The laser ensures an absolute wavelength accuracy of ± 15 picometers using a built in wavemeter with automatic wavelength calibration using a built in reference gas cell. Furthermore, in both experiments a fiber optic circulator connected to a tunable laser and detector (Thorlabs PDA10CS), as illustrated in Fig. 4-4(a) and Fig. 4-4(b), is used. The tunable laser is connected to port 1 of the circulator and a detector is connected to port 3. The optical connection between port 2 and the fiber under test is experiment dependent.

For the characterization of the polarization modes in a Panda PM fiber, the setup in Fig. 4-4(a) is used. A polarization controller ensures that power is evenly distributed into both polarization modes, effectively setting $\Delta = 0$ in Eq. 4-1. This allows both modes to be characterized simultaneously with high signal-to-noise ratio. Note that even if A_1 and A_2 are quite different (i.e. without the polarization controller), both modes can still be characterized simultaneously (though power will not be evenly distributed between modes). Although it is possible to measure each mode separately, it is desirable to measure each mode simultaneously as it eliminates the possibility of thermal fluctuations in fiber length between scans. In order to couple light simultaneously into multiple transverse modes of an FMF a new coupling strategy was developed. The coupling strategy involves the use of an FC/APC connector on the launch fiber and variation of the distance to the front facet of the test fiber. Variation of the coupling distance (gap between the FC/APC connector and the FC/PC connector of the test fiber) using this setup (via a precision translation stage) allowed for variation in the amount of coupled power into each mode. For the simultaneous characterization of multiple fiber modes it is desirable to have an even power distribution in all fiber modes. The longitudinal offset technique, introduced here, is employed in both the VRI based setup shown in Fig. 4-4(b) and the BSI based setup in 6-4(c). The results of VRI measurements are then compared to those made using BSI in the results section.

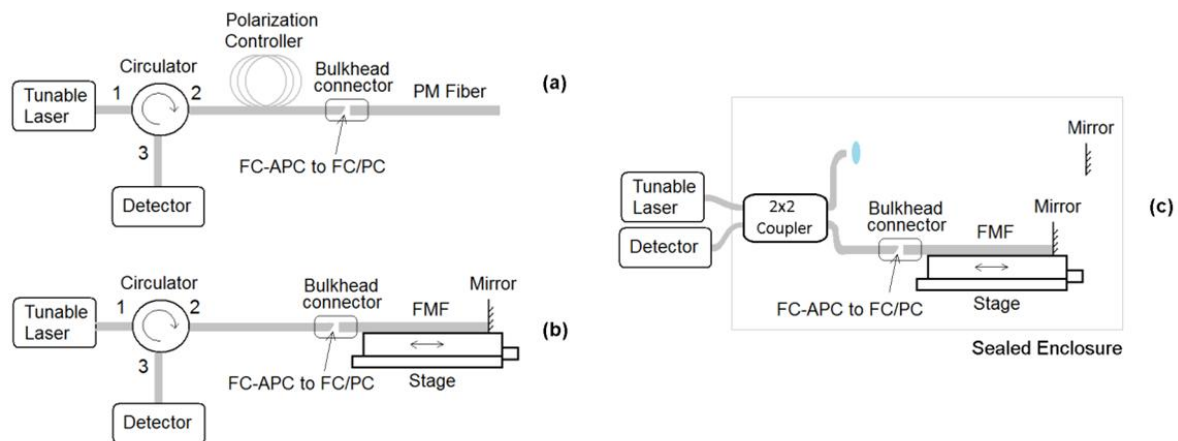


Fig. 4-4. Experimental setup for measurement of (a) polarization modes in PM fiber using VRI, (b) transverse modes in an FMF using VRI, and (c) transverse modes using BSI. Adapted (re-colored) with permission from [51].

4.4 Results

VRI based measurements of the first order dispersion (group delay) and second order dispersion (dispersion \times length) for the polarization modes in Panda PM fiber are illustrated in Fig. 4-5(a) and 6-5(b) respectively. The results of both polarization modes agree well with simulated curves provided by the manufacturer, Corning[®] Inc.

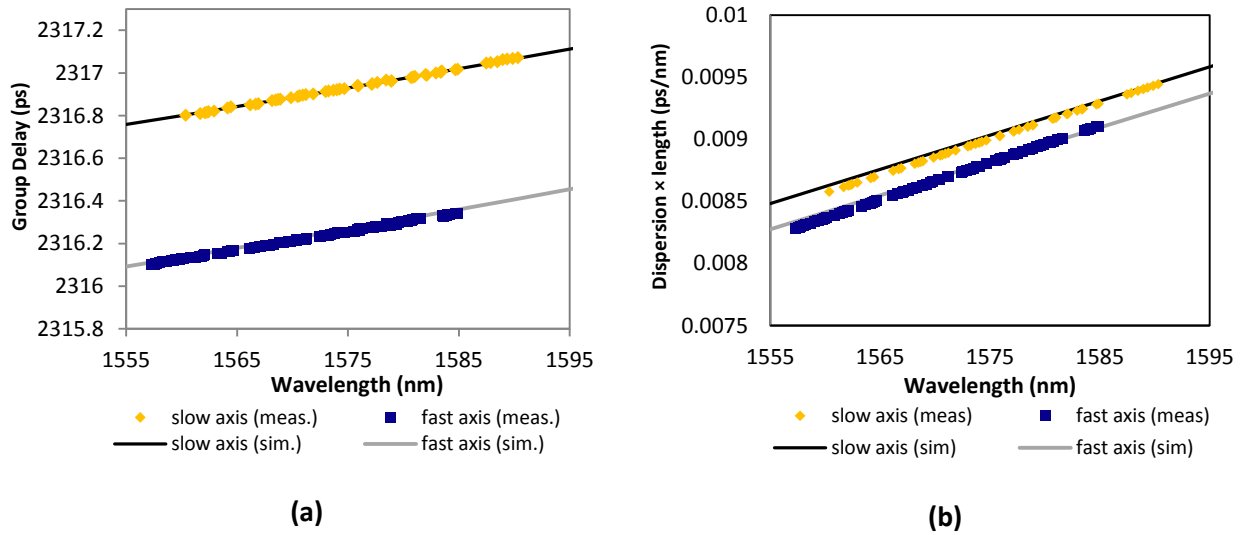


Fig. 4-5. Simultaneous absolute (a) group delay and (b) dispersion \times length measurements for both polarization modes of a 47.2 cm long Panda polarization maintaining fiber. Adapted (re-colored and axis labels corrected in (b)) with permission from [51].

VRI based measurements of the first order dispersion (group delay) and second order dispersion (dispersion \times length) for the transverse modes in a four mode FMF are compared to results obtained using conventional BSI in Fig. 4-6, Fig. 4-7(a)-(d) respectively. Since the low power coupled to each mode in the FMF increased the scatter in the group delay curves the second order dispersion (dispersion \times length) had to be extracted directly from the balanced interferogram, which is possible using both BSI and VRI, as described in [Chapter 2.4.2](#) and in [13] [49] [50]. In the VRI experiment the first three modes of the fiber (LP01, LP11 and LP02) were characterized in one scan. The gap position was then adjusted and a second scan was performed to increase the coupled power into the LP21 mode. As a result, the VRI curves in Fig. 4-6 and Fig. 4-7(a)-(d) were generated using only two scans, whereas, in the BSI experiment every point required a separate scan. The slight differences in scatter observed between experiments are due to variation in the power coupling (variation in SNR) between experiments for a given mode. The results for both first and second order dispersion, however, agree well in both experiments.

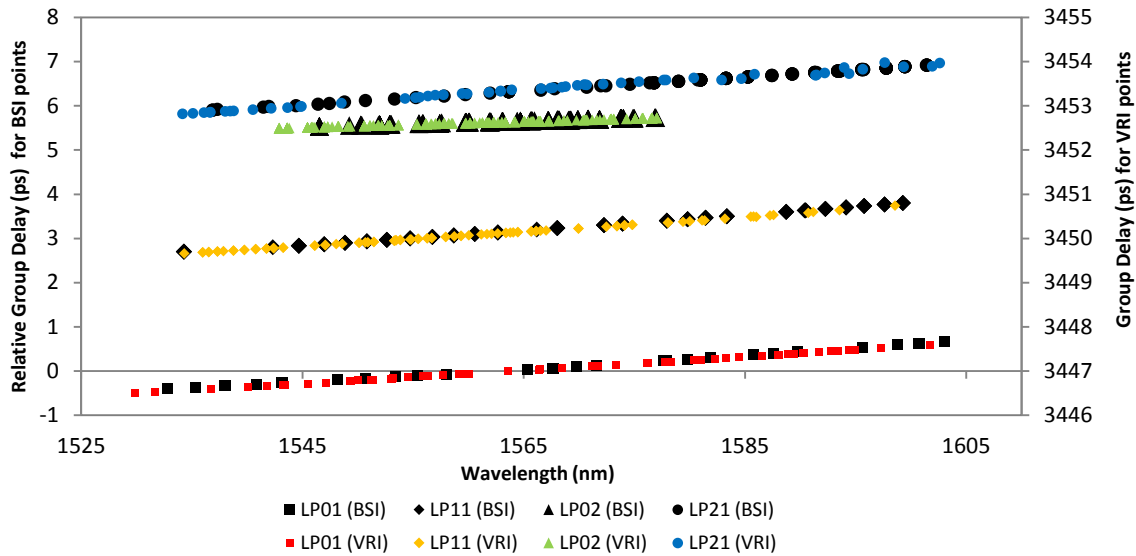


Fig. 4-6. Absolute group delay measurements of a 69.9 cm long few-mode fiber measured using balanced spectral interferometry and virtual reference interferometry. Adapted (re-colored) with permission from [51].

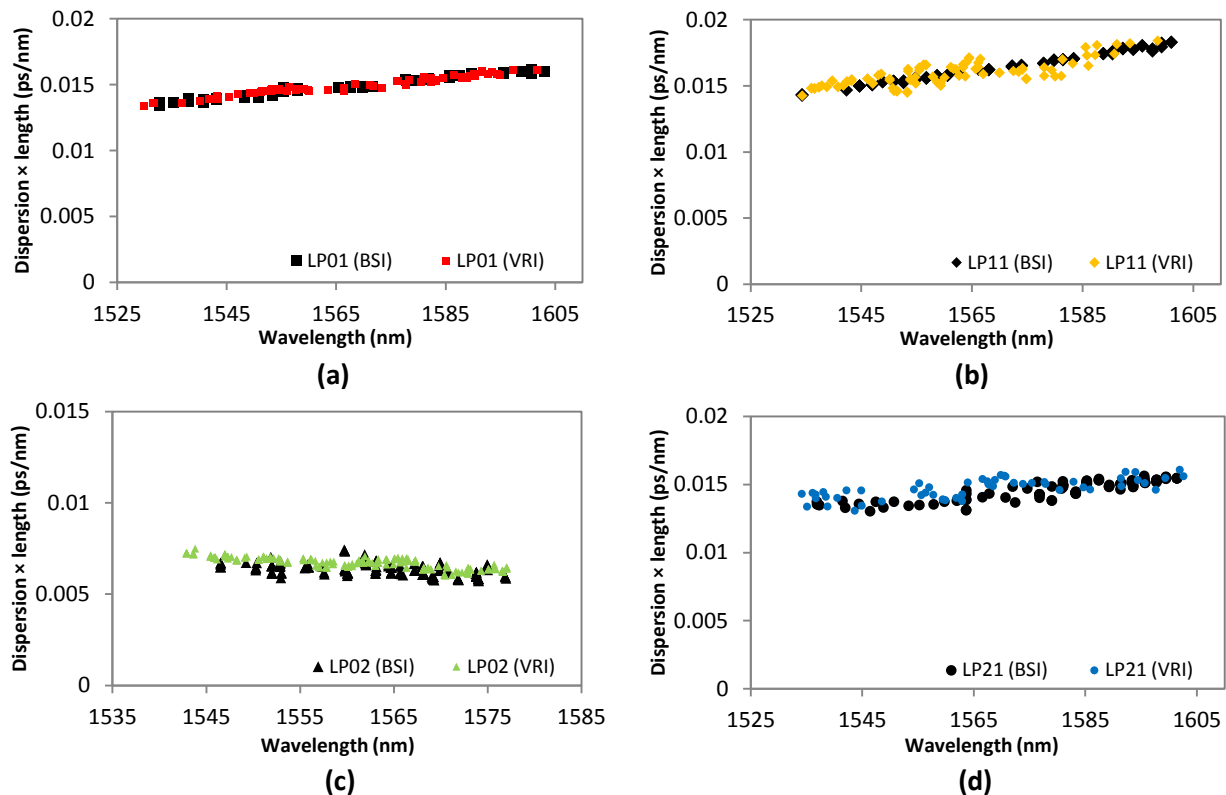


Fig. 4-7. Comparison of the dispersion \times length measurements for the (a) LP01 mode, (b) LP11, (c) LP02 mode, and (d) LP21 mode of a 69.9 cm length of few-mode fiber measured via Balanced Spectral Interferometry and Virtual Reference Interferometry. Adapted (re-colored) with permission from [51].

4.5 Conclusion

This chapter demonstrated the characterization of the first and second order dispersion of polarization modes in a Panda PM fiber and transverse modes in an FMF. This capability is of considerable interest for the development of mode-division multiplexing schemes in telecommunication networks. Like BSI, VRI is capable of directly measuring first and second order dispersion; however it does not require a complex free space reference path. The ability to measure second order dispersion directly from the interference pattern is especially useful when the first order dispersion curves have large scatter, as demonstrated in the experiment on the FMF in this chapter. Furthermore, full first and second order dispersion characterization of multiple modes can be completed in a single scan. Although USI based techniques are also capable of single scan characterization, only the first order dispersion can be characterized directly. However, since the peak width depends on the window size in USI, resolving the individual modes can be quite difficult since an optimum window size is unknown. Since the resolution is inherently optimized in BSI and VRI (see [Chapter 2.4.3](#) and [Appendix C](#)) these techniques are best suited to the characterization of multiple fiber modes. However, VRI is more convenient than BSI since it does not require a physical reference path.

Chapter 5.

Dispersive virtual reference interferometry

This chapter introduces Dispersive Virtual Reference Interferometry (DVRI). The use of a dispersive reference is useful for the characterization of fibers and optical components with near zero dispersion-length [67]. This capability is of considerable practical interest for short length (<1m) fibers. In this chapter DVRI will be shown to have an accuracy equivalent to that in standard balanced spectral interferometry (BSI), on the order of 10^{-3} ps and 10^{-5} ps/nm for the group delay and dispersion-length measurements, respectively. However, DVRI will be shown to be capable of achieving this accuracy without the need for wide spectral bandwidths or multiple spectral scans (as required by BSI). The technique will first be validated via comparison of results to manufacturer's specifications (simulation) and to experimental results obtained via standard VRI. After the technique is validated it will be used to characterize a 23.3-cm erbium-doped gain fiber (dispersion-length product <0.002 ps/nm), using a tunable laser with a bandwidth of 145nm. Furthermore, the dispersion in a 28.6-cm commercial dispersion shifted fiber will be characterized across the zero-dispersion wavelength and the zero-dispersion-wavelength and slope will be determined to be 1566.7 nm and 8.57×10^{-5} ps/(nm²·m) to a precision of ± 0.2 nm and $\pm 0.06 \times 10^{-5}$ ps/(nm²·m), respectively.

5.1 Introduction & motivation

Chromatic dispersion is an important physical parameter for a host of specialty fibers, such as photonic crystal fibers, twin-hole fibers, gain fibers, and dispersion-engineered fibers. Due to cost and other practical considerations, the capability for dispersion characterization on a short length (<1m) of fiber is highly desirable. Doped gain fibers, for example, have high absorption near the gain region when they are not pumped. The loss in the fiber, therefore, effectively limits the length of fiber that may be characterized. When length is constrained, so is the total dispersion-length product (DL), defined as the second-order dispersion parameter (D) multiplied by the length of the fiber (L). Stated in a different way, the DL product is the cumulative group delay difference per unit bandwidth over the entire fiber length. Commercial dispersion characterization instruments, based on time-of-flight (TOF) or modulation phase-shift (MPS), typically have a resolution of 0.1 to 1 ps/nm as described in [Chapter 2.1](#) and [Chapter 2.2](#). Because of this limitation, acceptable characterization accuracy can only be obtained on long fiber length samples, particularly when the fiber dispersion is low. To characterize short fiber lengths (<1m), however, interferometric techniques are most commonly employed [19]. As discussed in [Chapter 2.3](#) and [Chapter 2.4](#), interferometric techniques may be classified into two categories; temporal [28] [27] and spectral [13] [17] [30] [29] [41] interferometry. Spectral interferometry may be further subdivided into balanced spectral interferometry (BSI) [13] [17] [30] and unbalanced spectral interferometry (USI) [29] [41]. The advantage of BSI is the ability to extract both first and second-order dispersion directly from the interference pattern (i.e. independent of each other [13]). For BSI, however, this capability, however, comes at the cost of increased experimental complexity and duration as a variable

delay line must be incorporated into the reference arm and its length adjusted so that each point in the measured dispersion curve is generated from a different interferogram (requiring multiple scans). This is due to the fact that in BSI, the group delay in the test arm (containing the test fiber) must be balanced by the reference arm. Since the resulting interference pattern provides information about the differences between the test and reference path, the balancing removes the effect of the first order dispersion. This produces an interference pattern that is directly related to the second order dispersion in the test fiber. More accurately, balancing results in an interferogram whose intensity variation contains information about the difference (Δ) in the second-order dispersion length (DL) between the test and reference arm. The minimum spectral bandwidth needed to characterize a fiber using BSI is inversely proportional to $\sqrt{\Delta}$ [30] [50], as discussed in [Chapter 2.4.2](#). In BSI the reference path is typically chosen to be free space, since it has zero second order dispersion (don't need to calibrate out the second order dispersion of the reference) and therefore the Δ measured from the interferogram using a free space path is simply the DL of the test fiber itself. Therefore in standard BSI, which uses a free space reference path, the lower limit on the DL that can be measured is determined by the available bandwidth.

In [Chapter 3](#), virtual reference interferometry (VRI) [50] was introduced as an alternative to BSI where the free space reference arm used in BSI could be eliminated (if the common path configuration is used). In VRI a second-order interference pattern is produced using a simulated reference path to balance the group delay in the test path, from which the DL of the test fiber can be extracted directly, in a manner analogous to BSI [13] [50]. Like BSI, however, using a simulated free-space reference also puts a lower limit on the DL that can be measured. However, since the reference is simulated in VRI, it is possible to simulate a dispersive reference so that Δ can include the dispersion of the simulated reference path. This is useful since the second order dispersion length of the reference path can be increased arbitrarily to reduce the bandwidth required for characterization (lowering the DL measurement limit). Using a dispersive reference path (with high second-order dispersion) lowers the DL measurement limit (which is in principle, limited by the fringe resolution) without requiring an increase in the scan range (bandwidth). This is possible since artificially increasing the dispersion difference between the test arm and the virtual reference arm (i.e. by increasing the simulated dispersion of the virtual reference) leads to a spectrally denser second-order interference fringe pattern. This allows the extraction of Δ over a smaller spectral region. For the same reason, this strategy also leads to an increase in the wavelength range over which the second-order dispersion of the fiber can be characterized. In this chapter, VRI will be used to refer to the use of a non dispersive virtual reference and the terms dispersive-VRI or DVRI will be used to indicate the use of a simulated dispersive reference. The theoretical relationships between the dispersion in the virtual reference, that of the test fiber and the properties of the resulting second order interference pattern will first be developed. The DVRI technique will then be validated experimentally and used to perform direct measurements of first and second order dispersion, in short-length, low-dispersion gain fibers and dispersion shifted fibers, which would not be possible if a dispersive reference was not used.

5.2 Theory

The detailed steps in a DVRI measurement are exactly as presented for VRI in [Chapter 3](#) and in [50], with the exception that a dispersive reference is simulated instead of free space (non-dispersive reference). A summary of the steps in a DVRI measurement are now presented to demonstrate the use of a dispersive reference. The first step in a DVRI measurement is to obtain a spectral interference pattern using the reflections from the two cleaved or polished facets of the test fiber. The intensity measured at the detector, after normalization of the amplitude is given by [50]

$$I_{Real}(\lambda) \cong \cos(2\beta_f(\lambda)L_f) \quad \text{Eq. 5-1}$$

where λ is the wavelength, β_f is the propagation constant of the test fiber and L_f is its length. The second step in a DVRI experiment involves the numerical generation of a simulated interference pattern using a dispersive virtual reference described by

$$I_{virtual}(\lambda, \lambda_0) = \cos(2\beta_v(\lambda)L_v) \quad \text{Eq. 5-2}$$

where $\beta_v(\lambda)$ is the propagation constant of the dispersive virtual reference and L_v is its length, which is chosen to balance the group delay in the test fiber at a specific wavelength λ_0 , as shown in Fig. 5-1. The third step in a DVRI experiment involves the point-by-point multiplication of the interference pattern in Eq. 5-2 with the real interference pattern described by Eq. 5-1 to produce a second-order interference pattern described by

$$I_{SO}(\lambda, \lambda_0) = \frac{1}{2} \left(\underbrace{\cos(2(\beta_f(\lambda)L_f - \beta_v(\lambda)L_v))}_{\text{slow varying term}} + \underbrace{\cos(2(\beta_f(\lambda)L_f + \beta_v(\lambda)L_v))}_{\text{fast varying term}} \right) \quad \text{Eq. 5-3}$$

and illustrated in Fig. 5-1. The second order interference pattern has a fast-varying term, amplitude modulated by a slow-varying term. The modulation amplitude changes according to its phase as described by

$$\varphi_{Amp.mod.}(\lambda) = 2|\beta_f(\lambda)L_f - \beta_v(\lambda)L_v| = 2k_0|n_{eff_f}(\lambda)L_f - n_{eff_v}(\lambda)L_v| \quad \text{Eq. 5-4}$$

where k_0 is the propagation constant in free space, $n_{eff_f}(\lambda)$ is the refractive index of the test fiber, and $n_{eff_v}(\lambda)$ is the simulated refractive index of the reference path. Note that the magnitude is taken since $\cos(-\varphi) = \cos(\varphi)$.

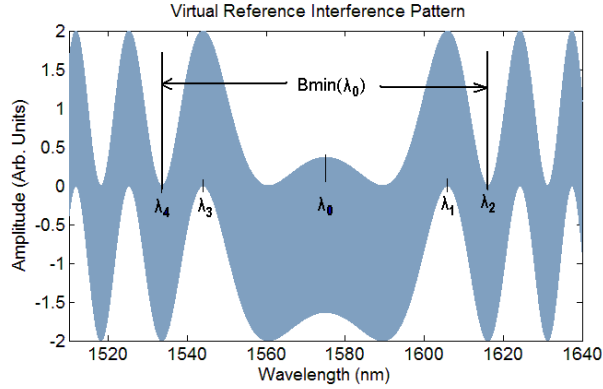


Fig. 5-1. Amplitude modulated interference pattern described by Eq. 5-3. The fast varying interference is shown in blue and is not resolved in the figure. The slow varying amplitude modulation with phase described by Eq. 5-4 is shown. Adapted (re-colored) with permission from [67].

An important note is that at the symmetry point λ_0 is an inflection point (local maximum or minimum) in the phase of the amplitude modulation function. Taking the first derivative of the phase function in Eq. 5-4 gives

$$\begin{aligned} \left. \frac{d\varphi_{Amp.mod.}}{d\lambda} \right|_{\lambda} &= 4\pi \left| \frac{d(n_{eff_f}(\lambda)L_f/\lambda)}{d\lambda} - \frac{d(n_{eff_v}(\lambda)L_v/\lambda)}{d\lambda} \right| \\ &= \left[\frac{4\pi}{\lambda^2} \left[- \left[n_{eff_f}(\lambda) - \lambda \frac{dn_{eff_f}(\lambda)}{d\lambda} \right] L_f + \left[n_{eff_v}(\lambda) - \lambda \frac{dn_{eff_v}(\lambda)}{d\lambda} \right] L_v \right] \right] \\ &= \left[\frac{4\pi}{\lambda^2} \left[N_{g_f}(\lambda)L_f - N_{g_v}(\lambda)L_v \right] \right] \end{aligned} \quad \text{Eq. 5-5}$$

Since the phase is minimized at $\lambda = \lambda_0$, this means that $d\varphi_{Amp.mod.}/d\lambda|_{\lambda=\lambda_0} = 0$, which implies that

$$N_{g_v}(\lambda_0)L_v = N_{g_f}(\lambda_0)L_f \quad \text{Eq. 5-6}$$

It also implies that the phase is minimized since $d^2\varphi_{Amp.mod.}/d\lambda^2|_{\lambda} > 0$. The amplitude modulation is symmetric at wavelength λ_0 (Fig. 5-1), where the group index \times length of the test fiber and that of the simulated virtual reference are balanced. It should be noted that since the value of $N_{g_v}(\lambda_0)L_v$ (the group index \times length of the virtual reference) is known and since it is equal to that in the test fiber, the only measured quantity is the wavelength λ_0 at which this equality occurs. Therefore by sweeping the simulated value of $N_{g_v}(\lambda_0)L_v$ (independent variable) and measuring the location λ_0 (dependent variable) where the equality in Eq. 5-6 occurs, one may produce a plot of $N_{g_f}(\lambda_0)L_f$ (the group index \times length of the fiber) as a function of wavelength.

Applying a Taylor expansion to $n_{eff_f}(\lambda)$ and $n_{eff_v}(\lambda)$ in Eq. 5-4 around λ_0 and neglecting terms higher than the third order (to include third order dispersion effects) gives the phase expression

$$\begin{aligned}
\varphi_{Amp.mod.}(\lambda) = & \frac{4\pi}{\lambda} \left[N_{g_f}(\lambda_0)L_f - N_{g_f}(\lambda_0)L_v \right] \\
& + 4\pi \left[\frac{dn_{eff_f}}{d\lambda} \Big|_{L_f} - \frac{dn_{eff_v}}{d\lambda} \Big|_{L_v} \right] \\
& + 4\pi \left[\frac{(\lambda - \lambda_0)^2}{2!\lambda} \left[\left[\frac{d^2n_{eff_f}}{d\lambda^2} \Big|_{L_f} - \frac{d^2n_{eff_v}}{d\lambda^2} \Big|_{L_v} \right] \right] \right] \\
& + 4\pi \left[\frac{(\lambda - \lambda_0)^3}{3!\lambda} \left[\left[\frac{d^3n_{eff_f}}{d\lambda^3} \Big|_{L_f} - \frac{d^3n_{eff_v}}{d\lambda^3} \Big|_{L_v} \right] \right] \right] \\
& + \dots
\end{aligned} \tag{Eq. 5-7}$$

Where the equality in Eq. 5-6 means that the first term in Eq. 5-7 is zero. Notice that at λ_0 the phase is not zero (it is minimized). Eq. 5-7 may be further simplified by making the substitutions

$$\Delta(\lambda_0) = \frac{d^2n_{eff_f}}{d\lambda^2} \Big|_{\lambda_0} L_f - \frac{d^2n_{eff_v}}{d\lambda^2} \Big|_{\lambda_0} L_v(\lambda_0) \tag{Eq. 5-8}$$

$$\frac{d\Delta}{d\lambda} \Big|_{\lambda_0} = \frac{d^3n_{eff_f}}{d\lambda^3} \Big|_{\lambda_0} L_f - \frac{d^3n_{eff_v}}{d\lambda^3} \Big|_{\lambda_0} L_v(\lambda_0) \tag{Eq. 5-9}$$

where $\Delta(\lambda_0)$ is the difference in second order dispersion and $\frac{d\Delta}{d\lambda} \Big|_{\lambda_0}$ is the difference in third order dispersion between the test and reference arms. Eq. 5-7 then simplifies to

$$\begin{aligned}
\varphi_{Amp.mod.}(\lambda) = & 4\pi \left[\frac{dn_{eff_f}}{d\lambda} \Big|_{L_f} - \frac{dn_{eff_v}}{d\lambda} \Big|_{L_v} \right] \\
& + 4\pi \left[\frac{(\lambda - \lambda_0)^2}{2!\lambda} \left[\Delta(\lambda_0) \right] \right] \\
& + 4\pi \left[\frac{(\lambda - \lambda_0)^3}{3!\lambda} \left[\frac{d\Delta}{d\lambda} \Big|_{\lambda_0} \right] \right] \\
& + \dots
\end{aligned} \tag{Eq. 5-10}$$

Taking the phase difference between two peak or valley points with known phase separation and neglecting terms above third order gives

$$\begin{aligned}
 \left| \varphi_{Amp. \text{ mod.}}(\lambda_m) - \varphi_{Amp. \text{ mod.}}(\lambda_n) \right| &\cong 2\pi \left| \left[\frac{(\lambda_m - \lambda_0)^2}{\lambda_m} - \frac{(\lambda_n - \lambda_0)^2}{\lambda_n} \right] \Delta(\lambda_0) \right. \\
 &\quad \left. + \left[\frac{(\lambda_m - \lambda_0)^3}{3\lambda_m} - \frac{(\lambda_n - \lambda_0)^3}{3\lambda_n} \right] \frac{d\Delta}{d\lambda} \Big|_{\lambda_0} \right| \\
 &\cong \pi(m-n)
 \end{aligned} \tag{Eq. 5-11}$$

where $m \neq 0$, $n \neq 0$ and $(m-n)$ is the number of peak-to-valley or valley-to-peak transitions between a peak or valley at λ_n and one at λ_m . The peak and valley points are chosen so that either $\lambda_m > \lambda_n > \lambda_0$ or $\lambda_m < \lambda_n < \lambda_0$. For example, in Fig. 5-1 $m=2$ and $n=1$ so that Eq. 5-11 gives the phase separation between λ_2 and λ_1 as π . The same result is obtained for $m=4$ and $n=3$. Using $D(\lambda_0) = -\frac{\lambda_0}{c} d^2 n_{eff} / d\lambda^2 \Big|_{\lambda_0}$, the $|\Delta(\lambda_0)|$ term in Eq. 5-11 can be expressed as

$$|\Delta(\lambda_0)| \cong \frac{c}{\lambda_0} |D_v(\lambda_0)L_v - D_f(\lambda_0)L_f| \tag{Eq. 5-12}$$

Note that in order to accurately locate the symmetry point λ_0 in the above equations, a peak and valley must be visible on each side of λ_0 as illustrated in Fig. 5-1 and discussed in [Chapter 2.4.2](#) and [Chapter 3.4](#). Furthermore, at least one peak and one valley on each side of λ_0 must also be visible within the scan range, in order to be able to measure second order dispersion directly from the interference pattern as described in [Chapter 2.4.2](#) and [Chapter 3.4.2](#) as well as in [13] [50]. As a result, the minimum bandwidth required ($B_{min}(\lambda_0)$) in Fig. 5-1) is given by the spectral separation between λ_2 and λ_4 . The next section follows a similar procedure as in [Chapter 2.4.2](#) or [Chapter 3.4.2](#) or [13] [50], to develop the relationship between the minimum bandwidth $B_{min}(\lambda_0)$ and the dispersion length difference between the test and reference paths $\Delta(\lambda_0)$.

5.2.1 Minimum bandwidth & spectral compression

A method for spectral compression of the interference pattern by virtual referencing of the higher order harmonics of the fiber was presented in [Chapter 3.3.1](#) and a derivation for the minimum bandwidth was presented in [Chapter 3.4.1](#). The spectral compression possible using the compression technique in [Chapter 3.3.1](#) was limited by a reduction in the fringe visibility due to loss experienced at the fiber facets. This limitation is not present when using DVRI since only the first harmonic is being referenced. What follows is a re-derivation of the minimum bandwidth for DVRI as a function of $\Delta(\lambda_0)$. It will be important to note that increasing $\Delta(\lambda_0)$ leads to compression which reduces the minimum bandwidth required for a measurement and increases the bandwidth of the measured results. The minimum bandwidth of the source required to measure the dispersion from the phase of the amplitude modulation is determined by the requirement that at least one peak and one valley be present on both sides of λ_0 (illustrated by λ_1 and λ_2 on the right side and λ_3 and λ_4 in Fig. 5-1). The minimum bandwidth is given by the

spectral distance between λ_2 and λ_4 in Fig. 5-1 and is also illustrated in Fig. 5-2. The bandwidth of the source B_{source} must therefore be greater than this minimum bandwidth, described as

$$B_{Source} \geq B_{min} = (\lambda_2 - \lambda_4) \cong 2(\lambda_2 - \lambda_0) \quad \text{Eq. 5-13}$$

An expression for the maximum wavelength spacing $(\lambda_2 - \lambda_0)$ is required to find the relationship between the dispersion of the dispersive virtual reference and B_{min} . Although Eq. 5-11 cannot be used to get an exact phase separation when $n=0$, the phase separation between λ_1 and λ_0 ($m=1$ and $n=0$) is still constrained to $\leq 2\pi$ as illustrated in Fig. 5-2. Using this gives the expression

$$\Delta\varphi_{Amp.mod.}(\lambda_1, \lambda_0) \cong \left| 4\pi \left[\frac{(\lambda_1 - \lambda_0)^2}{2! \lambda_1} \right] \Delta(\lambda_0) \right| \leq 2\pi \quad \text{Eq. 5-14}$$

which yields

$$(\lambda_1 - \lambda_0)^2 \leq \frac{\lambda_1}{|\Delta(\lambda_0)|} \quad \text{Eq. 5-15}$$

Substitution of this result into Eq. 5-11, with $m=2$ and $n=1$, and given the condition that $(\lambda_2 - \lambda_0) \ll \lambda_0$, the result simplifies to

$$(\lambda_2 - \lambda_0) < \left(\frac{3}{2} \frac{\lambda_0}{|\Delta(\lambda_0)|} \right)^{1/2} \quad \text{Eq. 5-16}$$

Substitution of Eq. 5-16 to Eq. Eq. 5-13 gives

$$B_{min} \cong \left(\frac{6\lambda_0}{|\Delta(\lambda_0)|} \right)^{1/2} \quad \text{Eq. 5-17}$$

where increasing $|\Delta(\lambda_0)|$ (via the simulated dispersion of the dispersive virtual reference in Eq. 5-12) reduces the minimum bandwidth. The measurable bandwidth B_{Meas} of the dispersion plot is therefore given by

$$B_{Meas} \cong B_{source} - B_{min} \quad \text{Eq. 5-18}$$

which also increases as B_{min} decreases. An important result of Eq. 5-12 and Eq. 5-17 is that an arbitrarily large $D_v(\lambda_0)L_v$ may be selected (simulated) to ensure that $|\Delta(\lambda_0)|$ is large enough so that $B_{min}(\lambda_0)$ is less than the bandwidth of the source (scan). The reduction in $B_{min}(\lambda_0)$ is referred to as *compression* of the interferogram. Note that since the sign of $\Delta(\lambda_0)$ is unknown, there are two possibilities for the value of $D_f(\lambda_0)L_f$. However, by comparing the second-order interferograms produced using both positive $D_v(\lambda_0)L_v$ and negative $D_v(\lambda_0)L_v$, one can easily remove this ambiguity. This section considered the effect that $|\Delta(\lambda_0)|$ has on the ability to compress

$B_{\min}(\lambda_0)$. The next section considers the design for the dispersive reference itself and how it may be used to measure first and second order dispersion.

5.2.2 Design of a dispersive virtual reference

The design of a dispersive virtual reference involves the development of mathematical expressions for the effective refractive index \times length, virtual group index \times length and virtual second order dispersion parameter \times length of the virtual reference for use in Eq. 5-2, Eq. 5-6, Eq. 5-11 and Eq. 5-12. There are many possibilities for the design of a dispersive virtual reference, however, the simplest designs using low order polynomials are considered in the sections that follow. The design of a dispersive reference may begin with an expression for the virtual effective refractive index \times length, from which the virtual group index \times length and virtual second order dispersion parameter \times length may be derived, or it may begin with an expression for the virtual group index \times length, from which the virtual effective refractive index \times length and virtual second order dispersion parameter \times length may be derived. In the following sections both approaches will be used and the simplest design will be chosen.

5.2.2.1 Design via the effective index

The goal in this approach is to develop the lowest order polynomial description for the virtual effective refractive index \times length but ensure that the expression for the virtual second order dispersion parameter \times length will not be zero (since it is obtained by second order derivative with respect to wavelength). For this to be the case, the lowest order polynomial that can be used in the expression for the virtual effective refractive index \times length is a second order quadratic polynomial as described by

$$n_{\text{eff}_v}(\lambda)L_v(\lambda) = Q(\lambda - r)^2 + s \quad \text{Eq. 5-19}$$

where Q , r and s are parameters of the polynomial used in the design of the dispersive virtual reference. This results in an expression for the group index \times length given by

$$N_{g_v}(\lambda)L_v = \left[n_{\text{eff}_v}(\lambda) - \lambda \frac{dn_{\text{eff}_v}}{d\lambda} \right]_{\lambda} L_v = -Q(\lambda^2 - r^2) + s \quad \text{Eq. 5-20}$$

Since Eq. 5-20 is a second order polynomial, this type of reference is known as a *second order dispersive reference*. It also has a second order dispersion \times length that is described by a first order polynomial as shown in

$$D_v(\lambda_0)L_v(\lambda_0) = \frac{1}{c} \frac{dN_{g_v}}{d\lambda} \Big|_{\lambda_0} L_v(\lambda_0) = -\frac{2Q\lambda_0}{c} \quad \text{Eq. 5-21}$$

Although this design may be used to model the dispersive virtual reference, it is not the simplest (lowest order polynomial) description. The next section considers the possibility of developing a simpler design by starting with a first order polynomial expression for $N_{g_v}(\lambda)L_v$.

5.2.2.2 Design via the group index

This section considers the possibility of developing a simpler *first order dispersive reference* in which the group index \times length is described by a first order polynomial

$$N_{g_v}(\lambda)L_v = K(\lambda - a) + b \quad \text{Eq. 5-22}$$

The constants K , a and b are parameters of the polynomial used in the design of the dispersive virtual reference, where K is a unitless parameter and b and a are expressed in meter units. This description makes the expression for the second order dispersion \times length constant as a function of wavelength

$$D_v(\lambda)L_v = \frac{1}{c} \frac{dN_{g_v}(\lambda)L_v}{d\lambda} = \frac{K}{c} \quad \text{Eq. 5-23}$$

The extraction of an expression for $n_{eff_v}(\lambda_0)L_v(\lambda_0)$, however, involves solving the first order differential equation

$$N_{g_v}(\lambda)L_v = \left[n_{eff_v}(\lambda) - \lambda \frac{dn_{eff_v}}{d\lambda} \right]_{\lambda} L_v = K(\lambda - a) + b \quad \text{Eq. 5-24}$$

The solution is obtained by re-writing the equation in standard form

$$\frac{dn_{eff_v}}{d\lambda} \Big|_{\lambda} - \frac{1}{\lambda} n_{eff_v}(\lambda) = -\frac{1}{\lambda} N_{g_v}(\lambda) \quad \text{Eq. 5-25}$$

where the solution is found by multiplying both sides by an integrating factor $\mu = 1/\lambda$

$$\frac{1}{\lambda} \frac{dn_{eff_v}}{d\lambda} \Big|_{\lambda} - \frac{1}{\lambda^2} n_{eff_v}(\lambda) = -\frac{1}{\lambda^2} N_{g_v}(\lambda) \quad \text{Eq. 5-26}$$

and using the chain rule to collect terms on the left hand side

$$\frac{1}{\lambda} \frac{dn_{eff_v}}{d\lambda} \Big|_{\lambda} - \frac{1}{\lambda^2} n_{eff_v}(\lambda) = \frac{d}{d\lambda} \Big|_{\lambda} \left[\frac{n_{eff_v}(\lambda)}{\lambda} \right] \quad \text{Eq. 5-27}$$

gives

$$\frac{d}{d\lambda} \Big|_{\lambda} \left[\frac{n_{eff_v}(\lambda)}{\lambda} \right] = -\frac{1}{\lambda^2} N_{g_v}(\lambda) \quad \text{Eq. 5-28}$$

Integrating both sides

$$n_{eff_v}(\lambda) = \frac{\int -\frac{1}{\lambda^2} N_{g_v}(\lambda)}{1/\lambda} \quad \text{Eq. 5-29}$$

Multiplying both sides by L_v

$$n_{eff_v}(\lambda)L_v = \frac{\int \left(-\frac{1}{\lambda^2} N_{gv}(\lambda)L_v \right) d\lambda}{1/\lambda} \quad \text{Eq. 5-30}$$

Substitution of Eq. 5-24 into Eq. 5-30 gives

$$n_{eff_v}(\lambda)L_v = \frac{\int \left(-\frac{1}{\lambda^2} (K(\lambda - a) + b) \right) d\lambda}{1/\lambda} \quad \text{Eq. 5-31}$$

The solution is

$$n_{eff_v}(\lambda)L_v = -K\lambda \ln|\lambda| - Ka + b + C\lambda \quad \text{Eq. 5-32}$$

where C is an arbitrary constant due to the indefinite integral in Eq. 5-31. The value of this constant is not important as it is not a factor in the group index (cancelled out in the group index expression). For simplicity setting $C = 0$ the solution simplifies to

$$n_{eff_v}(\lambda)L_v = -K\lambda \ln|\lambda| - Ka + b \quad \text{Eq. 5-33}$$

Although the expression for the effective index \times length may seem somewhat artificial due to the $\lambda \ln|\lambda|$ dependence it produces the lowest order dispersive reference in the group index \times length. The expression in Eq. 5-33 may be used to determine the propagation constant in Eq. 5-2 using the relation

$$\beta_v(\lambda)L_v = k_0 n_{eff_v}(\lambda)L_v \quad \text{Eq. 5-34}$$

where k_0 is the propagation constant in free space. Since the expressions developed in this section result in the lowest order (first order) and therefore simplest dispersive reference this model is the one that will be used throughout this chapter. The next section graphically illustrates the role of the constants K , a and b used in this model.

5.2.3 Role of the parameters of the dispersive reference

The parameter K in Eq. 5-22 determines the slope of the $N_{gv}(\lambda)L_v$ curve and since $D_v(\lambda)L_v$ is derived from the slope of $N_{gv}(\lambda)L_v$; it also directly sets the value of $D_v(\lambda)L_v$ in Eq. 5-23. The parameters a and b are used in conjunction in Eq. 5-22 to set the value $N_{gv}(\lambda)L_v$ at a specific wavelength, such that $N_{gv}(\lambda)L_v = b$ when $\lambda = a$. To ensure that $N_{gf}(\lambda)L_f$ is balanced by $N_{gv}(\lambda)L_v$ at some wavelength *within* the available spectral bandwidth the parameter a is chosen such to be the centre of the scan range such that $a = (\lambda_{\min} + \lambda_{\max})/2$. An estimate for the value of b that balances the test path at a may be found using $b = N_{gv}(a)L_v = N_{gf}(a)L_f \cong a^2/2T_{avg}(a)$, as described in [50] [49] and in [Chapter 3](#) (using Eq. 3-4). The effect of compression, achieved by using a dispersive virtual reference, is visualized by the two interferograms shown in Fig. 5-2. It demonstrates how the use of a

dispersive virtual reference with $K < 0$ compresses the interferogram, compared to using a non-dispersive reference where $K = 0$.

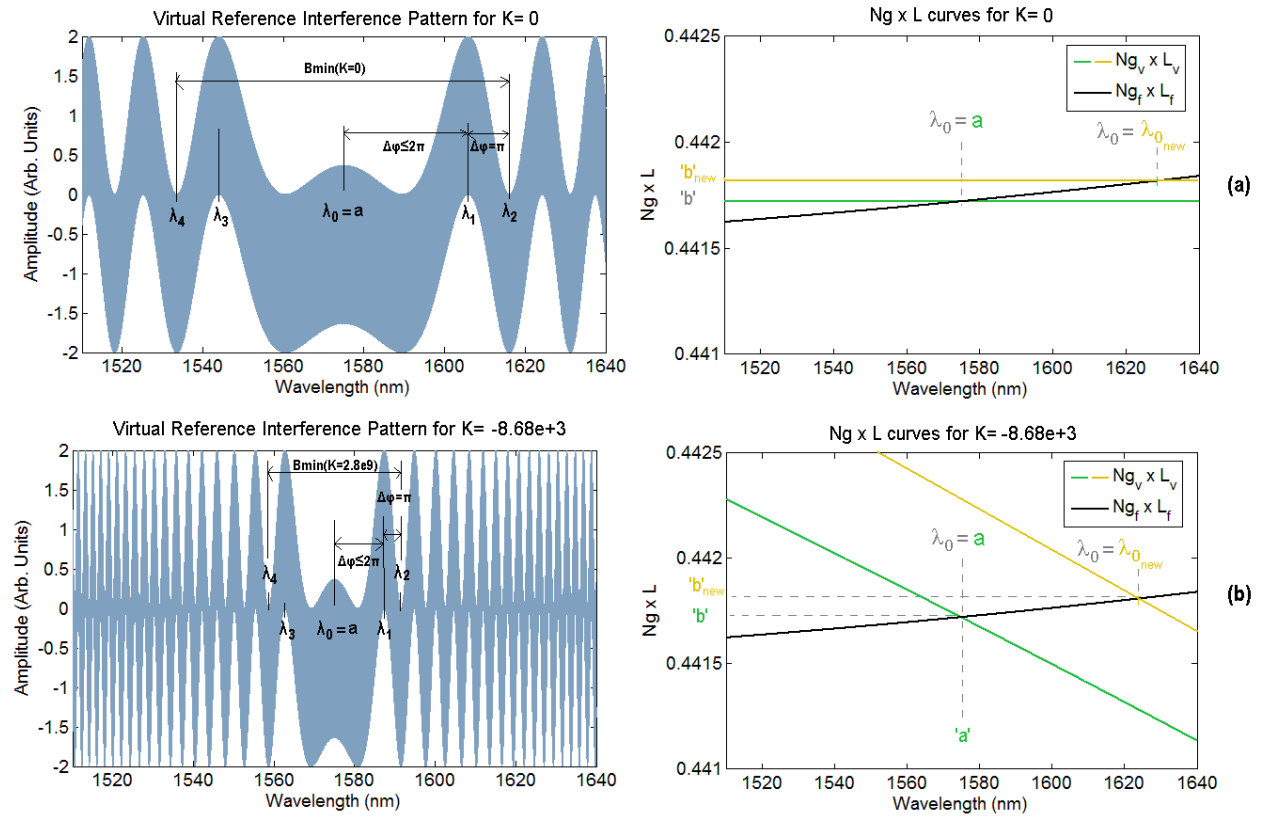


Fig. 5-2. Plot of the dispersive virtual reference interferograms and group index \times length curves for (a) $K=0$ (VRI with a non-dispersive reference) and (b) DVRI using $K=-8.68e+3$. Two $N_{gv}(\lambda)L_v$ curves are superimposed to show the curves that generate intersections at $\lambda_0 = a$ and $\lambda_0 = \lambda_{0\text{new}}$. Adapted (re-colored) with permission from [67].

The balance point (location of λ_0) in the second order interference pattern corresponds to the intersection point between the $N_{gv}(\lambda)L_v$ curve and the $N_{gf}(\lambda)L_f$ curve. At the intersection the condition $N_{gv}(\lambda_0)L_v = N_{gf}(\lambda_0)L_f$ occurs. The group delay plots in Fig. 5-2 show two superimposed $N_{gv}(\lambda)L_v$ curves to illustrate balancing at $\lambda_0 = a$ (interferogram shown for this case) and $\lambda_0 = \lambda_{0\text{new}}$. The two $N_{gv}(\lambda)L_v$ curves demonstrate how λ_0 may be varied by changing the value of b in Eq. 5-22 to some new value (i.e. b_{new}) so that the first order dispersion (group delay or group index \times length) may be plotted by sweeping the value of b and tracking λ_0 . Another important observation is that the difference in the slope of the curves at the intersection point is directly proportional to the magnitude of the compression given by $|\Delta(\lambda_0)|$ and controlled by $D_v(\lambda_0)L_v$ in Eq. 5-12. The second order dispersion of the fiber may be extracted directly from the interference pattern in Fig. 5-2 by solving for $|\Delta(\lambda_0)|$ in Eq. 5-11 using a peak/valley pair (with known phase separation) on each side of λ_0 (i.e. λ_2 and λ_1 as

well as λ_4 and λ_3) to generate a system of equations using Eq. 5-11. After solving for $|\Delta(\lambda_0)|$, the second order dispersion may then be extracted by combining Eq. 5-12 and Eq. 5-23 given $\text{sgn}(D_v(\lambda_0)L_v) = -\text{sgn}(K)$ (where sgn determines if the sign is positive or negative) and assuming $|D_v(\lambda_0)L_v| > |D_f(\lambda_0)L_f|$, the result is

$$D_f(\lambda_0)L_f = \frac{1}{c}(K - \text{sgn}(K)|\Delta(\lambda_0)|\lambda_0) \quad \text{Eq. 5-35}$$

5.2.4 Cost of using a dispersive reference: VRI vs. DVRI

It is important to note the cost of using a dispersive virtual reference. A comprehensive theoretical discussion and analysis is provided in [Appendix D](#) whereas this section only summarizes the conclusions. [Appendix D](#) shows that since the use of a dispersive virtual reference makes the slope to the simulated group delay curve non-zero (it is zero in VRI, as shown in Fig. 5-2), any uncertainty in the wavelength measurement of the balance point results in an uncertainty in the simulated group delay. The uncertainty in the group delay is proportional to the slope of the group delay curve (i.e. the second order dispersion) of the dispersive virtual reference at the balance point (intersection in Fig. 5-2). Therefore, the cost of using a dispersive virtual reference to the measurement of the first order dispersion is an increase in the uncertainty in the absolute magnitude of the group delay, compared to standard non-dispersive VRI.

The cost of using a dispersive virtual reference for the measurement of second order dispersion, however, is slightly more complicated. If a first order dispersive reference is used, [Appendix D](#) shows that there is no additional uncertainty in the second order dispersion measurement compared to VRI. However, if a second order (or higher) dispersive reference is used, then there is increased uncertainty in the second order dispersion measurement compared to VRI. This means that it is advantageous to use a first-order dispersive reference when using DVRI to measure second order dispersion.

Ultimately, DVRI is useful for enabling measurements that would otherwise be impossible (by compressing the interference so that the minimum bandwidth is less than that of the source); however using a dispersive reference increases the uncertainty in the group delay measurement. Therefore, if using DVRI is not necessary, the group delay can be measured with greater certainty by using VRI. However, if the objective of a particular experiment is to characterize the second order dispersion and the group delay is of no interest, then either VRI or DVRI (with a first order dispersive reference) will provide equivalent accuracy.

5.3 Experiments

This section demonstrates two practical applications of dispersive virtual reference interferometry. The technique is first validated by measurement of a dispersion standard and then it is used to make measurements that would not be possible using standard VRI or BSI with the given spectral bandwidth of the source. The experimental setups used to generate a real interference pattern in standard fibers and polarization maintaining gain fibers are illustrated in Fig. 5-3(a) and Fig. 5-3(b), respectively. In each experiment a tunable laser (Agilent 81600B Option 160 or 200), connected to port 1 of a fiber optic circulator, is swept continuously over a given bandwidth (experiment dependent) at 10 nm/s while an optical detector (attached to a data acquisition card), connected to port 3 of a fiber optic circulator, samples the signal at 100 kHz. The tunable laser has a built-in wavelength meter with a resolution of 0.1 picometers. It also has the capability to automatically calibrate wavelength measurements using a built-in gas cell. In both setups shown in Fig. 5-3, light is launched into the test fiber from an angled facet so that only one reflection is produced at the interface between the launch fiber and the front facet of the test fiber. An interference pattern is then generated using the reflections from the front and end facets of the fiber under test (FUT) and plotted as a function of wavelength via synchronization of the timing between wavelength and signal sampling. This common path interferometer setup is preferred to using a dual arm interferometer since it does not require calibration of the dispersion of the optical elements used in the (physical) reference path of these interferometer setups. Eliminating the need for calibration also removes the associated calibration error, making this configuration more accurate than a dual arm interferometer. Accuracy is especially important when the dispersion \times length of the fiber under test is low since the magnitude of the calibration error can exceed the magnitude of the measurement itself.

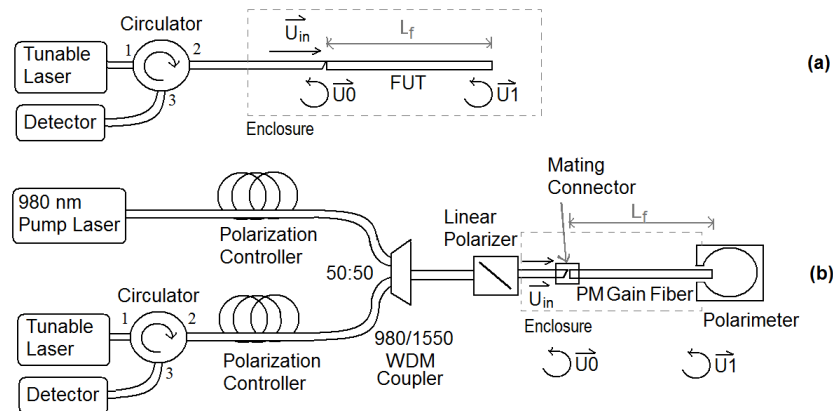


Fig. 5-3. Setup for dispersion measurement of (a) standard fibers (b) polarization maintaining gain fiber. Used with permission from [67].

Transmission-based, polarization-dependent gain measurements can be performed by converting the setup in Fig. 5-3(b) by replacing the polarimeter with a 980/1550 nm WDM coupler, and moving the detector from port 3 of the circulator to the 1550 nm side of the WDM coupler as illustrated in Fig. 5-4.

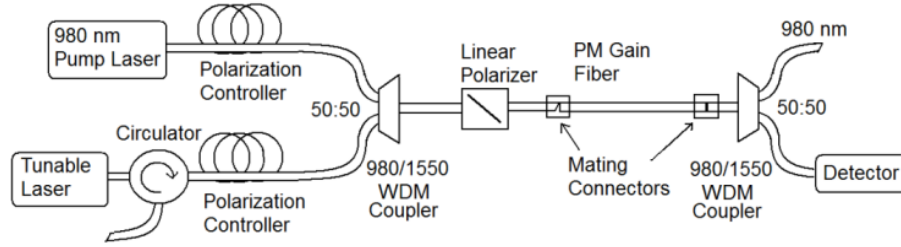


Fig. 5-4. Setup for the measurement of gain in PM (birefringent) gain fiber.

The gain for a given pumping condition is measured by comparing the intensity scan from the test fiber to a background measurement without the gain fiber and computed via

$$G(P, \lambda) = \frac{10 \log_{10} (I(P, \lambda) / I_{Background}(\lambda))}{L_f} \quad \text{Eq. 5-36}$$

Where P is the pump power, $I(P, \lambda)$ is the intensity plot of the gain fiber at a given pump power, $I_{Background}(\lambda)$ is the intensity plot of the background measurement (with zero loss and pump off) and L_f is the length of the gain fiber.

5.3.1 Experimental validation of theory

The first experiment in this chapter provides experimental validation of the theory previously developed for DVRI. The validation is performed via comparison to measurements on standard fiber (SMF28) to results produced via VRI (previously validated in [50] and in previous chapters). The results are also compared to the manufacturer's specification (simulated curves). The setup used in this experiment is shown in Fig. 5-3(a). This tunable laser used was an Agilent 81600B Option 200 tuned from 1440nm to 1640nm. The wide bandwidth is required for this validation experiment so that standard (non-dispersive) VRI may be used to characterize the fiber over a wavelength range sufficient for comparison. The results of the comparison illustrated in Fig. 5-5 indicate excellent agreement between both techniques and the manufacturer's specification. The accuracy of the DVRI measurements, defined by the standard deviation of the measured group delay and dispersion \times length plots, with respect to simulations based on the manufacturer's specification [68], was found to be 2.7×10^{-3} ps and 5.2×10^{-5} ps/nm, respectively. Note that the maximum deviation from the specification of the group delay and dispersion \times length points within the measurement range was 4.9×10^{-3} ps and 8.6×10^{-5} ps/nm, respectively. The precision of the group delay measurement, defined as the standard deviation of the measured points with respect to a second order polynomial fit was found to be 9×10^{-4} ps. The precision of the dispersion \times length measurement, defined as the standard deviation of the measured points with respect to a linear fit was found to be 1.9×10^{-5} ps/nm. The dispersion slope (found from a linear fit to the dispersion \times length curves) was found to be 4.7×10^{-2} ps/nm²·km in both the VRI and DVRI measurement compared to 5.5×10^{-2} ps/nm²·km in the simulation. The results in Fig. 5-5 illustrate that the wavelength range over which dispersion measurements may be achieved may also be increased by using DVRI.

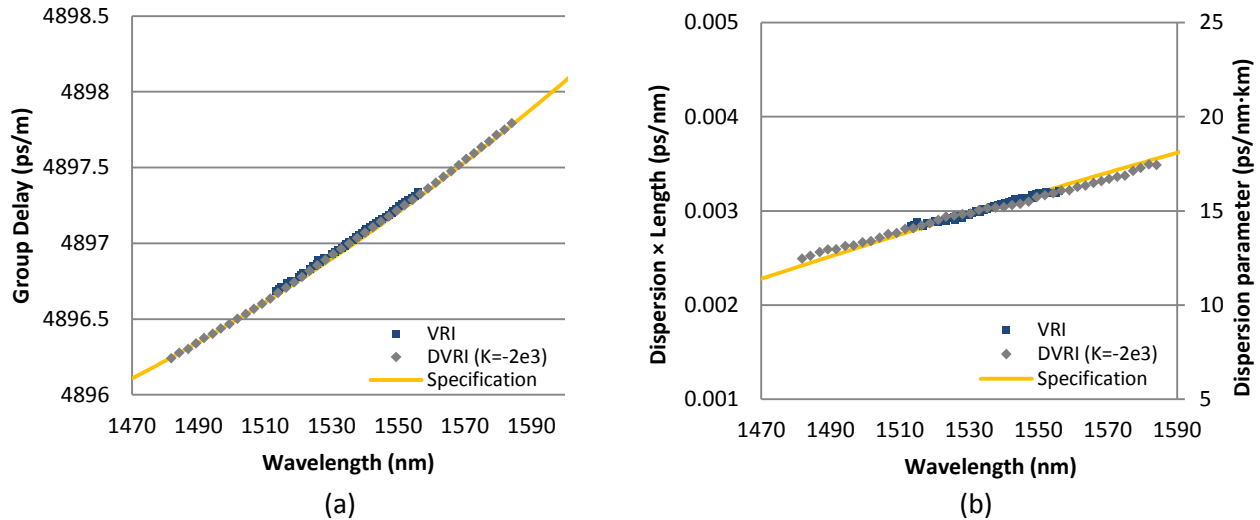


Fig. 5-5. Measurements of (a) group delay and (b) dispersion parameter on a 20 cm length of SMF28 using VRI and DVRI ($K=-2e+3$). Adapted (re-colored, secondary axis added to (b)) with permission from [67].

5.3.2 Characterization of gain fiber

The second experiment in this chapter demonstrates the generation of results that would be impossible for standard (non-dispersive) VRI and BSI. The experiment is a demonstration of DVRI for the characterization of both polarization modes in a 23.3-cm length of polarization maintaining erbium doped gain fiber, as a function of pump power, using the setup in Fig. 5-3(b). This fiber has a low second-order dispersion parameter (less than half that of SMF28) and the loss in the unpumped fiber limits the length that can be characterized. As a result, the total DL product of the test fiber in this experiment was 0.0012 ps/nm. Using Eq. 5-17, this measurement would require over 200 nm of bandwidth, far exceeding the 145 nm bandwidth of the source used in this experiment (Agilent 81600B option 160). This measurement would not be possible without using a dispersive reference to compress the interference pattern and ensure that the minimum bandwidth required is less than the bandwidth of the source. In the experimental setup shown in Fig. 5-3(b) the output of a 980nm pump laser (Lumics LU0980M500) is coupled via a WDM coupler to the output of port 2. Since this gain fiber is birefringent, both signal and pump power must be coupled to one polarization mode at a time using polarization controllers and a linear polarizer at the output of the WDM coupler. The linear polarizer used is broadband with an extinction ratio greater than 20 dB for both 980 and 1550 nm light. The polarization of the light launched into the birefringent gain fiber is controlled by rotating the polarizer at the launch side of the polarization maintaining gain fiber and observed using a polarimeter (PAT 9000) to ensure that light is coupled to one polarization mode at a time. The polarization controllers are adjusted to maximize the power from the tunable laser and the pump laser at the output of the linear polarizer. For each polarization mode and pump (gain) setting, the tunable laser (Agilent 81600B Option 160) is tuned from 1495nm to 1640nm and the detector samples the signal. Dispersion measurements are then performed from the sampled signal using DVRI. Following the completion of the dispersion measurements at various pump powers for a given polarization mode, the gain measurement is performed by converting the setup from that shown in Fig. 5-3(b) to that shown in Fig. 5-4 by replacing the polarimeter with a WDM to filter out the pump light and connecting the detector

to the signal port of the WDM. The dispersion and gain measurements may then be repeated for the other polarization mode. The results of the gain and group delay measurements are shown in Fig. 5-6(a) and Fig. 5-6(b), respectively. The standard deviation of the measured group delay curves with respect to a sixth order polynomial fit was found to be on the order of 10^{-3} ps for all curves. The results of dispersion parameter measurements obtained by differentiation of the sixth order polynomial fit to the group delay curves are illustrated in Fig. 5-7. In general, it is expected that the first and second order dispersion will change in the gain region, since a change in absorption (or gain) is associated with a change in refractive index through the Kramers-Kronig relations. Furthermore, the general shape of the curves in Fig. 5-6 and Fig. 5-7 and consistent with the curves obtained in [17] for erbium doped fiber.

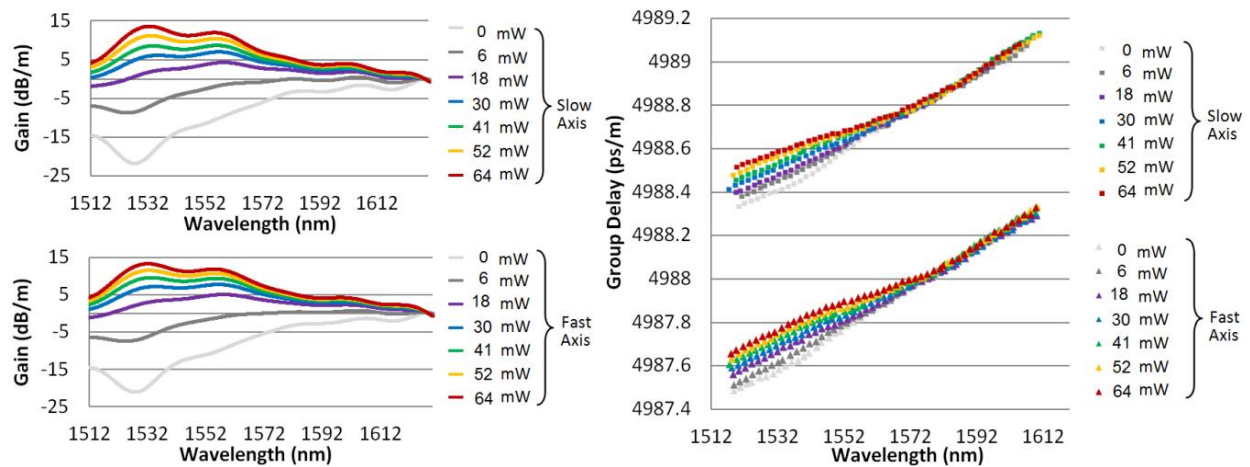


Fig. 5-6. (a) Gain and (b) group delay curves for a 23.3 cm length of erbium doped PM gain fiber pumped at 980 nm at various pump power conditions for both fast axis and slow axis measured using DVRI ($K=7.75e+3$). Adapted (re-colored) with permission from [67].

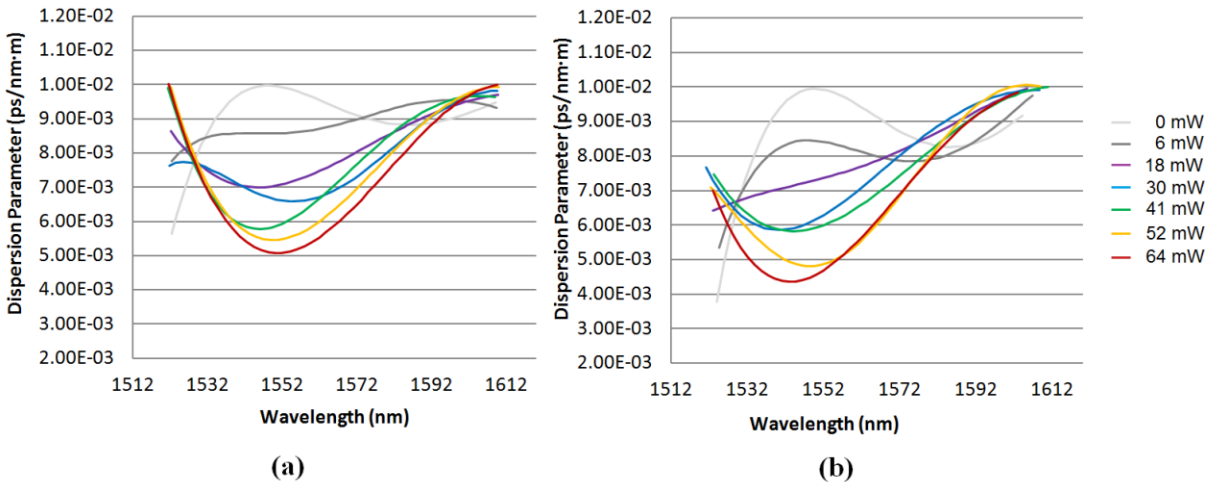


Fig. 5-7. Dispersion parameter curves for a 23.3 cm length of erbium doped PM gain fiber pumped at 980 nm for both (a) fast and (b) slow axes at various pump power conditions measured via DVRI ($K=7.75e+3$). Adapted (re-colored) with permission from [67].

5.3.3 Characterization of dispersion shifted fiber

The last experiment in this chapter pushes the DVRI technique to the limit by characterizing a 28.6-cm length of dispersion shifted fiber (DSF), using the setup in Fig. 5-3(a), across the zero-dispersion region using a limited bandwidth of 145nm. The tunable laser used is the Agilent 81600B Option 160 tuned from 1495nm to 1640nm. Measured group delay curves are shown in Fig. 5-8(a) and dispersion parameter curves (found using Eq. 5-35) are provided in Fig. 5-8(b). The standard deviation of the measured group delay points with respect to a third order polynomial fit was found to be 1.4×10^{-3} ps. The standard deviation of the measured second order dispersion \times length points with respect to a linear fit was found to be 4.0×10^{-5} ps/nm. Since the zero-dispersion wavelength and the dispersion slope (slope of the dispersion parameter) is of interest for DSF it is also measured in this experiment. After inversion of the axes in Fig. 5-8(b) followed by a linear fit, a linear regression analysis gives the zero-dispersion wavelength as 1566.7 nm (consistent with the zero-dispersion wavelength specification provided by the manufacturer) with a precision of ± 0.2 nm and the dispersion slope as 8.57×10^{-5} ps/(nm²·m) with a precision of $\pm 0.06 \times 10^{-5}$ ps/(nm²·m). These measurements would not be possible given the bandwidth of this laser without the use of a dispersive reference since $\Delta(\lambda_0) = 0$ in Eq. 5-17 at the zero dispersion wavelength. It should be noted that although it is not critical to characterize DSF on short length, this experiment demonstrates that using DVRI it is possible to characterize second order dispersion that is as low as zero. Furthermore, one of the goals of this experiment was to directly measure the zero-dispersion wavelength and the second order dispersion in the region of the zero-dispersion wavelength, as this is important in several applications (e.g. nonlinear and quantum optics applications) where although the dispersion is small, it must still be compensated.

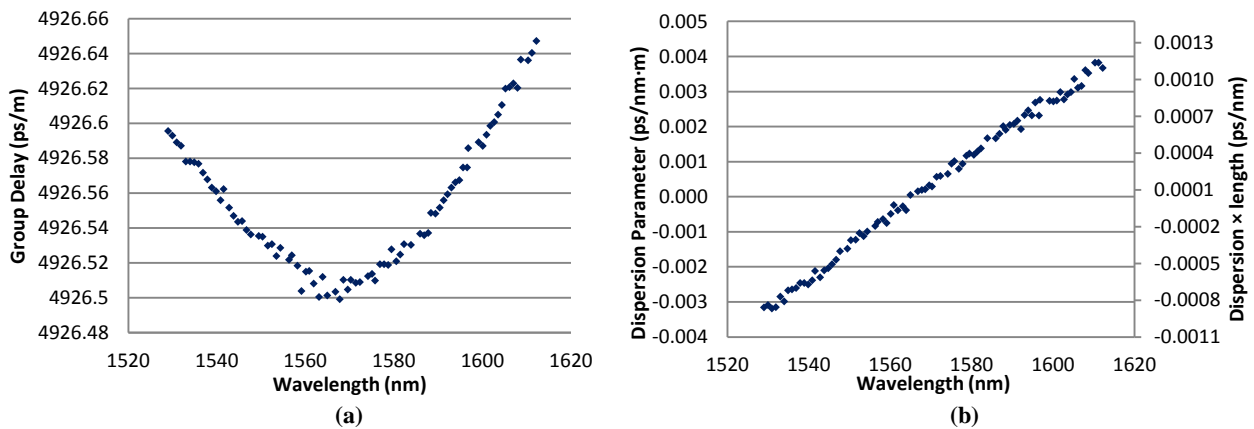


Fig. 5-8. Measurements of (a) group delay (b) dispersion parameter on a 28.6 cm length of dispersion shifted fiber via direct measurement using DVRI ($K=-8e+3$). Adapted (re-colored) with permission from [67].

5.4 Conclusion

The theory of dispersive virtual reference interferometry for the characterization of short length (<1m) low dispersion fiber is introduced and demonstrated in this chapter. The use of a dispersive virtual reference allows for compression of the interferogram which enables measurements that would otherwise not be possible with the available bandwidth using standard techniques that do not employ a dispersive reference. This technique is useful for characterizing fibers with low (or zero) second order dispersion \times length by enabling the compression of the interference pattern. The compression achieved using this technique is superior to that presented in [Chapter 3.3.1](#) since there is no associated reduction in interference fringe contrast. Compression of the interferogram has the additional benefit of enabling the generation of dispersion plots over a wider spectral range. The use of a dispersive virtual reference extends the flexibility, versatility and practical utility of the virtual reference technique.

Chapter 6.

Low-coherence virtual reference interferometry

This chapter presents the adaptation of Virtual Reference Interferometry (VRI) for use in a low coherence setup (low cost) to characterize dispersion in short-length fiber. When used in a low coherence setup, the technique is referred to as low-coherence virtual reference interferometry (LC-VRI) [69]. A low coherence setup consists of a broadband LED source (low coherence) and a low resolution spectrometer or spectrum analyzer. The LC-VRI technique is shown to be a simple and convenient alternative to balanced spectral interferometry (BSI), capable of measuring both first and second order dispersion directly from the interference pattern. The main advantage of using LC-VRI instead of BSI is that full characterization can be performed from a single spectral scan (high speed measurement), without the need for a precision variable delay line in the reference path (reduced cost). The LC-VRI technique is demonstrated by characterizing the dispersion in a dispersion standard (SMF28 fiber) and the results are compared to both the manufacturer's specifications and to measurements obtained using BSI. The standard deviation of the first and second order dispersion is found to be on the order of 10^{-3} ps and 10^{-4} ps/nm respectively for both BSI and LC-VRI.

6.1 Introduction & motivation

Spectrometers and broadband LED light sources can be useful low-cost tools for characterizing chromatic dispersion in short length (<1m) optical fibers via low-coherence spectral interferometry [29] [13] [30] [41] [48]. In low-coherence spectral interferometry, light from a broadband LED source is separated into two paths; a reference path for which the dispersion is known and a test path with unknown dispersion properties. When the light waves from the two paths are recombined, a spectral interference pattern that contains information about the difference in dispersion between the test and reference path is produced. The resolution required to adequately sample the interference pattern, however, is inversely proportional to the path length (group delay) difference between the two paths, since the period of the interference pattern decreases as the path length difference increases. As a result, a spectrometer with limited resolution can only resolve the fringes when this difference is sufficiently small. In spectral interferometry, the group delay may either be balanced at a wavelength outside the measurement range or at a wavelength within the measurement range. When balanced outside the measurement range the technique is referred to as unbalanced spectral interferometry (USI) [29] [41] and when balanced within the measurement range the technique is referred to as balanced spectral interferometry (BSI) [13] [30] [48]. In order to reduce the resolution required of the spectrometer (or spectrum analyzer), both USI and BSI based techniques employing a low coherence setup require a variable delay line to closely match the test and reference paths (so that the period of the interference fringes can be resolved by an optical spectrum analyzer or spectrometer). For BSI, the advantage of using the delay line is that second order dispersion may be directly obtained from the interference pattern [13]. The disadvantages, however, include the need for multiple spectral scans to produce a dispersion plots (time consuming) and that a

precision translation stage (expensive) is required to vary the path length in small increments. For USI, the only advantage of using a delay line is that it reduces the path length (group delay) between the test and measurement paths, which leads to a reduction in the resolution required to adequately sample the spectral interference pattern. USI, however is capable of generating first order dispersion (group delay) plots from a single spectral scan (fast measurements). The disadvantage of USI, however, is that it cannot measure second order dispersion directly from the interference pattern but must extract it indirectly from a fit to the group delay plot. Virtual reference interferometry (VRI) was first introduced in [Chapter 3](#) to combine the single scan measurement capability of USI with the direct second order measurement capability of BSI. The VRI technique discussed in [Chapter 3](#) and [Chapter 4](#), and the DVRI technique discussed in [Chapter 5](#), used a common path interferometer configuration to characterize fibers several tens of centimeters in length. This configuration required high spectral resolution and broad bandwidth, which could only be achieved using a tunable laser with a built-in wavemeter. The tunable lasers used in these experiments had a wavelength resolution of 0.1pm. These tunable lasers may not always be available, they may not be available in the wavelength range of interest, or they may be too costly. As a result, this chapter describes how a VRI based measurement may be employed in a low coherence interferometry setup that does not require high wavelength resolution. For these situations, an alternate setup for VRI that employs a low coherence setup with a broadband source and spectrometer (or spectrum analyzer), is proposed in this chapter. The use of the VRI technique in a low coherence setup is referred to as low-coherence virtual reference interferometry (LC-VRI). In LC-VRI, instead of balancing the paths at a wavelength within the scan range, as in BSI, the paths are balanced at a wavelength *just* outside the measurement range (as in USI or VRI); close enough that the interference fringes may be resolved by a low resolution spectrometer (or spectrum analyzer) but far enough that the balance point is still outside the scan range. The use of the VRI technique in a low coherence setup involves the acquisition of an unbalanced spectral interference pattern, generation of a virtual interference pattern (produced by simulating a free space interferometer with a group delay imbalance equal to the imbalance of the physical interferometer), followed by point-by-point multiplication of the two interference patterns. This results in the generation of an amplitude-modulated second order interference pattern in which the phase of the amplitude modulation is equivalent to that produced by physical balancing in BSI. Since the balance wavelength depends on the length of the simulated imbalance, it may be varied computationally rather than physically to generate direct first and second order dispersion plots. This has the advantage of single scan characterization and eliminates the need for precision, micron-level control to adjust the path length between scans (as required by BSI), as discussed in [Chapter 3.4.4](#). This is possible since the reference path only has to be adjusted once to within approximately 1 mm of the test path. This chapter develops LC-VRI as a simple, convenient and low cost alternative to BSI for the dispersion characterization of short length fiber.

6.2 Theory

A typical setup used in low-coherence spectral interferometry for characterizing chromatic dispersion in short length optical fiber is presented in Fig. 6-1.

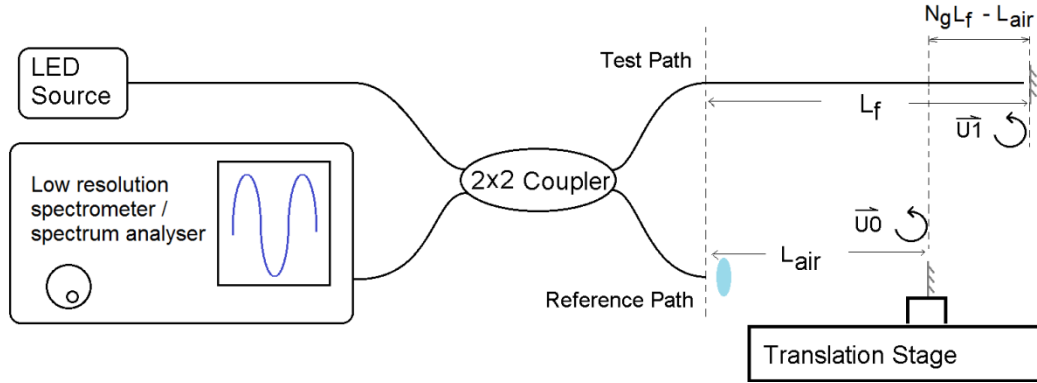


Fig. 6-1. Experimental setup for both a BSI and LC-VRI measurement. Adapted (re-colored) with permission from [69].

The interference pattern produced by the setup in Fig. 6-1 (for simplicity, assume the coupler arms are exactly equal in length so that the need for calibration is avoided) is described in Eq. 6-1.

$$I_{\text{Real}}(\lambda, \lambda_o) = |U0|^2 \left(2 + 2 \cos \left(2 \left(\beta_f(\lambda) L_f - k_o(\lambda) L_{\text{air}}(\lambda_o) \right) \right) \right) \quad \text{Eq. 6-1}$$

where L_f is the length of the test fiber, β_f is its propagation constant, L_{air} is the length of a free space (air) path and $k_o(\lambda)$ is the propagation constant in free space. The main difference between VRI, as described in the previous chapters, and LC-VRI is the degree of group delay imbalance between the arms of the interferometer (i.e. $N_g(\lambda_0)L_f - L_{\text{air}}$, where $N_g(\lambda_0)$ is the group index of the fiber at λ_0) between the test and reference path lengths (relative separation between the phase fronts $\bar{U}0$ and $\bar{U}1$) to allow for resolution of the interference pattern using a low resolution spectrometer. The real interference pattern is still produced by the phase fronts $\bar{U}0$ and $\bar{U}1$. In the setup in Fig. 6-1, the group delay in the test fiber may be balanced by that in the reference path at some point either within the spectral range scanned by the spectrometer (as in BSI) or somewhere near the spectral range scanned by a spectrometer (as in USI). In BSI the group delay in the test path is balanced by that of the reference path at a wavelength within the scan range (i.e. $N_g(\lambda_0)L_f - L_{\text{air}} = 0$ at the balance wavelength λ_0), resulting in the interference pattern shown in Fig. 6-2(a). Here, the first and second order dispersion of the test fiber may be extracted from the balanced spectral interference (BSI) pattern as described in [Chapter 2.4.2](#) (as well as in [13]). In LC-VRI the reference path length is chosen such that the test path is balanced at some wavelength just outside the scan range (partial balancing as in USI) to reduce the resolution requirements in the spectrometer by keeping $N_g(\lambda_0)L_f - L_{\text{air}}$ small. The relationship between the average period of the interference fringes and the degree of imbalance is given as $T_{\text{avg}}(\lambda_0) = \lambda^2 / 2 (N_g(\lambda_0)L_f - L_{\text{air}})$ so the interference fringes have a larger period that can be resolved by a low resolution spectrometer when the imbalance is small, as illustrated in Fig. 6-2(b). For example,

a spectrometer with a resolution of 0.2 nm is capable of adequately resolving and sampling the interference pattern produced by a path length difference between the test and reference path of $N_g(\lambda_0)L_f - L_{air} = 1$ mm.

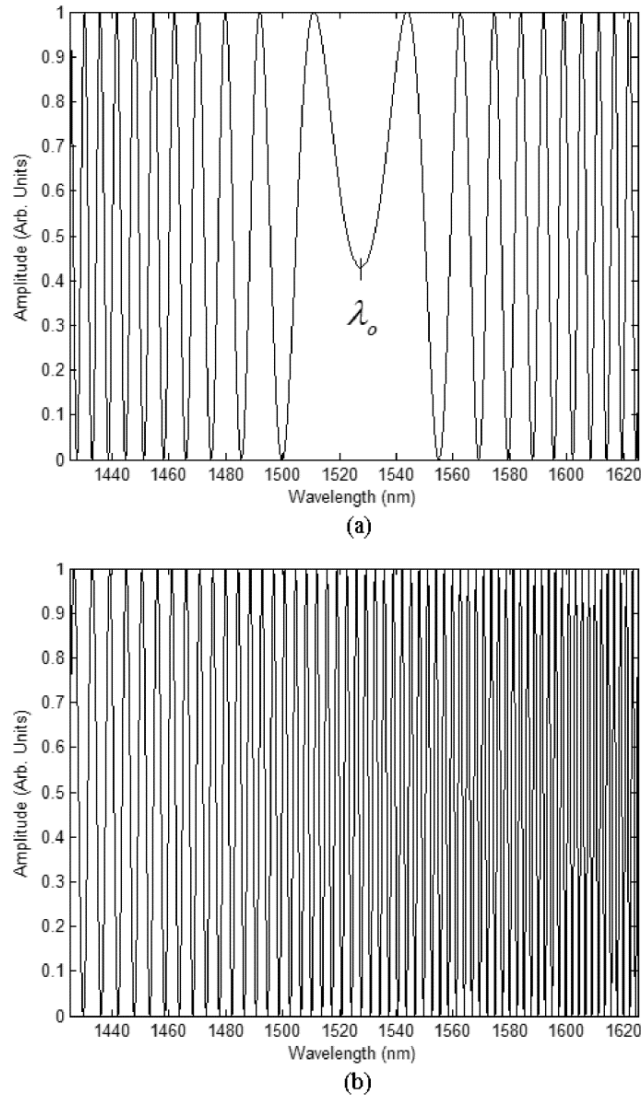


Fig. 6-2. Interference pattern produced in (a) BSI where the reference path length is chosen to balance the interferometer at a wavelength within the scan range (at 1525 nm) (b) USI and LC-VRI by choosing a reference path length that balances the interferometer at a wavelength outside (to the left of) the scan range. Used with permission from [69].

The following analysis assumes a reference path that is shorter than the test path and that the length of the reference path must be *physically* increased by an amount $\Delta L_v(\lambda_o) = N_g(\lambda_o)L_f - L_{air}$ to move the balance wavelength from a point outside the scan range to a point within it (if BSI was used). Furthermore, the wavelength λ_o is a wavelength within the scan range at which the test and reference arms may be balanced either physically or virtually. This balance point may be varied within the scan range by small changes to the value of $\Delta L_v(\lambda_o)$ to produce dispersion plots as a function of wavelength. In LC-VRI, the value of the interference pattern simulated by a virtual reference with length $\Delta L_v(\lambda_o)$ is given by

$$I_{virtual}(\lambda, \lambda_o) = \cos(2k_o(\lambda)\Delta L_v(\lambda_o)) \quad \text{Eq. 6-2}$$

Point-by-point multiplication of the interference pattern in Eq. 6-1 with the simulated interference pattern in Eq. 6-2 produces a second order interference pattern illustrated in Fig. 6-3 with an amplitude modulation described by

$$I_{\text{Amp.mod}}(\lambda, \lambda_o) = \cos(2(\beta_f(\lambda)L_f - k_o(\lambda)(L_{air} + \Delta L_v(\lambda_o)))) \quad \text{Eq. 6-3}$$

The amplitude modulation in the second order interference pattern has a phase that is equivalent to that produced by physical balancing in BSI. This can be seen by examination of the first order interference pattern produced by BSI shown in Fig. 6-2(a) and observing that it is equivalent to the amplitude modulation on the second order interference pattern in Fig. 6-3. The amplitude modulation can be extracted from the second order interference pattern via a low-pass filter. The advantage of the LC-VRI technique over BSI is that since $\Delta L_v(\lambda_o)$ is simulated its value may be varied computationally (by any arbitrarily small amount) to sweep the location of the balanced wavelength of the amplitude modulation λ_o across various wavelengths within the scan range. Therefore, using a single spectral scan (Eq. 6-1), BSI equivalent results (direct measure of both first and second order dispersion) may be produced (by varying $\Delta L_v(\lambda_o)$ in Eq. 6-2 and Eq. 6-3) without the need for high precision control of the reference path length (i.e. the reference path length can be incremented by an arbitrarily small amount to vary the balance point by small increments in the wavelength location, see [Chapter 3.4.4](#)). This both reduces experimental run time and eliminates the requirement for a high cost precision translation stage.

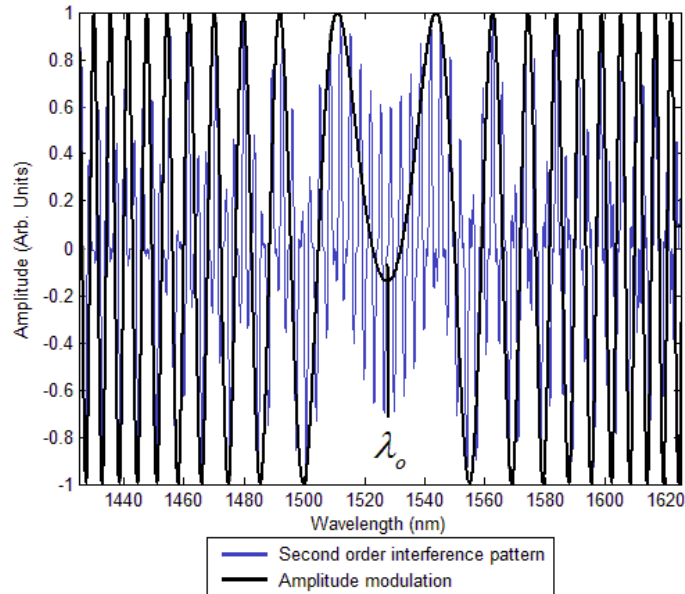


Fig. 6-3. Second order interference pattern produced by point-by-point multiplication of an interference pattern produced by an unbalanced interferometer with a virtual reference interference pattern produced by simulating a path length equal to the physical imbalance. The amplitude modulation (solid black line) is obtained by applying a low-pass filter to the second order interference pattern (solid grey line). The solid black line is equivalent to the interference pattern produced by BSI in Fig. 6-2(a). Adapted (re-colored) with permission from [69].

6.3 Experiment

The LC-VRI technique is validated experimentally by comparison of measurement results to BSI based dispersion measurements as well as to manufacturer's specifications (simulation). For this comparison LC-VRI and BSI are used to characterize a 73.5 cm-length of SMF28 fiber using the setup in Fig. 6-1. The physical length difference (group delay difference) between the test and reference paths (i.e. the phase fronts $\overline{U0}$ and $\overline{U1}$) from a balance at $\lambda_o = 1525$ nm is 0.7 mm. This enables adequate sampling of the interference pattern by the optical spectrum analyzer used in this experiment (ANDO AQ6317B) with a resolution setting of 0.2 nm, scanned between 1380 and 1670 nm. Alternatively, a low cost spectrometer with similar resolution [70] [71] could have been used, had it been available for this experiment. The LED source used in this experiment is the Agilent 83437A. The results of first and second order dispersion made using LC-VRI and BSI compared to the manufacturer's specification [68] are illustrated in Fig. 6-4(a) and Fig. 6-4(b). The standard deviation of the group delay (with respect to a second order polynomial fit) is 5.8×10^{-3} ps for the BSI plot and 5.6×10^{-3} ps for the LC-VRI plot. The standard deviation of the second order dispersion (with respect to a linear fit) is 1.4×10^{-4} ps/nm for the BSI plot and 1.1×10^{-4} ps/nm for the LC-VRI plot.

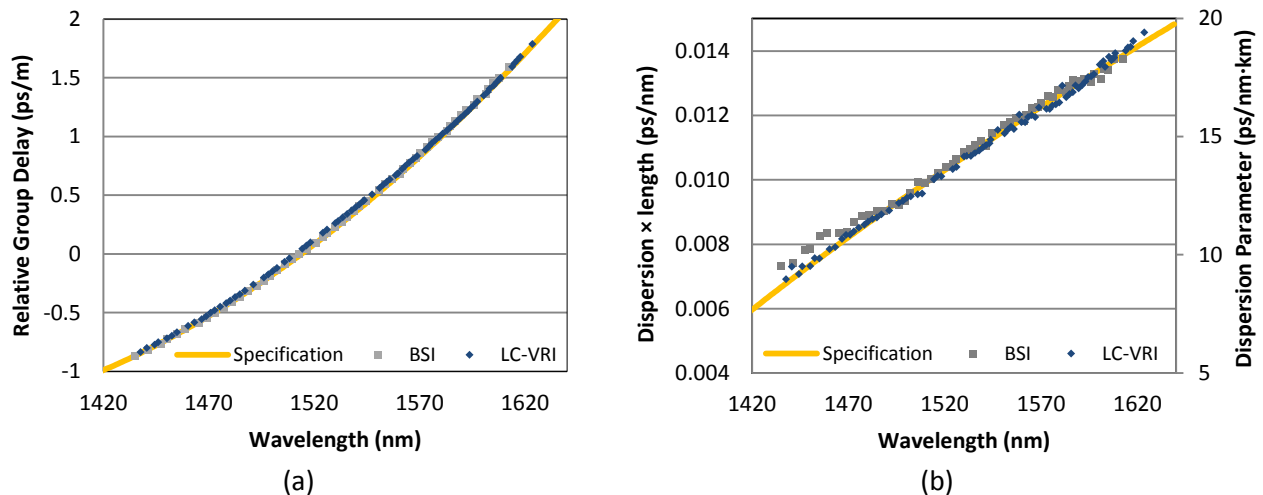


Fig. 6-4. (a) Group delay and (b) dispersion parameter measurements on a 73.5 cm length of SMF28. Results compare LC-VRI, BSI and simulations using the manufacturer's specification [7]. Adapted (re-colored, organized horizontally and secondary axis added to (b)) with permission from [69].

6.4 Conclusion

In this chapter, the LC-VRI technique is introduced as a simple and convenient alternative to BSI for fiber dispersion characterization. The advantages, compared to BSI, that were discussed include the ability to produce results of both first and second order dispersion from a single (physical) spectral scan, which reduces experiment run time, as well as eliminates the need for precision control of the reference path length (reducing the cost of the translation stage). This chapter illustrates how the VRI technique increases the practicality, versatility and utility of dispersion measurements produced in low-coherence interferometric setups.

Chapter 7.

Conclusions & future directions

This chapter concludes this thesis by discussing the academic and practical significance of the virtual reference technique. The chapter begins by considering the impact of the introduction of the idea that an *interferogram* can be used as a reference. It then discusses how this paradigm shift enables 'balanced' dispersion extraction techniques to be used to directly characterize first and second order dispersion on unbalanced spectral interferograms. This chapter then discusses the practical significance of the virtual reference to both common path and dual arm configurations. Furthermore, it discusses the impact of the virtual reference to both academia and industry and showcases the first commercial application of this technology in a commercial short length chromatic dispersion test system. This chapter also outlines the contribution of this work to the academic (accepted journal publications) and industrial literature (granted patents). The chapter concludes the thesis by looking forward to prospective future applications of this technology.

7.1 A paradigm shift - the interferogram as reference

The virtual reference technique is a hybrid between balanced spectral interferometry (BSI) and unbalanced spectral interferometry (USI) since the raw interference pattern is produced by USI but the dispersion extraction technique used is that of BSI. As discussed in [Chapter 2.4.2](#), balanced techniques (i.e. BSI, VRI, and DVRI) enable direct measurement of both first and second order dispersion by measuring the *difference* in the phase delay between a wave front in the test and the reference paths. This is done by interfering the two wave fronts with each other to produce an interferogram. The interferogram is an intensity profile that records the relative phase delay between the two wave fronts as a function of wavelength. Since the phase delay of the wave front in the reference path is known, it can be combined with the measured phase difference to extract the phase delay in the test path. This is the standard paradigm in which the reference is a *wave front with known phase delay*.

The goal of virtual reference interferometry is to eliminate the need for a reference path altogether, since variable delay lines are very difficult to construct and operate (as discussed in [Chapter 2.4.2](#)). However, since standard optical detectors can only measure the intensity of a wave front and are not sensitive to its phase, one cannot measure the phase of a test wave front and combine it with a simulated wave front to produce an interference pattern. The standard paradigm for the reference, therefore, cannot be used.

The virtual reference is a paradigm shift from the reference as a *wave front with known phase delay* to the reference as an *interferogram with a known phase delay difference*. The difference measurement recorded in the amplitude modulation of the virtual reference interferogram, therefore, is not the phase delay difference between the test and reference paths but the *second order difference* (i.e. difference of the difference) *of the phase delay* between the test and reference paths. Using this paradigm, interference patterns (which *can* be recorded using standard optical detectors) may be interfered with simulated interference patterns to produce second order interference patterns

(interference of interferograms) which results in an amplitude modulated interference pattern with a phase that gives the difference in the phase delay difference between the two paths. This capability is significant on a fundamental level, since it enables difference measurements (used in balanced spectral interferometry) to be used on an interference pattern produced with an unbalanced interferometer. The difference measurement based extraction techniques used in balanced spectral interferometry were shown to be superior to unbalanced techniques in [Chapter 2.4](#) because they can measure both first and second order dispersion directly from the interferogram and the resolution (scatter) is independent of the window size. This is now also possible for virtual referenced techniques.

7.2 A difference approach

Conventional techniques for extracting dispersion from an unbalanced spectral interference pattern (i.e. the USI based techniques discussed in [Chapter 2.4.1](#)) either attempt to extract the phase or the group delay directly using Fourier transform techniques. Since the techniques that attempt to measure the phase directly are highly susceptible to noise, techniques that attempt to measure the group delay directly are preferred. These techniques attempt to determine the single frequency sinusoid that *best fits* the measured interference pattern (within a window) using the Fourier transform

$$\hat{I}_{\text{Real}}(\nu) = \int I_{\text{Real}}(\lambda) e^{-j2\pi\nu\lambda} d\lambda \quad \text{Eq. 7-1}$$

and locating the frequency component with the largest amplitude. The problem with this approach, however, is that the raw unbalanced interference pattern is not a single frequency sinusoid but an aperiodic sinusoid with a phase that varies as a function of wavelength. Therefore, comparison with single frequency sinusoids will always have error since it *ignores the phase variation* of the raw unbalanced interferogram, as illustrated in Fig. 7-1(a). In virtual reference interferometry, however, the aperiodicity of the measured interference pattern is *used* to extract the phase information. This is done by multiplying the raw unbalanced interference pattern by a single aperiodic sinusoid (the virtual reference sinusoid) in which the phase varies (in a known manner) to produce an amplitude modulated interference pattern described by

$$I_{\text{Amp. Mod.}}(\phi(\lambda)) \propto \cos(\phi_{\text{measured}}(\lambda) - \phi_{\text{virtual reference}}(\lambda)) \quad \text{Eq. 7-2}$$

This enables the information about the phase difference $\phi_{\text{measured}}(\lambda) - \phi_{\text{virtual reference}}(\lambda)$ between the two paths to be directly extracted from the resulting amplitude modulation, as in Fig. 7-1(b).

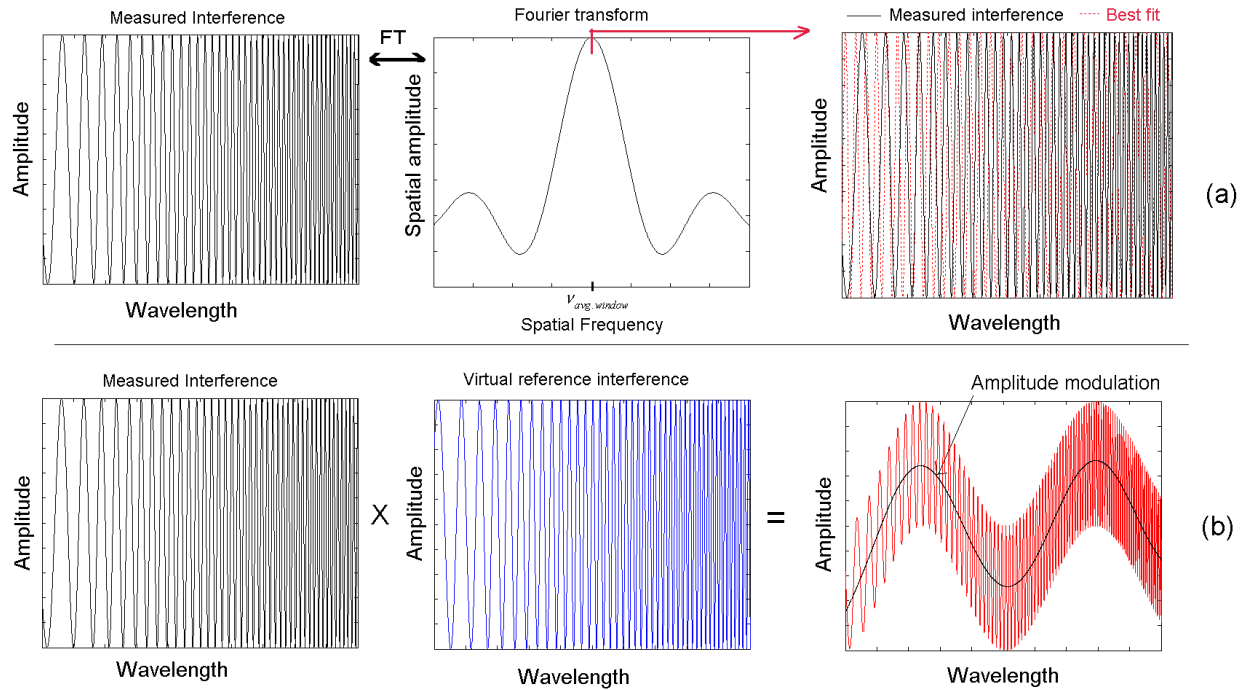


Fig. 7-1. Comparison of unbalanced techniques (which measure the degree of similarity or 'best fit' of the measured interference pattern to single frequency sinusoids, ignoring the phase variation) to virtual reference techniques that directly utilize the phase variation to directly measure phase difference (from the resulting amplitude modulation).

Therefore, where conventional unbalanced spectral interferometric techniques *ignore the phase (frequency) variation* of the raw interference pattern, virtual reference techniques *use the phase (frequency) variation* to make the measurement. The approach taken by unbalanced spectral interferometric techniques is therefore to measure the *degree of similarity* between the test and reference by finding the *best fit* whereas the approach taken in the virtual reference technique is to measure the *difference* directly. This approach (i.e. measuring difference directly) enables the direct measurement of second order dispersion, since the effect of the first order dispersion can be cancelled out by using a reference path with a first order dispersion equal to that in the test path. This cancelling of the first order dispersion leaves the second and higher order dispersion effects visible in the interferogram, so that they can be measured directly.

7.3 Practical significance

Origins

Virtual reference interferometry has its roots in a practical problem I encountered while working in industry. Before the concept of the virtual reference, the only way to directly (and most accurately) measure second order dispersion in short length fiber was to use BSI. The problem with using BSI, however, is the need for a physical reference path (see [Chapter 2.4.2](#)). At first, I had no concept of why this was such a difficult practical problem to solve. I thought that I could simply purchase a commercially available delay line. However, to my surprise, I discovered that there

were no fiber coupled optical delay lines with travel paths longer than a few centimeters. An optical delay line of a few centimeters was at least an order of magnitude too small to characterize fibers a few tens of centimeters long, so I had a problem.

The next option I considered was to see if an optical contract manufacturer could build one for me. So I decided to contact several of the small and large optical contract manufacturing firms. The response I received from each of them was that either they could not build such a system or that it would cost several hundred thousand dollars to do it. This closed the door on that option very quickly. The only option I had left was to try to build the variable reference path myself. It was during the ensuing 8 month process that I would realize just how difficult the undertaking would truly be (see [Chapter 2.4.2](#)) and the extraordinary level of manufacturing precision that would be required. Although I would ultimately be successful in building an optical delay line that was rugged enough to be transported and that could maintain its alignment over its entire 20 centimeter travel path (folded path gives a 40 cm total length), I would soon encounter several other problems.

Although I had successfully built a variable optical delay line that could fit inside a reasonably sized and portable box, the entire process for balancing the interferometer (i.e. making the reference path length equal to the fiber being tested) was a very time consuming process. At each incremental step toward the balance, the reference path length had to be adjusted and the spectrum scanned to see if balance had yet been achieved. This process usually took between 45 minutes to 2 hours. When balance was finally achieved and measurements could start being made, each point in the plot required its own separate scan. This too was yet another time consuming process. Furthermore, the spacing between the points in the plot was determined by the smallest increment that the translation stage was capable of resolving. So the resolution of the plot was also limited.

I was starting to wonder if the ability to directly measure second order dispersion (accurately) was worth all the trouble of building and using the reference path. If direct measurements were not important I could eliminate the reference path altogether and just use a common path configuration with USI to measure the group delay directly (see [Chapter 2.4.1](#)). This would also speed up my measurements since I would not have to spend time balancing the interferometer and I could produce first order dispersion plots with a single spectral scan and then get the second order dispersion plots from a fit to the group delay curve. The problem with this, I discovered, was that because of the scatter in the group delay curve the second order dispersion results depended on the type of fit I chose (see [Chapter 2.4.1](#)). Furthermore, depending on the size of the window chosen for the Fourier transform I had different amounts of scatter in the group delay plot. There was no way to know the size of the window that would minimize the scatter. As a result, I still preferred direct measurements of second order dispersion. What I really needed was a way to measure second order dispersion directly but with the ease and speed of unbalanced spectral interferometry. It was from this necessity that the virtual reference was invented.

Advantages of the virtual reference

In virtual reference interferometry, a simulated *interferogram* is the reference. Since optical detectors can be used to collect a 'test' interferogram, a 'reference' interferogram can be simulated and combined with the test interferogram instead of using a physical reference path. This enables *difference* measurements (so that both first and second order dispersion can be measured directly, as in balanced interferometry) using an unbalanced interferometer. This has several practical advantages that depend on the physical configuration of the interferometer used to generate the unbalanced interference pattern. Virtual reference interferometry may be used to convert a conventional interferometer to a virtually referenced one. For example an unbalanced spectral interferometer employing a common path configuration may be converted to employ a virtual reference (as shown in Chapters 4 to 7) or a dual arm balanced interferometer may be slightly imbalanced so that it may employ a virtual reference (as in [Chapter 6](#)). This conversion provides several advantages compared to conventional techniques for both dual arm and common path configurations.

Dual arm configuration

The dual arm configuration is typically used in an academic setting where a reference arm can be constructed on an optical table. The advantage of using a dual arm configuration (i.e. Michelson, Mach Zehnder interferometers) is that it reduces the wavelength resolution needed to acquire an interferogram by reducing the path length difference between the test and reference paths. This configuration is useful when high resolution tunable lasers are unavailable, not available in the wavelength range of interest or too costly. The advantage of using virtual reference interferometry in this type of Low-coherence setup (as discussed in [Chapter 6](#)), is that it eliminates the need for a costly precision variable delay line since the reference path length only needs to be adjusted so that it is near the length of the test path (coarse tuning). This is because the fine tuning needed to produce a dispersion plot is performed by the virtual reference. Elimination of the need for a tunable laser and high precision variable delay line lowers the cost envelope of the virtual reference technique. The ability to work with low cost broadband sources and spectrometers opens up possibilities for applications in new wavelength ranges. Furthermore, direct first and second order dispersion measurements can be obtained from a single spectral scan (saving time).

Common path configuration

The common path configuration is best used in commercial applications, where avoiding the need to use a folded reference path is essential. If a common path configuration is used ([Chapter 2.4.1](#)), the need for a reference path is eliminated altogether. This is significant since, as discussed in [Chapter 2.4.2](#), a reference path is costly, difficult to set up, time consuming to operate and requires calibration. The elimination of the variable delay line (or the reference path itself) has the following practical benefits: It reduces the cost of the measurement, since high precision stages can be very expensive. It also eliminates the need for optical components such as collimators and mirrors, which are also quite costly. Furthermore, it eliminates the need for a difficult optical alignment and coupling procedure. As discussed in [Chapter 2.4.2](#) the alignment process is very difficult since the number of

degrees of freedom increases with the number of lenses and mirrors used and since the free space to fiber coupling requires the fiber to be positioned exactly at the focal point of the lens. These two points are especially important in industry since free space delay lines can become misaligned during shipping. Elimination of the reference path also removes the need for calibration of the dispersion of the optical components (i.e. fiber, lenses, mirrors, etc.) in the reference path. This eliminates the associated calibration error that would otherwise be introduced into measurements (dispersion in the virtual reference path is known exactly), making the technique more accurate than balanced spectral interferometry (which uses a physical reference path for which there is uncertainty in the dispersion). Another benefit to the elimination of the reference path is that it reduces both the weight and footprint of the device, which is important for both shipping and storage considerations. Furthermore, the isolation and stabilization mechanisms required to prevent environmental fluctuations from affecting the reference path are also not required.

Both dual arm and common path configurations

The use of a virtual reference significantly reduces experiment run time since the reference can be tuned virtually to enable the extraction of first and second order dispersion as a function of wavelength. This compares to balanced spectral interferometry which requires a spectral scan for every point in the first and second order dispersion plots.

A summary of the practical advantages of using a virtual reference (compared to conventional alternatives) is given in Table 7-1. The important highlights are that USI based techniques (USI-WFT using windowed Fourier transforms, see [Chapter 2.4.1](#)) cannot be used to directly measure the second order dispersion in both dual arm and common path configurations. Furthermore, the resolution of the group delay plot depends on the window size chosen (as discussed in [Chapter 2.4.2](#)) which is always less than the resolution in BSI (as discussed in [Chapter 2.4.3](#)) or VRI since the optimum window size is unknown. This means that the scatter in the group delay plot will be larger than in balanced techniques (BSI or VRI based techniques). Dual arm techniques benefit from the ability to use broadband source, which are generally low cost in comparison to the broadband tunable lasers required by USI and VRI when the physical interferometer used is in the common path configuration. With Dispersive VRI it is possible to reduce the cost of the tunable laser by allowing tunable lasers with smaller bandwidths to be used. In BSI the reference can be quite expensive since a precision stage is required, whereas in the common path configuration no reference is required at all for USI, VRI or DVRI. One benefit of using LC-VRI (i.e. VRI in a low coherence dual arm configuration) is that a precision translation stage is not required (which reduces the cost of the reference path).

Table 7-1: Summary of practical advantages of using a virtual reference for first and second order dispersion measurements.

	Dual arm (Academic applications where a lab bench or optical table is available)				Common path (Commercial applications)		
	BSI	USI	LC-VRI	LC-DVRI	USI	VRI	DVRI
High precision group delay measurement (i.e. independent of window size)	√		√	√		√	√
Direct first and second order dispersion meas.	√		√	√		√	√
High resolution group delay plot	√		√	√		√	√
Low-cost source	√	√	√	√			√*
Low-cost detection	√	√	√	√	√	√	√
Low cost reference		√**	√**	√**	√	√	√
High speed (single scan)		√	√	√	√	√	√
Accuracy (no calibration error)					√	√	√
Ease of setup					√	√	√
Portability (alignment)					√	√	√
Light weight					√	√	√
Small footprint					√	√	√

* Compression of bandwidth allows for use of sources with smaller bandwidth which may be low-cost

** Precision translation stage not required

7.3.1 Significance to researchers in academia and industry

The virtual reference interferometer is presented as an alternative to conventional USI and BSI. This new interferometer is useful as a tool for the characterization of the first and second order dispersion in short length optical fibers. In the common path configuration, the technology eliminates the need for a reference arm. This is very convenient, since the difficulties associated with the setup and operation of the reference path are eliminated. It also makes measurements more accurate (elimination of calibration error) and fast (single scan characterization). This new type of interferometer will be useful to the academic community as a tool for simplifying the measurement of chromatic dispersion so that researchers can spend more time on their research and waste less time setting up and running difficult dispersion measurements. This tool is expected to have an impact on the development of specialty fibers and short length optical components.

7.4 Commercial significance

7.4.1 Current application: chromatic dispersion test

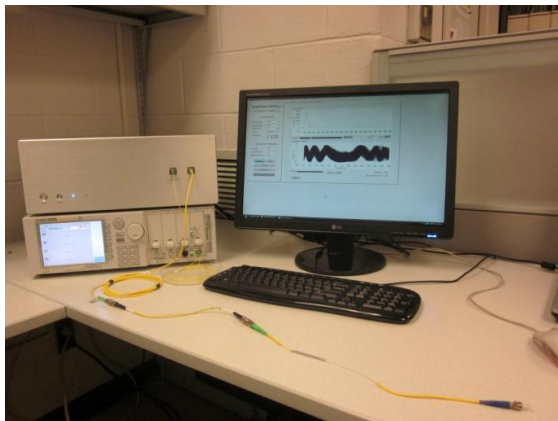
Virtual reference interferometry is currently being used in a commercially available dispersion test and measurement system called the Virtual Reference Dispersion Analyser, available from Inometrix, Inc. (<http://www.inometrix.com>). Images of the system are illustrated in Fig. 7-2.



(a)



(b)



(c)



(d)

Fig. 7-2. Images of the Virtual Reference Dispersion Analyser from Inometrix Inc.

7.5 Contributed publications and patents

The study and development of Virtual reference interferometry has led to the publication of several contributed papers and one patent in the field of interferometry and chromatic dispersion test. A list of contributed publications follows.

Accepted Papers

1. M. A. Galle, S. S. Saini, W. S. Mohammed, and Li Qian, 'Chromatic dispersion measurements using a virtually referenced interferometer,' *Optics Letters* **37**(10), 1598-1600 (2012).
2. M. A. Galle, S. S. Saini, W. S. Mohammed, and Li Qian, 'Virtual reference interferometry: theory and experiment,' *J. Opt. Soc. Am. B* **29**(11), 3201-3210 (2012).
3. M. A. Galle, S. S. Saini, W. S. Mohammed, Pierre Sillard, and Li Qian, 'Simultaneous dispersion measurements of multiple fiber modes using virtual reference interferometry,' *Optics Express* **22**(6), 6391-6399 (2014).
4. M. A. Galle, E. Y. Zhu, S. S. Saini, W. S. Mohammed, , and Li Qian, 'Characterizing short dispersion-length fiber via dispersive virtual reference interferometry,' *Optics Express* **22**(12), 14275-14284 (2014).
5. M. A. Galle, and Li Qian, 'Low-coherence virtual reference interferometry for chromatic dispersion characterization,' *Accepted by Photonics Technology Letters (detailed citation not yet available)*

Patents granted

1. M. A. Galle, 'System and method for a virtual reference interferometer', Patent number 8797539, Issue date 08/05/2014.

7.6 Prospective & future applications

Interferometers are used in many applications including testing, sensing and imaging. This section presents some forward looking possibilities for the virtual reference technique. Some of the capabilities of virtual referenced interferometers that were demonstrated for chromatic dispersion test are now shown to be potentially useful for similar measurements in other applications. The idea some of these potential applications is to adapt (convert) existing interferometers so that they can use virtual referencing.

Direct measurements of third (and higher) order dispersion

A dispersive virtual reference was used to enable compression of the interference pattern using DVRI. However, a potential future application of this technique is to use the dispersive virtual reference to obtain the third (and higher) order dispersion directly from the interference pattern. Both VRI and DVRI balance the first order dispersion in the test path with that of the reference path. This cancels out the effect of first order dispersion in the resulting interference pattern leaving only the effects of second and higher order dispersion in the resulting interference pattern. As a result there is direct access to the second order dispersion. One may take this approach one step further and use a dispersive virtual reference to cancel both first and second order dispersion in the test fiber, enabling direct access to the third and higher order dispersion. One may then continue this process to access higher order dispersion directly. Since this is impossible with physical referencing, the possibility to make such measurements shows the power of the paradigm shift introduced by the virtual reference technique.

Calibration of existing interferometers

One immediate application that a virtual reference can be used for is to calibrate existing dual arm interferometers and measure the dispersion imbalance between the test and reference arms. In this case, a large imbalance in the dispersion length between both arms may be measured using VRI and if the imbalance is too small for the available bandwidth then DVRI ([Chapter 5](#)) may be employed. An example of an application where dispersion must be calibrated and is very important is within an interferometer used for Optical Coherence Tomography, illustrated in Fig. 7-3. Since the wavelength range used by these systems is around 1300 nm such a system could be calibrated using a broadband source in this wavelength range (via LC-VRI which was demonstrated in [Chapter 6](#)) or by a tunable laser in this wavelength range. Tunable lasers in this wavelength range are available from Agilent Technologies (i.e. Agilent 81600B option 130 [72]).

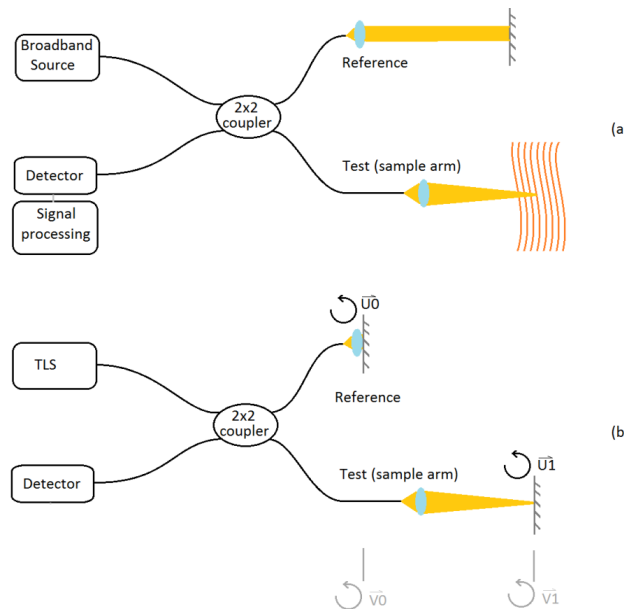


Fig. 7-3. (a) An illustration of a typical dual arm interferometric setup used in optical coherence tomography and (b) a possible setup for calibration of the dual arm interferometer using a dispersive reference to measure the difference in second order dispersion between the test and reference path.

Depth based imaging

In [Chapter 3](#) the virtual reference was shown to be capable of characterizing a fiber cascade. This same capability was shown to enable the characterization of multiple fiber modes in a Few-mode fiber in [Chapter 4](#). A possible extension of this capability could be used to develop depth based imaging using VRI, as illustrated in Fig. 7-4.

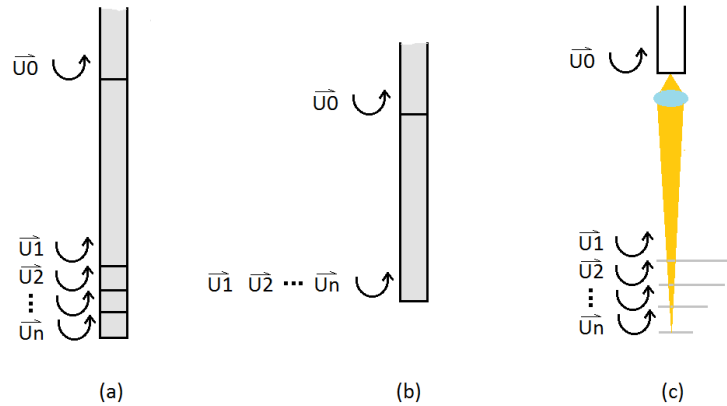


Fig. 7-4. Capabilities of virtual reference interferometry demonstrated for dispersion characterization of a (a) fiber cascade in Chapter 3 (b) few-mode fiber in Chapter 4 could be potentially extended for (c) depth based imaging.

Group index and second order dispersion based multi-parameter sensing

Similar setups used to characterize the chromatic dispersion in fiber could be used to produce a fiber sensor for measuring physical parameters. Since two parameters (first and second order dispersion) are measured it may be useful for applications in multi-parameter sensing (i.e. temperature, pressure, stress-strain or to measure changes in group index or second order dispersion directly). A potential setup for such a system is presented in Fig. 7-5. Both DVRI ([Chapter 5](#)) and LC-VRI ([Chapter 6](#)) would be very useful for this type of application. DVRI would allow devices with limited bandwidths to be used and LC-VRI (or LC-DVRI) would allow low-cost spectrometers and broadband sources to be used, instead of tunable lasers, to open up wavelength ranges where tunable lasers do not currently exist and to reduce costs. Furthermore, compact narrowband elements (i.e. fiber Bragg gratings) might also be used as sensing elements, where environmental changes could be detected via characterization using VRI or DVRI (as demonstrated in [Chapter 3](#) and [Chapter 5](#)).

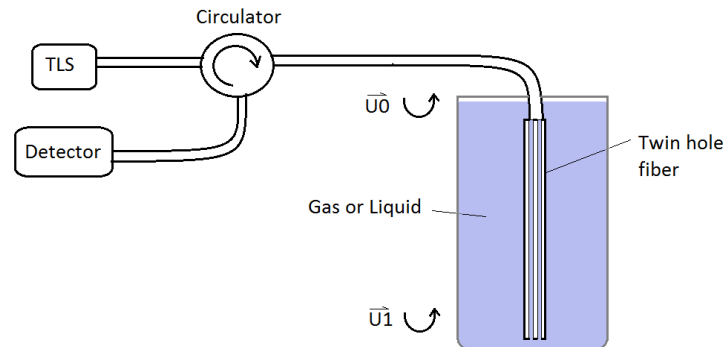


Fig. 7-5. Potential configuration of a fiber based multi-parameter sensor employing a virtual reference. A twin-hole fiber could be used to bring the evanescent field of light in the core into contact with the gas/liquid over the entire length of the fiber, increasing the interaction length.

7.7 Conclusion

Virtual reference interferometry is a paradigm shift in our thinking about what a reference can be. The technology has been developed for the dispersion characterization of short length fiber and optical components, bringing advantages and new capabilities over conventional techniques. In chromatic dispersion test, the technology is expected to have an impact on the development of specialty fibers and optical components, where accurate short length characterization is of critical importance. The future of the virtual reference looks to be very promising, as tunable lasers (used in the common path configuration) are becoming more economical and the use of the virtual reference eliminates the need for a physical reference path altogether. This is an especially important impairment to the economical commercial development of interferometric systems. Furthermore, spectrometers and broadband sources (used in the dual path VRI configuration in [Chapter 6](#)) are already economical and have widespread use across a multitude of interferometric applications for which a virtual reference can be employed. One of the most immediate potential applications of this technology, outside of dispersion test, is the use of the virtual reference to calibrate or modify the operation of existing interferometric systems.

References

- [1] C. Koebele, M. Salsi, D. Sperti, P. Tran, P. Brindel, H. Mardoyan, S. Bigo, A. Boutin, F. Verluise, P. Sillard, M. Astruc, L. Provost, F. Cerou and G. Charlet, "Two mode transmission at 2×100 Gb/s, over 40 km-long prototype few-mode fiber, using LCOS-based programmable mode multiplexer and demultiplexer," *Optics Express*, vol. 19, no. 17, pp. 16593-16600, 2011.
- [2] B. Neng, E. Ip, H. Yue-Kai, E. Mateo, F. Yaman, L. Ming-Jun, S. Bickham, S. Ten, J. Linares, C. Montero, V. Moreno, X. Prieto, V. Tse, M. C. Kit, A. P. T. Lau, T. Hwa-Yaw, L. Chao, L. Yanhua, P. Gang-Ding, L. Guifang and W. Ting, "Mode-division multiplexed transmission with inline few-mode fiber amplifier," *Optics Express*, vol. 20, no. 3, pp. 2668-2680, 2012.
- [3] S. Randel, R. Ryf, A. Sierra, P. J. Winzer, A. H. Gnauck, C. A. Bolle, R. -J. Essiambre, D. W. Peckham, A. McCurdy and R. J. Lingle, "6x56-Gb/s mode-division multiplexed transmission over 33-km few-mode fiber enabled by 6x6 MIMO equalization," *Optics Express*, vol. 19, no. 17, pp. 16697-16707, 2011.
- [4] F. Yaman, B. Neng, Y. K. Huang, M. F. Huang, B. Zhu, W. Ting and L. Guifang, "10 x 112 Gb/s PDM-QPSK transmission over 5032 km in few-mode fibers," *Optics Express*, vol. 18, no. 20, pp. 21342-21349, 2010.
- [5] F. Yaman, B. Neng, B. Zhu, T. Wang and G. Li, "Long distance transmission in few-mode fibers," *Optics Express*, vol. 18, no. 12, pp. 13250-13257, 2010.
- [6] E. Hect, *Optics: 4th Ed.*, San Francisco, CA: Addison Wesley, 2002.
- [7] G. P. Agrawal, *Fiber-Optic Communication Systems*, 3rd ed., New York: Wiley-Interscience, 2002.
- [8] L. F. Mollenauer, R. H. Stolen and J. P. Gordon, "Experimental observation of picosecond pulse narrowing and solitons in optical fibers," *Phys. Rev. Lett.*, vol. 45, no. 13, pp. 1095-1098, 1980.
- [9] M. Saleh and C. Teich, *Fundamentals of Photonics*, John Wiley and Sons, 2001.
- [10] J. M. Liu, *Photonic Devices*, Cambridge University, 2005.
- [11] K. C. Chan and H. F. Liu, "Effect of third-order dispersion on soliton-effect pulse compression," *Optics Lett.*, vol. 19, no. 1, pp. 49-51, 1994.
- [12] T. Mitzunami and T. Tsukada, "Quasi phase-matched second-harmonic generation in thermally poled twin-hole fiber by periodic UV depoling," in *30th European Conference on Optical Communication (ECOC)*, pt. 2, 2004.
- [13] P. Merrit, R. P. Tatam and D. A. Jackson, "Interferometric chromatic dispersion measurements on short lengths of monomode optical fiber," *J. Lightwave Technol.*, vol. 7, no. 4, pp. 703-716, 1989.
- [14] T. Matsui, K. Nakajima and I. Sankawa, "Dispersion Compensation Over All the Telecommunication Bands With Double-Cladding Photonic-Crystal Fiber," *J. Lightwave Technol.*, vol. 25, no. 3, pp. 757-762, 2007.
- [15] E. Desurvire, *Erbium Doped Fiber Amplifiers: Principles and Applications*, Wiley-Interscience, 1994.
- [16] R. K. Hickernell, K. Takada, M. Yamada, M. Shimizu and M. Horiguchi, "Pump-induced dispersion of erbium-doped fiber measured by Fourier-transform spectroscopy," *Optics Letters*, vol. 18, no. 1, pp. 19-21, 1993.
- [17] R. Cella and W. Wood, "Measurement of chromatic dispersion in erbium doped fiber using low coherence interferometry," in *Proc. of the Sixth Optical Fiber Measurement Conference (OFMC, 2001)*, 2001.

- [18] J. M. Wiesenfeld and J. Stone, "Measurement of Dispersion Using Short Lengths of an Optical Fiber and Picosecond Pulses from Semiconductor Film Lasers," *J. Lightwave Technol.*, Vols. LT-2, no. 4, pp. 464-468, 1984.
- [19] L. G. Cohen, "Comparison of single-mode fiber dispersion measurement techniques," *J. Lightwave Technol.*, vol. 3, pp. 958-966, 1985.
- [20] J. Cheng, M. E. V. Penderson, K. Wang, C. Xu, L. Gruner-Nielson and D. Jakobsen, "Time-domain multimode dispersion measurement in a higher-order-mode fiber," *Optics Letters*, vol. 37, no. 3, pp. 347-349, 2012.
- [21] J. Brendel, H. Zbinden and N. Gisin, "Measurement of chromatic dispersion in optical fibers using pairs of correlated photons," *Optics Comm.*, vol. 151, no. 1-3, pp. 35-39, 1998.
- [22] B. Costa, D. Mazzoni, M. Puleo and E. Vezzoni, "Phase shift technique for the measurement of chromatic dispersion in optical fibers using LEDs," *IEEE Trans. on Microwave Theory and Techniques*, , Vols. MTT-30, no. 10, pp. 1497-1503, 1982.
- [23] L. Cherbi, M. Mehenni and R. Aksas, "Experimental investigation of the modulation phase-shift method for the chromatic dispersion in a single-mode fiber coiled on a covered spool," *Microw. and Opt. Technol. Lett.*, vol. 48, no. 1, pp. 174-178, 2006.
- [24] Agilent Technologies, "Agilent 86038B Photonic Dispersion and Loss Analyzer," January 2007. [Online]. Available: <http://cp.literature.agilent.com/litweb/pdf/5989-2325EN.pdf>. [Accessed 3 March 2014].
- [25] D. Liu, W. Tong, S. Liu and H. Liu, "Study on the fabrication techniques of photonic crystal fiber and PCF based structures," *Proc. SPIE*, vol. 5722, no. 1, pp. 123-129, 2005.
- [26] D. J. Richardson, F. Poletti, J. Y. Y. Leong, X. Feng, H. E. Heidepreim, H. V. Finazzi, K. E. Frampton, S. Asimakis, R. C. Moore, J. C. Baggett, J. R. Hayes, M. N. Petrovich, M. L. Tse, R. Amezcua, J. H. V. Price, N. G. R. Broderick, P. Petropoulos and T. M. Monro, "Advances in microstructured fiber technology," in *Fibres and Optical Passive Components, 2005. Proceedings of 2005 IEEE/LEOS Workshop on*, 2005.
- [27] Sears, F., L. G. Cohen and J. Stone, "Interferometric measurements of dispersion-spectra variations in a single-mode fiber," *J. Lightwave Technol.*, Vols. LT-2, no. 2, pp. 181-184, 1984.
- [28] C. Palavicini, Y. Jaouen, G. Debarge, E. Kerrinckx, M. Quiquempois, M. Douay, C. Lepers, A.-F. Obaton and G. Melin, "Phase-sensitive optical low-coherence reflectometry technique applied to the characterization of photonic crystal fiber properties," *Opt. Lett.*, vol. 30, pp. 361-363, 2005.
- [29] J. Y. Lee and D. Y. Kim, "Versatile chromatic dispersion measurement of a single mode fiber using spectral white light interferometry," *Opt. Express*, vol. 14, pp. 11608-11615, 2006.
- [30] L. Ping, D. Huimin and S. J. Mihailov, "Direct measurement of the zero-dispersion wavelength of tapered fibres using broadband-light interferometry," *Meas. Sci. & Technol.*, vol. 16, no. 8, pp. 1631-1636, 2005.
- [31] J. Gehler and W. Spahn, "Dispersion measurement of arrayed-waveguide gratings by Fourier transform spectroscopy," *Electron. Lett.*, vol. 36, no. 4, pp. 338-339, 2000.
- [32] A. Wax, C. Yang and J. A. Izatt, "Fourier-domain low-coherence interferometry for light-scattering spectroscopy," *Optics Lett.*, vol. 28, no. 14, pp. 1230-1232, 2003.
- [33] H. K. Tsang, C. S. Wong, T. K. Liang, I. E. Day, S. W. Roberts, A. Harpin, J. Drake and M. Asghari, "Optical dispersion, two-photon absorption and self-phase modulation in silicon waveguides at 1.5 um wavelength," *Applied Phys. Lett.*, vol. 80, no. 3, pp. 416-418, 2002.
- [34] M. A. Galle, W. Mohammed, L. Qian and P. W. E. Smith, "Single-arm three-wave interferometer for measuring

- dispersion of short lengths of fiber," *Optics Express*, vol. 15, pp. 16896-16908, 2007.
- [35] M. A. Galle, "Single-arm Three Wave Interferometer for Measuring Dispersion in Short Lengths of Fiber," *University of Toronto*, 2007.
- [36] P. Hlubina, "White-light spectral interferometry to measure intermodal dispersion in two-mode elliptical-core optical fibres," *Optics Comm.*, vol. 218, no. 4-6, pp. 283-289, 2003.
- [37] P. Hlubina, T. Martynkien and W. Urbanczyk, "Dispersion of group and phase modal birefringence in elliptical-core fiber measured by white-light spectral interferometry," *Optics Express*, vol. 11, no. 22, pp. 2793-2798, 2003.
- [38] J. Tignon, M. V. Marquezini, T. Hasche and D. S. Chemla, "Spectral interferometry of semiconductor nanostructures," *IEEE J. Quantum Electron.*, vol. 35, no. 4, pp. 510-522, 1999.
- [39] C. Dorrer, N. Belabas, J.-P. Likforman and M. Joffre, "Spectral resolution and sampling issues in Fourier-transform spectral interferometry," *J. Opt. Soc. Am. B*, vol. 17, no. 10, pp. 1795-1802, 2000.
- [40] P. Hlubina, M. Szpulak, D. Ciprian, T. Martynkien and W. Urbanczyk, "Measurement of the group dispersion of the fundamental mode of holey fiber by white-light spectral interferometry," *Optics Express*, vol. 15, no. 18, pp. 11073-11081, 2007.
- [41] W. Mohammed, J. Meier, M. A. Galle, L. Qian, J. S. Aitchison and P. W. E. Smith, "Linear and quadratic dispersion characterization of millimetre-length fibers and waveguides using common path interferometry," *Opt. Lett.*, vol. 32, pp. 3312-3314, 2007.
- [42] P. Hlubina, R. Chlebus and D. Ciprian, "Differential group refractive index dispersion of glasses of optical fibres measured by a white-light spectral interferometric technique," *Meas. Sc. Technol.*, vol. 18, pp. 1547-1552, 2007.
- [43] T. Sunner, M. Gellner, M. Scholz, A. Löffler, M. Kamp and A. Forchel, "Dispersive properties of photonic crystal waveguide resonators," *Phys. stat. sol. A*, vol. 204, no. 11, pp. 3727-3738, 2007.
- [44] X. Cui, X. Zheng, Y. Li, Y. Xu and S. Liu, "Research on phase reconstruction and chromatic dispersion characteristic of thin film filters," *Opt. Comm.*, vol. 256, no. 1-3, pp. 123-131, 2005.
- [45] M. Takeda, H. Ina and S. Kobayashi, "Fourier-transform method of fringe-pattern analysis for computer-based topography and interferometry," *J. Optical. Soc. Am.*, vol. 72, no. 1, pp. 156-160, 1982.
- [46] J. Zhong and J. Weng, "Generalized Fourier analysis for phase retrieval of fringe pattern," *Optics Express*, vol. 18, no. 26, pp. 26806-26820, 2010.
- [47] S. Haykin and B. Van Veen, *Signals and Systems: Second Edition*, New York: John Wiley & Sons, Inc., 2003.
- [48] H. T. Shang, "Chromatic dispersion measurement by white-light interferometry on metre-length single-mode optical fibres," *Electron. Lett.*, vol. 17, no. 17, pp. 603-605, 1981.
- [49] M. A. Galle, S. S. Saini, W. Mohammed and L. Qian, "Chromatic Dispersion measurements using a virtually referenced interferometer," *Optics Lett.*, vol. 37, pp. 1598-1600, 2012.
- [50] M. A. Galle, S. S. Saini, W. Mohammed and L. Qian, "Virtual reference interferometry: theory and experiment," *J. Opt. Soc. Am. B*, vol. 29, no. 11, pp. 3201-3210, 2012.
- [51] M. A. Galle, S. S. Saini, W. S. Mohammed, P. Sillard and L. Qian, "Simultaneous dispersion measurements of multiple fiber modes using virtual reference interferometry," *Optics Express*, vol. 22, no. 6, pp. 6391-6399, 2014.

- [52] P. Sillard, M. Bigot-Astruc, D. Boivin, H. Maerten and L. Provost, "Few-mode fiber for uncoupled mode-division multiplexing transmissions," *Proc. Europ. Conf. Opt. Commun*, vol. paper Tu.5.LeCervin.7., p. 3, 2011.
- [53] A. Galtarossa, L. Palmieri, M. Schiano and T. Tambosso, "Single-end polarization mode dispersion measurement using backreflected spectra through a linear polarizer," *J. Lightwave Technol.*, vol. 17, no. 10, pp. 1835-1842, 1999.
- [54] B. L. Heffner, "Automated measurement of polarization mode dispersion using Jones matrix eigenanalysis," *IEEE Photon. Technol. Lett.*, vol. 4, no. 9, pp. 1066-1069, 1992.
- [55] B. L. Heffner, "Accurate, automated measurement of differential group delay dispersion and principle state variation using Jones matrix eigenanalysis," *IEEE Photon. Technol. Lett.*, vol. 5, no. 7, pp. 814-817, 1993.
- [56] F. Tang, X. -Z. Wang, Y. Zhang and W. Jing, "Distributed measurement of birefringence dispersion in polarization-maintaining fibers," *Optics Lett.*, vol. 31, no. 23, pp. 3411-3413, 2006.
- [57] F. Tang, X. -Z. Wang, Y. Zhang and W. Jing, "Characterization of birefringence dispersion in polarization-maintaining fibers by use of white-light interferometry," *Applied Optics*, vol. 46, no. 19, pp. 4073-4080, 2007.
- [58] D. A. Flavin, R. McBride and J. D. C. Jones, "Dispersion of birefringence and differential group delay in polarization-maintaining fiber," *Optics Lett.*, vol. 27, no. 12, pp. 1010-1012, 2002.
- [59] M. G. Shlyagin, A. V. Khomenko and D. Tentori, "Birefringence dispersion measurement in optical fibers by wavelength scanning," *Optics Lett.*, vol. 20, no. 8, pp. 869-871, 1995.
- [60] R. Posey, L. Phillips, D. Diggs and A. Sharma, "LP01-LP02 interference using a spectrally extended light source: measurement of the non-step-refractive-index profile of optical fibers," *Optics Lett.*, vol. 21, no. 17, pp. 1357-1359, 1996.
- [61] P. Hlubina, "Measuring intermodal dispersion in optical fibres using white-light spectral interferometry with the compensated Michelson interferometer," *J. Mod. Opt.*, vol. 48, no. 14, pp. 2087-2096, 2001.
- [62] P. Hlubina, T. Martynkien and W. Urbanczyk, "Measurements of intermodal dispersion in few-mode optical fibres using a spectral-domain white-light interferometric method," *Meas. Sci. & Technol.*, vol. 14, no. 6, pp. 784-789, 2003.
- [63] J. W. Nicholson, A. D. Yablon, S. Ramachandran and S. Ghalmi, "Spatially and spectrally resolved imaging of modal content in large-mode-area fibers," *Optics Express*, vol. 16, no. 10, pp. 7233-7243, 2008.
- [64] K. Jespersen, Z. Li, L. Gruner-Nielsen, B. Palsdottir, F. Poletti and J. W. Nicholson, "Measuring distributed mode scattering in long, few-moded fibers," in *Optical Fiber Communication Conference and Exposition (OFC/NFOEC), 2012 and the National Fiber Optic Engineers Conference, 2012*.
- [65] Y. Z. Ma, Y. Sych, G. Onishchukov, S. Ramachandran, U. Peschel, B. Schmauss and G. Leuchs, "Fiber-modes and fiber-anisotropy characterization using low-coherence interferometry," *Applied Phys. B: Lasers and Optics*, vol. 96, no. 2-3, pp. 345-353, 2009.
- [66] P. Hlubina, D. Ciprian, M. Kadulova, T. Martynkien, P. Mergo and W. Urbanczyk, "Spectral interferometry-based dispersion characterization of microstructured and specialty optical fibers using a supercontinuum source," *Proc. SPIE*, vol. 8426, p. 84260N (13 pp), 2012.
- [67] M. A. Galle, E. Y. Zhu, S. S. Saini, W. S. Mohammed and L. Qian, "Characterizing short dispersion-length fiber via dispersive virtual reference interferometry," *Optics Express*, vol. 22, no. 12, pp. 14275-14284, 2014.
- [68] Corning Inc., "Corning SMF-28 Product Information," Corning Inc., [Online]. Available: <http://ece466.groups.et.byu.net/notes/smf28.pdf>. [Accessed 10 April 2014].

- [69] M. A. Galle and L. Qian, "Low-coherence virtual reference interferometry for chromatic dispersion characterization," *Photonics Technology Letters*, 2014.
- [70] Ocean Optics, "USB4000 Miniature Fiber Optic Spectrometer," Ocean Optics, 7 May 2014. [Online]. Available: <http://www.oceanoptics.com/products/usb4000.asp>. [Accessed 7 May 2014].
- [71] Optics, Ocean, "HR4000 High-Resolution Spectrometer," Ocean Optics, 7 May 2014. [Online]. Available: <http://www.oceanoptics.com/products/hr4000.asp>. [Accessed 7 May 2014].
- [72] Agilent Technologies, Inc., "Agilent 81600B Tunable Laser Source Family," August 2013. [Online]. Available: <http://cp.literature.agilent.com/litweb/pdf/5989-7321EN.pdf>. [Accessed 31 May 2014].
- [73] K. Kawano and T. Kitoh, *Introduction to Optical Waveguide Analysis: Solving Maxwell's Equations and the Schrodinger Equation*, New York: John Wiley & Sons, Inc., 2001.
- [74] A. A. Kumar, *Signals and Systems: Third Edition*, Delhi: PHI Learning Limited, 2013.
- [75] M. Drosig, *Dealing with Uncertainties: A Guide to Error Analysis*, New York: Springer, 2007.
- [76] D. M. Harrison, "Error Analysis in Experimental Physical Science," 10 September 2011. [Online]. Available: <http://www.upscale.utoronto.ca/PVB/Harrison/ErrorAnalysis/All.pdf>. [Accessed 30 May 2014].
- [77] G. Renaud, P. Hamel, Y. Jaouen, A.-F. Obaton, V. Lanticq and G. Debarge, "Versatile characterization of specialty fibers using the phase-sensitive optical low-coherence reflectometry technique," *J. Lightwave Technol.*, vol. 27, no. 15, pp. 3021-3033, 2009.
- [78] K. Inoue, "Four-wave mixing in an optical fiber in the zero-dispersion wavelength region," *J. Lightwave Technol.*, vol. 10, no. 11, pp. 1553-1561, 1992.

Appendix A: Detailed background

Chromatic dispersion is the phenomenon that describes the wavelength or frequency dependence of the refractive index of a material [6]. This variation may be caused either by the optical properties of the material itself (material dispersion) or by the optical confinement produced by the geometry of a waveguide (waveguide dispersion). The combined effect that includes both waveguide and material dispersion is referred to as the total dispersion. In this appendix the physical cause and mathematical description of chromatic dispersion are identified and developed.

A.1. Material dispersion

Material dispersion refers to the wavelength (frequency) dependent response of the electron cloud of atoms or molecules to transiting electromagnetic waves. Material dispersion is caused by atomic resonance, which causes atoms/molecules to absorb and re-radiate electromagnetic waves more efficiently as the frequency of the radiation approaches a certain characteristic frequency ω for that atom/molecule (i.e. the resonance frequency) [6].

An impinging electric field distorts the electron cloud of an atom/molecule polarizing it by an amount that depends on the relative difference between its frequency ω_o and the resonance frequency ω of the atom/molecule [6]. The closer the frequency of the electric field is to the resonance of the atom/molecule the greater the polarization and displacement of the electron cloud. The relative displacement between the positive nucleus and the negative electron cloud of the atom/molecule can be modeled as a Lorentz Oscillator and described by [6]

$$\bar{x} = \frac{q_e / m_e}{(\omega^2 - \omega_o^2)} \bar{E} \quad \text{Eq. A-1 [6]}$$

where q_e is the charge of the electron, m_e is its mass, ω is the resonance frequency of the particular atom/molecule, ω_o is the particular frequency of the electromagnetic radiation, \bar{E} is the electric field vector and \bar{x} is the displacement vector. The polarization induced in the electron cloud is defined by

$$\bar{P} = Nq_e \bar{x} = (\varepsilon - \varepsilon_o) \bar{E} \quad \text{Eq. A-2 [6]}$$

where ε is the permittivity of the material, ε_o is the permittivity of free space and N is the number of electrons per unit volume. The index of refraction $n(\omega_o)$ at a particular wavelength ω_o is determined by the ratio between the permittivity in the material and the permittivity of free space, which can be determined using Eq. A-1 and Eq. A-2 as the dispersion equation given by

$$n^2(\omega_o) = \frac{\varepsilon}{\varepsilon_o} = 1 + \frac{\bar{P}}{\varepsilon_o \bar{E}} = 1 + \frac{Nq_e^2}{\varepsilon_o m_e} \left(\frac{1}{\omega^2 - \omega_o^2} \right) \quad \text{Eq. A-3 [6]}$$

The index of refraction of the material in Eq. A-3 applies to light travelling through bulk material. It shows that the index of refraction observed by an electromagnetic wave of frequency ω_o is inversely proportional to how close its

frequency is to the resonance frequency of the atom/molecule, ω . From the refractive index the group index may be determined by

$$N_G(\omega_o) = n(\omega_o) + \omega_o \left. \frac{dn}{d\omega} \right|_{\omega_o} \quad \text{Eq. A-4 [6]}$$

Conversion from the frequency domain to the wavelength domain may be achieved using $\omega_o = 2\pi c/\lambda_o$ (where c is the speed of light in vacuum and λ_o is the wavelength of light in vacuum) and using the chain rule to convert $dn/d\omega|_{\omega_o}$ to $dn/d\lambda|_{\lambda_o}$. The resulting expression in terms of the wavelength in vacuum is given by

$$N_G(\lambda_o) = n(\lambda_o) - \lambda_o \left. \frac{dn}{d\lambda} \right|_{\lambda_o} \quad \text{Eq. A-5 [6]}$$

The second order dispersion of a bulk material may then be determined from the slope of the group index plotted as a function of wavelength as described by

$$D_{Material}(\lambda_o) = \frac{1}{c} \left. \frac{dN_G(\lambda_o)}{d\lambda} \right|_{\lambda_o} = - \frac{\lambda_o}{c} \left. \frac{d^2n}{d\lambda^2} \right|_{\lambda_o} \quad \text{Eq. A-6 [10]}$$

A.2. Waveguide dispersion

Waveguide dispersion is the variation in the velocity of different frequencies of light due to waveguide geometry. This variation is due to changes in the index of refraction caused by the confinement of light in an optical mode [10]. Although there are many possible geometries for a waveguide we will restrict our discussion of possible waveguides to a step index optical fiber with the cross sectional geometry illustrated in Fig. A-1. The waveguide dispersion is a function of the core index $n_1(\lambda)$, the cladding index $n_2(\lambda)$ and the core radius a , where the core index is slightly higher than that in the cladding so that the optical field is mostly confined within the core.

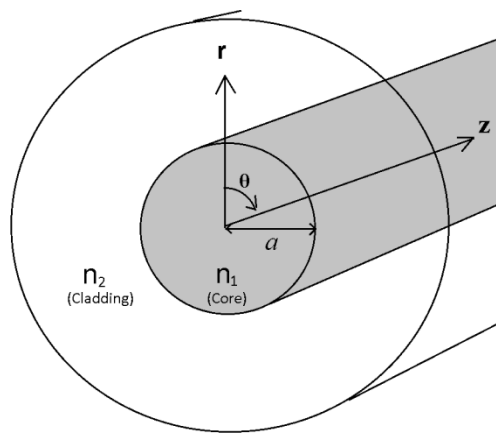


Fig. A-1. Cross sectional geometry of an optical fiber (core size exaggerated).

The index experienced by a particular mode in an optical fiber is known as the effective index $n_{eff}(\lambda)$ because the mode propagates within both the core and cladding region and therefore experiences an index that is between these

two values. The effective index $n_{eff}(\lambda)$ experienced by a particular mode in an optical fiber may be obtained by solving Maxwell's Equations for the transverse electric (TE) and transverse magnetic (TM) fields to obtain the wave equation in cylindrical coordinates. Solutions are then obtained by applying appropriate boundary conditions in the core, cladding and at the interface between the core and cladding [73].

We begin by defining the terms in Maxwell's equations and define the electric flux density D (in coulombs per meter squared) and the magnetic flux density B (in amperes per meter squared) as

$$\begin{aligned} D &= \varepsilon E \\ B &= \mu H \end{aligned} \tag{Eq. A-7 [73]}$$

where E is the electric field (in volts per meter) and H is the magnetic field (in amperes per meter). The permittivity ε and the permeability μ are defined by

$$\begin{aligned} \varepsilon &= \varepsilon_o \varepsilon_r \\ \mu &= \mu_o \mu_r \end{aligned} \tag{Eq. A-8 [73]}$$

where ε_o and μ_o are the permittivity and permeability of free space and ε_r and μ_r are the relative permittivity and permeability of the material. Since an optical fiber is non-magnetic this means that $\mu_r = 1$. If we assume that the electromagnetic field oscillates at a single angular frequency denoted by ω_o then the fields may be expressed in time independent phasor form given by [73].

$$E(r,t) = \text{Re}\{\bar{E}(r)e^{j\omega t}\} \tag{Eq. A-9}$$

$$H(r,t) = \text{Re}\{\bar{H}(r)e^{j\omega t}\} \tag{Eq. A-10}$$

$$D(r,t) = \text{Re}\{\bar{D}(r)e^{j\omega t}\} \tag{Eq. A-11}$$

$$B(r,t) = \text{Re}\{\bar{B}(r)e^{j\omega t}\} \tag{Eq. A-12}$$

Where the time independent phasor forms are given by $\bar{E}, \bar{H}, \bar{D}$ and \bar{B} . Maxwell's Equations are empirically derived relationships between the electric and magnetic fields. They are summarized for an optical fiber (which is a non conductive non-magnetic medium) by

$$\nabla \times \bar{E} = -j\omega \bar{B} = -j\omega \mu_o \bar{H} \tag{Eq. A-13}$$

$$\nabla \times \bar{H} = j\omega \bar{D} = -j\omega \varepsilon \bar{E} \tag{Eq. A-14}$$

$$\nabla \cdot \bar{D} = \nabla \cdot \varepsilon \bar{E} = 0 \tag{Eq. A-15}$$

$$\nabla \cdot \bar{B} = \nabla \cdot \mu \bar{H} = 0 \tag{Eq. A-16}$$

The wave equation for both the electric and magnetic field may be obtained by applying a vector rotation operator $\nabla \times$ to Eq. A-13 and Eq. A-14 and using the vector formula given by

$$\nabla \times (\nabla \times \bar{A}) = \nabla (\nabla \cdot \bar{A}) - \nabla^2 \bar{A} \quad \text{Eq. A-17} \quad [73]$$

where ∇^2 is a Laplacian, given by Eq. A-18 for a Cartesian coordinate system and by Eq. A-19 for a cylindrical coordinate system.

$$\nabla^2 = \frac{\partial^2}{\partial x^2} + \frac{\partial^2}{\partial y^2} + \frac{\partial^2}{\partial z^2} \quad \text{Eq. A-18} \quad [73]$$

$$\nabla^2 = \frac{\partial^2}{\partial r^2} + \frac{1}{r} \frac{\partial}{\partial r} + \frac{1}{r^2} \frac{\partial^2}{\partial \theta^2} + \frac{\partial^2}{\partial z^2} \quad \text{Eq. A-19} \quad [73]$$

For a waveguide with dimensions that do not vary in the z-direction it is convenient to define the Tangential components of the Laplacian as

$$\nabla_{\perp}^2 = \frac{\partial^2}{\partial x^2} + \frac{\partial^2}{\partial y^2} \quad \text{Eq. A-20} \quad [73]$$

$$\nabla_{\perp}^2 = \frac{\partial^2}{\partial r^2} + \frac{1}{r} \frac{\partial}{\partial r} + \frac{1}{r^2} \frac{\partial^2}{\partial \theta^2} \quad \text{Eq. A-21} \quad [73]$$

After applying the vector rotation and assuming that the relative permittivity and permeability of the medium is constant (assuming the weakly guiding approximation may be used since the refractive index between the core and cladding is small) results in the Helmholtz or Wave Equation for each field given by [73].

$$\nabla^2 \bar{E} + k^2 \bar{E} = 0 \quad \text{Eq. A-22}$$

$$\nabla^2 \bar{H} + k^2 \bar{H} = 0 \quad \text{Eq. A-23}$$

For an optical fiber, it is convenient to work in cylindrical coordinates and the Laplacian definition in Eq. A-19 may be used. In addition, since the structure of an optical fiber is uniform in the z-direction the derivative of the electromagnetic field with respect to z is constant. This is illustrated by

$$\bar{E}(r) = \left| \bar{E}(r) \right| e^{-jkz} \quad \text{Eq. A-24}$$

$$\frac{d}{dz} \bar{E}(r) = -jk_z \left| \bar{E}(r) \right| e^{-jkz} \quad \text{Eq. A-25}$$

$$\frac{d^2}{dz^2} \bar{E}(r) = -k_z^2 \left| \bar{E}(r) \right| e^{-jkz} \quad \text{Eq. A-26}$$

where k_z is the component of the propagation constant in the z-axis. Using this and the definition for the tangential Laplacian Eq. A-22 and Eq. A-23 reduce to

$$\nabla_{\perp}^2 \bar{E} + (k^2 - k_z^2) \bar{E} = 0 \quad \text{Eq. A-27}$$

$$\nabla_{\perp}^2 \bar{H} + (k^2 - k_z^2) \bar{H} = 0 \quad \text{Eq. A-28}$$

Given that the propagation constant in the medium is related to the propagation constant in free space k_o via the refractive index n of the medium (i.e. $k = k_o n$) and that the propagation constant in the z direction k_z is related to propagation constant in free space by the effective refractive index n_{eff} within the waveguide (i.e. $k_z = k_o n_{eff}$) we may express Eq. A-27 and Eq. A-28 as

$$\nabla_{\perp}^2 \bar{E} + k_o^2 (n^2 - n_{eff}^2) \bar{E} = 0 \quad \text{Eq. A-29}$$

$$\nabla_{\perp}^2 \bar{H} + k_o^2 (n^2 - n_{eff}^2) \bar{H} = 0 \quad \text{Eq. A-30}$$

The solutions to Eq. A-29 and Eq. A-30 may be obtained via the method of separation of variables. This is done by assuming the tangential electric and magnetic fields may be described by

$$\bar{E}_{\perp}(r, \theta) = R(r) \Theta(\theta) \quad \text{Eq. A-31}$$

$$\bar{H}_{\perp}(r, \theta) = R(r) \Theta(\theta) \quad \text{Eq. A-32}$$

where the tangential component is either the x or y component of the field. Substitution of Eq. A-24 into Eq. A-22 (or substitution of Eq. A-25 into Eq. A-23) followed by division by $R(r) \Theta(\theta)$ gives

$$\frac{r^2}{R(r)} \left(\frac{\partial^2 R(r)}{\partial r^2} + \frac{1}{r} \frac{\partial R(r)}{\partial r} \right) + r^2 k_o^2 (n^2 - n_{eff}^2) = - \frac{1}{\Theta(\theta)} \frac{\partial^2 \Theta(\theta)}{\partial \theta^2} \quad \text{Eq. A-33} \quad [73]$$

Since the left side of Eq. A-33 is only a function of the variable r and the right hand side is only a function of θ both sides must be equal to a constant such that we now have Eq. A-34 and Eq. A-35.

$$\frac{r^2}{R(r)} \left(\frac{\partial^2 R(r)}{\partial r^2} + \frac{1}{r} \frac{\partial R(r)}{\partial r} \right) + r^2 k_o^2 (n^2 - n_{eff}^2) = l^2 \quad \text{Eq. A-34} \quad [73]$$

$$\frac{1}{\Theta(\theta)} \frac{\partial^2 \Theta(\theta)}{\partial \theta^2} = -l^2 \quad \text{Eq. A-35} \quad [73]$$

which may be simplified to

$$\frac{\partial^2 R(r)}{\partial r^2} + \frac{1}{r} \frac{\partial R(r)}{\partial r} + k_o^2 \left(n^2 - n_{eff}^2 - \frac{l^2}{r^2} \right) R(r) = 0 \quad \text{Eq. A-36} \quad [73]$$

$$\frac{\partial^2 \Theta(\theta)}{\partial \theta^2} + l^2 \Theta(\theta) = 0 \quad \text{Eq. A-37} \quad [73]$$

The solution to Eq. A-37 is simply a sinusoid of frequency l given by

$$\Theta(\theta) = \sin(l\theta + \phi) \quad \text{Eq. A-38} \quad [73]$$

where l is an integer and ϕ is an arbitrary phase constant. Eq. A-36 may be put into standard form by transforming the variables as

$$u^2 = k_o^2 \left(n(r)^2 - n_{eff}^2 \right) \quad \text{Eq. A-39} \quad [73]$$

$$\xi = ur \quad \text{Eq. A-40} \quad [73]$$

$$\frac{\partial}{\partial r} = \frac{\partial}{\partial \xi} \frac{\partial \xi}{\partial r} = u \frac{\partial}{\partial \xi} \quad \text{Eq. A-41} \quad [73]$$

$$\frac{\partial^2}{\partial r^2} = u \frac{\partial^2}{\partial \xi^2} \frac{\partial \xi}{\partial r} = u^2 \frac{\partial^2}{\partial \xi^2} \quad \text{Eq. A-42} \quad [73]$$

where the index of the material is a function of r (the distance from the origin at the centre of the core). In standard form Eq. A-36 becomes

$$\frac{\partial^2 R(r)}{\partial \xi^2} + \frac{1}{\xi} \frac{\partial R(r)}{\partial \xi} + k_o^2 \left(1 - \frac{l^2}{\xi^2} \right) R(r) = 0 \quad \text{Eq. A-43} \quad [73]$$

The solutions are Bessel functions written as

$$R(r) = \begin{cases} AJ_l \left(\frac{ur}{a} \right) & \text{for } r \leq a \\ CK_l \left(\frac{wr}{a} \right) & \text{for } r \geq a \end{cases} \quad \text{Eq. A-44} \quad [73]$$

where $J_l(ur/a)$ is the l^{th} order Bessel function of the first kind, and $K_l(wr/a)$ is the l^{th} order modified Bessel function of the first and second kind. The parameters u^2 and w^2 are defined as.

$$u(\lambda)^2 = k_o^2 a^2 \left(n_1(\lambda)^2 - n_{eff}(\lambda)^2 \right) \quad \text{Eq. A-45} \quad [73]$$

$$w(\lambda)^2 = k_o^2 a^2 \left(n_{eff}(\lambda)^2 - n_2(\lambda)^2 \right) \quad \text{Eq. A-46} \quad [73]$$

where n_1 is the refractive index of the core and n_2 is the refractive index of the cladding. The relationship between u and w is given by

$$u(\lambda)^2 + w(\lambda)^2 = V(\lambda)^2 \quad \text{Eq. A-47} \quad [73]$$

where the $V(\lambda)$ gives the confinement in the core and is defined by

$$V(\lambda) = \frac{2\pi}{\lambda} a \left(n_1(\lambda)^2 - n_2(\lambda)^2 \right)^{1/2} \quad \text{Eq. A-48} \quad [73]$$

At the boundary between the core and the cladding the two definitions for $R(a)$ must be equal and continuous so that there is no discontinuity at the boundary as

$$R(a-0) = R(a+0) \quad \text{Eq. A-49} \quad [73]$$

$$\left. \frac{dR(r)}{dr} \right|_{a-0} = \left. \frac{dR(r)}{dr} \right|_{a+0} \quad \text{Eq. A-50} \quad [73]$$

This produces a system of equations given by

$$\begin{bmatrix} J_l(u) & -K_l(w) \\ uJ_l'(u) & -wK_l'(w) \end{bmatrix} \quad \text{Eq. A-51} \quad [73]$$

where the prime denotes the derivative with respect to r . If there is a solution to the system of equations then the determinant must be zero so that

$$\begin{vmatrix} J_l(u) & -K_l(w) \\ uJ_l'(u) & -wK_l'(w) \end{vmatrix} = -wJ_l(u)K_l'(w) + uJ_l'(u)K_l(w) = 0 \quad \text{Eq. A-52} \quad [73]$$

This results in the characteristic equation

$$\frac{uJ_l'(u)}{J_l(u)} = \frac{wK_l'(w)}{K_l(w)} \quad \text{Eq. A-53} \quad [73]$$

Using the properties of the Bessel functions, explicit forms for $LP_{l,m}$ modes are given by

$$\begin{aligned} \frac{J_0(u)}{uJ_1(u)} &= \frac{K_0(w)}{wK_1(w)} \quad \text{for } l=0 \quad \text{and } m \geq 1 \\ \frac{J_l(u)}{uJ_{l-1}(u)} &= -\frac{K_l(w)}{wK_{l-1}(w)} \quad \text{for } l \geq 1 \quad \text{and } m \geq 1 \end{aligned} \quad \text{Eq. A-54} \quad [73]$$

One may obtain $n_{eff}(\lambda)$ for each mode in an optical fiber by solving Eq. A-54 by looking for the intersection of the curves generated by the functions on both sides of the equation. Given Eq. A-47 and knowledge of $V(\lambda)$ from Eq. A-48 the equality is only a function of $n_{eff}(\lambda)$. As a result $n_{eff}(\lambda)$ may be obtained from the solution to Eq. A-54. In many applications the fiber is designed to support only one mode, however, the use of fibers with few modes is becoming important for increasing data throughput in an optical network as discussed in [Chapter 1](#). Matlab code using the developments in this section to solve $n_{eff}(\lambda)$ for SMF28 fiber is presented in [Appendix F](#). The dispersion within an optical fiber is determined by both the material dispersion and the waveguide dispersion (due to geometry of the fiber). As a result, if the material dispersion is known then knowledge of the dispersion in an optical

channel requires either accurate measurement of the dimensions of the waveguide (since fabrication not perfect) or direct empirical measurement of the total dispersion (material and waveguide effects) using a characterization technique. In the next sections we will look at the meaning of the effective index and its relationship to the chromatic dispersion in a fiber.

Appendix B: Alternative dispersion extraction techniques

This section describes alternative techniques for extracting second order dispersion from a balanced spectral interferogram such as that produced using balanced spectral interferometry or virtual reference interferometry.

B.1.1. Extraction of second order dispersion from the group delay curve

It is possible to measure the second order dispersion by differentiating the fit to the first order dispersion (group delay) via (2-12). This method is only practical if the noise in the group delay curve is very low as the noise (scatter) in the group delay plot greatly affects the slope of the fit, which makes the results dependent on the type of fit chosen. This technique is useful when it is necessary to generate dispersion curves with low scatter (analytical differentiation of fit has no scatter). As the accuracy of this technique depends on the noise in the group delay plot (fit to scattered points produces second order dispersion curves with large error, as demonstrated in [Chapter 2](#)) these measurements may be checked using direct second order dispersion measurements.

B.1.2. Extraction of the second order dispersion via a polynomial fit

In this section a method for extracting the second order dispersion from a balanced spectral interferogram is presented. This method was developed to achieve high immunity to noise in the interference pattern by using all (or most) of the peaks and valleys in the interference pattern to compute the second order dispersion. This method operates under the assumption that third and higher order dispersion is negligible which is true for most optical fibers. Starting with Eq. 2-32 and simplifying the equation by cutting off all of the terms above $d^2 n_{eff} / d\lambda^2 \Big|_{\lambda_0}$ gives

$$\begin{aligned} |\varphi(\lambda_m) - \varphi(\lambda_n)| &\cong 4\pi \left\{ \left[\frac{(\lambda_m - \lambda_0)^2}{2!\lambda_m} - \frac{(\lambda_n - \lambda_0)^2}{2!\lambda_n} \right] \frac{d^2 n_{eff}}{d\lambda^2} \Big|_{\lambda_0} L_f \right\} \\ &\cong |m - n| \pi \end{aligned} \quad \text{Eq. B-1}$$

The error associated with this approximation is given by

$$\Delta |\varphi(\lambda_m) - \varphi(\lambda_n)|_{ERROR} \cong 4\pi \left\{ \left[\frac{(\lambda_m - \lambda_0)^3}{3!\lambda_m} - \frac{(\lambda_n - \lambda_0)^3}{3!\lambda_n} \right] \frac{d^3 n_{eff}}{d\lambda^3} \Big|_{\lambda_0} L_f + \dots \right\} \quad \text{Eq. B-2}$$

A plot is then produced by applying Eq. B-1 to the phase difference between λ_1 and all the peaks and valleys on the right side of λ_0 as well as to the phase difference between λ_{-1} and all the peaks and valleys on the left side of λ_0 such that

$$|\varphi(\lambda_m) - \varphi(\lambda_1)| \cong 4\pi \left\{ \left[\frac{(\lambda_m - \lambda_0)^2}{2!\lambda_m} - \frac{(\lambda_1 - \lambda_0)^2}{2!\lambda_1} \right] \frac{d^2 n_{eff_f}}{d\lambda^2} \Big|_{\lambda_0} L_f \right\} \quad \text{Eq. B-3}$$

$$\cong |m-1|\pi$$

$$|\varphi(\lambda_p) - \varphi(\lambda_{-1})| \cong 4\pi \left\{ \left[\frac{(\lambda_p - \lambda_0)^2}{2!\lambda_p} - \frac{(\lambda_{-1} - \lambda_0)^2}{2!\lambda_{-1}} \right] \frac{d^2 n_{eff_f}}{d\lambda^2} \Big|_{\lambda_0} L_f \right\} \quad \text{Eq. B-4}$$

$$\cong |p+1|\pi$$

Where λ_m is chosen from the peaks or valleys to the right of λ_1 from the set $[\lambda_2, \lambda_3, \dots, \lambda_\infty]$ with $m = [2, 3, \dots, \infty]$ and λ_p is chosen from the peaks or valleys to the left of λ_{-1} from the set $[\lambda_{-2}, \lambda_{-3}, \dots, \lambda_{-\infty}]$ where $p = [-2, -3, \dots, -\infty]$. The points from the right side of λ_0 are plotted in the upper right quadrant of the plot using Eq. B-3 and the points from the left side of λ_0 are plotted in the lower left quadrant using Eq. B-4, as illustrated in Fig. B-1.

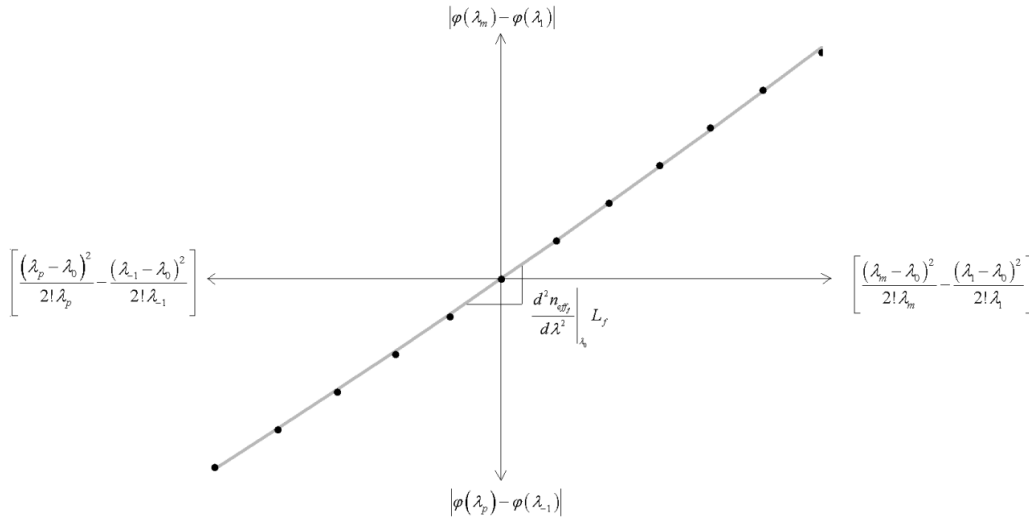


Fig. B-1. Plot generated using all the peaks and valleys in the interferogram

A polynomial fit (may be second or third order) to the plot in Fig. B-1, followed by analytical differentiation, gives $d^2 n_{eff_f} / d\lambda^2 \Big|_{\lambda_0} L_f$ which may be converted to dispersion \times length values using Eq. 1-7. Note that a requirement for an absolute minimum or maximum number of points in the plot may be imposed to further improve noise immunity. Additionally, noise immunity may also be improved by imposing a tolerance to the change in the period between peak and valley points in order to limit the number of points allowed in the plot.

B.1.3. Extraction of the second order dispersion: multiple measurements

In this approach, the average dispersion length is calculated using multiple phase difference measurements in the interferogram. Solving for $d^2 n_{eff} / d\lambda^2 \big|_{\lambda_0} L_f$ in Eq. B-1 gives

$$D(\lambda_0)L_f \cong -\frac{\lambda_0}{c} \frac{|m-n|}{2 \left[\frac{(\lambda_m - \lambda_0)^2}{\lambda_m} - \frac{(\lambda_n - \lambda_0)^2}{\lambda_n} \right]} \quad \text{Eq. B-5}$$

The dispersion parameter is then calculated using all (or as many as desired) peaks and valleys from each side of the interferogram. An expression for this process is given as

$$D(\lambda_0)L_f \cong \sum_{m=1}^K \sum_{n=1}^L \left\{ \frac{1}{KL} \frac{-\lambda_0 |m-n|}{2c \left[(\lambda_m - \lambda_0)^2 / \lambda_m - (\lambda_n - \lambda_0)^2 / \lambda_n \right]} \right\} \quad \text{Eq. B-6}$$

The combined average from both sides of the balance point λ_0 is the average over the entire interference pattern. The advantage of this technique is that it has high immunity to noise in the interference pattern due to the averaging of the phase over all peaks and valleys. In the next section, the accuracy of this approach will be improved by including the effect of the third order dispersion by combining this approach and the matrix approach discussed earlier.

B.1.4. Combined matrix & multiple measurements

This section describes a slightly more complex method for extraction of the second order dispersion that is immune to noise and includes the contribution of third order dispersion. In this section the method discussed in the previous section is expanded to include the third order dispersion by combining it with the Matrix approach discussed earlier. Here, two phase difference equations are produced from Eq. 2-32, given as

$$\begin{aligned}
|\varphi(\lambda_m) - \varphi(\lambda_n)| &= \left\{ \begin{aligned} &\overbrace{\left[\frac{(\lambda_m - \lambda_0)^2}{\lambda_m} - \frac{(\lambda_n - \lambda_0)^2}{\lambda_n} \right]}^{p_{m,n}} \frac{d^2 n_{\text{eff}_f}}{d\lambda^2} \Big|_{\lambda_0} L_f + \\ &\overbrace{\left[\frac{(\lambda_m - \lambda_0)^3}{3\lambda_m} - \frac{(\lambda_n - \lambda_0)^3}{3\lambda_n} \right]}^{q_{m,n}} \frac{d^3 n_{\text{eff}_f}}{d\lambda^3} \Big|_{\lambda_0} L_f + \dots \end{aligned} \right\} = |m-n|/2 \\
|\varphi(\lambda_{m+1}) - \varphi(\lambda_n)| &= \left\{ \begin{aligned} &\overbrace{\left[\frac{(\lambda_{m+1} - \lambda_0)^2}{\lambda_{m+1}} - \frac{(\lambda_n - \lambda_0)^2}{\lambda_n} \right]}^{r_{m+1,n}} \frac{d^2 n_{\text{eff}_f}}{d\lambda^2} \Big|_{\lambda_0} L_f + \\ &\overbrace{\left[\frac{(\lambda_{m+1} - \lambda_0)^3}{3\lambda_{m+1}} - \frac{(\lambda_n - \lambda_0)^3}{3\lambda_n} \right]}^{s_{m+1,n}} \frac{d^3 n_{\text{eff}_f}}{d\lambda^3} \Big|_{\lambda_0} L_f + \dots \end{aligned} \right\} = |m-n+1|/2
\end{aligned} \tag{Eq. B-7}$$

which, if the terms above $d^2 n_{\text{eff}_f} / d\lambda^2 \Big|_{\lambda_0} L_f$ are cut off, may be expressed in Matrix form as

$$\begin{bmatrix} p_{m,n} & q_{m,n} \\ r_{m+1,n} & s_{m+1,n} \end{bmatrix} \begin{bmatrix} d^2 n_{\text{eff}_f} / d\lambda^2 \Big|_{\lambda_0} \\ d^3 n_{\text{eff}_f} / d\lambda^3 \Big|_{\lambda_0} \end{bmatrix} L_f \cong \begin{bmatrix} |m-n|/2 \\ |m-n+1|/2 \end{bmatrix} \tag{Eq. B-8}$$

The solution to the system is given by

$$\begin{bmatrix} d^2 n_{\text{eff}_f} / d\lambda^2 \Big|_{\lambda_0} \\ d^3 n_{\text{eff}_f} / d\lambda^3 \Big|_{\lambda_0} \end{bmatrix} L_f \cong \frac{1}{(p_{m,n} s_{m+1,n} - q_{m,n} r_{m+1,n})} \begin{bmatrix} s_{m+1,n} & -q_{m,n} \\ -r_{m+1,n} & p_{m,n} \end{bmatrix} \begin{bmatrix} |m-n|/2 \\ |m-n+1|/2 \end{bmatrix} \tag{Eq. B-9}$$

Since we are typically only interested in calculating the second order dispersion (the dispersion parameter \times length)

we are interested in the $d^2 n_{\text{eff}_f} / d\lambda^2 \Big|_{\lambda_0}$ term which is given by

$$d^2 n_{\text{eff}_f} / d\lambda^2 \Big|_{\lambda_0} L_f \cong \frac{s_{m+1,n} |m-n| - q_{m,n} |m-n+1|}{2(p_{m,n} s_{m+1,n} - q_{m,n} r_{m+1,n})} \tag{Eq. B-10}$$

The second order dispersion \times length can then be found by combining Eq. B-10 and Eq. 1-7 which results in

$$D(\lambda_0) L_f \cong -\frac{\lambda_0}{c} \frac{s_{m+1,n} |m-n| - q_{m,n} |m-n+1|}{2(p_{m,n} s_{m+1,n} - q_{m,n} r_{m+1,n})} \tag{Eq. B-11}$$

Summation over multiple peaks and valleys in the inference pattern is described by

$$D(\lambda_0) L_f \cong \sum_{m=1}^{K-1} \sum_{n=1}^L \frac{1}{(K-1)L} \frac{\lambda_0 (s_{m+1,n} |m-n| - q_{m,n} |m-n+1|)}{2c (p_{m,n} s_{m+1,n} - q_{m,n} r_{m+1,n})} \tag{Eq. B-12}$$

Appendix C: Comparison of resolution/scatter in USI vs. BSI (VRI)

This section formally compares the first order dispersion (group delay) resolution (and scatter) in USI to that in BSI (or VRI). This comparison is appropriate since both techniques are capable of measuring first order dispersion (group delay) directly from the interference pattern. This section demonstrates that since the resolution in USI is dependent on the window size used in the Fourier transform, the resolution in USI only approaches that in BSI if the optimum window size is chosen. However, since the optimum window size cannot be known apriori, BSI techniques generally provide higher resolution than USI based techniques. This is the reason why experimentalists go to the trouble of setting up and balancing a reference path so that BSI can be used. It should also be noted here that the comparisons in this section between USI and BSI will also apply to USI and virtual reference interferometry (VRI) since the virtual reference takes the place of the physical reference in BSI making the two techniques equivalent.

C.1. Resolution and scatter in USI

This section provides a formal mathematical treatment of this problem. The application of a Fourier transform to a windowed section of the interference pattern may be described mathematically as a multiplication between the cosine function and the rectangular function, where the rectangular function is defined by

$$\text{rect}(a(\lambda - \lambda_{0_{avg}})) = \begin{cases} 0 & \text{if } |a(\lambda - \lambda_{0_{avg}})| > \frac{1}{2} \\ \frac{1}{2} & \text{if } |a(\lambda - \lambda_{0_{avg}})| = \frac{1}{2} \\ 1 & \text{if } |a(\lambda - \lambda_{0_{avg}})| < \frac{1}{2} \end{cases} \quad \text{Eq. C-1}$$

and the width of the window is given as $1/a$, as illustrated in Fig. C-1(a). The signal input to the Fast Fourier Transform (FFT) algorithm is also illustrated in Fig. C-1(b).

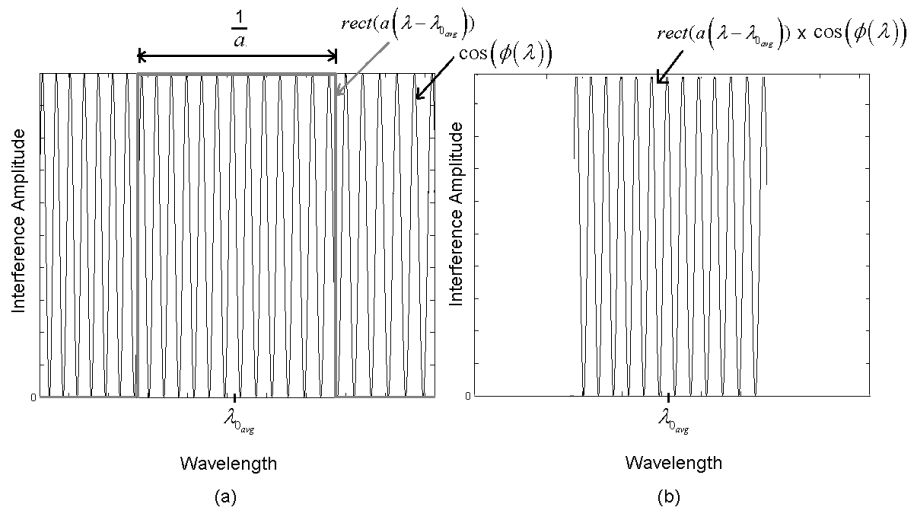


Fig. C-1. Windowing a section of the interference pattern is equivalent to multiplication of the cosine with the rectangular function.

The small window approximation

If the size of the window chosen is small enough, the frequency of the interference fringes within the window can be considered approximately periodic (in reality it is continuously variable as a function of wavelength). The effect of the aperiodic nature of the interference pattern (aperiodicity is due to dispersion) will be included in the next part of the derivation. The function input to the Fourier transform may therefore be described by

$$h_{\text{window}}(\lambda) = \text{rect}\left(a(\lambda - \lambda_{0\text{avg}})\right) \cos\left(\frac{2\pi|\nu_0|\lambda}{b}\right) \quad \text{Eq. C-2}$$

where $|\nu_0|$ is the average frequency of the interference within the window (given by Eq. 2-21) and $\lambda_{0\text{avg}}$ is the wavelength at the centre of the window. The Fourier transform of the rectangular function is

$$\text{rect}(a\lambda) \xrightarrow{FT} \frac{1}{|a|} \text{sinc}\left(\frac{\nu}{a}\right) \quad \text{Eq. C-3} \quad [47]$$

The rectangular function in Eq. C-2, however, is shifted in the wavelength domain; therefore, the shifting property of the Fourier transform must be applied. This property is given by

$$x(\lambda - \lambda_0) \xrightarrow{FT} e^{-j\nu\lambda_0} X(\nu) \quad \text{Eq. C-4} \quad [47]$$

phase shift

Applying this property to Eq. C-3 gives

$$\text{rect}\left(a(\lambda - \lambda_0)\right) \xrightarrow{FT} e^{-j\nu a \lambda_0} \frac{1}{|a|} \text{sinc}\left(\frac{\nu}{a}\right) \quad \text{Eq. C-5}$$

The Fourier transform of the cosine function is defined as

$$\cos(b\lambda) \xrightarrow{FT} \frac{1}{2} \left(\delta\left(\nu - \frac{b}{2\pi}\right) + \delta\left(\nu + \frac{b}{2\pi}\right) \right) \quad \text{Eq. C-6} \quad [47]$$

Applying the Fourier transform rule

$$f(\lambda)g(\lambda) \xrightarrow{FT} (F \otimes G)(\nu) \quad \text{Eq. C-7} \quad [47]$$

to Eq. C-2 gives

$$H(\nu) = e^{-j\nu a \lambda_0} \frac{1}{a} \text{sinc}\left(\frac{\nu}{a}\right) \otimes \frac{1}{2} \left(\delta(\nu - |\nu_0|) + \delta(\nu + |\nu_0|) \right) \quad \text{Eq. C-8}$$

where c is the speed of light in vacuum. Since only one side of the frequency spectrum (Fig. 2-10(b)) is required this expression may be simplified to

$$H(\nu) = e^{-j\nu a \lambda_0} \frac{1}{2a} \operatorname{sinc}\left(\frac{\nu}{a}\right) \otimes (\delta(\nu - |\nu_0|)) \quad \text{Eq. C-9}$$

Using the sifting property of the delta δ function given by

$$\begin{aligned} f(\nu) \otimes \delta(\nu - \tau) &= \int_{-\infty}^{\infty} f(x) \cdot \delta(\nu - \tau - x) dx \\ &= \int_{-\infty}^{\infty} f(x) \cdot \delta(x - (\nu - \tau)) dx \quad \text{since } \delta(x) = \delta(-x) \\ &= f(\nu - \tau) \end{aligned} \quad \begin{array}{l} \text{Eq. C-10} \\ [47] \end{array}$$

Eq. C-9 simplifies to

$$H(\nu) = \frac{1}{2a} \operatorname{sinc}\left(\frac{\nu - |\nu_0|}{a}\right) e^{-j\nu_0 a \lambda_0} \quad \text{Eq. C-11}$$

Since only the magnitude of the Fourier transform is considered here, the phase component may be neglected and the function further simplifies to

$$|H(\nu)| = \frac{1}{2a} \operatorname{sinc}\left(\frac{\nu - |\nu_0|}{a}\right) \quad \text{Eq. C-12}$$

The Fourier transform applied to a small windowed section of the interference is illustrated in Fig. C-2.

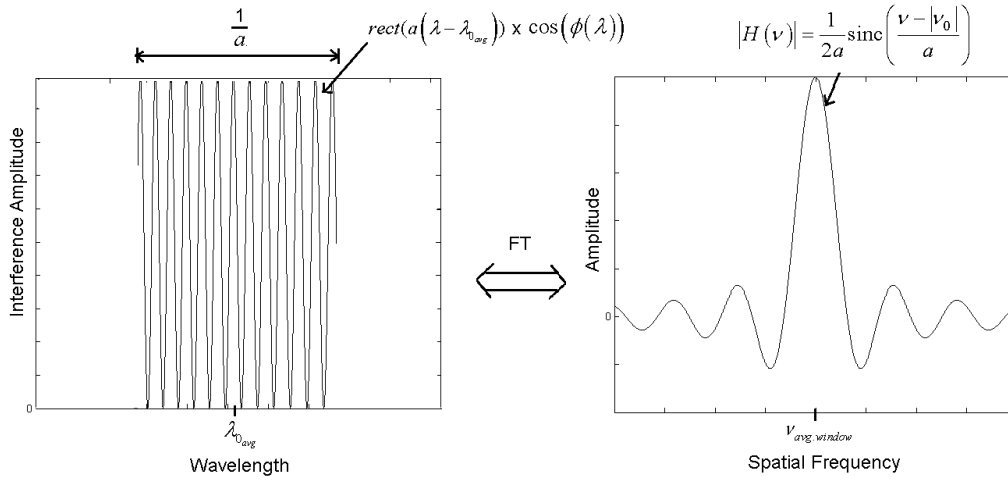


Fig. C-2. Visualization of Fourier transform on a windowed section of the interference pattern for small window size.

The result in Eq. C-12 assumed a small window size so that the aperiodicity of the interference pattern could be neglected. However, Eq. C-12, shows that choosing a window size (given by $1/a$ in Fig. C-1 and Fig. C-2) can be detrimental since a small window size means that a must be large in which produces a wider peak in the $\operatorname{sinc}(\)$ function. An illustration of this effect is provided in Fig. C-3, which shows that when the window size is reduced (by

increasing the magnitude of a the peak of the $\text{sinc}(\)$ function is broadened in the spatial frequency (Fourier) domain.

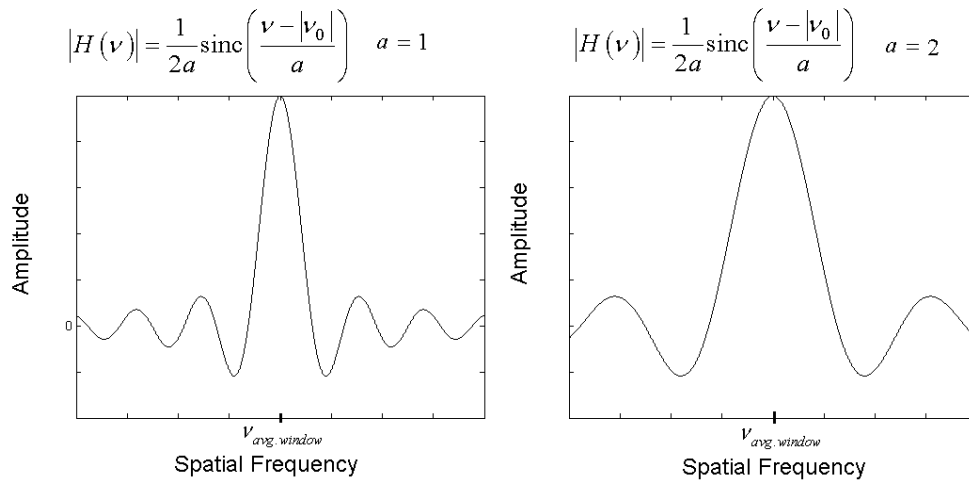


Fig. C-3. An illustration showing how a reduction in the window size (i.e. increasing the magnitude of a) results in a broadening of the peak of the $\text{sinc}(\)$ function in the spatial frequency domain.

This inverse relationship between the bandwidth of a signal and its Fourier transform is a fundamental property of the Fourier transform. As a result, choosing a window size that is too small broadens the width of the spatial frequency spectrum of $|H(\nu)|$. The broadening of the spatial frequency spectrum increases the width of the $\text{sinc}(\)$ function, resulting in increased uncertainty in the location of the peak at $|\nu_{avg.window}|$. This increase in peak width also ultimately lowers resolution by increasing the spacing required to resolve multiple peaks. In order to resolve two closely spaced peaks they must be no closer than the full width at half the maxima (FWHM) of each $\text{sinc}(\)$ function, as illustrated in Fig. C-4.

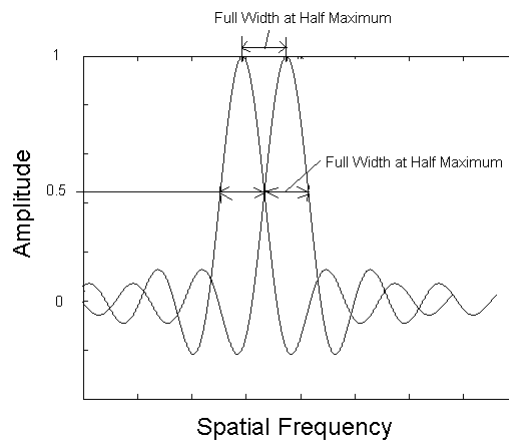


Fig. C-4. Minimum separation between peaks of each $\text{sinc}(\)$ function

Since the $\text{sinc}(\)$ function has no inverse the location where this occurs can be solved graphically by plotting

$$\text{sinc}(x) = \frac{\sin(\pi x)}{\pi x} \quad \text{Eq. C-13}$$

and solving for x at the FWHM point graphically (using Matlab) as shown in Fig. C-5.

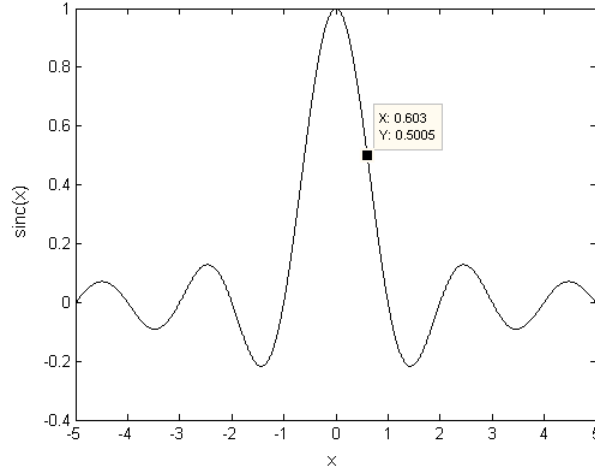


Fig. C-5. The $\text{sinc}(\)$ function reaches half its maximum value when $x = 0.6$

The $\text{sinc}(\)$ function reaches half of its maximum when $x = 0.6$. Therefore the $\text{sinc}(\)$ function in Eq. C-13 is equal to half its maximum when

$$v - |v_0| = 0.6a \quad \text{Eq. C-14}$$

Since this is only half the width of the peak it must be multiplied by a factor of 2 to be equal to the full width at half maximum (FWHM).

$$\Delta v_{\text{Small Window Limit (FWHM)}} = 2|v - v_0| = 1.2a \quad \text{Eq. C-15}$$

This part of the derivation considers small window sizes for which the frequency variation in the window can be ignored. It shows that choosing a window that is too small is detrimental since the width of the $\text{sinc}(\)$ function increases as the window size is reduced. The next part of the derivation will consider the choice of a larger window where the frequency variation in the interference pattern cannot be ignored and becomes significant. It will show that the variation in frequency adds new frequency content and broadens the peak of the $\text{sinc}(\)$ function, resulting in higher uncertainty and lower resolution.

Large window (including the effect of frequency variation)

If a large window with multiple frequency components is chosen then the aperiodic nature of the interference pattern (due to dispersion) must be considered. For large window sizes this effect dominates in broadening the peak of the

$\text{sinc}(\)$ function and ultimately erodes resolution. The analysis begins by considering a large window as the summation of multiple small windows (small enough that the frequency of the interference is approximately periodic within the small windows, as discussed in the previous section), each producing a $\text{sinc}(\)$ function of its own that is slightly shifted in frequency as illustrated in Fig. C-6.

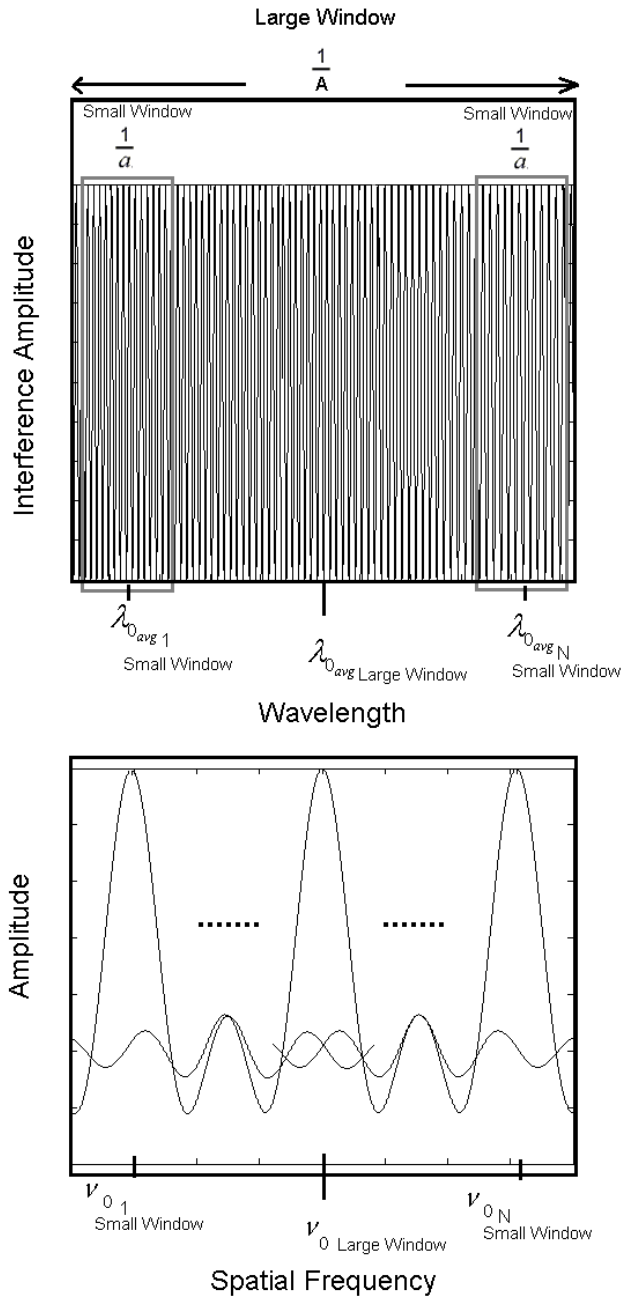


Fig. C-6. Multiple small windows used to take into account the aperiodicity in the interference pattern due to dispersion (in a large window) and the resulting Fourier transforms for each of the small windows.

The effective summation of all the $\text{sinc}(\)$ functions within the small window can be seen as convolution of the $\text{sinc}(\)$ functions with the rectangular function.

$$H_{\text{Total}}(\nu) = \frac{1}{2a} \text{sinc}\left(\frac{\nu - |v_{0_{\text{small window}}}|}{a}\right) \otimes \text{rect}\left(A\left(\nu - |v_{0_{\text{large window}}}| \right)\right) \quad \text{Eq. C-16}$$

The solution of this equation is not important, however, it is important to notice that its spectral width is *at least* $1/A$ (from the $\text{rect}(\)$ function). The spectral width in the large window limit is therefore given by

$$\Delta v_{\text{Large Window}} \geq \frac{1}{A} = \left| v_{0_N} \left(\lambda_{0_{\text{avg}N}} \right) \right|_{\text{Small Window}} - \left| v_{0_1} \left(\lambda_{0_{\text{avg}1}} \right) \right|_{\text{Small Window}} \quad \text{Eq. C-17}$$

Substitution of Eq. 2-21 into Eq. C-17 gives

$$\Delta v_{\text{Large Window Limit}} \geq 2L_f \left(\frac{N_g(\lambda_{0_{\text{avg}N}})}{\lambda_{0_{\text{avg}N}}^2} - \frac{N_g(\lambda_{0_{\text{avg}1}})}{\lambda_{0_{\text{avg}1}}^2} \right) \quad \text{Eq. C-18}$$

Assuming $\lambda_{0_{\text{avg}N}} - \lambda_{0_{\text{avg}1}} \ll \lambda_{0_{\text{avg}}}$ Eq. C-18 may be simplified to

$$\Delta v_{\text{Large Window Limit}} \geq \frac{2L_f}{\lambda_{0_{\text{avg}}}} \left(N_g(\lambda_{0_{\text{avg}N}}) - N_g(\lambda_{0_{\text{avg}1}}) \right) = \frac{2L_f}{\lambda_{0_{\text{avg}}}} \Delta N_g(\lambda_{0_{\text{avg}N}}, \lambda_{0_{\text{avg}1}}) \quad \text{Eq. C-19}$$

Furthermore, rearranging Eq. 1-7 to

$$\Delta N_g(\lambda_{0_{\text{avg}N}}, \lambda_{0_{\text{avg}1}}) = D \left(\lambda_{0_{\text{avg}}} \right) c(\lambda_{0_{\text{avg}N}} - \lambda_{0_{\text{avg}1}}) \quad \text{Eq. C-20}$$

followed by substitution into Eq. C-19 gives

$$\Delta v_{\text{Large Window Limit}} \geq \frac{2L_f}{\lambda_{0_{\text{avg}}}} D \left(\lambda_{0_{\text{avg}}} \right) c(\lambda_{0_{\text{avg}N}} - \lambda_{0_{\text{avg}1}}) \quad \text{Eq. C-21}$$

and since (see Fig. C-6)

$$\left(\lambda_{0_{\text{avg}N}} - \lambda_{0_{\text{avg}1}} \right) = \frac{1}{A} \quad \text{Eq. C-22}$$

The equation further simplifies to

$$\Delta v_{\text{Large Window}} \geq \frac{2L_f}{\lambda_{0,\text{avg. Large Window}}^2} D \left(\lambda_{0,\text{avg. Large Window}} \right) c \cdot \frac{1}{A} \quad \text{Eq. C-23}$$

The total resolution

The spectral width of a sinc() function produced by taking the Fourier transform of a windowed section of the interference pattern depends on the window size (Eq. C-15) and on the aperiodicity due to dispersion of the interference pattern within the window (Eq. C-23). The function that describes these two effects (given by Eq. C-16) is a convolution of these two phenomena. Therefore, the resulting width of the spatial frequency peak in Eq. C-16 can be determined by using the width property of convolution [74] given by

$$\begin{aligned} \Delta v_{\text{Total}} &= \Delta v_{\text{Small Window Limit}} + \Delta v_{\text{Large Window Limit}} \\ &= 1.2a + \frac{2L_f}{\lambda_{0,\text{avg. Large Window}}^2} D \left(\lambda_{0,\text{avg. Large Window}} \right) c \cdot \frac{1}{A} \end{aligned} \quad \text{Eq. C-24}$$

Recognizing that both a and A in Eq. C-24 both refer to the window size (the former to the small window limit and the latter to a large window). We replace these two terms with $1/\Delta\lambda_{\text{window}}$ in Eq. C-24 so the equation becomes

$$\begin{aligned} \Delta v_{\text{Total}} &= \Delta v_{\text{Small Window Limit}} + \Delta v_{\text{Large Window Limit}} \\ &= \frac{1.2}{\Delta\lambda_{\text{window}}} + \frac{2D \left(\lambda_{0,\text{avg. Window}} \right) L_f c}{\lambda_{0,\text{avg. Window}}^2} \Delta\lambda_{\text{window}} \end{aligned} \quad \text{Eq. C-25}$$

The first term dominates as the window size gets smaller (due to inverse nature of the bandwidth of a signal and its Fourier transform) and the second term dominates as the window size increases (due to increase in the frequency content within the window). The effect this has on both the resolution and scatter in the group delay plot is now examined. To determine how the minimum separation in the spatial frequency (Fourier) domain relates to the minimum group delay separation that can be measured, consider the interference pattern produced by a fiber with two modes

$$\begin{aligned}
I_{\text{Real}}(\lambda) &= A \cos(\phi_1(\lambda)) + B \cos(\phi_2(\lambda)) \\
&= A(\cos(\phi_1(\lambda)) + \cos(\phi_2(\lambda))) + (B - A)\cos(\phi_2(\lambda)) \\
&= 2A \cos\left(\frac{\phi_1(\lambda) + \phi_2(\lambda)}{2}\right) \underbrace{\cos\left(\frac{\phi_1(\lambda) - \phi_2(\lambda)}{2}\right)}_{\text{Low freq. Beat}} + (B - A)\cos(\phi_2(\lambda))
\end{aligned} \tag{Eq. C-26}$$

where $\phi_1(\lambda)$ is the phase of the first mode and $\phi_2(\lambda)$ is the phase of the second (adjacent) mode. The low frequency beat between modes is given by

$$I_{\text{Beat}}(\lambda) = \cos\left(\frac{\phi_1(\lambda) - \phi_2(\lambda)}{2}\right) \tag{Eq. C-27}$$

Assuming that the size of the window chosen is large enough to include several periods of the beat, a windowed Fourier transform may be used to extract the frequency of the beat where

$$\cos\left(\frac{\phi_1(\lambda) - \phi_2(\lambda)}{2}\right) = \cos\left(2\pi \left| \Delta \nu_{\text{Beat}} \left(\lambda_{0, \text{avg. Window}} \right) \right| \lambda\right) \tag{Eq. C-28}$$

Following a similar procedure as in Eq. 2-14 to Eq. 2-22, the beat frequency can be described by

$$\left| \Delta \nu_{\text{Beat}} \right| = c \frac{\Delta \tau_g}{\lambda_{0, \text{avg. Window}}^2} \tag{Eq. C-29}$$

Each of the elements in the cascade or modes in the fiber results in a separate group delay curve. Assuming that the group delay curves have equal slope (for simplicity), then each group delay curve produces a sinc() function in the spatial frequency domain, as illustrated in Fig. C-7.

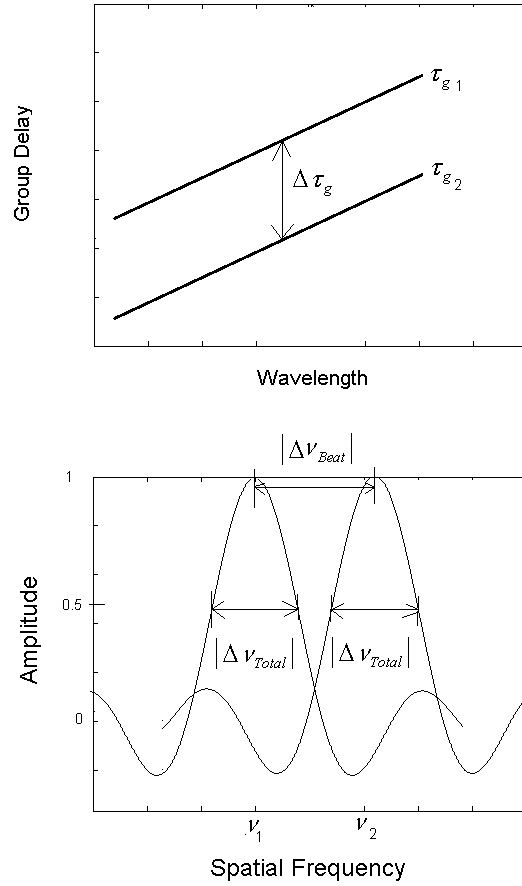


Fig. C-7. Relationship between beat frequency and group delay separation

In order to be able to resolve the peaks of the two $\text{sinc}(\)$ functions (i.e. resolve the modes)

$$|\Delta \nu_{Beat}| \geq |\Delta \nu_{Total}| \quad \text{Eq. C-30}$$

Substitution of Eq. C-25 and Eq. C-29 into Eq. C-30 gives

$$\Delta \tau_g \geq \frac{1.2 \lambda_{0, \text{avg. Window}}^2}{c \Delta \lambda_{\text{window}}} + 2D \left(\lambda_{0, \text{avg. Window}} \right) L_f \Delta \lambda_{\text{window}} \quad \text{Eq. C-31}$$

This equation gives the minimum group delay separation that can be resolved using a windowed Fourier transform

$$\Delta \tau_{g_{\text{min Windowed FT}}} = \frac{1.2 \lambda_{0, \text{avg. Window}}^2}{c \Delta \lambda_{\text{window}}} + 2D \left(\lambda_{0, \text{avg. Window}} \right) L_f \Delta \lambda_{\text{window}} \quad \text{Eq. C-32}$$

The resolution is also related to the scatter in the group delay curve produced using this technique. This is illustrated in Fig. C-8 which shows that the peaks of two modes are the closest they can get to each other when

$$|\Delta v_{Beat}| = |\Delta v_{Total}| \tag{Eq. C-33}$$

This can be related to a measure of the scatter in the group delay plot, as illustrated in Fig. C-8.

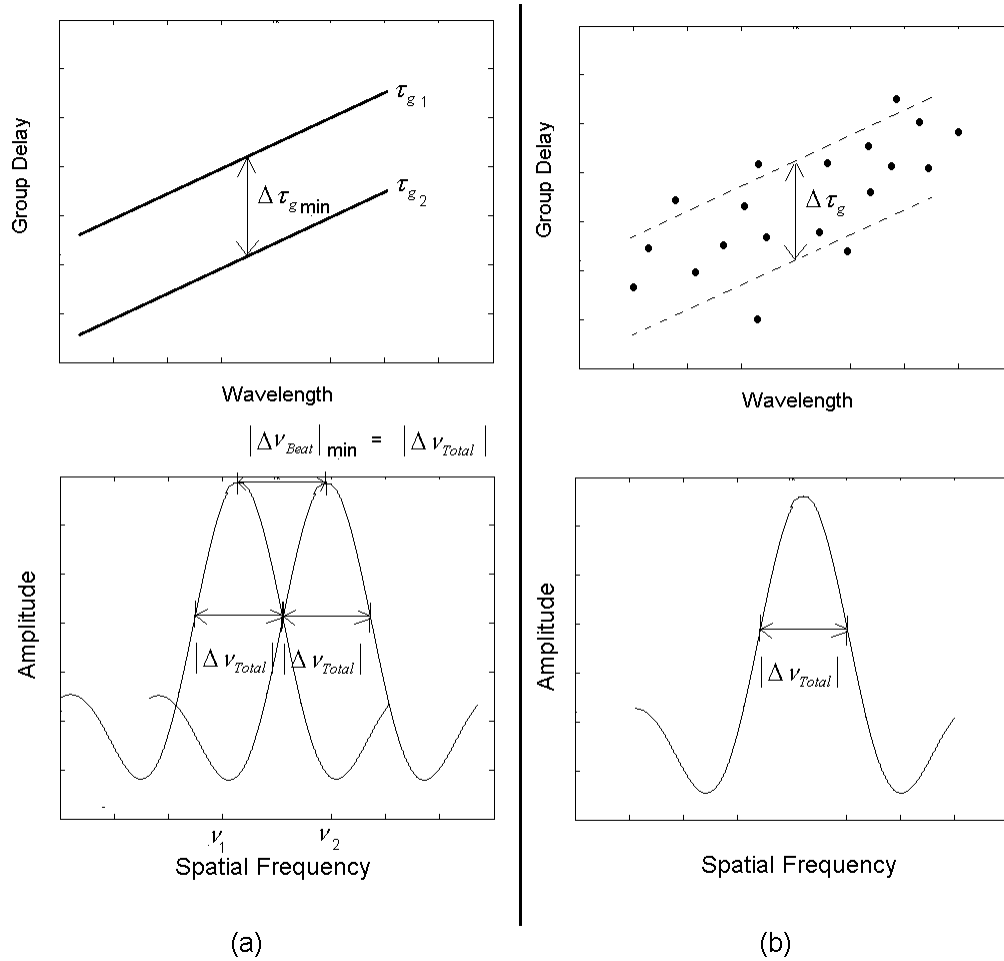


Fig. C-8. Equivalence of (a) spectral resolution (b) scatter in the group delay curve

where substitution of Eq. C-29 into Eq. C-33 gives

$$|\Delta v_{Total}| = c \frac{\Delta \tau_g}{\lambda_{0,avg.Window}^2} \tag{Eq. C-34}$$

which means that the scatter in the group delay plot, in the worst case scenario, is also given by Eq. C-32. This result indicates that the scatter in the group delay plot for USI also depends on the window size, which cannot be known a priori. This scatter is important since the measurement of second order dispersion requires curve fitting (cannot be measured directly) followed by analytical differentiation and the scatter affects the fit. This is the key problem with all USI based techniques.

C.2. Resolution and scatter in BSI

The resolution of a measurement technique is related to the ability to distinguish between features that have a small spatial separation. In balanced spectral interferometry, spatial resolution is related to the minimum spectral separation between multiple balance points. Multiple balance points can be produced by two closely spaced reflection points or even two closely spaced modes in a fiber to produce an interference pattern described by Eq. C-26. The resulting interference pattern has two balance points, with a minimum spectral separation that is equal to the sum of half the minimum bandwidth of each balance point, as shown in Fig. C-9.

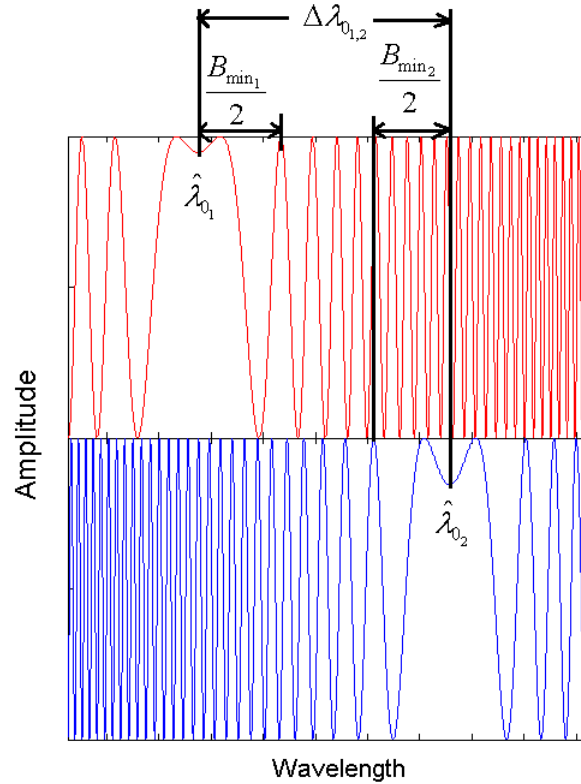


Fig. C-9. Relationship between minimum spectral separation and minimum bandwidth

where $\hat{\lambda}_{0_1}$ and $\hat{\lambda}_{0_2}$ are two balance points observed within a spectral scan. In order to resolve the balance points, they can be no closer to each other than

$$\hat{\lambda}_{0_2} - \hat{\lambda}_{0_1} \geq \frac{B_{\min_1}}{2} + \frac{B_{\min_2}}{2} \geq \frac{1}{2} \sum_{w=1}^2 \frac{\sqrt{6}}{\left(cL_{f_w} D_w(\hat{\lambda}_{0_w})\right)^{1/2}} \hat{\lambda}_{0_w} \quad \text{Eq. C-35}$$

This equation, therefore, gives the maximum spectral resolution for BSI based measurements. This equation may be converted to spatial resolution (i.e. minimum group delay separation) between balance points by assuming that the two modes have a similar dispersion $D_1(\hat{\lambda}_{0_1}) \cong D_2(\hat{\lambda}_{0_2})$ so that Eq. C-35 simplifies to

$$\Delta\lambda_{0,2} = |\hat{\lambda}_{0_2} - \hat{\lambda}_{0_1}| \geq \left(\frac{6}{cD(\hat{\lambda}_{0_{avg}})L_f} \right)^{\frac{1}{2}} (\hat{\lambda}_{0_{avg}}) \tag{Eq. C-36}$$

where $\hat{\lambda}_{0_{avg}} = (\hat{\lambda}_{0_1} + \hat{\lambda}_{0_2})/2$. Substitution of Eq. 1-1 into Eq. C-36 gives

$$\Delta\tau_{g_{\min}}^{\text{VRI}}(\lambda_{0,2}) = D(\hat{\lambda}_{0_{avg}})L_f\Delta\lambda_{0,2} = \left(\frac{6D(\hat{\lambda}_{0_{avg}})L_f}{c} \right)^{\frac{1}{2}} (\hat{\lambda}_{0_{avg}}) \tag{Eq. C-37}$$

The minimum resolution is illustrated in Fig. C-10(a). It is also important to note that this equation is also related to the scatter in the group delay points in the worst case scenario where $\Delta\lambda_{0,2} \equiv B_{\min}$ as illustrated in Fig. C-10(b).

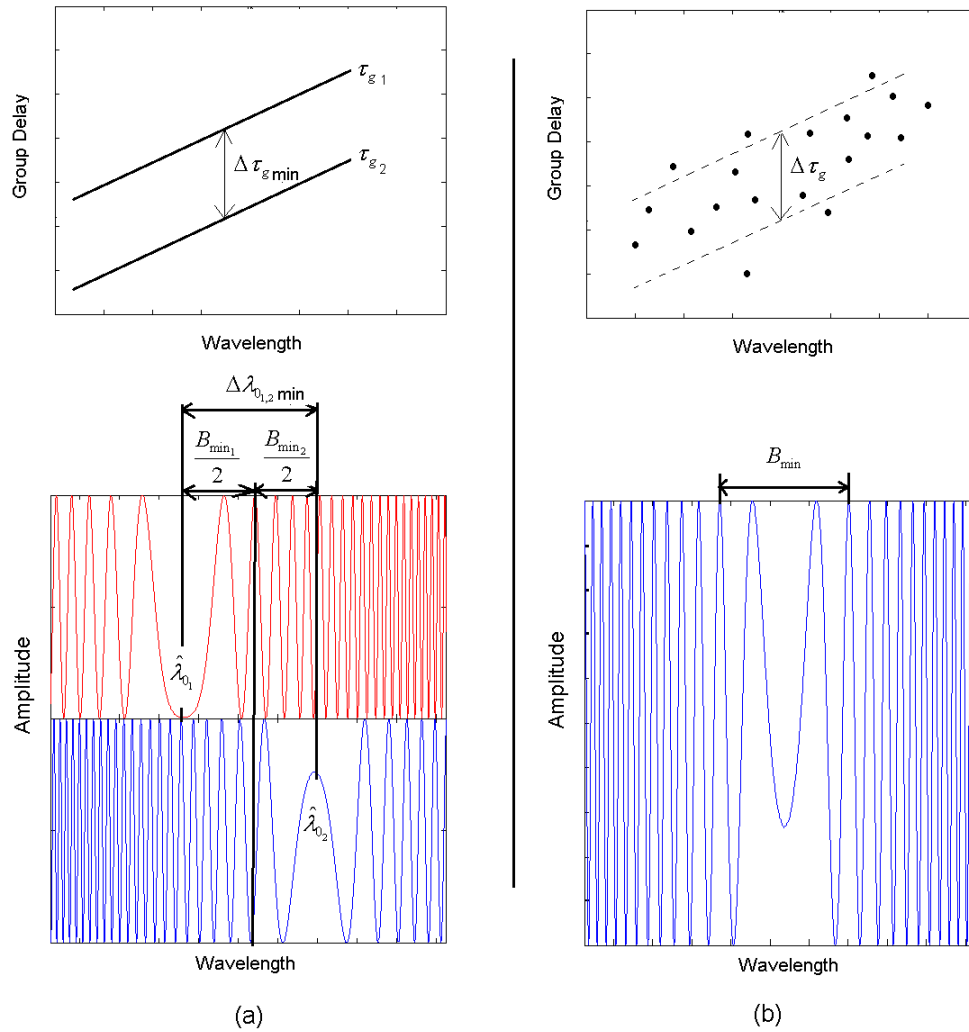


Fig. C-10. Equivalence of (a) spectral resolution and (b) scatter in the group delay curve

C.3. Comparison of the resolution and scatter in USI to BSI (VRI)

In this section, the performance of the USI technique that uses a windowed Fourier transform (USI-WFT) to directly measure the group delay is compared to balanced spectral interferometry for the ability to measure group delay. This comparison is appropriate since both of these techniques are capable of measuring group delay directly from the interference pattern. Although the USI-WFT technique is not capable of characterizing the second order dispersion directly from the interference pattern like BSI, one may only be interested in generating group delay curves. In this case, the USI-WFT technique may seem competitive with BSI. This section compares the resolution and scatter of the group delay plot in BSI to that in USI-WFT. It will demonstrate that the resolution and scatter in the USI-WFT technique depends on the window size. Since an optimum window size cannot be known apriori, the resolution of the USI-WFT technique is generally lower than BSI since the scatter cannot be minimized. Furthermore, this section compares the resolution in BSI to the hypothetical case when the optimum window size is chosen for the USI-WFT technique and shows that BSI is still slightly better in this case.

The minimum group delay resolution for BSI was given in Eq. C-37. Solving for $D(\lambda_{0,avg,Window})L_f$ in this equation gives

$$\left| D(\lambda_{0,avg,Window}) \right| L_f = \frac{c}{6} \left(\frac{\Delta \tau_{g_{BSI}^{min}}}{\lambda_{0,avg,Window}} \right)^2 \quad \text{Eq. C-38}$$

The minimum group delay resolution for USI-WFT was given in Eq. C-32. Solving for $D(\lambda_{0,avg,Window})L_f$ in this equation gives

$$\left| D(\lambda_{0,avg,Window}) \right| L_f = \frac{\Delta \tau_{g_{FT}^{min,Windowed}}}{2\Delta \lambda_{window}} - \frac{0.6}{c} \left(\frac{\lambda_{0,avg,Window}}{\Delta \lambda_{window}} \right)^2 \quad \text{Eq. C-39}$$

Equating Eq. C-38 and Eq. C-39 gives

$$\left(\frac{c}{6} \left(\frac{\Delta \tau_{g_{BSI}^{min}}}{\lambda_{0,avg,Window}} \right)^2 \right)^2 = \frac{\Delta \tau_{g_{FT}^{min,Windowed}}}{2\Delta \lambda_{window}} - \frac{0.6}{c} \left(\frac{\lambda_{0,avg,Window}}{\Delta \lambda_{window}} \right)^2 \quad \text{Eq. C-40}$$

Solving this equation for $\Delta \tau_{g_{FT}^{min,Windowed}}$ gives

$$\Delta \tau_{g_{\min}^{\text{Windowed FT}}} = C_1 \Delta \lambda_{\text{window}} + C_2 \cdot \frac{1}{\Delta \lambda_{\text{window}}} \quad \text{Eq. C-41}$$

where the terms $C_1 = \left(c \Delta \tau_{g_{\min}^{\text{BSI}}} / 3 \lambda_{0, \text{avg. Window}} \right)^2$ and $C_2 = 1.2 \lambda_{0, \text{avg. Window}}^2 / c$. This equation is a function of $\Delta \lambda_{\text{window}}$ and it can be minimized by finding

$$\frac{d \Delta \tau_{g_{\min}^{\text{Windowed FT}}}}{d \Delta \lambda_{\text{window}}} = C_1 - C_2 \cdot \frac{1}{\Delta \lambda_{\text{window}}^2} = 0 \quad \text{Eq. C-42}$$

so that the optimum window size is given as

$$\Delta \lambda_{\text{window}} = \left(\frac{C_2}{C_1} \right)^{\frac{1}{2}} = (3.6)^{\frac{1}{2}} \frac{\lambda_{0, \text{avg. Window}}^2}{c \Delta \tau_{g_{\min}^{\text{BSI}}}} \quad \text{Eq. C-43}$$

To ensure that and ensuring that $\Delta \tau_{g_{\min}^{\text{Windowed FT}}}$ is minimized, check that the curvature is positive

$$\frac{d^2 \Delta \tau_{g_{\min}^{\text{Windowed FT}}}}{d \Delta \lambda_{\text{window}}^2} = 2 C_2 \cdot \frac{1}{\Delta \lambda_{\text{window}}^3} = 2 \frac{1.2 \lambda_{0, \text{avg. Window}}^2}{c} \frac{1}{\Delta \lambda_{\text{window}}^3} > 0 \quad \text{Eq. C-44}$$

Since the curvature is positive the function is minimized and using the window size in Eq. C-43 gives the optimum window size. Substitution of the optimum window size in Eq. C-43 into Eq. C-41 gives

$$\Delta \tau_{g_{\min}^{\text{Windowed FT}}} = \frac{2.4}{(3.6)^{\frac{1}{2}}} \Delta \tau_{g_{\min}^{\text{BSI}}} \cong 1.265 \Delta \tau_{g_{\min}^{\text{BSI}}} \quad \text{Eq. C-45}$$

This result indicates that USI-WFT approaches the resolution of BSI when the optimum window size is chosen. However, since it is impossible to know the optimum window size for a given interference pattern, the resolution (minimum group delay difference and scatter in the group delay plot) of the BSI technique is generally better than the resolution in the USI-WFT technique, which cannot be minimized. This illustrates that the BSI technique is not only superior to the USI technique for its ability to directly characterize second order dispersion but it is also superior in its ability to characterize first order dispersion (assuming a high precision stage is available, of course). It demonstrates why experimentalists go to all the trouble of setting up a reference path. It should be noted here that this advantage of BSI will also be present in VRI except that the need for the high precision stage will be removed. A complete discussion of VRI is introduced in [Chapter 3](#).

Appendix D: Comparison of standard VRI and DVRI

Chapters 3 to 5 demonstrated several applications of both VRI and DVRI; however, one may question the need for VRI given that DVRI allows for the generation of dispersion plots with expanded bandwidths or measurements that would otherwise be impossible. This appendix shows what situations VRI is the optimal technique and what situations DVRI is optimal. Intuitively, one may consider that since DVRI provides a benefit (bandwidth compression), there must be an associated cost. This is in fact the case since bandwidth compression increases the certainty of the balance point which has a spatial dimension (in nm units) therefore by the uncertainty principle there must be greater uncertainty in the group delay which has a temporal dimension (in ps units). To demonstrate this with mathematical rigor requires a comparative error analysis between VRI and DVRI. This appendix, therefore, presents an analysis of the errors in each technique to identify situations where each technique is optimum.

D.1. Calibration error

In this thesis virtual reference has been used in both single arm configurations and dual arm configurations. The analysis that follows in the next sections will assume the common path configuration. The use of a dual arm configuration requires calibration of the dispersion of the optical components in the reference arm (i.e. fibers, collimators, mirrors, etc.) which has an associated error. The equations which will be developed for the common path configuration (which is free from calibration error) will also apply if the dual arm configuration is used. The only difference is that the calibration error must be included with the error in the measurement using a common path configuration (which does not have calibration error). When a measurement is determined by n independent components with individual uncertainties, the total absolute uncertainty ΔF in the result where $F = F(x_1, x_2, \dots, x_n)$ is given by [75] [76]

$$\Delta F = \sqrt{\sum_{i=1}^N (dF/dx_i)^2 \cdot (\Delta x_i)^2} \quad \text{Eq. D-1}$$

Therefore since the calibration error is independent of the other sources of measurement error, the total absolute error in the dual arm configuration may be obtained by adding the calibration error to the measurement error using a common path configuration in quadrature as

$$\Delta_{dual\ arm} = \sqrt{\left(\Delta_{common\ path}\right)^2 + \Delta_{calibration}^2} \quad \text{Eq. D-2}$$

One of the advantages of the virtual reference technique in general is the ability to utilize the common path configuration (VRI and DVRI presented in Chapters 3 to 5) when a tunable laser with sufficient resolution is available. The ability to operate using this configuration is a key advantage compared to using a physical reference path (as in balanced spectral interferometry). This is because a physical reference requires that the dispersion of the optical components used in the path (i.e. fibers, collimators, lenses etc) must be calibrated, which introduces calibration error into the resulting measurements. In the VRI and DVRI setups that employ a common path

interferometer, the reference path is entirely virtual, therefore its dispersion and length are known with absolute certainty. This eliminates the need for calibration and makes virtual reference interferometers using this configuration more accurate than balanced spectral interferometers. Furthermore, the use of an air path in dual arm interferometer configurations results in additional noise in the interference due to environmental changes in the temperature and pressure in the air path. Air flow in the air path can also cause further noise, especially if the air flow occurs during the scan when the interference pattern is being obtained. In order to mitigate these errors in a dual arm interferometer with a free space reference path, the free space path must be isolated from the environment. If the effects of variations in temperature and pressure are to be mitigated, the free space reference path must be vacuum sealed. Otherwise the environment (i.e. altitude (pressure) and climate (humidity)) will produce variable results for the same test fiber. A VRI or DVRI based system employing a common path configuration is immune to these effects. This advantage can be important for quality control applications in a manufacturing process where test facilities can be located anywhere around the world.

D.2. Interference phase noise

Neither common path nor dual arm interferometers, however, are immune to environmental factors, such as those that cause thermal fluctuations in fiber length during the scan. These environmental sources of error can be mitigated (though not completely eliminated) by isolating the test fiber from the environment (i.e. enclosing it in an air tight container). Other sources of error common to both configurations are those that reduce the fidelity of the raw interference pattern (errors in the measured intensity or wavelength points) leading to phase errors in the amplitude modulation. One example of this is noise in the intensity of the interference pattern due to a low signal-to-noise ratio. Another example is error in the wavelength location due to limited resolution or nonlinearity in the wavelength sweep. Another source of error is variation in the sampling frequency of the (detector) intensity and wavelength (wavemeter) measurements leading to a loss of synchronization between the two measurements. This effect can be mitigated by synchronization of the clocks via triggering mechanisms.

Interference phase noise may be caused by a number of factors, as discussed above. The main effect of noise, however, is that it leads to variations in the phase of the raw interference pattern, which translates into a variation of the phase of the amplitude modulation. The next section will show the effect of this variation on a virtual reference measurement.

D.3. Effects of interference phase noise on peak/valley location

In all virtual reference interferometry (i.e. both VRI and DVRI), a real interference pattern is produced in the first step (see [Chapter 3.2](#)). All of the phase error in a virtual reference measurement comes from this step. A real interference pattern containing some phase error may be described by

$$I_{Real}(\lambda) \cong U_{in}^2 I_1^4 R \left(2 - 2 \cos(2\beta_f L_f + \Delta\phi(\lambda)) \right) \quad \text{Eq. D-3}$$

where $\Delta\phi(\lambda)$ is the phase error as a function of wavelength due to the interference phase noise. In the second step of a virtual reference measurement, the length of the virtual reference L_v that balances the group delay of the test fiber is estimated from the phase (period) of $I_{Real}(\lambda)$, which is more difficult as the interference phase noise increases. In the third step, a spectral interference pattern is generated by simulating a virtual reference with a length that balances the test path at a wavelength within the scan range.

$$I_{virtual}(\lambda) = \cos(2\beta_v L_v) \quad \text{Eq. D-4}$$

where $\beta_v = k_0$ for VRI or defined by the dispersion of the virtual reference in DVRI. When the spectral interference pattern of the virtual reference is multiplied point-by-point with that of the raw interference pattern, a second order interference pattern with an amplitude modulation is produced.

$$I_{SO}(\lambda) = I_{Real}(\lambda) \times I_{virtual}(\lambda) \quad \text{Eq. D-5}$$

$$\propto \left(\underbrace{\cos((\beta_f L_f - \beta_v L_v + \Delta\phi(\lambda))) + \cos((\beta_f L_f + \beta_v L_v + \Delta\phi(\lambda)))}_{\text{Amplitude modulation}} \right)$$

In the fourth step, the amplitude modulation is extracted from the second order interference pattern by low pass filtering.

$$I_{amp.mod}(\lambda) \propto \cos((\beta_f L_f - \beta_v L_v + \Delta\phi(\lambda))) \quad \text{Eq. D-6}$$

The amplitude modulation, illustrated in Fig. D-1 is approximately symmetric across a balance point at λ_0 which is the wavelength location where the group delay of the reference path equals that of the test path. This wavelength location λ_0 therefore is one measured quantity in VRI which is subject to error (dependent variable). To locate λ_0 , a peak/valley pair on either side of λ_0 is required (i.e. $\lambda_{-2}, \lambda_{-1}, \lambda_1, \lambda_2$ in Fig. D-1). These same peak/valley points are also used to measure the dispersion \times length of the fiber. Therefore, the only measured quantities in a virtual reference measurement (or also a BSI measurement) are the locations of these four peaks/valleys. The error in locating these four peak/valley locations (i.e. $|\Delta\lambda_{-2}|, |\Delta\lambda_{-1}|, |\Delta\lambda_1|, |\Delta\lambda_2|$ in Fig. D-1) is due to the phase error $\Delta\phi(\lambda)$ in the raw interference pattern $I_{Real}(\lambda)$ (due to the interference phase noise).

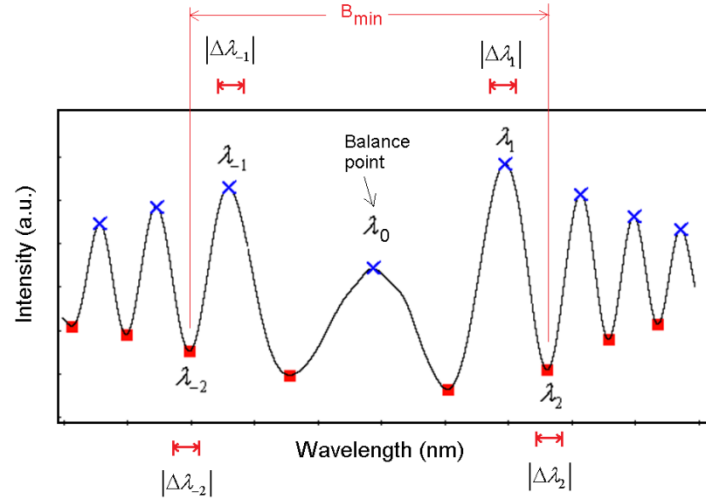


Fig. D-1. Amplitude modulation extracted from second order interference pattern via low pass filtering. The phase error in the raw interference pattern (due to interference phase noise) leads to errors in the peak locations $\lambda_{-2}, \lambda_{-1}, \lambda_1, \lambda_2$

D.4. Effect of error in peak/valley location on balance point

The balance point λ_0 is determined using Eq. 2-24. Assuming that $\lambda_{-2}, \lambda_{-1}, \lambda_1, \lambda_2$ are independent variables then the total absolute uncertainty (error) in λ_0 may be found using Eq. D-1 as

$$\Delta\lambda_0 = \sqrt{\sum_{n=-2,-1,1,2} \left(\frac{\lambda_0}{\lambda_n}\right)^4 \cdot (\Delta\lambda_n)^2} \quad \text{Eq. D-7}$$

A simplifying approximation can be made by assuming that $|\lambda_n - \lambda_0| \ll \lambda_0$ so that

$$\Delta\lambda_0 = \sqrt{\sum_{n=-2,-1,1,2} (\Delta\lambda_n)^2} \quad \text{Eq. D-8}$$

This means that the total absolute uncertainty in the balance point is equivalent the sum of the uncertainties in the peak/valley locations added in quadrature.

D.5. Effect of peak/valley error on first order dispersion

D.5.1. Standard VRI

In standard VRI the group delay is known with absolute certainty since it is simulated. Therefore there is no error in the value of group delay as it is the independent variable. This is effectively because in VRI

$$\frac{d\tau_{g_v}}{d\lambda_0} = D_v(\lambda)L_v = 0 \quad \text{Eq. D-9}$$

The wavelength of the group delay, however, is measured by locating λ_0 which is subject to error. Therefore, in a group delay plot generated via standard VRI the scatter is only along the wavelength axis with a total absolute uncertainty of $\Delta\lambda_0$ given in Eq. D-7 (or Eq. D-8).

D.5.2. Dispersive VRI

In DVRI, however, it is not the exact value of the group delay that is known but the curve that defines the group delay. The exact value of the group delay is only determined after the balance point λ_0 is measured from the interferogram, since at the balance point $\tau_{g_{test\ path}}(\lambda_0) = \tau_{g_v}(\lambda_0)$. Therefore an error in measuring the balance point (i.e. $\Delta\lambda_0$) leads to an error in $\tau_{g_v}(\lambda_0)$, which is therefore also an error in the measurement of $\tau_{g_{test\ path}}(\lambda_0)$, (i.e. $\Delta\tau_{g_{test\ path}}(\lambda_0) = \Delta\tau_{g_v}(\lambda_0)$). The uncertainty in the group delay is related to the uncertainty in the balance point according to

$$\frac{d\tau_{g_v}}{d\lambda_0} = D_v(\lambda)L_v \quad \text{Eq. D-10}$$

so that

$$\Delta\tau_{g_{test\ path}}(\lambda) = \Delta\tau_{g_v} = D_v(\lambda)L_v\Delta\lambda_0 \quad \text{Eq. D-11}$$

Which basically shows that increasing the second order dispersion of the dispersive virtual reference increases the slope of the simulated group delay curve, therefore an error in the wavelength axis is magnified in the group delay axis by an amount proportional to the slope of the group delay (the second order dispersion), as illustrated in Fig. D-2. If, for example, a first order dispersive virtual reference is used (see [Chapter 5.2.2.2](#)) then $D_v(\lambda)L_v = K/c$ and the error in the group delay measurement is related to the error in the balance point measurement as

$$\Delta\tau_{g_{test\ path}}(\lambda) = \frac{K}{c}L_v\Delta\lambda_0 \quad \text{Eq. D-12}$$

If a second order dispersive reference is used instead (see [Chapter 5.2.2.1](#)), then the $D_v(\lambda)L_v = -2Q\lambda_0/c$ and the error in the group delay measurement is related to the error in the balance point as

$$\Delta\tau_{g_{test\ path}}(\lambda) = \frac{2Q\lambda_0}{c}L_v\Delta\lambda_0 \quad \text{Eq. D-13}$$

However, to achieve the same compression we must have that $K = 2Q\lambda_0$ so that the error is approximately the same for both types of dispersive references (it is only slightly worse for the second order dispersive reference for small $\Delta\lambda_0$). The result is that using any dispersive reference results in an increased uncertainty in the group delay

measurement compared to standard (non-dispersive) VRI where the slope of the simulated group index curve is zero, so that there is no uncertainty in the group delay.

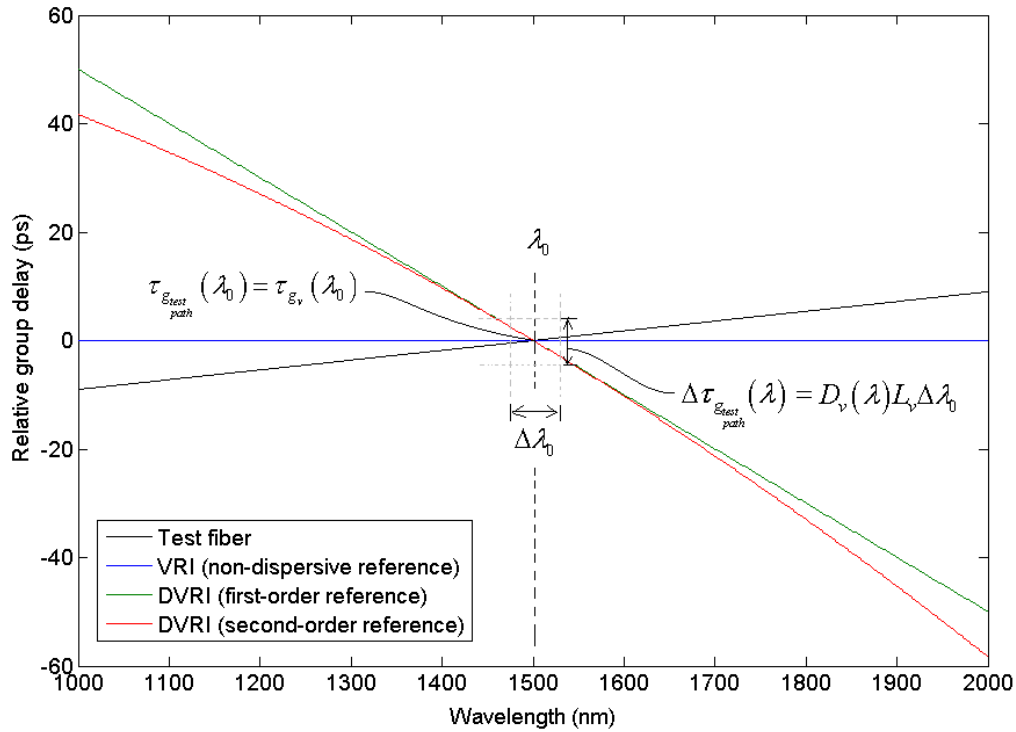


Fig. D-2. Comparison of uncertainty in the group delay measurement for VRI (non-dispersive virtual reference), DVRI with a first order dispersive reference, and DVRI with a second order dispersive reference. The illustration shows that VRI has no uncertainty in the group delay (slope is zero); however for DVRI the uncertainty depends on the slope of the simulated group delay curve (i.e. the simulated second order dispersion).

It should, however, be noted that a large $D_v(\lambda)L_v$ results in compression of the interference pattern which means that the peaks $\lambda_{-2}, \lambda_{-1}, \lambda_1, \lambda_2$ in Fig. D-1 are narrower. This means that the error in locating the peaks $|\Delta\lambda_{-2}|, |\Delta\lambda_{-1}|, |\Delta\lambda_1|, |\Delta\lambda_2|$ in Fig. D-1 is smaller. This results in a smaller $\Delta\lambda_0$, which mitigates the effect of the uncertainty introduced by the dispersive virtual reference. However, this effect does not negate the increased uncertainty of using a dispersive virtual reference. To show this, note that higher compression results in narrower peaks as well as a smaller minimum bandwidth. Therefore the width of the peaks is proportional to the minimum bandwidth. Which ultimately means that $\Delta\lambda_0 \propto B_{\min}(\lambda_0)$ and

$$\begin{aligned} \Delta\tau_{g_{test path}}(\lambda_0) &= D_v(\lambda_0)L_v\Delta\lambda_0 \\ &\propto D_v(\lambda_0)L_vB_{\min}(\lambda_0) \end{aligned} \tag{Eq. D-14}$$

where substitution of Eq. 5-12 into Eq. 5-17 and substitution of the result into Eq. D-14 gives

$$\Delta \tau_{\text{path}}^{\text{g}_{\text{test}}}(\lambda_0) \propto D_v(\lambda_0)L_v \left(\frac{6}{c|D_v(\lambda_0)L_v - D_f(\lambda_0)L_f|} \right)^{1/2} \lambda_0 \quad \text{Eq. D-15}$$

Typically $D_v(\lambda_0)L_v \gg D_f(\lambda_0)L_f$ so that $|D_v(\lambda_0)L_v - D_f(\lambda_0)L_f| \cong |D_v(\lambda_0)L_v|$ and

$$B_{\min}(\lambda_0) \cong \left(\frac{6}{c|D_v(\lambda_0)L_v|} \right)^{1/2} \lambda_0 \quad \text{Eq. D-16}$$

Using this approximation, Eq. D-15 becomes

$$\Delta \tau_{\text{path}}^{\text{g}_{\text{test}}}(\lambda_0) \propto \left(\frac{6|D_v(\lambda_0)L_v|}{c} \right)^{1/2} \lambda_0 \quad \text{Eq. D-17}$$

this shows that the increase in certainty in the balance point due to compression does not negate the increase in uncertainty in the group delay. An interesting insight into the dispersive reference can be obtained by re-substitution of Eq. D-16 back into Eq. D-17 to give

$$\Delta \tau_{\text{path}}^{\text{g}_{\text{test}}}(\lambda_0) B_{\min}(\lambda_0) \propto \Delta \tau_{\text{path}}^{\text{g}_{\text{test}}}(\lambda_0) \Delta \lambda_0 \propto \left(\frac{6}{c} \right) \lambda_0^2 \quad \text{Eq. D-18}$$

This result indicates that as the wavelength location (spatial) becomes known with greater certainty (due to compression), the group delay (temporal) is known with less certainty. This is effectively a statement of the uncertainty principle.

D.6. Effects of wavelength error on second order dispersion

In both VRI and DVRI the second order dispersion parameter is obtained by solving a system of equations in which the constants are determined using the peak locations of $\lambda_{-2}, \lambda_{-1}, \lambda_1, \lambda_2$ in Fig. D-1. The process for solving this system of equations is the same for both VRI and DVRI and is discussed in [Chapter 2.4.2](#).

The system of equations in both VRI and DVRI used to solve for the second order dispersion can be produced using Eq. 2-35 in [Chapter 2](#) or Eq. 5-11 in [Chapter 5](#).

$$\begin{aligned}
|\varphi(\lambda_2) - \varphi(\lambda_1)| &= 4\pi \left[\overbrace{\left[\frac{(\lambda_2 - \lambda_0)^2}{2!\lambda_2} - \frac{(\lambda_1 - \lambda_0)^2}{2!\lambda_1} \right]}^p \Delta(\lambda_0) \right. \\
&\quad \left. + \overbrace{\left[\frac{(\lambda_2 - \lambda_0)^3}{3!\lambda_2} - \frac{(\lambda_1 - \lambda_0)^3}{3!\lambda_1} \right]}^q \frac{d\Delta}{d\lambda} \Big|_{\lambda_0} \right] \square \pi \\
|\varphi(\lambda_{-2}) - \varphi(\lambda_{-1})| &= 4\pi \left[\overbrace{\left[\frac{(\lambda_{-2} - \lambda_0)^2}{2!\lambda_{-2}} - \frac{(\lambda_{-1} - \lambda_0)^2}{2!\lambda_{-1}} \right]}^r \Delta(\lambda_0) \right. \\
&\quad \left. + \overbrace{\left[\frac{(\lambda_{-2} - \lambda_0)^3}{3!\lambda_{-2}} - \frac{(\lambda_{-1} - \lambda_0)^3}{3!\lambda_{-1}} \right]}^s \frac{d\Delta}{d\lambda} \Big|_{\lambda_0} \right] \square \pi
\end{aligned} \tag{Eq. D-19}$$

where for standard VRI in a common path configuration

$$|\Delta(\lambda_0)| \equiv \frac{c}{\lambda_0} |D_f(\lambda_0) L_f| \tag{Eq. D-20}$$

and for DVRI in a common path configuration

$$|\Delta(\lambda_0)| \equiv \frac{c}{\lambda_0} |D_v(\lambda_0) L_v - D_f(\lambda_0) L_f| \tag{Eq. D-21}$$

(Please note that $\Delta\lambda_0$ refers to the absolute error in the location of the balance point whereas $|\Delta(\lambda_0)|$ refers to the second order dispersion length difference between the test and reference paths, the symbols may be confusing but have been chosen this way to follow convention and for consistency with the notation used in this thesis). The system of equations is used to solve for $|\Delta(\lambda_0)|$ by locating the peaks/valleys (i.e. $\lambda_{-2}, \lambda_{-1}, \lambda_1, \lambda_2$ in Fig. D-1) to calculate the constants p, q, r, s in Eq. D-19. Following the steps in [Chapter 2.4.2](#) that led to Eq. 2-38, $|\Delta(\lambda_0)|$ is given as

$$|\Delta(\lambda_0)| \equiv \frac{s - q}{2(ps - qr)} \tag{Eq. D-22}$$

Assuming that these constants are independent variables, the total absolute error in $|\Delta(\lambda_0)|$ can be determined using Eq. D-1. The elements of the sum are as follows

$$\frac{d|\Delta(\lambda_0)|}{dp} = \frac{-s(s-q)}{2(ps-qr)^2} \quad \text{Eq. D-23}$$

$$\frac{d|\Delta(\lambda_0)|}{dr} = \frac{q(s-q)}{2(ps-qr)^2} \quad \text{Eq. D-24}$$

$$\frac{d|\Delta(\lambda_0)|}{ds} = \frac{q(p-r)}{2(ps-qr)^2} \quad \text{Eq. D-25}$$

$$\frac{d|\Delta(\lambda_0)|}{d} = \frac{-s(p-r)}{2(ps-qr)^2} \quad \text{Eq. D-26}$$

Therefore the total absolute error in $|\Delta(\lambda_0)|$ can be found using Eq. D-1 as

$$\begin{aligned} \Delta|\Delta(\lambda_0)| &= \frac{1}{2(ps-qr)^2} \sqrt{s^2(s-q)^2 \cdot (\Delta p)^2 + q^2(s-q)^2 \cdot (\Delta r)^2} \\ &\quad + \frac{1}{2(ps-qr)^2} \sqrt{q^2(p-r)^2 \cdot (\Delta s)^2 + s^2(p-r)^2 \cdot (\Delta q)^2} \\ &= \frac{1}{2(ps-qr)^2} \sqrt{(s-q)^2 \cdot (s^2(\Delta p)^2 + q^2(\Delta r)^2)} \\ &\quad + \frac{1}{2(ps-qr)^2} \sqrt{(p-r)^2 \cdot (s^2(\Delta q)^2 + q^2(\Delta s)^2)} \end{aligned} \quad \text{Eq. D-27}$$

Note that Eq. D-27 gives the exact expression for the error but it can be simplified further if desired by assuming that the interference pattern is approximately symmetric (this essentially assumes low third order dispersion, which is approximately true for most fiber). Under this assumption $p \cong r$ and $s \cong q$ so that $(s-q)^2 \cong (p-r)^2$ and $q^2 \cong s^2$ so that Eq. D-27 can be simplified to the approximate expression

$$\Delta|\Delta(\lambda_0)| \cong \frac{s(p-r)}{2(ps-qr)^2} \sqrt{(\Delta p)^2 + (\Delta q)^2 + (\Delta r)^2 + (\Delta s)^2} \quad \text{Eq. D-28}$$

The total absolute error in $|\Delta(\lambda_0)|$ (in either the exact expression in Eq. D-27 or the approximate expression in Eq. D-28) is a function of the error in the constants (i.e. $\Delta p, \Delta q, \Delta r, \Delta s$), which are themselves determined by the error in locating the peaks/valleys (i.e. $|\Delta\lambda_{-2}|, |\Delta\lambda_{-1}|, |\Delta\lambda_1|, |\Delta\lambda_2|$ in Fig. D-1). Therefore the errors in the constant $\Delta p, \Delta q, \Delta r, \Delta s$ must also be determined. The errors in p and r can be determined using Eq. D-1 as

$$\Delta p = \sqrt{\left(\frac{\lambda_2^2 - \lambda_0^2}{2!\lambda_2^2}\right)^2 \cdot (\Delta\lambda_2)^2 + \left(\frac{\lambda_1^2 - \lambda_0^2}{2!\lambda_1^2}\right)^2 \cdot (\Delta\lambda_1)^2 + \left(\frac{(\lambda_1 - \lambda_0)}{\lambda_1} - \frac{(\lambda_2 - \lambda_0)}{\lambda_2}\right)^2 (\Delta\lambda_0)^2} \quad \text{Eq. D-29}$$

$$\Delta r = \sqrt{\left(\frac{\lambda_{-2}^2 - \lambda_0^2}{2!\lambda_{-2}^2}\right)^2 \cdot (\Delta\lambda_{-2})^2 + \left(\frac{\lambda_{-1}^2 - \lambda_0^2}{2!\lambda_{-1}^2}\right)^2 \cdot (\Delta\lambda_{-1})^2 + \left(\frac{(\lambda_{-1} - \lambda_0)}{\lambda_{-1}} - \frac{(\lambda_{-2} - \lambda_0)}{\lambda_{-2}}\right)^2 (\Delta\lambda_0)^2} \quad \text{Eq. D-30}$$

Note that λ_0 is an independent variable for p since it also depends on λ_{-1} and λ_{-2} in Eq. 2-24 and it is an independent variable for r since it also depends on λ_1 and λ_2 in Eq. 2-24. The errors in q and s can be determined using Eq. D-1 as

$$\Delta q = \sqrt{\left(\frac{(\lambda_2 - \lambda_0)^2 (2\lambda_2 + \lambda_0)}{3!\lambda_2^2}\right)^2 \cdot (\Delta\lambda_2)^2 + \left(\frac{(\lambda_2 - \lambda_0)^2 (2\lambda_2 + \lambda_0)}{3!\lambda_2^2}\right)^2 \cdot (\Delta\lambda_1)^2 + \left(\frac{(\lambda_1 - \lambda_0)^2}{2!\lambda_1} + \frac{(\lambda_2 - \lambda_0)^2}{2!\lambda_2}\right)^2 (\Delta\lambda_0)^2} \quad \text{Eq. D-31}$$

$$\Delta s = \sqrt{\left(\frac{(\lambda_{-2} - \lambda_0)^2 (2\lambda_{-2} + \lambda_0)}{3!\lambda_{-2}^2}\right)^2 \cdot (\Delta\lambda_{-2})^2 + \left(\frac{(\lambda_{-2} - \lambda_0)^2 (2\lambda_{-2} + \lambda_0)}{3!\lambda_{-2}^2}\right)^2 \cdot (\Delta\lambda_{-1})^2 + \left(\frac{(\lambda_{-1} - \lambda_0)^2}{2!\lambda_{-1}} + \frac{(\lambda_{-2} - \lambda_0)^2}{2!\lambda_{-2}}\right)^2 (\Delta\lambda_0)^2} \quad \text{Eq. D-32}$$

Note that λ_0 is an independent variable for q since it also depends on λ_{-1} and λ_{-2} in Eq. 2-24 and it is an independent variable for s since it also depends on λ_1 and λ_2 in Eq. 2-24. Therefore the total absolute error in $|\Delta(\lambda_0)|$ can be found by substitution of Eq. D-29, Eq. D-30, Eq. D-31 and Eq. D-32 into Eq. D-27 (or Eq. D-28).

D.6.1. Standard VRI

$|\Delta(\lambda_0)|$ was defined in Eq. D-20 for standard VRI in the common path configuration. Rearranging the terms in Eq. D-20 gives

$$|D_f(\lambda_0)L_f| \equiv \frac{\lambda_0}{c} |\Delta(\lambda_0)| \quad \text{Eq. D-33}$$

where $|D_f(\lambda_0)L_f|$ is a function of both $|\Delta(\lambda_0)|$ and λ_0 . Therefore the total absolute error in $|D_f(\lambda_0)L_f|$ may be found using Eq. D-1 as

$$\Delta |D_f(\lambda_0)L_f| = \sqrt{\left(\frac{d|D_f(\lambda_0)L_f|}{d\lambda_0}\right)^2 (\Delta\lambda_0)^2 + \left(\frac{\lambda_0}{c}\right)^2 (\Delta|\Delta(\lambda_0)|)^2} \quad \text{Eq. D-34}$$

Where the first term is due to the error in measuring the balance point and the second term is due to the error in $|\Delta(\lambda_0)|$ which is determined by Eq. D-27 (or Eq. D-28)

D.6.2. Dispersive VRI

$|\Delta(\lambda_0)|$ was defined in Eq. D-21 for DVRI in the common path configuration. Rearranging the terms in Eq. D-21 gives

$$|D_v(\lambda_0)L_v - D_f(\lambda_0)L_f| \equiv \frac{\lambda_0}{c} |\Delta(\lambda_0)| \quad \text{Eq. D-35}$$

where $|D_f(\lambda_0)L_f|$ is a function of both $|\Delta(\lambda_0)|$ and λ_0 . Therefore the total absolute error in $|D_f(\lambda_0)L_f|$ may be found using Eq. D-1 as

$$\Delta |D_v(\lambda_0)L_v - D_f(\lambda_0)L_f| = \sqrt{\left(\frac{d|D_v(\lambda_0)L_v - D_f(\lambda_0)L_f|}{d\lambda_0}\right)^2 (\Delta\lambda_0)^2 + \left(\frac{\lambda_0}{c}\right)^2 (\Delta|\Delta(\lambda_0)|)^2} \quad \text{Eq. D-36}$$

Where $D_v(\lambda_0)L_v$ is known from the simulation so there is no uncertainty in its value so that Eq. D-36 becomes

$$\Delta |D_f(\lambda_0)L_f| = \sqrt{\left(\frac{d|D_v(\lambda_0)L_v - D_f(\lambda_0)L_f|}{d\lambda_0}\right)^2 (\Delta\lambda_0)^2 + \left(\frac{\lambda_0}{c}\right)^2 (\Delta|\Delta(\lambda_0)|)^2} \quad \text{Eq. D-37}$$

Where the first term is due to the error in measuring the balance point and the second term is due to the error in $|\Delta(\lambda_0)|$ which is determined by Eq. D-27 (or Eq. D-28). The key difference between Eq. D-34 and Eq. D-37 is the first term. The slope of the second order dispersion curve of the virtual reference leads to uncertainty in the second order dispersion measurement due to uncertainty in the balance point. This is a similar effect observed in the group delay measurement. Note that we are assuming that the second order dispersion of the dispersive reference has an opposite sign to that of the fiber under test to achieve compression (as discussed in [Chapter 5](#)).

A special case occurs if a first order dispersive reference is used where $D_v(\lambda_0)L_v = K/c$ (see [Chapter 5.2.2.2](#)) since this means that $d|D_v(\lambda_0)L_v|/d\lambda_0 = 0$ and

$$\Delta |D_f(\lambda_0)L_f| = \sqrt{\left(\frac{d|D_f(\lambda_0)L_f|}{d\lambda_0}\right)^2 (\Delta\lambda_0)^2 + \left(\frac{\lambda_0}{c}\right)^2 (\Delta|\Delta(\lambda_0)|)^2} \quad \text{Eq. D-38}$$

Which is the same total absolute error as for VRI in Eq. D-34 (if we assume that the $\Delta|\Delta(\lambda_0)|$ term is similar for both VRI and DVRI and is small compared to the first term). This result might have been anticipated since a first order dispersive reference has a second order dispersion that is constant. Therefore the error in locating the balance point would have no effect on the simulated second order dispersion. This is a special case, however, since clearly if a second order dispersive reference is used (see [Chapter 5.2.2.1](#)) then $D_v(\lambda_0)L_v = -2Q\lambda_0/c$ which is a function of λ_0 and the error in the location of the balance point is magnified by the slope of the second order dispersion curve in the first term in Eq. D-37.

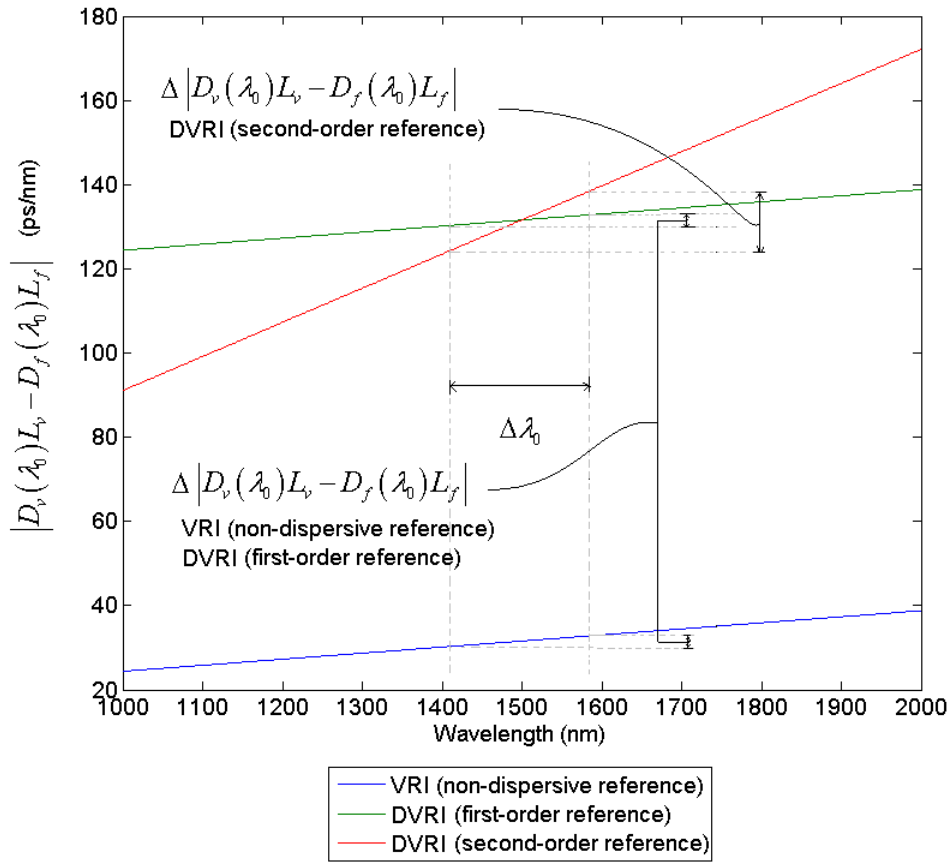


Fig. D-3. Comparison of uncertainty in the second order dispersion measurement using VRI (non-dispersive virtual reference), DVRI with a first-order dispersive reference, and DVRI with a second order dispersive reference. The illustration shows that both VRI and DVRI with a first order dispersive reference have no additional uncertainty in the second order dispersion plot, however for DVRI with a second order dispersive reference the uncertainty depends on the slope of the simulated second order dispersion curve (i.e. the simulated dispersion slope (or third order dispersion))

D.7. Conclusion

This appendix compared the uncertainty in the first and second order dispersion measurements made using VRI and DVRI (with both a first and second order dispersive reference). It showed that in DVRI the uncertainty in measuring the balance point wavelength is magnified by the slope of the dispersive virtual reference, thereby increasing the uncertainty in the group delay measurement compared to standard non-dispersive VRI. It also showed that if DVRI with a first order dispersive reference is used, then there is no additional uncertainty in the second order dispersion measurement compared to VRI. However, higher order dispersive references would increase the uncertainty. This shows that a first-order dispersive reference is the best choice when using DVRI. This appendix showed that, although DVRI is useful for enabling measurements that would otherwise be impossible (by compressing the interference so that the minimum bandwidth is less than that of the source), the cost of doing so is an increased uncertainty in the group delay measurement, which is an effect of the uncertainty principle. Therefore, if using DVRI is not necessary, the group delay can be measured with greater certainty by using VRI. If however, the objective of a particular experiment is to characterize the second order dispersion and the group delay is of no interest, then either VRI or DVRI (with a first order dispersive reference) will provide equivalent certainty.

Appendix E: Why BSI/VRI cannot be used to extract the phase or the effective index

In [Chapter 2.4.1](#) unbalanced spectral interferometry using the phase spectrum of a Fourier transform of the interference pattern was shown to be capable of extracting the phase from the interference pattern. This enables the extraction of the effective index of the fiber. Balanced spectral interferometry, however, removes the linear portion of the phase term (balanced by the reference arm), making it difficult to extract the phase directly. This section describes why balanced spectral interferometry (or virtual reference interferometry) cannot be used to extract the effective refractive index (it directly measures the group index or group delay). The phase of the interference pattern in balanced spectral interferometry is the same as the phase of the amplitude modulation of the second order interference pattern in virtual reference interferometry. This phase was given in Eq. 2-30 as

$$\varphi(\lambda) = 4\pi \left\{ \underbrace{\left(N_g(\lambda_0) L_f - L_{air} \right)}_{=0} + \left. \frac{dn_{eff_f}}{d\lambda} \right|_{\lambda_0} L_f \right. \\ \left. + \frac{(\lambda - \lambda_0)^2}{2! \lambda} \left. \frac{d^2 n_{eff_f}}{d\lambda^2} \right|_{\lambda_0} L_f + \frac{(\lambda - \lambda_0)^3}{3! \lambda} \left. \frac{d^3 n_{eff_f}}{d\lambda^3} \right|_{\lambda_0} L_f + \dots \right\} \quad \text{Eq. E-1}$$

where $L_{air} \equiv L_v$ in a virtual reference interferometry experiment. From this equation the group index \times length may be extracted using

$$N_g(\lambda_0) L_f = L_{air} \equiv L_v \quad \text{Eq. E-2}$$

where either L_{air} or L_v must be known (note that it is easier to determine L_v than L_{air} which must be measured). This comes from the fact that the balance point is the location where the phase function is minimized (not zero - see what happens in Eq. E-1 when $\lambda = \lambda_0$). As a result a plot of $N_g(\lambda_0)$ may be produced if L_f is known. The effective index is related to the group index as

$$N_g(\lambda) = n_{eff}(\lambda) - \lambda \left. \frac{dn_{eff}}{d\lambda} \right|_{\lambda} \quad \text{Eq. E-3}$$

One might consider the possibility of extracting a plot of $n_{eff}(\lambda)$ from the plot of $N_g(\lambda)$ given that this is a first order differential equation for which $n_{eff}(\lambda)$ may be solved for a given boundary condition. If this equation is written in standard form

$$\left. \frac{dn_{eff}}{d\lambda} \right|_{\lambda} - \frac{1}{\lambda} n_{eff}(\lambda) = -\frac{1}{\lambda} N_g(\lambda) \quad \text{Eq. E-4}$$

it may be solved by multiplying both sides by an integrating factor $\mu(\lambda) = 1/\lambda$

$$\frac{1}{\lambda} \frac{dn_{eff}}{d\lambda} \bigg|_{\lambda} - \frac{1}{\lambda^2} n_{eff}(\lambda) = -\frac{1}{\lambda^2} N_g(\lambda) \quad \text{Eq. E-5}$$

and noticing that the left hand side can be simplified using the chain rule

$$\frac{1}{\lambda} \frac{dn_{eff}}{d\lambda} \bigg|_{\lambda} - \frac{1}{\lambda^2} n_{eff}(\lambda) = \frac{d}{d\lambda} \bigg|_{\lambda} \left[\frac{n_{eff}}{\lambda} \right] \quad \text{Eq. E-6}$$

so that the expression becomes

$$\frac{d}{d\lambda} \bigg|_{\lambda} \left[\frac{n_{eff}}{\lambda} \right] = -\frac{1}{\lambda^2} N_g(\lambda) \quad \text{Eq. E-7}$$

integrating both sides gives the solution

$$n_{eff}(\lambda) = \frac{\int -\frac{1}{\lambda^2} N_g(\lambda) d\lambda}{1/\lambda} \quad \text{Eq. E-8}$$

Since the integral has no limits the result includes an arbitrary constant. For example, if the group index curve is fit using a second order polynomial

$$N_g(\lambda) = C\lambda^2 + B\lambda + A \quad \text{Eq. E-9}$$

where the parameters A, B, C are determined from the fit, Eq. E-9 may be solved as

$$n_{eff}(\lambda) = -C\lambda^2 - B\lambda \ln|\lambda| + A + Q\lambda \quad \text{Eq. E-10}$$

where Q is an unknown constant that can only be determined by knowledge of the boundary conditions, which cannot be determined experimentally. An additional problem is that the group index curve for most fiber is approximately linear and the experimental plot will contain noise. The noise introduces errors into the fit, resulting in error in the effective index curve. Since the technique that measures phase directly using the phase of a Fourier transform ([Chapter 2.4.1.1](#)) does not require a fit it is not susceptible to this noise. As a result, for measuring the effective index, the technique that measures phase directly using the phase of a Fourier transform would be the best way to measure the effective index. A summary of the capabilities of each measurement type follows in Table E.2.1.

Table E.2.1: Capabilities of each measurement type

Measurement	USI (FT Phase)	USI (FT Amplitude)	BSI/VRI
Effective index (phase)	√		
Group index (group delay)		√*	√
Second order dispersion			√

Appendix F: Matlab code

F.1. Matlab code to simulate SMF28

```
clear all
close all
clc
format long

% Part 1 - Generate neff curve for GeO2 doped silica fiber using weighted average in Kobayashi Paper
%%%%%%%%%%%%%%%%%%%%%%%%%%%%%%%%%%%%%%%%%%%%%%%%%%%%%%%%%%%%%%%%%%%%%%%%
% 1. a) Declare all values for SMF28
a = 3.88e-6; % Spec is a = 4.1e-6 (3.88e-6)
Lf = 0.200577;
NA_1310 = 0.1228; % NA_1310 = 0.1227 Spec is 0.14 but this was adjusted so that the Specs Ng(1550nm) =
1.4682 and refractive index difference <0.36% (Used 0.109)
Vnumber_1310 = (2*pi/(1310*10^-9))*a*NA_1310
% 1. b) Declare all values for the simulation
wavestep = 0.001;
wavestart = 1.470;
wavestop = 1.605;
neff_step = 0.5*10^-7; % Resolution of neff step calculation (Resolution of LS = RS measurement)

% 1. b) Solve for A given delta_n
%%%%%%%%%%%%%%%%%%%%%%%%%%%%%%%%%%%%%%%%%%%%%%%%%%%%%%%%%%%%%%%%%%%%%%%%
lambda_sim = 1.310; % micron units -- This is the wavelength where delta_n is as indicated
% Cladding Kobayashi
Aa1 = 0.6961663; Aa2 = 0.4079426; Aa3 = 0.8974994; Ab1 = 0.004679148; Ab2 = 0.01351206; Ab3 = 97.934002;
nclad_1310 = ( 1 +((Aa1*lambda_sim.^2)/(lambda_sim.^2-Ab1)) + ((Aa2*lambda_sim.^2)/(lambda_sim.^2-Ab2)) +
((Aa3*lambda_sim.^2)/(lambda_sim.^2-Ab3)) ).^(0.5);

% Core at 1310nm
ncore_1310 = sqrt(NA_1310^2 + nclad_1310^2);
delta_n = ncore_1310 - nclad_1310;

% Core GeO2 3.5m% Doped
Ca1 = 0.7042038; Ca2 = 0.4160032; Ca3 = 0.9074049; Cb1 = 0.00264623; Cb2 = 0.0166823; Cb3 = 97.93390;
ncore2_1310 = ( 1 +((Ca1*lambda_sim.^2)/(lambda_sim.^2-Cb1)) + ((Ca2*lambda_sim.^2)/(lambda_sim.^2-Cb2)) +
((Ca3*lambda_sim.^2)/(lambda_sim.^2-Cb3)) ).^(0.5);

% Core GeO2 5.8m% Doped
Da1 = 0.7088896; Da2 = 0.4206803; Da3 = 0.8956551; Db1 = 0.00370945; Db2 = 0.01573806; Db3 = 97.93402;
ncore3_1310 = ( 1 +((Da1*lambda_sim.^2)/(lambda_sim.^2-Db1)) + ((Da2*lambda_sim.^2)/(lambda_sim.^2-Db2)) +
((Da3*lambda_sim.^2)/(lambda_sim.^2-Db3)) ).^(0.5);

A = (ncore3_1310 - (ncore_1310)) / (ncore3_1310 - ncore2_1310);

% 1. c) Plot the curve for the new core index ncoreNew
%%%%%%%%%%%%%%%%%%%%%%%%%%%%%%%%%%%%%%%%%%%%%%%%%%%%%%%%%%%%%%%%%%%%%%%%
lambda_sim = wavestart:wavestep:wavestop; % micron units
% Cladding Kobayashi
Aa1 = 0.6961663; Aa2 = 0.4079426; Aa3 = 0.8974994; Ab1 = 0.004679148; Ab2 = 0.01351206; Ab3 = 97.934002;
nclad = ( 1 +((Aa1*lambda_sim.^2)/(lambda_sim.^2-Ab1)) + ((Aa2*lambda_sim.^2)/(lambda_sim.^2-Ab2)) +
((Aa3*lambda_sim.^2)/(lambda_sim.^2-Ab3)) ).^(0.5);

% Core GeO2 3.5m% Doped
Ca1 = 0.7042038; Ca2 = 0.4160032; Ca3 = 0.9074049; Cb1 = 0.00264623; Cb2 = 0.0166823; Cb3 = 97.93390;
ncore2 = ( 1 +((Ca1*lambda_sim.^2)/(lambda_sim.^2-Cb1)) + ((Ca2*lambda_sim.^2)/(lambda_sim.^2-Cb2)) +
((Ca3*lambda_sim.^2)/(lambda_sim.^2-Cb3)) ).^(0.5);

% Core GeO2 5.8m% Doped
Da1 = 0.7088896; Da2 = 0.4206803; Da3 = 0.8956551; Db1 = 0.00370945; Db2 = 0.01573806; Db3 = 97.93402;
ncore3 = ( 1 +((Da1*lambda_sim.^2)/(lambda_sim.^2-Db1)) + ((Da2*lambda_sim.^2)/(lambda_sim.^2-Db2)) +
((Da3*lambda_sim.^2)/(lambda_sim.^2-Db3)) ).^(0.5);

ncoreNew = A*ncore2 + (1-A)*ncore3; % New core index using weighted average of core indices that produce index
steps between 0.008876 and 0.01222

% 2. a) Simulate neff for the modes
%%%%%%%%%%%%%%%%%%%%%%%%%%%%%%%%%%%%%%%%%%%%%%%%%%%%%%%%%%%%%%%%%%%%%%%%
lambda = lambda_sim; % Stay in micron units
n2_wavelength = nclad;
n1_wavelength = ncoreNew;

for j=1:round((wavestop-wavestart)/wavestep)+1
```

```

ko = 2*pi/(lambda(j)*10^-6);
neff = n2_wavelength(j)+(10^-20):(neff_step):n1_wavelength(j)-(10^-20);
u = ko*a*(n1_wavelength(j)^2 - neff.^2).^0.5;
w = ko*a*(neff.^2 - n2_wavelength(j)^2).^0.5;
v = ko*a*(n1_wavelength(j)^2 - n2_wavelength(j)^2)^0.5;
LS = (besselj(0,u)./(u.*besselj(1,u)));
RS = (besselk(0,w)./(w.*besselk(1,w)));
LP0m = LS - RS;
% Find the zero crossings - Two zero crossings will be found
count = 1;
for k=1:length(LP0m)-1
    if ((LP0m(k) <= 0) && (LP0m(k+1)>= 0))
        uvalue(count) = u(k); % No linear
interpolation
        uvalue(count) = (u(k+1)-u(k))*((-1*LP0m(k))/(LP0m(k+1)-LP0m(k))) + u(k); % Linear interpolation
for higher accuracy
        count = count + 1;
    end
end
neff01(j) = (n1_wavelength(j)^2 - (uvalue(length(uvalue))^2/(ko*a)^2))^0.5;
end

Clight = 299792458.6; % m/s

% 4. a) Numerical differentiation to obtain simulated group delay and dispersion directly from calculated
values (i.e. No fit)
%%%%%%%%%%%%%%%%%%%%%%%%%%%%%%%%%%%%%%%%%%%%%%%%%%%%%%%%%%%%%%%%%%%%%%%%
% Group delay (ps)
%%%%%%%%%%%%%%%%%%%%%%%%%%%%%%%%%%%%%%%%%%%%%%%%%%%%%%%%%%%%%%%%%%%%%%%%
% numerical differentiation
dlambda = diff(lambda);
dneff01 = diff(neff01);

% make same size
neff01 = neff01(1:length(neff01)-1);
lambda = lambda(1:length(lambda)-1);

% Generate Group Index values
Ng01 = neff01 - (lambda.*(dneff01./dlambda));
GD01 = (Ng01/299792458.6)*10^12*Lf; % Group delay in ps

% Fit to directly calculated Group Delay
%%%%%%%%%%%%%%%%%%%%%%%%%%%%%%%%%%%%%%%%%%%%%%%%%%%%%%%%%%%%%%%%%%%%%%%%
% GD01_fit = polyfit(lambda, GD01, 2); % Fit vs. lambda in um units then convert to nm units so that
slope is in ps/nm
% D01_fitted(1) = 2*GD01_fit(1);
% D01_fitted(2) = 1*GD01_fit(2);
% D01_simulated = polyval(D01_fitted, lambda)*10^-3; % *10^-3 to convert to per nm units

GD01_fit = polyfit(lambda, GD01, 4); % Fit vs. lambda in um units then convert to nm units so that
slope is in ps/nm
D01_fitted(1) = 4*GD01_fit(1);
D01_fitted(2) = 3*GD01_fit(2);
D01_fitted(3) = 2*GD01_fit(3);
D01_fitted(4) = 1*GD01_fit(4);
D01_simulated = polyval(D01_fitted, lambda)*10^-3; % *10^-3 to convert to per nm units

% Dispersion using equation in SMF spec sheet
So = (0.086/1000); % ps/nm^2-km % Note: spec reads So = 0.086 ps/nm^2-km
lambda0_sim = 1313; % nm
D_eqtn = (So/4)*(lambda*10.^3 - (lambda0_sim^4./(lambda*10^3).^3)*Lf; %ps/nm

% 5. Import Experimental Measurement Data
%%%%%%%%%%%%%%%%%%%%%%%%%%%%%%%%%%%%%%%%%%%%%%%%%%%%%%%%%%%%%%%%%%%%%%%%
load DVRI_Wavelength.txt % Wavelength in nm
load DVRI_GroupDelay.txt % Group Delay in ps units
load DVRI_Dispersion.txt % Dispersion in ps/nm units

load VRI_Wavelength.txt % Wavelength in nm
load VRI_GroupDelay.txt % Group Delay in ps units
load VRI_Dispersion.txt % Dispersion in ps/nm units

% 6. Output Results
%%%%%%%%%%%%%%%%%%%%%%%%%%%%%%%%%%%%%%%%%%%%%%%%%%%%%%%%%%%%%%%%%%%%%%%%
figure
plot(lambda*10^3, GD01, DVRI_Wavelength, DVRI_GroupDelay, '.', VRI_Wavelength, VRI_GroupDelay, 'x' )
xlabel('Wavelength (nm)')
ylabel('Group Delay (ps/m)')
title('Numerically Computed values for Group Delay vs. wavelength')

```

```

legend('GD01 Matlab sim', 'GD01 Measured DVRI', 'GD01 Measured VRI')

figure
plot(lambda*10^3, D01_simulated,lambda*10^3, D_eqtn, DVRI_Wavelength, DVRI_Dispersion, '.', VRI_Wavelength,
VRI_Dispersion, 'x' )
xlabel('Wavelength (nm)')
ylabel('D (ps/nm)')
title('D from fit to Numerically Computed values for GD')
legend('D01 from Matlab sim','D01 from SMF28 spec sheet Eqtn', 'D01 from DVRI measurement', 'D01 from VRI
measurement')

% 6. Check compliance with specified parameters
%%%%%%%%%%%%%%%%%%%%%%%%%%%%%%%%%%%%%%%%%%%%%%%%%%%%%%%%%%%%%%%%%%%%%%%%
lambda_1550_index = 0;
for i = 1:length(lambda)
    if lambda(i) == 1.55
        lambda_1550_index = i;
    end
end
lambda(lambda_1550_index)
Ng_at_1550 = Ng01(lambda_1550_index)
percentdiff_1310 = (delta_n/ncore_1310)*100

% 7. Ouput simulated values for group delay and dispersion x length (to put in Excel file)
%%%%%%%%%%%%%%%%%%%%%%%%%%%%%%%%%%%%%%%%%%%%%%%%%%%%%%%%%%%%%%%%%%%%%%%%
% output1 = [lambda*10^3; GD01];
% dlmwrite('GroupDelay_simulation.txt', output1 , 'delimiter', '\t','newline', 'pc', 'precision', 10)
%
% output2 = [lambda*10^3; D01_simulated];
% dlmwrite('Dispersion_simulation.txt', output2 , 'delimiter', '\t','newline', 'pc', 'precision', 10)

```

Copyright acknowledgements

I would like to acknowledge Optics Letters, Journal of the Optical Society of America B, Optics Express and Photonics Technology letters for allowing me to use my published (adapted) graphs and figures in this thesis.

